

High-temperature plasmonic and photonic structures for thermophotovoltaic use

A DISSERTATION PRESENTED
BY
ALEXANDER SYLVESTER ROBERTS
TO
SDU NANO OPTICS

IN PARTIAL FULFILMENT OF THE REQUIREMENTS
FOR THE DEGREE OF
PHD
IN THE SUBJECT OF
FUNCTIONAL MATERIALS AND NANOTECHNOLOGY

UNIVERSITY OF SOUTHERN DENMARK
ODENSE, DENMARK
JUNE 2017

HIGH-TEMPERATURE PLASMONIC AND PHOTONIC
STRUCTURES FOR THERMOPHOTOVOLTAIC USE

© 2017 - *ALEXANDER SYLVESTER ROBERTS*

ALL RIGHTS RESERVED.

NO PART OF THIS PUBLICATION MAY BE REPRODUCED, TRANSMITTED OR TRANSLATED IN ANY FORM OR BY ANY MEANS, ELECTRONIC OR MECHANICAL, INCLUDING PHOTOCOPY, RECORDING, OR ANY INFORMATION STORAGE AND RETRIEVAL SYSTEM, WITHOUT PRIOR PERMISSION IN WRITING FROM THE AUTHOR.

SUMMARY

This PhD thesis presents investigations of plasmonic and photonic selective thermal emitters and solar absorbers with high-temperature stability designed for thermophotovoltaic energy conversion and, in the case of selective solar absorbers, solar-thermal applications. The optical properties of the emitting and absorbing structures are designed and optimised by analytical and numerical methods, and subsequently fabricated by either electron-beam lithography, focussed-ion beam milling or lithography-free thin-film deposition techniques. Emitting and absorbing structures are characterised with regard to the optical properties by linear reflectance spectroscopy, Fourier-transform infrared spectroscopy and thermal emission measurements. The thermal stability of the spectrally selective surfaces is investigated by annealing in vacuum, inert atmosphere or ambient atmospheric conditions. Various other measurement techniques are drawn upon to determine other properties as necessary.

The thesis is structured as follows: The thesis consists of two main blocks. The first part contains chapters 1 - 6. chapter 1 provides an introduction to the subject of thermophotovoltaics. Chapter 2 contains an introduction to the optics of interfaces based on the transfer-matrix formalism which conveniently finds exact solutions to Maxwell's equations for both the photonic and plasmonic modes of interest in this thesis within a unified framework. An introduction to thermal radiation and the design of selective thermal emitters and selective solar absorbers is presented in 3. chapters 4 and 5 and provides an overview of results obtained during the research project, where chapter 4 reviews the results of the investigation of emitting and absorbing structures, with the main focus on decisions leading to each investigation and conclusions drawn. ?? describes the ongoing work with a thermophotovoltaic prototype. Chapter 6 concludes the first part of the thesis with an outlook and perspective on the research presented.

The second part of thesis, comprising appendices A to F, contains publications which have resulted from the work during my PhD.

RESUMÉ

Denne Phd afhandling præsenterer resultater opnået indenfor forskningen i plasmoniske og fotoniske termiske emittere med høj termisk modstandsdygtighed, egnet til anvendelse i termofotovoltaiske anvendelser, og i tilfældet af absorbere, til termosolare anvendelser. De optiske egenskaber af de udstrålende overflader designes og optimeres ved hjælp af numeriske og analytiske metoder og fabrikeres vha. elektronstråle litografi, FIB (focussed ion-beam milling) eller tyndfilmsdeponering. De optiske egenskaber af de fremstillede strukturer karakteriseres ved hjælp af lineær reflektansspektroskopi, FTIR (Fourier-transform infrarød) spektroskopi, og ved hjælp af målinger af den termiske udstråling. Modstandsdygtigheden overfor høje temperaturer undersøges ved udglødning (annealing) i enten vakuum, inert atmosfære eller i almindelig atmosfærisk luft. En række andre målemetoder tages i anvendelse efter behov.

Afhandlingen er struktureret som følgende: Den første del består af kapitlerne 1 - 6. Kapitel 1 giver en indledning i emnet termofotovoltaik. Kapitel 2 præsenterer transfermatrix-metoden som danner et teoretisk grundlag for diskussionen af både plasmoniske og fotoniske strukturer indenfor en fælles ramme. En indledning til termisk udstråling og designet af termiske emittere til termofotovoltaiske og termosolare anvendelser gives i chapter 3. Kapitel 4 og 5, giver et overblik over de opnåede resultater i løbet af forskningsprojektet. Kapitel 4 er en beskrivelse af resultater opnået indenfor forskningen i selektivt emitterende og absorberende overflader, med fokus beslutninger mellem delprojekter og konklusioner. Kapitel 5 præsenterer nuværende status indenfor arbejdet med design, fremstilling og evaluering af en termofotovoltaisk prototype. Kapitel 6 afslutter første del af afhandlingen med et perspektiverende udsyn.

Den anden del af afhandlingen, bestående af Appendiks A-F, indeholder de hidtil udgivne publikationer.

PREFACE

This PhD thesis presents results obtained during my PhD study at SDU Nano Optics at the University of Southern Denmark, from November 2013 to June 2017 under the supervision Professor Dr. Scient. Sergey I. Bozhevolnyi. The project included a five months research stay at the research groups of Professor Alexandra Boltasseva and Professor Vladimir Shalaev at the Birck Nanotechnology Park, Purdue University in Indiana, USA. The subjects of the Ph.D. thesis are selective solar absorbers and selective emitters for thermophotovoltaics.

The thesis is based on five scientific journal papers, which are appended in appendices A to E, and two manuscripts which are under preparation. Main results from the two manuscripts under preparation are included in chapter 4. Another manuscript is in review at the time of writing and can therefore not be included in the thesis. Involvement in various other research projects has resulted in one additional publication so far, which is enclosed in appendix F. A complete list of my publications can be found in the list of publications.

Acknowledgement

I would like to extend my deepest thanks to my supervisor, Prof. Dr. Sergey I. Bozhevolnyi for his skilful guidance and encouragement during the course of my Ph.D., without which constant progress would certainly not have been guaranteed.

I would also like to sincerely thanks to Professors Alexandra Boltasseva and Vladimir Shalaev for generously offering me the possibility of visiting their inspiring research group at Birck Nanotechnology center, Purdue University, Indiana, USA.

Thanks to Kasper Thilsing-Hansen for his invaluable help and guidance in the cleanroom, and Thomas Søndergaard and Anders Pors for many fruitful and insightful discussions and for their excellent contributing with both numerical simulations and priceless knowledge of analytical optics. Thanks to Manohar Chirumamilla, who has been my collaborator throughout this project, for his tireless work in the cleanroom and laboratories at Aalborg University.

I would like to thank many more for interesting and challenging discussions, Ole Albrektsen, Michael G. Nielsen, Sebastian K. H. Andersen, Jonas Beermann, Shailesh Kumar, Nathaniel Kinsey, Mikhail Shalaginov, René L. Eriksen, Morten Henneberg, Jacek Fiutowski and Kjeld Pedersen and many others deserving of mentioning here. I would finally also like to thank all collaborators not explicitly mentioned above and my colleagues at SDU Nano Optics for creating a pleasant social environment and for all of the interesting and entertaining discussions over lunch or in the laboratory.

Table of contents

List of acronyms	xi
List of variables	xiii
1 Introduction	1
1.1 The Shockley-Queisser limit	2
1.2 Minimizing losses	4
1.3 The economy of thermophotovoltaics	6
1.4 The broader case for spectral control	7
2 Optics of interfaces	9
2.1 Maxwell's equations	9
2.2 Propagating solutions	12
2.3 Boundary conditions at planar interfaces	12
2.4 The transfer matrix method	15
2.5 Surface plasmon polaritons	21
2.5.1 Surface plasmon polaritons	22
2.5.2 Gap surface plasmons	24
3 Thermal emission	27
3.1 Blackbody radiation	27
3.2 Thermal radiation of real surfaces	31
3.3 The view factor	32
3.4 Illumination of a photovoltaic band gap material	34
3.5 Selective solar absorbers	36
4 Spectrally selective surfaces	39
4.1 Plasmonic colour printing	39
4.2 Trench gap surface plasmon resonators	40
4.3 Continuous-layer Fabry-Pérot Resonators	42

4.4	Gold-based continuous-layer Fabry-Pérot resonators (cl-FPRs)	45
4.5	Titanium nitride-based continuous-layer Fabry-Pérot resonators (cl-FPRs)	46
4.6	Multilayer tungsten solar absorbers	48
5	Prototype evaluation of selective emitters	51
5.1	Prototype description	51
5.2	TPV efficiency with a bi-layer Tungsten-dielectric emitter	55
6	Outlook	63
Reprint of papers		
Appendix A	Subwavelength Plasmonic Color Printing ...	65
Appendix B	Near-infrared tailored thermal emission ...	75
Appendix C	Light extinction and scattering from individual and arrayed ...	85
Appendix D	Multilayer tungsten-alumina-based broadband light absorbers ...	101
Appendix E	Hot-spot Engineering in 3D Multi-branched Nanostructures ...	113
Appendix F	Excitation of surface plasmon polariton modes with multiple NV centers ...	133
Authorship agreements		147
References		155
List of publications		
	Articles in peer-reviewed journals	163
	Presentations	164

List of acronyms

2d	Two-dimensional
AC	Alternating current
AE	Absorber-emitter
ALD	Atomic layer deposition
AM_{1.5}	Air-mass coefficient: 1.5
BB	Blackbody
BE	Bose-Einstein
CHP	Combined heat and power generation
cl-FPR	Continuous-layer Fabry-Pérot resonator
CMOS	Complementary metal-oxide-semiconductor
CNT	Carbon nano-tube
CVD	Chemical vapour deposition
DC	Direct current
EBL	Electron-beam lithography
EHP	Electron-hole pair
EQE	External quantum efficiency
FD	Fermi-Dirac
FIB	Focussed ion-beam
FOM	Figure of merit
GSP	Gap surface plasmon
GSP-FPR	Gap surface plasmon Fabry-Pérot resonator
GSPR	Gap surface plasmon resonator
IMI	Insulator-metal-insulator

ITO	Indium tin oxide
IV	Current-voltage
MIM	Metal-insulator-metal
NIR	Near infrared
PV	Photovoltaic
PVC	Photovoltaic cell
RF	Radio-frequency
RMS	Root mean square
SA	Solar absorber
SE	Selective emitter
SIMS	Secondary-ion mass spectroscopy
SPP	Surface plasmon-polariton
SQL	Shockley-Queisser limit
SSA	Selective solar absorber
STPV	Solar thermophotovoltaics
TE	Transverse-electric
tGSPR	Trench gap surface plasmon resonator
TiN	Titanium nitride
TM	Transverse-magnetic
TMM	Transfer-matrix method
TPV	Thermophotovoltaics
TPVC	Thermophotovoltaic cell
UHV	Ultra high vacuum
VF	View factor

List of variables

B	Magnetic flux density
c	Vacuum speed of light
D	Electric displacement
E	Electric field
ϵ_0	Vacuum permittivity
η_C	Carnot efficiency
η_{rec}	Efficiency due to recombination
η_u	Ultimate efficiency
η_Z	Efficiency of impedance matching
H	Magnetic field strength
I_{MP}	Current at maximum power
I_{SC}	Short-circuit current
J_{ext}	External (free) current density
J_{tot}	Total current density
k	Wave vector
M	Magnetisation field
μ_0	Vacuum permeability
∇	Nabla differential operator
ω	Angular frequency
P	Polarisation field
P_{MP}	Maximum power
ρ_{ext}	External (free) charge density
ρ_{tot}	Total charge density

θ_j	Angle to optical axis in medium j
u	Spatial energy density
V_{MP}	Voltage at maximum power
V_{OC}	Open-circuit voltage

Chapter 1

Introduction

Human annual energy consumption approached 14 gigatonnes of oil equivalent in 2014, corresponding to an average power consumption nearly 19 TW [1]. At this rate oil, coal and nuclear power sources have the capacity to power human endeavours for many centuries to come. However, no current solutions exist for the safe and long-term storage and management of the emissions and waste products from either fossil or nuclear fuels. Exhausts from fossil fuel combustion are primarily disposed of by dilution in the atmosphere, with ensuing direct risks to human health and indirect risks through adverse consequences of climate change. While the severity of risks emerging from fissile nuclear power is more hotly debated, it is clear that the concentration of years worth of fissile material near and in reactors leads to some degree of vulnerability to attacks and accidents. The same can be said for the storage of fissile waste products, which require management for many years into the future to ensure safe storage and restricted access. In either case, significant risks and costs arise immediately and persist for generations after the original energy conversion. Moreover, natural deposits of fossil and nuclear fuels tend to be concentrated in certain geographic regions, leading potentially to political instability and unwanted supply dependency. These reasons, amongst others, are strong motivators driving the development of alternative sources and storage forms of energy with the ability or potential to provide commercially viable sources of energy, ideally with little or no adverse environmental and economic long-term impact. In particular, solar conversion has seen a drastic decrease in the cost per kilowatt-hour in recent years and has in recent public tenders been able to outcompete coal on price-per-Watt without subsidies, albeit in the sunnier parts of the world. It is only reasonable to assume a long-term continuation of the downward price trend of photovoltaic (PV) energy since research and scaling of production will likely intensify as the solar energy market grows. While interesting in its own right, this development also affects the viability of technologies which are derived from photovoltaic cells (PVCs), most notably thermophotovoltaics (TPV).

TPV is such an area of energy conversion; here a PVC is illuminated by a man-made thermal emitter, as opposed to the thermal emission from the sun. This approach to the utilisation of a PVC allows one to shape the spectrum of the illuminating light and in doing so to address two of the main drawbacks of conventional PV operation. Firstly, it is possible to eliminate some of

the inefficiencies associated with the properties of the solar light. Secondly, it becomes possible to increase the efficiency of existing energy conversion by using excess or waste heat to cogenerate electricity in combustion or other high-temperature processes.

1.1 The Shockley-Queisser limit

The conversion of solar energy into electric power is performed primarily with photovoltaic (PV) cells, a semiconductor device which functions by absorbing (solar) photons in a process which creates one pair of charged particles per absorbed photon, a so-called electron-hole pairs (EHPs). Electrons and holes are separated and build up at separate electrodes of the cell, which in turn builds up a potential difference that can be used to drive an electrical load. However, the PVC is subject to several inefficiencies which limit the maximum efficiency possible for PVC.

The first limit to the efficiency is the *spectrum loss*, which occurs because the energies of the photons do not match the energy of the created EHPs. The energy of an EHP is determined by the properties of the PVC; therefore the extractable energy of an EHP is fixed for a given cell (and fixed load conditions). The fixed energy per EHP poses a problem when converting light originating from thermal emission, such as the sun, as thermal emission provides a broad range of photonic energies (fig. 1.1a) while the outcome of the absorption process is given by how the energy of the photon compares to the band gap energy of the photovoltaic material. Since the energy for creation of one EHP, is supplied by a single photon, any mismatch between the band gap energy and the photon energy leads to either partial or total waste of the photon energy. For a photon possessing more energy than necessary to create an EHP, the excess energy is lost as heat in a process known as thermalisation, in which the excited electron undergoes a series of non-radiative scattering processes with lattice phonons until it reaches the bottom of the conduction band. If, however, the photon does not possess the necessary energy, it cannot contribute at all to the generation of electricity, and its energy is entirely unavailable. This mechanism constitutes by far the single largest fundamental limit to PVC efficiency, setting an upper limit at 44 %, if it is assumed that the blackbody at 6000 K and the material used is silicon [2]. This limit is known as the ultimate limit μ , as it poses the upper limit to the energy that can be extracted by a photovoltaic process with a cut-off and a solar spectrum. This loss mechanism is the primary efficiency limitation to the conversion of sunlight, setting an upper limit of 44 % if the sun is assumed to be blackbody at 6000 K.

The second source of losses is the reverse process of photon absorption: the annihilation of an electron and a hole under the creation of a photon. Since it is the reverse process of the desired photon absorption, this process cannot be forbidden and will inevitably occur in the cell (at some rate) - a process called *recombination*, causing the cell to give off thermal radiation at wavelength at which it absorbs, in correspondence with Kirchhoff's law of thermal radiation. An ideal PVC, which is entirely non-absorbing at energies below its band gap E_B and fully absorbs all photon with energies above E_B , ultimately emits like a blackbody for photon energies with $hc/\lambda \geq E_B$, see fig. 1.1b.

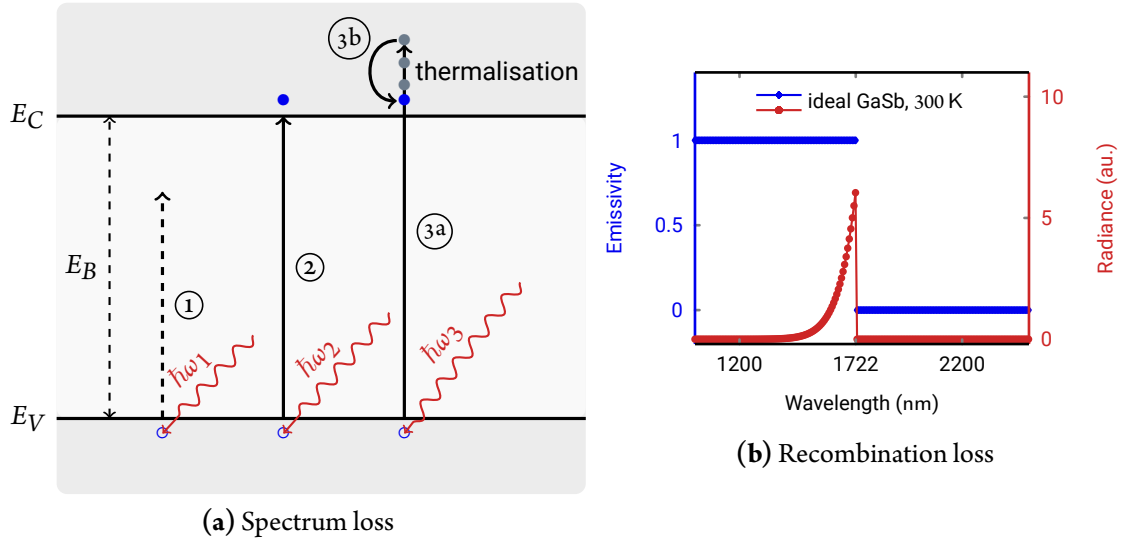


Figure 1.1: Illustration of spectrum losses (a) and thermal re-radiation due to recombination of charge carriers (b). (a) Schematic band diagram showing the effect of the cut-off exhibited by a photovoltaic device. Three distinct cases are shown: ① An incoming photon with energy $\hbar\omega_1 < E_B$ cannot excite an electron-hole pair. Its energy is entirely unavailable. ② An incoming photon has exactly the energy that is required to create an electron-hole pair, i.e. $\hbar\omega_2 = E_B$. Photons with this energy are converted with the highest efficiency. ③ In the case where the absorbed photon has an energy larger than the bandgap of the semiconductor (③a), $\hbar\omega_3 > E_B$, the excess energy is rapidly lost to phonons and the excited electron is thermalised to the lower edge of the conduction band (③b). (b) Emissivity of an ideal GaSb pn -junction with a band gap energy corresponding to a wavelength of 1722 nm (blue) and resulting thermal emission resulting from recombination of charge carriers (red).

Finally, the electrical power output is given as the product of current and voltage delivered to a load. The maximum amount of energy per EHP (and thus maximum amount of energy per photon) is extracted when the cell is operated at the open-circuit voltage (V_{OC}). However, this voltage can only be maintained when no current is drawn from the cell (fig. 1.3a). Any non-zero current lowers the output voltage of cell and the extent to which the energy of the EHP is converted. The maximum power is drawn when the impedance of the cell and load are matched, satisfying the impedance matching condition. The impedance matching factor is given by $V_{MP}I_{MP}/V_{OC}I_{SC}$. Thus, the total efficiency considered by Shockley and Queisser, η_{PV} , for a PVC can be written

$$\eta_{PV} = \underbrace{t_s}_{100\%} \cdot \underbrace{\eta_u}_{44\%} \cdot \underbrace{\eta_{rec} \cdot \eta_Z}_{95\%}, \quad (1.1)$$

where η_u , η_{rec} and η_Z denote the spectral efficiency u , efficiency associated with thermal re-radiation due to recombination and efficiency of impedance matching, respectively. t_s is a factor describing the probability that an incident photon creates an EHP, allowing for e.g. partially reflective PVC

surfaces. t_s can in reach unity for an ideal PVC. Equation (1.1) also shows in brackets the maximum efficiencies that can be reached for an ideal PVC. The value in brackets for $\eta_{rec} \cdot \eta_Z$ is inferred from the provided values for η_{PV} and η_u in [2] and correspond well to the Carnot efficiency (η_C). The Carnot efficiency is the thermodynamic efficiency limit for a heat engine connected to two heat reservoirs of temperatures T_1 and T_2 , with $T_1 < T_2$:

$$\eta_C = 1 - \frac{T_1}{T_2}. \quad (1.2)$$

For temperatures of 300 °C and 6000 °C, corresponding roughly to atmospheric temperatures of the earth and sun, $\eta_C = 0.95$, while more realistic assumptions (such as non-zero entropy generation) yield slightly lower values by a few percent [3].

The consequences of the above-mentioned limits to solar cell efficiency were first formalised by W. Shockley and HJ. Queisser [2], who derived fundamental limits for all η entering eq. (1.1). The ultimate efficiency η_u of 44 %, which does not take into account the need to deliver the need to deliver the power generated by a PV cell to a load, or thermal radiation from the cell. For the impedance-matched efficiency including re-radiation, the so-called impedance matched efficiency is derived. It is defined as the power delivered into a matched impedance divided by the power incident on the cell and characterises the overall cell efficiency. For this efficiency, a limit of 41 % is derived. This limit is derived for a cell inside a solar "cavity" i.e. for a cell in an ideal solar concentrator. This efficiency can only be approached with a conventional PVC in a concentrator setup. Interestingly, the ultimate efficiency limit can be exceeded utilising a PVC that incorporates plasmonic nanostructures capable of providing the concentration of light cell-internally [4]. For a PVC under non-concentrated illumination, the impedance matched PVC silicon PVC with a band gap of 1.1 eV the limiting efficiency is derived by Shockley and Queisser to be 30 %. It is finally worth mentioning that Shockley and Queisser make several assumptions that can easily be treated more accurately, such as, for example, the spectrum of the sun. For this reason, later calculations of the same quantities often differ by several percents.

1.2 Minimizing losses

The vast discrepancy between the Shockley-Queisser limit (SQL) and the Carnot efficiency is strong motivator for finding other photovoltaic conversion schemes with higher limiting efficiencies. Several strategies are being pursued to address this inherent shortcoming of PVCs, most of which fall into two distinct categories. One set of solutions centre on modifying the PVC to accept photons of several energies. The multi-junction PVCs works by this principle. It is, essentially, a stack of individual PVCs, stacked by order of decreasing band gap. This layout ensures that the most energetic photons are converted by a large band gap material at the top of the cell, while lower energy photons are converted by deeper lying cells. Multi-junction PV-cells have been found to have thermodynamic limits of 64 % to 81 % for non-concentrated solar irradiation to concentrated

solar irradiation with a concentration factor of 10^4 [5]. However, while multi-junction cells have improved efficiencies compared to single-junction PV-cells, their production is significantly more complex, resulting in high production and development cost, which have so far prevented multi-junction cells from being competitive. Another proposed strategy is to insert semi-stable states within the bandgap, which then enables two subsequent single-photon processes to excite an EHP. Since this process can be driven either by one photon only or by two less energetic subsequent photons, the efficiency of such a cell is not bound by the SQL and can reach efficiencies exceeding 60 % [6, 7]. Other modifications to the bandgap of the active material, such as the down-conversion of photons with energies higher than the bandgap have also been proposed [8].

All of the strategies mentioned above to achieve increased efficiency in PVCs require the modification of the band gap structure of the active layer, or, alternatively, the inclusion of band gaps of additional layers above the solar cell. An altogether different approach is to use classical absorption and emission tailoring to shape the solar spectrum before the interaction with the PVC takes place. The working principle of such a scheme is rather simple, requiring only a hot surface to replace the role of the sun as a thermal emitter. Such an emitter can be heated by any means, including by sunlight, as long as it can generate sufficiently high temperatures. Heating the emitter by sunlight obviously requires the emitter to be in thermal contact with a good solar absorber, resulting in a combined absorber-emitter (AE). The AE needs to have an absorbing sun-facing surface and a selectively emitting surface facing the PVC (see fig. 1.2). The absorber side converts incoming radiation into heat, while the emitter re-emits the heat as photons which ideally match the bandgap energy of the PVC. The emitter can alternatively be heated without the need for an absorber, if heat is otherwise available such as in waste incineration, metal or glass furnaces, gas- and oil-driven water boilers or by catalytic combustion inside the emitter itself.

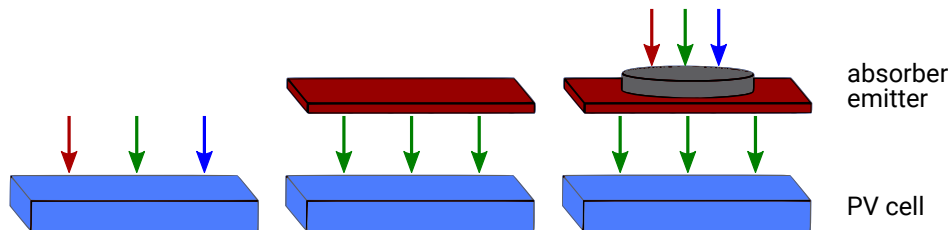


Figure 1.2: Schematic comparison of a conventional photovoltaic cell (left) a thermophotovoltaic cell (mid) and a thermophotovoltaic cell (right). The conventional photovoltaic cell is subjected to light of a range of wavelengths. In (solar) thermophotovoltaic cells, by using a selective emitter, the bandwidth of the light incident on the photovoltaic cell is reduced, leading to an increased spectral efficiency.

The reshaping of the spectrum illuminating the PVC potentially results in significantly reduced intensity outside of the high external quantum efficiency (EQE) of the PVC, leading to higher limiting efficiencies. In fact, an ideal thermophotovoltaic cell (TPVC) can run at $u = 1$ for a purely monochromatic emitter. Efficiency limits for TPV systems have been reported at 85 % and 54 %

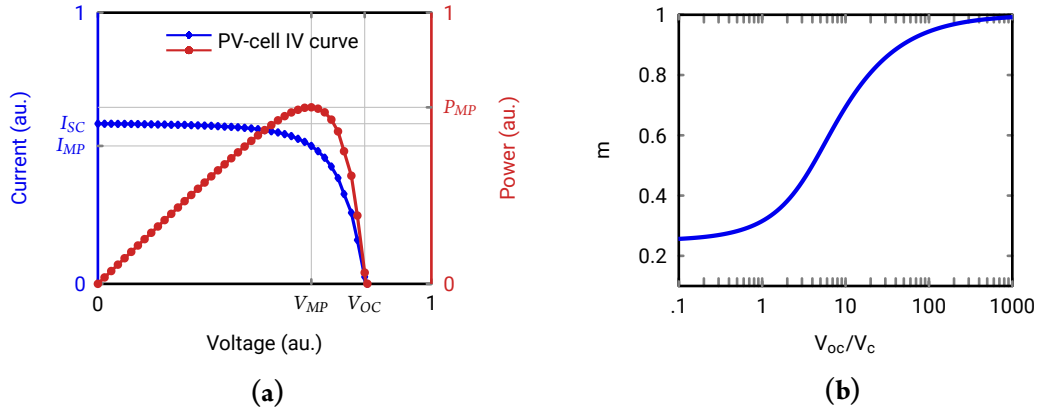


Figure 1.3: (a) Current-voltage characteristic (red) and power output (blue) of a photovoltaic cell under illumination, with indicated short-circuit current I_{SC} , open-circuit voltage V_{OC} , maximum power P_{MP} current at maximum power I_{MP} and voltage at maximum power V_{MP} . (b) The dependence of the impedance matching factor m and the ratio of the open circuit voltage of the cell to its thermal voltage. Based on the analytical expression in [2].

for concentrated and non-concentrated sunlight, respectively. However, more interestingly realistic material and geometric assumption yield limiting efficiencies of 32.8 % and 60 %, for non-concentrated and concentrated conversion schemes [9].

1.3 The economy of thermophotovoltaics

Real-life performance of TPV-conversion has so far lagged far behind both the thermodynamic limits and the efficiencies of regular PV-cells. Despite originally being proposed in the 1950's [10], and receiving some interest in following years [11, 12], TPV still has a long way to go, to compete with PV in terms of efficiency. While record efficiencies are currently improving drastically, the best-reported efficiencies are still in the single-digits [13–17].

These - at first glance - rather modest efficiencies are briefly put in perspective by the literature that exists on the economic feasibility of TPV operation. It turns out that thermophotovoltaic power conversion compares relatively favourably to conventional power conversion, even given realistic efficiencies and with current-state technology if it is applied in appropriate circumstances. This applies in particular to TPV cogeneration, where a TPV cell is used to generate electricity from heat generated in other processes, such as e.g. residential gas-fired water boilers. Electricity cogeneration is particularly interesting in that the economic break-even for presently available solutions lies at relatively low efficiencies, as shown in the study by Palfinger et al [18]. The study demonstrates that for decentralised electric cogeneration, there can be economic break-even for efficiencies as low as 1 % when compared to a gas engine with an efficiency of 25 % or with an economic upside when compared to a fuel engine with an efficiency of 40 %. Another study from 2012 reaches

a similarly positive conclusion in the evaluation of realistic domestic power consumption scenarios with and without TPV cogeneration [19]. The most developed prototypes in terms closeness to application, is therefore also done cogeneration in combined heat and power generation (CHP) applications for residential [20–23] and industrial [24] purposes.

1.4 The broader case for spectral control

As shown above, the freedom to tailor the illumination spectrum of the PVC means that the losses associated with u can in principle be eliminated fully. A prerequisite for this higher efficiency, however, is the precise spectral control over the absorbing and emitting surfaces at high temperatures. More importantly, TPV cogeneration is approaching an economic break-even under favourable conditions, and advances in emitter and absorber technology hold the promise of adding to the rapid development in PVC to bring about commercially viable TPV cogeneration in decentralised or grid-independent application. Since emitters and absorbers play such a crucial role in the efficiency of TPV and solar thermophotovoltaics (STPV) system, their continued development is decidedly among the factors determining the future of this (still) nascent form of energy conversion.

The ability to tailor thermal radiation spectra can be put to use in various unrelated fields where energy balances are influenced significantly by thermal radiation. For instance, it was recently demonstrated that using the same principles involved in TPV, one can passively cool a surface in direct sunlight to several degrees below the ambient air temperature [25], with significant potential for the reductions in energy consumptions of air-conditioned buildings. Another innovative use of selective thermal emission was demonstrated in efficient incandescent lightbulbs, with a potential efficiency reaching 40 % [26]. While not a topic in this context, it is very conceivable that the research presented in this thesis can find application in areas such the above.

A third contribution to the decrease in efficiency stems from the fact that selective thermal emission and cold spectral selectivity are closely related through Kirchhoff's law of thermal radiation, which equates emissivity ϵ and the absorptive power α . For this reason, the work within selective thermal emission benefits greatly from an understanding of the physics of selective absorbers independently from their high-temperature application and results might find application within both, or either, field.

Chapter 2

Optics of interfaces

2.1 Maxwell's equations

With the aim of establishing a theoretical footing for this thesis, it is instructive to begin with Maxwell's equation and derive properties of interest, such as the optical properties of plasmonic and photonic resonators and their thermal emission. Essentially, the classical theory of electrodynamics is contained within Maxwell's four (vectorial) equations, in addition to the Lorentz force law, which describes the force with which an electromagnetic field acts on a moving charge distribution [27]. In modern vector notation Maxwell's equations read:

$$\nabla \cdot \mathbf{E}(\mathbf{r}, t) = \frac{1}{\epsilon_0} \rho_{\text{tot}} \quad (2.1a)$$

$$\nabla \cdot \mathbf{B}(\mathbf{r}, t) = 0 \quad (2.1b)$$

$$\nabla \times \mathbf{E}(\mathbf{r}, t) = -\frac{\partial \mathbf{B}(\mathbf{r}, t)}{\partial t} \quad (2.1c)$$

$$\nabla \times \mathbf{B}(\mathbf{r}, t) = \mu_0 \mathbf{J}_{\text{tot}} + \mu_0 \epsilon_0 \frac{\partial \mathbf{E}(\mathbf{r}, t)}{\partial t}, \quad (2.1d)$$

where \mathbf{r} and t are space- and time coordinates, \mathbf{E} and \mathbf{B} are the electric field and magnetic field, respectively, ϵ_0 and μ_0 are the vacuum permittivity and vacuum permeability, while ρ_{tot} is total charge density and \mathbf{J}_{tot} is the total current density. ∇ is the *nabla*-operator; a vectorial differentiating operator that allows for the often used quantities of curl and divergence of a vector field to be calculated by the inner and outer product, respectively:

$$\nabla = \hat{\mathbf{x}} \frac{\partial}{\partial x} + \hat{\mathbf{y}} \frac{\partial}{\partial y} + \hat{\mathbf{z}} \frac{\partial}{\partial z}, \quad (2.2)$$

where $\hat{\mathbf{x}}$, $\hat{\mathbf{y}}$ and $\hat{\mathbf{z}}$ are Cartesian unit vectors along the denoted direction.

The above equations form a closed description of Maxwell's equations and are suitable for a full description of classical electromagnetic phenomena. However, in the presence of materials, ad-

ditional bound charges and currents may arise in response to fields, which are not directly controllable. The generating terms ρ_{tot} and \mathbf{J}_{tot} thus contain a component which is solely due to the material response. This description is not very useful for an experimenter, who can only hope to directly control the free charges and currents. Therefore, it is often desirable to reformulate Maxwell's equations in such a way, that the source terms contain only "free" charges, which can be directly manipulated. This requires the introduction of additional fields describing the material response. These fields are the polarisation \mathbf{P} and the magnetisation \mathbf{M} , fields describing effect of the generation of bound charge densities and bound current densities, respectively. The total charge and current densities are the sum of external (free) and internal (bound) densities $\rho_{\text{tot}} = \rho_{\text{int}} + \rho_{\text{ext}}$ and $\mathbf{J}_{\text{tot}} = \mathbf{J}_{\text{int}} + \mathbf{J}_{\text{ext}}$.

$$\nabla \cdot \mathbf{D}(\mathbf{r}, t) = \rho_{\text{ext}}(\mathbf{r}, t) \quad (2.3a)$$

$$\nabla \cdot \mathbf{B}(\mathbf{r}, t) = 0 \quad (2.3b)$$

$$\nabla \times \mathbf{E}(\mathbf{r}, t) = -\frac{\partial \mathbf{B}(\mathbf{r}, t)}{\partial t} \quad (2.3c)$$

$$\nabla \times \mathbf{H}(\mathbf{r}, t) = \mathbf{J}_{\text{ext}}(\mathbf{r}, t) + \frac{\partial \mathbf{D}(\mathbf{r}, t)}{\partial t}, \quad (2.3d)$$

where \mathbf{D} is the electric displacement and \mathbf{H} is the magnetic field strength, while ρ_{ext} is the external (free) charge density and \mathbf{J}_{ext} is the external (free) current density. This description necessitates constitutive relations which describe the fields \mathbf{D} and \mathbf{H} as a function of \mathbf{E} and \mathbf{B} and the material responses \mathbf{P} and \mathbf{M} , respectively. In short, the constitutive relations relate the fields \mathbf{E} and \mathbf{D} and the fields \mathbf{H} and \mathbf{B} :

$$\mathbf{D}(\mathbf{r}, t) = \epsilon_0 \mathbf{E}(\mathbf{r}, t) + \mathbf{P}(\mathbf{r}, t) \quad (2.4a)$$

$$\mathbf{H}(\mathbf{r}, t) = \mu_0^{-1} \mathbf{B}(\mathbf{r}, t) - \mathbf{M}(\mathbf{r}, t). \quad (2.4b)$$

The bound charges and currents, ρ_{int} and \mathbf{J}_{int} can now be derived as

$$\rho_{\text{int}}(\mathbf{r}, t) = -\nabla \cdot \mathbf{P}(\mathbf{r}, t) \quad \text{and} \quad (2.5a)$$

$$\mathbf{J}_{\text{int}}(\mathbf{r}, t) = \nabla \times \mathbf{M}(\mathbf{r}, t) + \frac{\partial \mathbf{P}(\mathbf{r}, t)}{\partial t}. \quad (2.5b)$$

For linear, local and isotropic media the polarisation and magnetisation are linear, local and scalar functions of \mathbf{E} and \mathbf{B} :

$$\begin{aligned} \mathbf{D}(\mathbf{r}, t) &= \epsilon_0(1 - \chi_e)\mathbf{E}(\mathbf{r}, t) = \epsilon_0 \epsilon_r \mathbf{E}(\mathbf{r}, t) \\ \mathbf{H}(\mathbf{r}, t) &= \frac{1}{\mu_0(1 + \chi_m)} \mathbf{B}(\mathbf{r}, t) = \frac{1}{\mu_0 \mu_r} \mathbf{B}(\mathbf{r}, t) \end{aligned} \quad (2.6)$$

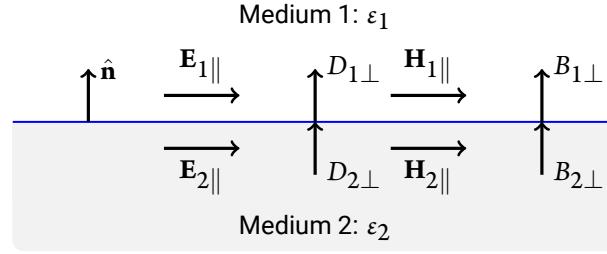


Figure 2.1: Schematic of a planar interface between two media 1 and 2 with dielectric functions ϵ_1 and ϵ_2 , respectively, showing the field components and boundary conditions at the interface. $\hat{\mathbf{n}}$ is a unit vector perpendicular to the interface and pointing into medium 1.

where χ_e and χ_m are electric and magnetic susceptibilities, respectively. ϵ_r and μ_r are the relative permittivity and permeability. In the remainder of this work it will be assumed that all considered materials are indeed linear, local and isotropic. Furthermore, in the context of this work only non-magnetic materials are considered, which means that the magnetisation vanishes, i.e. $\mathbf{M} = 0$.

The Lorentz force law describing the force F on an electrical charge q , which is moving with velocity $\dot{\mathbf{r}}$ in an electromagnetic field, is given by

$$F(\mathbf{r}, t) = q [\mathbf{E}(\mathbf{r}, t) + \dot{\mathbf{r}} \times \mathbf{B}(\mathbf{r}, t)]. \quad (2.7)$$

For time-periodic phenomena it is advantageous to express the Maxwell's equations in the basis of time-harmonic functions $e^{-i\omega t}$ with the angular frequency ω . This can be done, without loss of generality, by application of the Fourier transform, corresponding to a change of basis to the basis of time-harmonic functions. In the frequency domain, Maxwell's equations read:

$$\nabla \cdot \mathbf{D}(\mathbf{r}, \omega) = \rho_{\text{ext}} \quad (2.8a)$$

$$\nabla \cdot \mathbf{B}(\mathbf{r}, \omega) = 0 \quad (2.8b)$$

$$\nabla \times \mathbf{E}(\mathbf{r}, \omega) = i\omega \mathbf{B}(\mathbf{r}, \omega) \quad (2.8c)$$

$$\nabla \times \mathbf{H}(\mathbf{r}, \omega) = \mathbf{J}_{\text{ext}}(\mathbf{r}, \omega) - i\omega \mathbf{D}(\mathbf{r}, \omega), \quad (2.8d)$$

where constitutive relations give the relationship between the \mathbf{E} and \mathbf{D} , and \mathbf{B} and \mathbf{H} , in terms of material properties. For local, non-magnetic and isotropic, the constitutive relations in the frequency domain are

$$\mathbf{D}(\mathbf{r}, \omega) = \epsilon_0 \epsilon(\mathbf{r}, \omega) \mathbf{E}(\mathbf{r}, \omega) \quad (2.9a)$$

$$\mathbf{H}(\mathbf{r}, \omega) = \mu_0^{-1} \mu^{-1}(\mathbf{r}, \omega) \mathbf{B}(\mathbf{r}, \omega) \quad (2.9b)$$

$$\mathbf{J}(\mathbf{r}, \omega) = \sigma(\mathbf{r}, \omega) \mathbf{E}(\mathbf{r}, \omega). \quad (2.9c)$$

2.2 Propagating solutions

In an isotropic, local and (piecewise) homogeneous medium ϵ , μ and ρ are position-independent. Taking the curl of eq. (2.8c) and eq. (2.8d), and applying equations eq. (2.9a) and eq. (2.9b), results in the inhomogeneous wave equation:

$$\nabla \times \nabla \times \mathbf{E}(\mathbf{r}, \omega) - \frac{\omega^2}{c^2} \epsilon_r \mu_r \mathbf{E}(\mathbf{r}, \omega) = i\omega \mu_r \mathbf{J}_{\text{ext}} \quad (2.10)$$

$$\nabla^2 \mathbf{E}(\mathbf{r}, \omega) + \frac{\omega^2}{c^2} \epsilon_r \mu_r \mathbf{E}(\mathbf{r}, \omega) = \epsilon_0^{-1} \nabla \left[\epsilon^{-1}(\mathbf{r}, \omega) \rho_{\text{ext}} \right] - i\omega \mu_r \mathbf{J}_{\text{ext}}, \quad (2.11)$$

where c is the vacuum speed of light. The second line results from the vector identity $\nabla \times \nabla \times = \nabla \nabla \cdot - \nabla^2$. In the case of a region with no external charges or current, the right side of the equation becomes equal to zero and the equation reduces to the homogeneous Helmholtz equation

$$\left[\nabla^2 + \frac{\omega^2}{c^2} \epsilon_r \mu_r \right] \mathbf{E}(\mathbf{r}, \omega) = 0. \quad (2.12)$$

For non-magnetic materials, which are the interest of this thesis, the equation further simplifies with $\mu_r = 1$. It can be shown by insertion that the following travelling plane-wave solution satisfies the homogeneous Helmholtz equation, eq. (2.12)

$$\mathbf{E} = \mathbf{E}_0 e^{i\varphi(\mathbf{r}, t)}, \quad (2.13)$$

with

$$\varphi(\mathbf{r}, t) = \mathbf{k} \cdot \mathbf{r} - \omega t + \varphi_0, \quad (2.14)$$

where \mathbf{E}_0 is the complex electric field amplitude, φ_0 is a phase constant. The wave vector \mathbf{k} points in the direction of propagation and describes the wave periodicity in units of radians per unit length. It is not necessary to specify the magnetic field since the wave is fully characterised by the electric field and the magnetic field can be calculated by means of eq. (2.8c). Finally, it is implicitly assumed that one takes the real part of the field, to get the observable electrical field.

2.3 Boundary conditions at planar interfaces

From Maxwell's equations one can directly derive boundary conditions, relating the electric and magnetic field on both sides of an interface, here denoted by subscripts 1 and 2. This is done in any comprehensive textbook on the matter, and here we shall simply state the results [28]. Considering a well-defined interface between two materials, labelled 1 and 2 (Fig. 2.1), the following boundary conditions for the fields on either side of the boundary (but infinitesimally close to it) can be

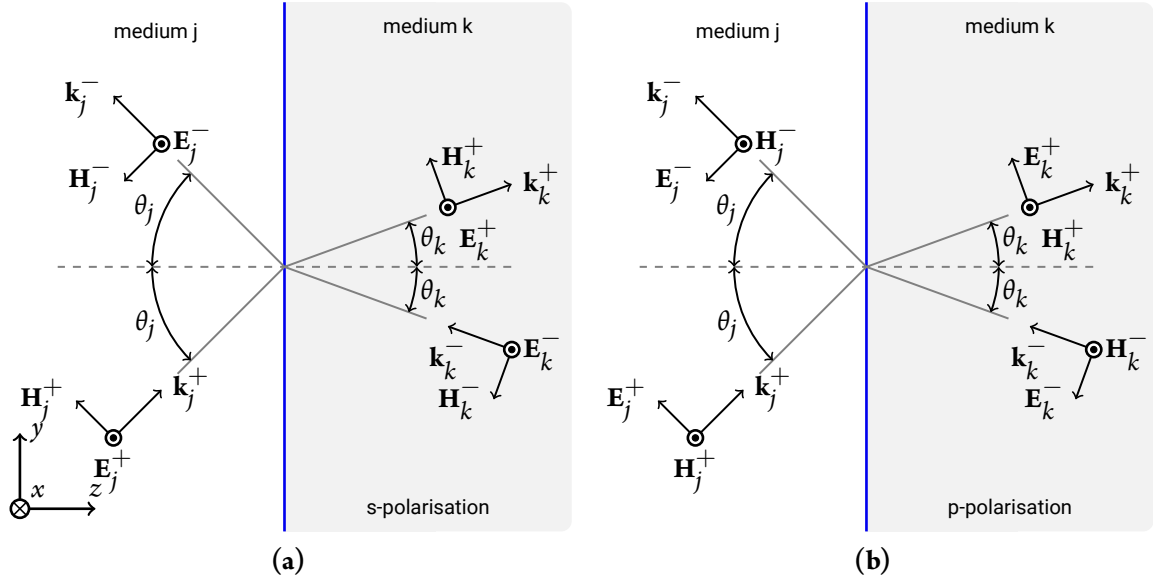


Figure 2.2: Geometry and notation at the planar interface between media j and k for an s -polarised incident plane-wave (a), and p -polarised incident plane-wave (b), relating the electric field (\mathbf{E}), magnetic field strength (\mathbf{H}), wave vector (\mathbf{k}) and angle to optical axis in medium j ($\theta_{j/k}$) on either side of the i/j -interface.

derived:

$$\mathbf{E}_{1\parallel} - \mathbf{E}_{2\parallel} = 0 \quad (2.15a)$$

$$\mathbf{H}_{1\parallel} - \mathbf{H}_{2\parallel} = \mathbf{J}_{s,ext} \times \hat{\mathbf{n}} \quad (2.15b)$$

$$D_{1\perp} - D_{2\perp} = \rho_{s,ext} \quad (2.15c)$$

$$B_{1\perp} - B_{2\perp} = 0, \quad (2.15d)$$

It is seen that \mathbf{E}_{\parallel} and B_{\perp} are continuous across the boundary. In the absence of generating surface current or charge densities, the source terms on the right side can be set to zero. This forces \mathbf{E}_{\parallel} and \mathbf{H}_{\parallel} to be continuous across the interface and leads to the boundary conditions:

$$\mathbf{E}_1^{\parallel} = \mathbf{E}_2^{\parallel} \quad (2.16a)$$

$$\mathbf{B}_1^{\parallel}/\mu_1 = \mathbf{B}_2^{\parallel}/\mu_2 \quad (2.16b)$$

$$\varepsilon_1 E_1^{\perp} = \varepsilon_2 E_2^{\perp} \quad (2.16c)$$

$$B_1^{\perp} = B_2^{\perp}. \quad (2.16d)$$

Again, since only non-magnetic materials are considered, $\mu_j = \mu_k = 1$. As a result, the continuity of the parallel field components extends to all field components of \mathbf{B} , while the orthogonal e-field sees

a jump which is proportional to the the ratio of dielectric functions. However, it is worth pointing out, that if the boundary conditions on the parallel components of the field are satisfied, then the boundary conditions for the perpendicular are automatically satisfied. To summarize, for an interface between two isotropic, homogeneous and non-magnetic materials, one needs only to match the fields on either side of the interface in such a way that the tangential field components are continuous across the interface. Since the plane waves form a complete, orthonormal set, they can be used as a basis, in which to completely describe the behaviour of light-related phenomena. Therefore, the description of the behaviour of a general plane-wave, is a full description of the behaviour of light in the given situation.

For plane-wave incident on a (locally) planar interface between two linear, isotropic media j and k , one can from the boundary conditions eqs. (2.15a) and (2.15b) derive the following relations for the real parts of the parallel \mathbf{E} - and \mathbf{H} -field components:

$$E_{j,x}^+ + E_{j,x}^- = E_{k,x}^+ + E_{k,x}^- \quad (2.17a)$$

$$n_j(-E_{j,x}^+ + E_{j,x}^-) \cos \theta_j = n_k(-E_{k,x}^+ + E_{k,x}^-) \cos \theta_k \quad (2.17b)$$

$$E_{j,y}^+ + E_{j,y}^- = E_{k,y}^+ + E_{k,y}^- \quad (2.17c)$$

$$n_j \frac{E_{j,y}^+ + E_{j,y}^-}{\cos \theta_j} = n_k \frac{E_{k,y}^+ + E_{k,y}^-}{\cos \theta_k}. \quad (2.17d)$$

Equations (2.17a) and (2.17b) describe \mathbf{E} - and \mathbf{H} -fields for s -polarized light, while eqs. (2.17c) and (2.17d) describe \mathbf{E} - and \mathbf{H} -fields for p -polarised light, respectively. This system of equations can be more conveniently formulated as a matrix equation [29]:

$$\begin{bmatrix} E_{j,x}^+ \\ E_{j,x}^- \\ E_{j,y}^+ \\ E_{j,y}^- \end{bmatrix} = \frac{1}{2} \begin{bmatrix} 1 + \zeta_{jk}^{s-pol} & 1 - \zeta_{jk}^{s-pol} & 0 & 0 \\ 1 - \zeta_{jk}^{s-pol} & 1 + \zeta_{jk}^{s-pol} & 0 & 0 \\ 0 & 0 & 1 + \zeta_{jk}^{p-pol} & 1 - \zeta_{jk}^{p-pol} \\ 0 & 0 & 1 - \zeta_{jk}^{p-pol} & 1 + \zeta_{jk}^{p-pol} \end{bmatrix} \begin{bmatrix} E_{k,x}^+ \\ E_{k,x}^- \\ E_{k,y}^+ \\ E_{k,y}^- \end{bmatrix}, \quad (2.18)$$

where $\zeta_{jk}^{s-pol} = \frac{n_k \cos \nu_k}{n_j \cos \nu_j}$ and $\zeta_{jk}^{p-pol} = \frac{n_k \cos \nu_j}{n_j \cos \nu_k}$. In the above matrix equation, it clearly emerges that the polarisation state with a transverse electric relative to the plane of incidence xz , called the s -polarisation (or transverse-electric (TE)) and the polarisation state with purely transverse magnetic field, the p -polarisation (or transverse-magnetic (TM)), do not mix at planar interfaces between two isotropic materials. Therefore, it is convenient to treat TE- and TM-polarisation separately. Solving eq. (2.18) for the ratio of reflected and refracted field amplitudes to the incident amplitude, $E_{j,x}^-/E_{j,x}^+$ and $E_{k,x}^+/E_{j,x}^+$, now yields the Fresnel coefficients for reflection and transmission through the interface, r and t , for each respective polarisation: In the case of s -polarised waves, Fresnel's

coefficients are given by

$$r_{jk} = \frac{q_j - q_k}{q_j + q_k} \quad (2.19a)$$

$$t_{jk} = \frac{2q_j}{q_j + q_k}, \quad (2.19b)$$

and for p -polarised waves by

$$r_{jk} = \frac{n_k^2 q_j - n_j^2 q_k}{n_k^2 q_j + n_j^2 q_k} \quad (2.20a)$$

$$t_{jk} = \frac{2n_j n_k q_j}{n_k^2 q_j + n_j^2 q_k}, \quad (2.20b)$$

where

$$q_i = n_i \cos \theta_i. \quad (2.21)$$

The following condition arises on the angle of incidence θ_i , angle of reflection θ_r , and angle of refraction θ_k refracted light in two arbitrary layers j and k , respectively:

$$\theta_i = \theta_r \quad (2.22a)$$

$$n_j \sin \theta_j = n_k \sin \theta_k, \quad (2.22b)$$

where the latter is known as Snell's law. The angle of propagation changes solely due to a change in the wave vector component normal to the interface, whereas the parallel wave vector component is invariant.

2.4 The transfer matrix method

Having solved the problem of matching plane-wave solutions in a stratified structure, one can devise a compact but comprehensive analytical framework with which it is possible to investigate the optical properties of the structure in the far-field. Furthermore, one can determine the guided modes which are travelling along the interfacial direction and are decreasing exponentially into the sub- and superstrate. The method is the so-called transfer-matrix method (TMM), which allows for the solving of Maxwell's equations in all involved layers. These solutions include both photonic (plane-wave) solutions travelling perpendicular to the interfaces and also plasmonic modes which are bound to the interface(s), decaying exponentially away from the interface(s). The TMM can be used for multi-layer structures, in which the superposition of the waves is assumed to be coherent, as well as for partially coherent superposition, which will not be treated here. For more detailed introduction to the subject, the reader is referred to various textbooks [28], while research literature is also widely

available [30–32], and [33] which presents a general treatment of decoherence. This method is a standard method in optics and can be found widely in textbooks on optics, however in the following the method will be laid out as presented in [31].

The starting point for the transfer-matrix method is a multilayer structure consisting of N stratified layers (with parallel, planar interfaces), each identified with the subscript j (fig. 2.3). The layers have thicknesses d_j and refractive indices

$$n_j \equiv \eta_j + i\kappa_j. \quad (2.23)$$

Apart from the superstrate layer, all layers can have complex refractive indices. For calculating reflectivity, the superstrate, must have a real refractive index since it is semi-infinite and must support an incoming wave. The angle of incidence is θ_0 , while the angle of propagation in subsequent layers is θ_j with a corresponding wave vector k_j . A semi-infinite substrate is also included, which and can have an arbitrary refractive index as it does not need to support an incident wave. With this framework in place, it is now possible to write the field solutions inside all involved layers in a multilayer structure.

The interfacial matrix

Let us assume that a plane-wave is propagating along the positive z -direction and is incident on the interface separating layer i and j . We shall denote forward-propagating (in the positive z -direction) waves by E^+ and backwards propagating waves by E^- . For the waves just before and after the interface, the amplitudes of the waves are related by the relation:

$$\begin{bmatrix} \mathbf{E}_k^+ \\ \mathbf{E}_j^- \end{bmatrix} = \begin{bmatrix} t_{jk} & r_{kj} \\ r_{jk} & t_{kj} \end{bmatrix} \begin{bmatrix} \mathbf{E}_j^+ \\ \mathbf{E}_k^- \end{bmatrix}. \quad (2.24)$$

It is often more useful to describe the fields at an ‘output’, which could be the substrate side of the sample, as a function of the input, e.g. the illumination conditions at the superstrate side of the sample:

$$\begin{bmatrix} \mathbf{E}_j^+ \\ \mathbf{E}_j^- \end{bmatrix} = \frac{1}{t_{jk}} \begin{bmatrix} 1 & r_{jk} \\ r_{jk} & 1 \end{bmatrix} \begin{bmatrix} \mathbf{E}_k^+ \\ \mathbf{E}_k^- \end{bmatrix}. \quad (2.25)$$

It is, therefore, clear that the matrix describing the transfer through the interface between layer j and k , is given by

$$\mathbf{I}_{jk} = \frac{1}{t_{jk}} \begin{bmatrix} 1 & r_{jk} \\ r_{jk} & 1 \end{bmatrix}. \quad (2.26)$$

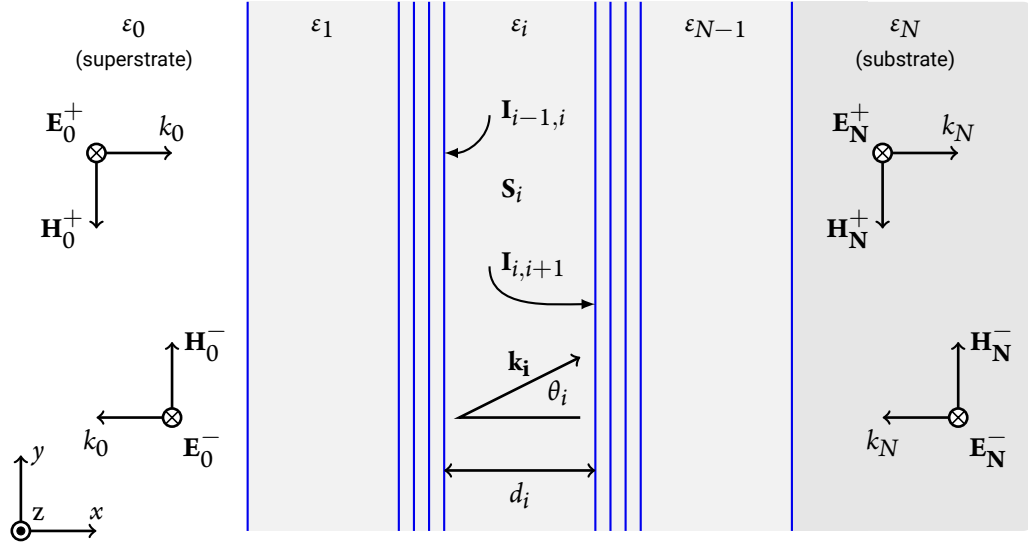


Figure 2.3: Illustration of the geometry of the stratified layer-stack under consideration, which consists of N isotropic and homogeneous layers, separated by parallel interfaces. Each layer j has the complex dielectric function, ϵ_j , and thickness t . The superstrate layer is required to have a purely real refractive index to allow for incoming travelling waves. Both superstrate and substrate are considered to be semi-infinite and can be set to vacuum properties for finite structures.

The propagation matrix

The propagation matrix describing the influence on the complex field amplitude of propagating through the bulk of layer j , follows directly from the fact that the field for layer j can be written as

$$\mathbf{E}_j^+(x_{j,j+1}) = \mathbf{E}_j^+(x_{j-1,j})e^{-i\xi_j d_j} \quad (2.27a)$$

$$\mathbf{E}_j^+(x_{j-1,j}) = \mathbf{E}_j^+(x_{j,j+1})e^{i\xi_j d_j}, \quad (2.27b)$$

where ξ_j is a complex wave number which describes the phase and amplitude modulation of the wave when propagating through the layer j . In the absence of scattering, this propagation can be described by a phase factor of $e^{\mp i\xi_j d_j}$, with the sign of the exponent depending on the propagation direction. Therefore, the matrix \mathbf{S}_j , describing the propagation through layer i , excluding its interfaces, is given by

$$\mathbf{S}_j = \begin{bmatrix} e^{-i\xi_j d_j} & 0 \\ 0 & e^{i\xi_j d_j} \end{bmatrix}, \quad (2.28)$$

where ξ_j is the x-component of the wave vector in layer j and is given by

$$\xi_j = \frac{2\pi}{\lambda_0} q_j = \frac{2\pi}{\lambda_0} n_j \cos \theta_j. \quad (2.29)$$

Finally, the angle of propagation, θ_j , is given by Snell's law, eq. (2.22b):

$$\theta_j = \sin^{-1} \left(\frac{n_0}{n_j} \sin \theta_0 \right). \quad (2.30)$$

The transfer matrix for a multi-layer stack

With matrices describing both propagation through the layers of the multilayer structure and the phase shifts occurring at the interfaces, it is now possible to formulate a compact equation for the total response of a multilayer system, as seen in Fig. fig. 2.3, simply by multiplying the matrices corresponding to the complete multilayer system. Thus, one obtains a direct relation between the fields in the superstrate and substrate, which determine important observables such as reflection, transmission and absorption:

$$\begin{bmatrix} \mathbf{E}_0^+ \\ \mathbf{E}_0^- \end{bmatrix} = \mathbf{S} \begin{bmatrix} \mathbf{E}_N^+ \\ \mathbf{E}_N^- \end{bmatrix} \equiv \begin{bmatrix} S_{11} & S_{12} \\ S_{21} & S_{22} \end{bmatrix} \begin{bmatrix} \mathbf{E}_N^+ \\ \mathbf{E}_N^- \end{bmatrix}, \quad (2.31)$$

with

$$\mathbf{S} = \left(\prod_{l=1}^{N-1} \mathbf{I}_{l-1,l} \mathbf{L}_l \right) \cdot \mathbf{I}_{N-1,N}. \quad (2.32)$$

For a sample illuminated solely from the superstrate side, there is no incident wave on the substrate side, i.e. $\mathbf{E}_N^- = 0$. In this case, the total complex field reflection and transmission coefficients, r and t , can be obtained directly from the transfer matrix elements of the multilayer structure.

$$r = \frac{\mathbf{E}_0^-}{\mathbf{E}_0^+} = \frac{S_{21}}{S_{11}} \quad (2.33a)$$

$$t = \frac{\mathbf{E}_N^+}{\mathbf{E}_0^+} = \frac{1}{S_{11}}. \quad (2.33b)$$

On closer investigation of the above equations, it is seen that poles exist in the transmission and reflection of the structure, namely when the matrix element $S_{11} = 0$. It can be shown that these poles in reflection (and in transmission) correspond to the fulfilment of guiding conditions of the layered structure [30, 34]. By observing the phase variation of the matrix element S_{11} , this approach of finding guided modes can be expanded to find leaky modes. This method is known as the reflection-pole-method. It is worth pointing out that since the poles indicate guided modes, the fields in substrate and superstrate are evanescent and the wave vector of the wave in the superstrate and substrate are, therefore, non-real. When, on the other hand, a plane wave *is* incident on the structure, $|r| < 1$, such that the calculated reflection coefficients do not yield unphysical values greater than unity. The reflection-pole-method will be used in a later chapter to derive the

dispersion of plasmonic modes inherent to metal-dielectric interfaces – so-called surface-plasmon-polaritons (surface plasmon-polaritons (SPPs)), and the modes inherent to metal-dielectric-metal structures, called gap surface plasmons (GSPs).

Partial transfer matrices

For the calculation of the fields in layer j within a structure, it is advantageous to decompose the total transfer matrix into partial transfer matrices that describe the influence of the layers and interfaces separating layer j from the sub- and superstrate side:

$$\mathbf{S} = \mathbf{S}'_j \mathbf{L}_j \mathbf{S}''_j. \quad (2.34)$$

This yields partial transfer matrices, which can be obtained by truncating the product in 2.18 accordingly:

$$\begin{bmatrix} \mathbf{E}_0^+ \\ \mathbf{E}_0^- \end{bmatrix} = \mathbf{S}' \begin{bmatrix} \mathbf{E}_j'^+ \\ \mathbf{E}_j'^- \end{bmatrix} \equiv \begin{bmatrix} S'_{11} & S'_{12} \\ S'_{21} & S'_{22} \end{bmatrix} \begin{bmatrix} \mathbf{E}_j'^+ \\ \mathbf{E}_j'^- \end{bmatrix}. \quad (2.35)$$

with

$$\mathbf{S}' = \left(\prod_{l=1}^{j-1} \mathbf{I}_{l-1,l} \mathbf{L}_l \right) \cdot \mathbf{I}_{j-1,j}. \quad (2.36)$$

Correspondingly, a partial transfer matrix can be formulated for the part of the multi-layer structure which separates layer j from the substrate side of the sample:

$$\begin{bmatrix} \mathbf{E}_j''^+ \\ \mathbf{E}_j''^- \end{bmatrix} = \mathbf{S}'' \begin{bmatrix} \mathbf{E}_N'^+ \\ \mathbf{E}_N'^- \end{bmatrix} \equiv \begin{bmatrix} S''_{11} & S''_{12} \\ S''_{21} & S''_{22} \end{bmatrix} \begin{bmatrix} \mathbf{E}_N^+ \\ \mathbf{E}_N^- \end{bmatrix}. \quad (2.37)$$

with

$$\mathbf{S}'' = \left(\prod_{l=j+1}^N \mathbf{I}_{l-1,l} \mathbf{L}_l \right) \cdot \mathbf{I}_{j-1,j}. \quad (2.38)$$

Finally, one can write reflection and transmission coefficients for the partial layer structure. In this way, one can regard each layer as resonator with the remaining layer structure on either side

acting as a distributed reflector. The resulting coefficients are:

$$r_j' = \frac{S_{j,21}'}{S_{j,11}'} \quad (2.39a)$$

$$t_j' = \frac{1}{S_{j,11}'} \quad (2.39b)$$

$$r_j'' = \frac{S_{j,21}''}{S_{j,11}''} \quad (2.39c)$$

$$t_j'' = \frac{1}{S_{j,11}''}. \quad (2.39d)$$

The total field within a multilayer structure

Having obtained the partial transfer matrices in eqs. (2.36) and (2.38), it is now possible to directly relate the fields within a given layer to the fields in the superstrate and substrate side of the sample. With the aim of deriving the field inside layer j , one can formulate a transmission coefficient t_j^+ which describes the field transmitted into layer j for a given incident field \mathbf{E}_0^+ :

$$t_j^+ = \frac{\mathbf{E}_j^+}{\mathbf{E}_0^+} = \frac{t_j'}{1 - r_{j-}' r_j'' e^{i\xi_j d_j}}. \quad (2.40)$$

The part of the multilayer structure described by \mathbf{S}' (the part to the left of the interface in fig. 2.3) transmits a plane wave with efficiency t_j' into layer j and simultaneously acts as a distributed reflector for a wave in layer j propagating in the negative direction. Simultaneously the layer-stack described by \mathbf{S}'' acts as a reflector for the wave propagating in the positive direction. In addition to the reflection phases and corresponding amplitude modulations, the wave experiences a phase retardation of $e^{-i\xi_j d_j}$ due to propagation through the layer, the total field in layer j for waves propagating in the positive direction, can be written as the geometric series seen in eq. (2.40). Exchanging the transmission t_j' for $t_j'' e^{i2\xi_j d_j}$, which corresponds to an additional reflection in the \mathbf{S}'' -part of the structure, as well as the double propagation through the layer, the identical argument leads to an expression for the total field of the wave propagating in the negative direction:

$$t_j^- = \frac{\mathbf{E}_j^-}{\mathbf{E}_0^+} = \frac{t_j'' e^{i2\xi_j d_j}}{1 - r_{j-}' r_j'' e^{i\xi_j d_j}} = t_j'' r_j'' e^{i2\xi_j d_j}. \quad (2.41)$$

It is now possible to write the expression for the total field inside layer j .

$$\begin{aligned}\mathbf{E}_j(x) &= \mathbf{E}_j^+(x) + \mathbf{E}_j^-(x) \\ &= \left(t_j^+ e^{i\xi_j x} + t_j^- e^{-i\xi_j x} \right) \mathbf{E}_0^+.\end{aligned}\quad (2.42)$$

This procedure is valid for all layers and thus one can calculate the field inside the entire multilayer structure through use of eqs. (2.39) to (2.42).

Since the total field inside the structure of interest is now known, it is also possible to calculate quantities which are derived from the field, such as Poynting's vector field or the local absorption. Most interestingly for this study is the local absorption, as it determines both where in the structure power is absorbed or emitted and thus has consequences for the requirements on the thermal conductivity and thermal expansion of materials incorporated into the sample. The relation between the electric field and the local absorption in layer j , Q_j , is a well-known result from elementary electrodynamics:

$$Q_j(x) = \frac{1}{2} c \varepsilon_0 a_j \eta_j \left| \mathbf{E}_j(x) \right|^2, \quad (2.43)$$

with the absorption coefficient a_j given by

$$a_j = \frac{4\pi\kappa_j}{\lambda}. \quad (2.44)$$

While the local optical absorption is not directly relevant for the overall optical properties of the multilayer structure, it is often of interest to assess the local absorption (and, therefore, emission) in order to estimate the flow of heat in the structure. As will be seen later the absorption can very localized to a specific film, in which case it is necessary to choose materials that will minimize the thermal gradient in the structure.

2.5 Surface plasmon polaritons

The transfer matrix formalism is also useful for the calculation of bound modes which are guided along the direction of the interface(s). As such the TMM is ideal for finding the plasmonic modes, which are of interest for this thesis. For a mode to be guided, within a given multilayer structure, it should be evanescent in the sub- and superstrate layers corresponding to purely imaginary wave vectors. For semi-infinite sub- and superstrates and purely imaginary wave vectors, incident waves must be zero for normalisability [35]. These latter condition correspond to setting $\mathbf{E}_0^- = \mathbf{E}_N^+ = 0$ in eq. (2.31), resulting in the following relation:

$$\begin{bmatrix} 0 \\ \mathbf{E}_0^- \end{bmatrix} = \begin{bmatrix} S_{11} & S_{12} \\ S_{21} & S_{22} \end{bmatrix} \begin{bmatrix} \mathbf{E}_N^+ \\ 0 \end{bmatrix}. \quad (2.45)$$

This condition can only be satisfied for $S_{11} = 0$, apart from the trivial zero-field solution. It follows that guided modes can be found by solving for element $S_{11} = 0$ [34].

2.5.1 Surface plasmon polaritons

Surface plasmon polaritons are waves occurring at the interfaces between metals and dielectrics. As such, they are bounded to the interface and can be considered as guided modes, appropriate for the examination using the reflection pole method. The characteristic matrix for a dielectric-metal (DM) interface is

$$\mathbf{I}_{DM} = \frac{1}{t_{DM}} \begin{bmatrix} 1 & r_{DM} \\ r_{DM} & 1 \end{bmatrix}, \quad (2.46)$$

which means that the requirement for the matrix element $S_{11} = 0$ translates into $1/t_{DM} = 0$. From eqs. (2.19a) and (2.20a) the following requirements emerge for s - and p -polarisation, respectively:

$$q_D = -q_M \quad (s\text{-pol}) \quad (2.47a)$$

$$\frac{q_D}{\varepsilon_D} = -\frac{q_M}{\varepsilon_M} \quad (p\text{-pol}). \quad (2.47b)$$

The former requirement, eq. (2.47a), is not a bound solution, increasing exponentially into either substrate or superstrate. Considering two semi-infinite half-spaces it is, in fact, not a physically meaningful solution. In other words, no guided modes exist along the interface for s -polarised light. The latter requirement, eq. (2.47b), can be fulfilled, provided the dielectric functions of materials M and D have opposite signs of the real part of their dielectric functions. This requires material M to have a negative real part of the dielectric function. Conservation of momentum requires the wave vector of the guided mode β to fulfil

$$q_i^2 + \beta^2 = k_0^2 \varepsilon_i(\omega). \quad (2.48)$$

Inserting equation 2.48 into 2.47b yields the dispersion relation of the mode confined to the interface the interface; the surface plasmon-polariton:

$$\beta = k_0 \sqrt{\frac{\varepsilon_M \varepsilon_D}{\varepsilon_M + \varepsilon_D}}. \quad (2.49)$$

The electric field components of the mode can now be written

$$\mathbf{E}(y > 0) = \begin{pmatrix} 0 \\ E_D^y \\ E_D^z \end{pmatrix} e^{i(\beta z - \omega t)} e^{-iyq_i}, \quad (2.50a)$$

$$\mathbf{E}(y < 0) = \begin{pmatrix} 0 \\ E_M^y \\ E_D^z \end{pmatrix} e^{i(\beta z - \omega t)} e^{iyq_i}, \quad (2.50b)$$

where the fields are matched across the interface by the relation $\epsilon_D E_D^y = \epsilon_M E_M^y$.

For a lossless Drude metal, the dielectric function ϵ_M can be written as

$$\epsilon_M(\omega) = \epsilon_\infty - \left(\frac{\omega_p}{\omega}\right)^2, \quad (2.51)$$

where ϵ_∞ is the high-frequency limit of $\epsilon_M(\omega)$, ω_p is the plasma frequency. In its simplest form, a lossy metal can be approximated as

$$\epsilon_M(\omega) = \epsilon_\infty - \left(\frac{\omega_p^2}{\omega^2 + i\omega\gamma_0}\right). \quad (2.52)$$

A damping term has been added, where γ_0 is the damping strength. The acspp dispersion curves resulting from use eqs. (2.51) and (2.52) are shown in fig. 2.4a and fig. 2.4b, respectively. of which a plot can be seen in fig. 2.4a. However, it should be noted that eq. (2.51) is only strictly valid in the regime $\omega \ll \omega_p$.

The SPP dispersion for a Drude metal fitted to the optical properties of gold is seen in fig. 2.4a, plotted with the light line for light propagating in vacuum. It is seen that the SPP dispersion and the light line (of light in the dielectric) do not intersect, and therefore SPPs and freely propagating light are not momentum matched. In order to excite SPPs it is therefore necessary to provide a momentum matching mechanism. Several schemes of momentum matching exist, such as prism coupling or scattering on gratings.

The wave vector perpendicular to the interface determines the *skin depth*, \tilde{z} , the distance from the surface at which the SPP-field amplitude has dropped to $1/e$ times the values in the vicinity of the interface

$$\tilde{z} = \frac{1}{q_i}, \quad (2.53)$$

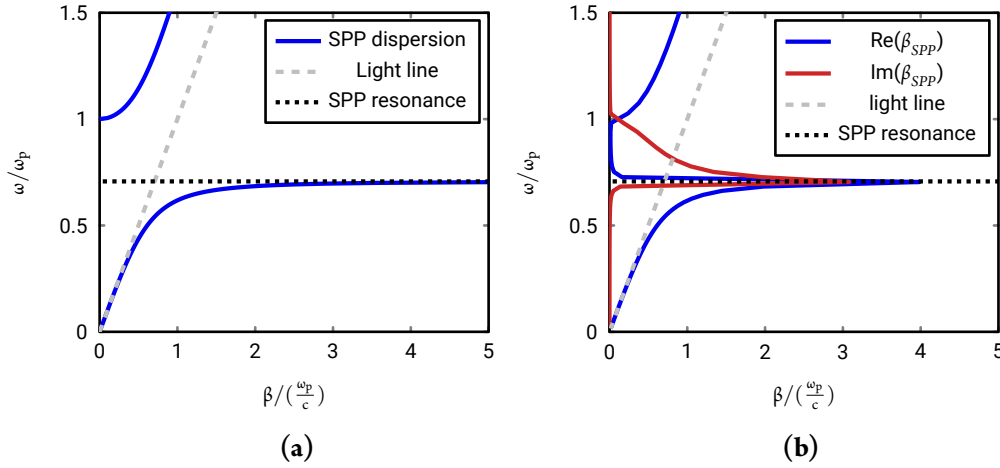


Figure 2.4: Dispersion of an surface plasmon-polariton (SPP) on a metal-dielectric interface assuming (a) lossless Drude metal response fitted to gold and (b) a lossy Drude metal fitted to the properties of gold. In both cases, a dielectric with $\epsilon = 1$ is assumed. The light line (dashed) and the SPP resonance frequency (dotted) are indicated in both cases).

while the corresponding definition for the SPP-amplitude along the direction of propagation, i.e. along the interface yields the propagation length, L_i [36]:

$$L_i = \frac{1}{2\beta}. \quad (2.54)$$

2.5.2 Gap surface plasmons

In the case of two, parallel metallic-dielectric surfaces, the modes inherent to each interface hybridises with the mode on the adjacent interface, provided the distance is low enough to warrant coupling between the interfaces, i.e. on the scale of the decay length of the SPP mode. Naturally, there are two kinds of such combined interfaces, the metal-insulator-metal (MIM) geometry and the insulator-metal-insulator (IMI). These structures both have modes which turn out to have huge applicability. Both will be derived in the following, however, special attention will be given to GSP mode, which will be of importance for a significant part of the work presented in this thesis.

The GSP mode can be derived in similar manner to the SPP mode, that is by the reflection pole method. The transfer matrix of interest is thus of the form $\mathbf{I}_{MD}\mathbf{S}_D\mathbf{I}_{DM}$, as given by eqs. (2.26) and (2.28).

$$\mathbf{S}_{GSP} = \frac{1}{t_{MD}t_{MD}} \begin{bmatrix} 1 & r_{MD} \\ r_{MD} & 1 \end{bmatrix} \begin{bmatrix} e^{-i\xi_D d_D} & 0 \\ 0 & e^{i\xi_D d_D} \end{bmatrix} \begin{bmatrix} 1 & r_{DM} \\ r_{DM} & 1 \end{bmatrix} \quad (2.55)$$

Equating the matrix element $S_{11} = 0$, now directly leads to the dispersion of the GSP mode supported by the metal-dielectric-metal structure.

$$S_{11} = 0 = \frac{(n_D^2 q_M + n_M^2 q_D)^2}{2n_M^2 n_D^2 q_D q_M} e^{-i\xi_D d} + \frac{-(n_D^2 q_M - n_M^2 q_D)^2}{2n_M^2 n_D^2 q_D q_M} e^{i\xi_D d}, \quad (2.56)$$

which is satisfied for

$$\begin{aligned} 0 &= (\varepsilon_D^2 q_M^2 + \varepsilon_M^2 q_D^2)(e^{-i\xi_D d} - e^{i\xi_D d}) + 2\varepsilon_M \varepsilon_D q_D q_M (e^{-i\xi_D d} + e^{i\xi_D d}) \\ &= (\varepsilon_D^2 q_M^2 + \varepsilon_M^2 q_D^2) \tanh(-i\xi_D d) + 2\varepsilon_M \varepsilon_D q_D q_M. \end{aligned} \quad (2.57)$$

Equation 2.57 is the dispersion relation for the GSP mode. The equation has no analytical solution, so a solution must be found either numerically or by developing an approximations analytical expression. Figures 2.5a and 2.5b show the longitudinal and transverse E -field components, respectively, and the mode effective index and propagation loss obtained numerically from eq. (2.57) are shown in fig. 2.5c. It is clear that GSPs do not propagate over long distances, with propagation length not exceeding a few tens of micrometres for large gap widths d , as a significant part of the mode resides on the metal leading to ohmic heating. For decreasing gap widths an increasing part of the mode is situated in the metals, leading to decreasing propagation lengths, while the mode effective index increases. Across most gap widths GSPs have a propagation length significantly longer than their wavelength, enabling resonators at optical and near-infrared frequencies with subwavelength dimensions. This opens up for a wide range of applications as it allows for the precise and efficient control of the phase and amplitude control of light that is reflected, transmitted or thermally emitted from a structure with a closely spaced lattice of GSP-resonators on its surface, a metasurface.

A treatment based on the latter approach is done in [37], yielding relatively simple relations for the GSP dispersion. For gap widths that are not too large, the approximation $\tanh(x) \approx x$ holds, which leads to

$$\beta_{GSP} = k_0 \sqrt{\varepsilon_D + \frac{1}{2} \left(\frac{\beta_{GSP}^0}{k_0} \right)^2 + \sqrt{\left(\frac{\beta_{GSP}^0}{k_0} \right)^2 \left[\varepsilon_D - \varepsilon_M + \frac{1}{4} \left(\frac{\beta_{GSP}^0}{k_0} \right)^2 \right]}}, \quad (2.58)$$

where

$$\beta_{GSP}^0 = -\frac{2\varepsilon_D}{t\varepsilon_M}. \quad (2.59)$$

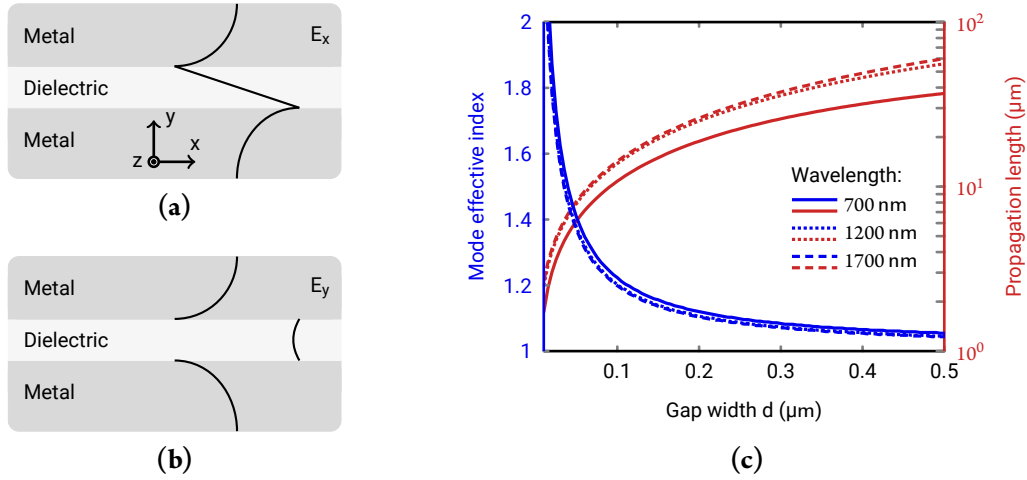


Figure 2.5: (a) Schematic of the tangential electric field component E_x . (b) Schematic of the orthogonal electric field component E_y . (c) Mode effective index (blue) and propagation length (red) of the gap surface plasmon (GSP), obtained from the GSP dispersion relation [eq. (2.57)] using an exact (i.e. with user-defined accuracy) numerical method (lines) and eq. (2.60), the approximation for moderate separations of the interfaces (diamonds). It is seen that the analytical approximation yields satisfactory correspondence over a wide range of gap widths.

For later use, a further simplification will be introduced, based on the assumption that $t > (\lambda_0 \epsilon_D) / (\pi |\epsilon_M|)$, leads to

$$\beta_{GSP} = k_0 \sqrt{\epsilon_D - \frac{2\epsilon_D \sqrt{\epsilon_D - \epsilon_M}}{k_0 t \epsilon_M}}. \quad (2.60)$$

The assumption on t entering the dispersion in eq. (2.60), corresponds to wavelengths that are not too small. A rough estimation of $\epsilon_D / \pi |\epsilon_M|$, based on values for vacuum and gold in around a wavelength of 1 μm gives a value 1/300 [38]. It is thus safe to say that the above approximation holds good even for gap widths significantly below the wavelength, only losing validity at extremely narrow separations below a handful of nanometres. The analytical form of the GSP dispersion now allows for closed-form description of resonators, etc. in which GSP modes propagate.

Chapter 3

Thermal emission

This chapter is meant as an outline of theory essential to the understanding of thermal radiation selective thermal emitters, providing essential background and defining terms and notation. An outline of the derivation of the BB-spectrum (section 3.1) is provided, followed by a brief discussion of Kirchhoff's law, the equality between absorption and emission. Finally, figures of merit are described which can provide guidelines for the design of selective emitter.

3.1 Blackbody radiation

Fundamental to the treatment of thermal radiation is the understanding of the emission of a surface which absorbs all electromagnetic radiation incident on it - a so-called blackbody (BB). As will emerge from the following treatment, the emitted from a blackbody is a function only of the wavelength and of the temperature. To derive the BB spectrum it is helpful to consider a photon gas in an arbitrary cavity. For a gas of N non-interacting, identical particles, with discrete single-particle states $1, 2, \dots, r, \dots$, with respective energies ϵ_r , the state of the gas is fully specified by the associated occupation numbers describing the number of particles in the state r :

$$n_1, n_2, \dots, n_r, \dots, \quad (3.1)$$

where

$$\sum_r n_r = N. \quad (3.2)$$

One can define an exchange operator P_{jk} acting on a many-body wave function Ψ , which interchanges the labels of particles j and k . It is clear that $P_{jk}^2 = 1$, from which it follows that the allows eigenvalues for P are ± 1 , i.e., $P_{jk}(\Psi) = \pm \Psi$, with eigenvalues $+1$ and -1 correspond to symmetric and antisymmetric particle wave functions under exchange. It is a fundamental result from relativistic quantum mechanics that these two classes of particles, possess two distinct sets of internal angular momentum (or spin) quantum numbers.

Particles that possess spin values equal to integer multiple values of \hbar ($\hbar, 2\hbar, \dots$), have symmetric wave functions under exchange and have no restrictions on their occupation numbers:

$$n_r \in \mathbb{N}^+, \quad (3.3)$$

where \mathbb{N}^+ is the set of non-negative integers. These particles are called bosons and follow Bose-Einstein (BE) statistics. The second class of particles, the so-called fermions, has an intrinsic angular momentum (spin) equal to half integer multiples of \hbar ($\frac{1}{2}\hbar, \frac{3}{2}\hbar, \dots$). For fermions, which follow so-called Fermi-Dirac (FD) statistics, the wave function is antisymmetric under exchange, leading to the following restriction on the occupation numbers:

$$n_r \in \{0, 1\}. \quad (3.4)$$

One can now write the partition function Z for the quantal gas of photons which has the advantage that it allows for the derivation of the mean occupation number of all states at a given temperature. Z is given of volume V , temperature T and particle number N :

$$Z(T, V, N) = \sum_{n_r} e^{-\beta \sum_r n_r \epsilon_r}, \quad (3.5)$$

where β is the thermodynamic *beta*, $(k_B T)^{-1}$. The summation is over all sets of occupation numbers satisfying simultaneously eqs. (3.2) and (3.3) or eqs. (3.2) and (3.4), depending on the particle statistics.

As a gas of photons, the gas follows BE-statistics of eq. (3.3). It is important to realize that a photon gas at thermal equilibrium with surroundings at temperature T does not have a constant number of photons N , due to the stochastic process of photon emission. Therefore, a photon gas (at thermal equilibrium) does not follow eq. (3.2). This relaxes the summation in eq. (3.5), which can now be written:

$$\begin{aligned} Z_{ph}(T, V) &= \prod_r \sum_{n_r} e^{-\beta n_r \epsilon_r} \\ &= \prod_r \frac{1}{1 - e^{-\beta \epsilon_r}}, \end{aligned} \quad (3.6)$$

where the convergence of the geometric series is guaranteed, since $-\beta \epsilon_r < 0$. The mean occupation number of a given state j , \bar{n}_j , can be straight-forwardly be derived from the partition function:

$$\begin{aligned} \bar{n}_j &= \frac{-1}{\beta} \frac{\partial}{\partial \epsilon_j} \ln Z_{ph} \\ &= \frac{1}{e^{\beta \epsilon_j} - 1} \end{aligned} \quad (3.7)$$

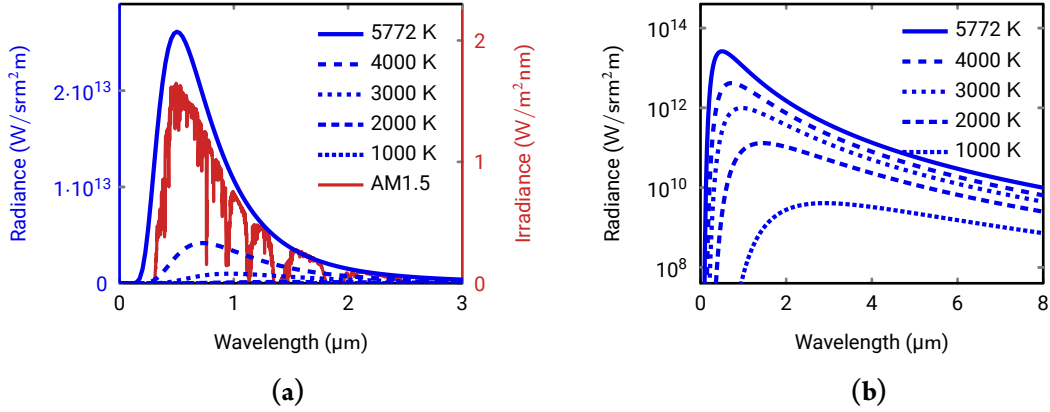


Figure 3.1: (a) Linear and (b) semilogarithmic plots of the spectral radiance for black-bodies at temperatures of 1000 K, 2000 K, 3000 K, 4000 K, 5772 K, the latter corresponding to the effective temperature of the visible part of the solar atmosphere (photosphere) [41, 42]. The direct solar irradiance through 1.5 atmospheres (AM1.5) is shown in grey (a).

For the calculation of the spatial energy density, it is additionally necessary to know the density of states. The density of states $f(\omega)$ of a particle in a box is a standard result and will be used without derivation here [39, 40]. For a photon, the density of states needs to be corrected for two-fold polarisation degeneracy, resulting in:

$$f(\omega)d\omega = \frac{V\omega^2 d\omega}{\pi^2 c^3} \quad (3.8)$$

Observing that $\varepsilon = \hbar\omega$, one arrives from the mean number of photons dN_ω at the mean energy dE_ω in the frequency range from ω to $\omega + d\omega$:

$$dE_\omega = \hbar\omega dN_\omega = \hbar\omega \frac{V}{\pi^2 c^3} \frac{\omega^2 d\omega}{e^{\beta\hbar\omega} - 1}. \quad (3.9)$$

It remains to be pointed out that the volume V matters only in the sense of its size, not its shape. Therefore, it follows that the mean spatial density of photons and mean spatial density of energy are independent of the spatial position. Now the spectral spatial energy density $u(\omega, T)$, which has units of energy per unit volume and unit spectral variable can be calculated as

$$\begin{aligned} u(\omega, T) &= \frac{1}{V} \frac{dE_\omega}{d\omega} \\ &= \frac{\hbar\omega}{\pi^2 c^3 [e^{\beta\hbar\omega} - 1]}. \end{aligned} \quad (3.10)$$

Equation (3.10) is Planck's law describing the spatial energy density per unit volume per spectral unit (here angular frequency) [43]. It is more often used in its *radiance* form, $B(\omega, T)$, which

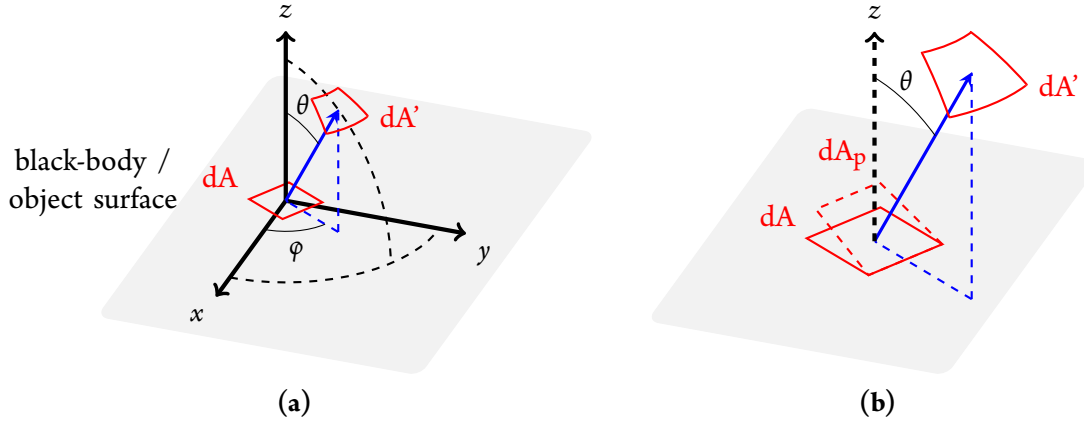


Figure 3.2: (a) Schematic of geometry in spherical coordinates. It is implicitly assumed that the surface of the emitting/absorbing body lies in the xy -plane. Indicated in red are the infinitesimal emitting/absorbing area dA which emits radiation into an area dA' , subtending the solid angle $d\Omega$, as seen from dA (not indicated). (b) Enlarged geometry from (a), showing the relation between the projected area dA_p , the actual surface area dA and the receiving area dA' for the energy transfer from dA to dA' .

describes the power, $d\dot{Q}$, emitted per unit projected area (see fig. 3.2b), per unit solid angle, and per unit spectral unit:

$$\begin{aligned}
 B(\omega, T) &\equiv \frac{d\dot{E}}{dA_p d\Omega} = \frac{d\dot{E}}{dA \cos \theta \sin \theta d\theta d\varphi} = \frac{c}{4\pi} u(\omega, T) \\
 &= \frac{\hbar\omega}{4\pi^3 c^2} \frac{1}{e^{\beta\hbar\omega} - 1}.
 \end{aligned} \tag{3.11}$$

For the sake of convenience, Planckian radiation is often reformulated in terms of other spectral variables of interest. In terms of wavelength, λ , the blackbody radiation reads

$$B(\lambda, T) = \frac{2\hbar c^2}{\lambda^5} \frac{1}{e^{\frac{\hbar c\beta}{\lambda}} - 1}. \tag{3.12}$$

It should be pointed out that the intensity entering the spectral radiance is defined in terms of the projected area dA_p (see fig. 3.2), i.e. the size of the area as seen from an observer. From this, it can follow that the blackbody radiance follows a cosine law with regard to θ :

$$\frac{B(\lambda, T, \theta, \varphi)}{\cos \theta} = B(\lambda, T). \tag{3.13}$$

Figure 3.1 shows the spectral radiance of the blackbody radiation [eq. (3.12)] at different temperatures. It is immediately noticeable that the wavelength of maximum emission shifts to shorter wavelengths for increasing temperatures, and that the energy emitted increases drastically with temperature. The (spectral) point of maximum blackbody emission, ω_{\max} , λ_{\max} , etc., and the total power

emitted by a blackbody, $u(T)$, can both be straight-forwardly derived by returning to eq. (3.10). Setting the first derivative of eq. (3.10) equal to zero to obtain the wavelength of maximum radiance results in an transcendental equation with the rather straight-forward numerical solution

$$\lambda_{\max} = \frac{hc}{\lambda_{\max}} \cdot \beta. \quad (3.14)$$

Equation (3.14) is widely referred to as Wien's displacement law. Conversely, the integration of eq. (3.10) over the entire spectrum yields the spatial energy density of a blackbody radiation field, u :

$$u(T) = \int_0^{\infty} u(\omega, T) d\omega = aT^4. \quad (3.15)$$

with the constant of proportionality, a , defined as

$$a \equiv \frac{4}{c} \sigma \equiv \frac{\pi^2 k_B^4}{15 \hbar^3 c^3}. \quad (3.16)$$

Through spectral integration of the blackbody radiance in eq. (3.12), instead of the spectral energy density, one obtains the total emitted power per unit area, $B(T)$:

$$B(T) = \sigma T^4. \quad (3.17)$$

3.2 Thermal radiation of real surfaces

All real surfaces emit thermal radiation at a lower rate than a blackbody, with the ratio between the spectral radiance I and the spectral blackbody radiance defined as the emissive power or emissivity, $\varepsilon(\lambda, T, \theta, \varphi)$:

$$\varepsilon(\lambda, T, \theta, \varphi) = \frac{I(\lambda, T, \theta, \varphi)}{B(\lambda, T, \theta, \varphi)}. \quad (3.18)$$

As indicated by the notation, the emissivity is, in general, a function of both wavelength, temperature and direction (for coordinates, see fig. 3.2). From both thermodynamic arguments and the reciprocity inherent to Maxwell's equations, one can arrive at the so-called Kirchhoff's reciprocity for thermal radiation, which equates the directional emissivity with the absorbance, $a(\lambda, T, \theta, \varphi)$, of a surface [44, 45]. The thermodynamic argument can be briefly outlined, based on an isothermal body b at temperature T placed in a large (relative to the body b), isothermal cavity c at the same temperature T . To the extent that the cavity is undisturbed by the body, it will emit as a BB, emitting σT^4 onto the body b , which will absorb the flux $A_b a_b \sigma T^4$, where A_b is the surface area of b and a_b is the absorbance of b . At the same time, the body emits the energy $A_b \varepsilon_b \sigma T^4$. Since the body and the cavity are isothermal, they must be in thermodynamic equilibrium, wherefore their net energy exchange must equal zero. From this it straightforwardly follows that $a(T) = \varepsilon(T)$. Spectral and di-

rectional versions can be derived with little complication following the derivation outlined above, leading to:

$$\varepsilon(\lambda, T, \theta, \varphi) = \alpha(\lambda, T, \theta, \varphi). \quad (3.19)$$

Obviously, hemispherical, spectrally or otherwise integrated versions of ε and α can be obtained through integration of the appropriate variables. Kirchhoff's law has a significant impact on the design of thermal emitters since the optical requirement can be addressed by surface absorption engineering, which is a problem with a broad range of well-established fabrication techniques. From the definition of the emissivity, it follows that the radiant intensity $I(\lambda, T)$ from a surface with emissivity ε_λ has the form

$$\begin{aligned} I(\lambda, T) &= \varepsilon(\lambda, T)B(\lambda, T) \\ &= \alpha(\lambda, T)B(\lambda, T). \end{aligned} \quad (3.20)$$

It is worth pointing out that eqs. (3.19) and (3.20) are strictly valid only in thermodynamic equilibrium, a requirement that is not strictly satisfied in a measurement where a hot body is exchanging heat with a detector at room temperature. Since any energy transfer process is the result of a non-equilibrium situation, Kirchhoff's emissivity can not - in a rigorous sense - be applied to the situation of energy transfer. However, the above relations are also applied to non-equilibrium situations. For measurements, it is usually sufficient to place the sample in a thermally homogeneous cavity, with a relatively small opening through which the measurement is performed. If the opening is sufficiently small, it will not disturb the thermal equilibrium between inside the sample and between the sample and the cavity. Enclosing a sample in a cavity also helps reduce internal thermal stresses in the sample as well as helps in the temperature control of the sample environment.

It can be seen from eq. (3.20) that, as far as the optical properties are concerned, the design of the optical properties of a thermal emitter is analogous to the engineering of optical absorption. Since, for TPV, energy efficiency hinges on the ability to generate thermal radiation within a limited wavelength interval, it is natural to look for resonant structures, which can provide enhanced absorption at their resonant wavelengths. The work presented in this thesis centres on two such structures, the continuous-layer Fabry-Pérot resonator (cl-FPR) and the vertical trench gap surface plasmon Fabry-Pérot resonator (GSP-FPR).

3.3 The view factor

When considering the radiant heat exchange between two surfaces, naturally any description has to take into account both the spectral properties of both surfaces as well as the geometric configuration that determines how and if the radiation from surface 1 impinges on surface 2. If one assumes that the surfaces are Lambertian emitters, then the view factor (VF) is defined as the fraction of radiation leaving surface 1 that impinges onto surface 2. For the exchange of energy between two diffusely emitting areas, dA_1 and dA_2 (fig. 3.3a), the view factor for infinitesimal areas $dA_1 \rightarrow dA_2, F_{1 \rightarrow 2}$, is

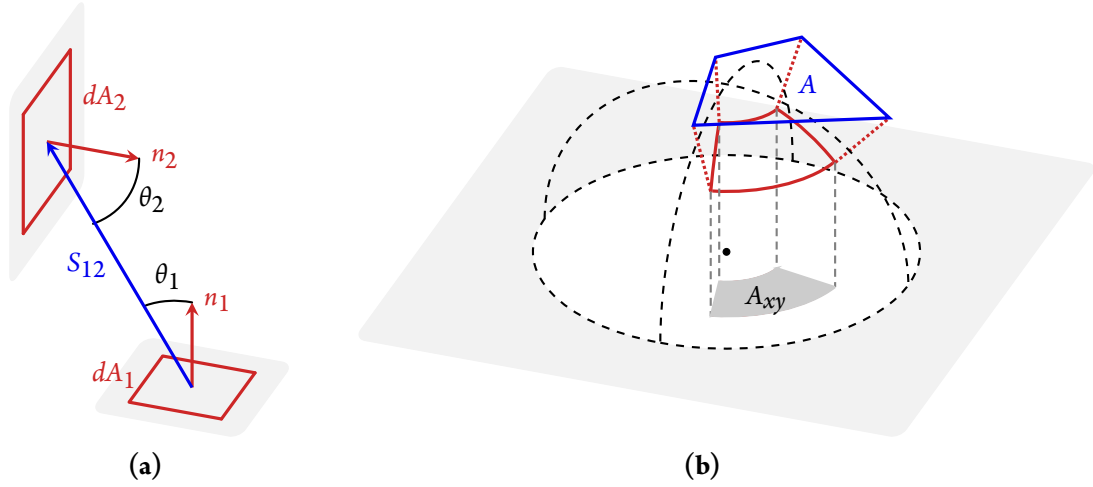


Figure 3.3: (a) Geometry in view factor calculations between two differential areas, dA_1 and dA_2 , with respective normal vectors n_1 and n_2 . The orientation of dA_1 and dA_2 with respect to the vector connecting the differential areas, S_{12} , is defined by the angles θ_1 and θ_2 . (b) Geometric illustration of the view factor from an infinitesimal surface area dA , situated in the xy -plane at the origo, to an area A . The view factor corresponds to the ratio between the area A_{xy} (dark grey), and the total projection of the hemisphere onto the xy -plane (white). A_{xy} is obtained by point-projecting the area A onto the hemisphere (red), then parallel-projecting it onto the xy -plane (grey dashed).

given as

$$F_{1 \rightarrow 2} = \frac{\cos \theta_1 \cos \theta_2}{\pi S_{12}^2} dA_2. \quad (3.21)$$

For energy transfer between two general surfaces, the view factor differential VF is integrated over both surfaces:

$$F_{1 \rightarrow 2} = \frac{1}{A_1} \int_{A_1} \int_{A_2} \frac{\cos \theta_1 \cos \theta_2}{\pi S_{12}^2} dA_2 dA_1. \quad (3.22)$$

In the context of TPV design, the VF is used to characterise the geometric idealness of the setup, with a VF of 1 describing the ideal setup in which every photon emitted by the emitter is incident on the PVC.

A geometrical analogue – Nusselt’s analogue – can be drawn upon to visualise the view factor from a differential area dA to an arbitrary area A . The view factor in this geometry corresponds to the ratio between the area A_{xy} and the projection of the hemisphere onto the xy -plane. A_{xy} is obtained by a point-projection onto the hemisphere and a subsequent orthogonal projection onto the plane of dA (see fig. 3.3b).

3.4 Illumination of a photovoltaic band gap material

As briefly outlined in chapter 1, the illumination of a band gap material with a broadband source leads to energy losses which need to be understood by an interplay between the band gap structure of the PVC material and the spectrum of emitted energies from the selective emitter (SE). A brief expansion on the spectral loss discussion of chapter 1 follows, and some figures of merit (FOMs) which quantify efficiencies and inefficiencies are discussed.

Figure of merit for the illumination of a pn -junction

It is worth returning briefly to the absorption of a photon in a pn -junction, as depicted in fig. 3.4. It is evident from the previous discussion that the extractable energy per photon is closely related to the band gap energy, and that photons with energies below do not lead to the generation of charge carriers in the PVC. For this reason, the emissivity below the band gap energy should be suppressed for the efficiency to be maximised. Above the band gap, the picture is less straightforward. For a *per-photon* consideration, minimal energy is wasted for a photon energy at the band gap. The per-photon energy utilisation is therefore maximised in the limit where the SE has a delta distribution emissivity position directly above the band gap. However, in this limit the spectral irradiance approaches zero, leading the requirement of an infinite emitter area. A wider bandwidth of emission above the band gap alleviated this issue at the cost of (some) energy being lost to thermalisation. It is, therefore necessary - to some extent - to sacrifice efficiency to strike a good balance between efficiency and power output density that determines the size of a TPV device with a given power output.

Following the above discussion, it is clear that any figure of merit characterising the match between an SE and a PVC should include a term describing the degree of suppression of emission below the band gap energy E_B and a term quantifying the emission above the band gap. However, since the trade-off between efficiency and throughput, as outlined above, is dependent on the emitter surface area and output power requirements, amongst others, there is no one-dimensional metric that could be encapsulated by an FOM. To circumvent this complication, one solution is to define the ideal emission as unity for all energies above the band gap and zero for all other wavelengths below the bandgap. With this modification, it becomes possible to define an ideality factor of the emitter in the wavelength range above the bandgap as the ratio of energy emitted in this wavelength relative to the energy emitted by a BB.

In a recent publication [46] the above outlined approach is used to derive the following FOMs, c_{FOM} :

$$c_{\text{FOM}} = c_{\text{wf}} \frac{\int_{\lambda_i}^{\lambda_B} \varepsilon_{\lambda} B_{\lambda} d\lambda}{\int_{\lambda_i}^{\lambda_B} B_{\lambda} d\lambda} - (1 - c_{\text{wf}}) \frac{\int_{\lambda_B}^{\lambda_f} \varepsilon_{\lambda} B_{\lambda} d\lambda}{\int_{\lambda_B}^{\lambda_f} B_{\lambda} d\lambda}, \quad (3.23)$$

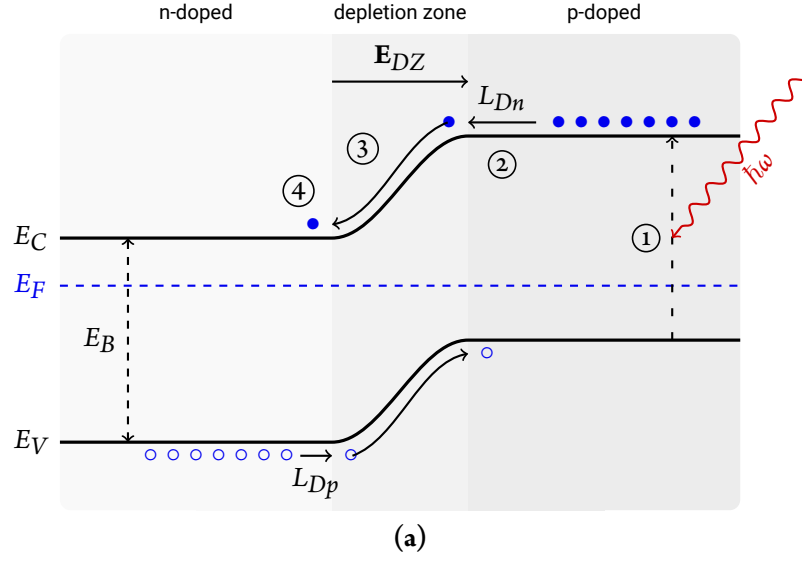


Figure 3.4: Schematic of photon absorption in the band structure of a pn -junction. The process of photon absorption, electron-hole pair (EHP) generation and diffusion of charge carriers through the depletion zone are indicated by encircled numbers. A photon (red) with energy $\hbar\omega$ larger than the band gap energy, E_B , is absorbed near the pn -junction exciting an electron from the valence band (E_V) to the conduction band (E_C). If the electron is excited roughly within a diffusion length for electrons (L_{Dn}) away from the depletion zone (depletion zone (DZ)), they can diffuse into the DZ, where the DZ field E_{DZ} transports them to the p -side of the junction.

where ε_λ is used for readability as the short-hand notation of spectral emissivity, λ_i and λ_f denote the analysed spectral interval, for which $1 \mu\text{m}$ $10 \mu\text{m}$ are used in besaid publication. λ_B is the band gap wavelength of the cell in use and c_{wf} is a weighting factor that describes extent to which the first term in eq. (3.23) is weighted relative to the second term, i.e. the relative weight of emitter properties above the band gap to the properties below the band gap. In other words, $c_{wf} = 1$ leads to a c_{FOM} that only takes into account the emission of convertible emission above the band gap, conversely for $c_{wf} = 0$, c_{FOM} describes the degree of suppression of thermal emission below the band gap. While the authors of [46] comment little on the physical meaning of c_{wf} , it should be pointed out that c_{wf} is not a free parameter. The extent to which the suppression of emission below E_B should be weighted versus the emission above E_B , is not arbitrary. It instead depends on the fraction of energy in the BB spectrum at the emitter temperature that is situated above the band gap. If, for example, one were to operate an emitter at an extremely high temperature compared to the band gap energy E_B of the PVC, there would be little emission below the the gap energy, regardless of the emissivity, simply due to a relatively little part of the BB emission at the emitter temperature being emitted below E_B . For a given temperature T and band gap energy E_B , this weighting factor c_{wf} is therefore fixed and it is view of this author that it should be calculated as the proportion of power in the illuminating spectrum which has photon energies above the band gap energy, corresponding

to the wavelength λ_B :

$$c_{\text{wf}} = \frac{\int_{\lambda_i}^{\lambda_B} B_\lambda d\lambda}{\int_{\lambda_i}^{\lambda_f} B_\lambda d\lambda}. \quad (3.24)$$

Here, λ_i and λ_f are the limits of the integration, which ideally should be 0 and ∞ . In practice this requirement can be relaxed such that the limits simply cover spectral regions with significant intensity.

A point worthwhile making in this context is that the above-outlined treatment is rather simplistic, being based solely on the consideration of a *pn*-junction with a cutoff wavelength for absorption. It specifically disregards several important influences of real TPV systems, radiation reflected back to the emitter from the PVC surface, to name an example. However, a more in-depth treatment quickly becomes very setup specific, and even the above treatment assumes an (unrealistically) unity quantum efficiency above the band gap. This might explain, to some extent, the absence of a widely accepted figure of merit in the vast body of research. However, it is the view of this author that more broadly accepted figures of merits would be helpful for the field - even given above-mentioned flaws since it would lead the increased reporting on long-wavelength properties of the used materials/structures, which is a prerequisite for any meaningful evaluation of any proposed TPV emitter.

3.5 Selective solar absorbers

The conversion of sunlight to heat plays an important role in several schemes of energy conversion, such as concentrated solar thermal or TPV. Between these fields, the demands to the spectral properties of the selective solar absorbers (SSAs) do not differ significantly. An ideal SSA possesses a region of high absorption covering the entire solar spectrum (see fig. 3.5). The desired region of high absorbance should cover the solar spectrum $S(\lambda)$, and should transition to ideally zero absorption where the emission from the BB spectrum exceeds the solar flux. Depending on the concentration, this occurs at a wavelength of around 2 μm to 2.5 μm . With increasing temperature, the transition to shorter wavelengths needs to occur at decreasing wavelengths, since the cross-over between the solar spectrum and the BB spectrum shifts due to the change in the blackbody spectrum. As a consequence, an increase in absorber temperature, which is an advantage from a thermodynamic standpoint, reduces the range of absorbed wavelengths. This issue necessitates the use of concentrated solar light when for hot absorbers, which is used in practically all solar thermal and STPV schemes. If concentrated solar light is used, the solar spectrum shown in fig. 3.5 must be multiplied with the concentrations factor, which decreases the influence of absorber temperature on the cut-off wavelength drastically.

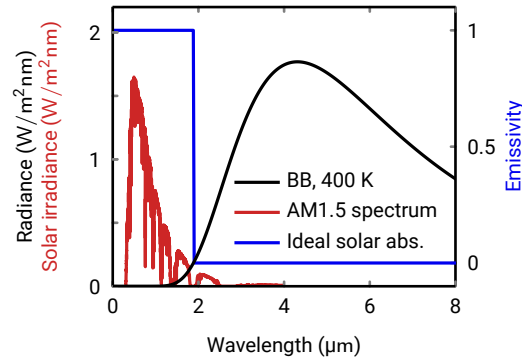


Figure 3.5: Solar spectrum (non-concentrated AM1.5, red) and blackbody spectrum at 400 K (black). The emittance black of an ideal solar absorber is a step function with unity absorption for wavelengths at which the solar spectrum dominates and zero absorption at longer wavelengths is (blue) to minimise losses due to re-radiation.

The efficiency of the solar absorber, η_{SA} can be defined as ratio of the difference between the absorbed and re-radiated flux, Q_a and Q_e , and the incoming (possibly concentrated) solar flux Q_s :

$$\eta_{SA} = \frac{Q_a - Q_e}{Q_s}. \quad (3.25)$$

The solar absorber efficiency of the solar absorber (SA) is dependent on its temperature and the concentration of the illumination, and not quantifiable independently from the operating conditions. However, the fraction of the absorbed radiation is not strongly dependent on these quantities, although it does so to a lesser extent if thermo-optic changes in the absorber are sizeable. Thus, one can define a solar absorbance, a_s , as the fraction of absorbed solar irradiance to the total irradiance [47, 48]:

$$a_s = \frac{\int_0^\infty a_\lambda S_\lambda d\lambda}{\int_0^\infty S_\lambda d\lambda}. \quad (3.26)$$

Equation (3.26) allows for the absorbed solar flux to be rewritten in terms of the incoming solar flux as $Q_a = a_s Q_s$. The fraction of thermal emission to the total emission of a blackbody (at the same temperature as the solar absorber) is defined as the solar emissivity ϵ_s :

$$\epsilon_s = \frac{\int_0^\infty \epsilon_\lambda B_\lambda d\lambda}{\int_0^\infty B_\lambda d\lambda}. \quad (3.27)$$

The thermal efficiency of the selective solar absorber in eq. (3.25) can now be brought into the form

$$\eta_{SA} = a_s - \epsilon_s \frac{\sigma T^4}{H_s}, \quad (3.28)$$

where σ is the Stefan-Boltzmann constant and H_s is the wavelength-integrated solar flux. From eq. (3.28), it is clear that the thermal efficiency of the SSA is maximised for simultaneously large values of a_s and small values of ε_s . It is worth pointing out that the one should take the hemispherical emittance in eq. (3.27), for the suppression of re-radiation into the entire hemisphere. In eq. (3.26), since non-concentrated sunlight includes a scattered off-normal component, the solar absorber should ideally exhibit high absorption over a broad range of angles, a point with increased importance for concentrated sunlight.

One can conclude that the design SEs and SSAs is similar to some extent, in that a sharp cross-over is needed at a certain wavelength where the absorption ideally transitions from unity to zero for increasing wavelengths. For SEs the cross-over wavelengths is given by the band gap of the PVC material whereas for SSAs the cross-over wavelength is determined by the intersection of the radiant flux of thermal emission and incoming solar radiation.

Chapter 4

Spectrally selective surfaces

This chapter aims to provide a brief recapitulation of the considerations leading to each of the main research projects, which have resulted in publication so far, and two additional projects which are under preparation for submission. Main conclusions are highlighted where important for the logical connections between separate projects, in the hope that a common thread might stand out clearer to the reader, as well as the reasons for shift of focus in the principal direction of research, from plasmonic to photonic resonators.

4.1 Plasmonic colour printing

The research into surfaces with subwavelength lattices of plasmonic resonators, so-called plasmonic metasurfaces, has enjoyed persistent popularity in the last decade. Metasurfaces consisting of gap surface plasmon resonators (GSPRs) allow for the design of surfaces which interact strongly with light, allowing for perfectly absorbing surfaces or the modulation of the reflection phase in the entire 2π -phase space. Conveniently, through alteration of the dielectric spacer thickness GSPRs can be made to be either strongly scattering or strongly absorbing. Predominantly scattering GSPRs are obtained by choosing a thick dielectric thickness, while a thin spacer pushes the GSP into the metal which leads to increased propagation losses of the GSP and absorbing GSPRs. Since GSPRs can have resonances at optical frequencies with physical sizes on the order of tens to hundreds of nanometres, while having absorption cross sections on the order of the wavelength, they are ideally suited for use in colour printing with an extremely high density of pixels on or near the diffraction limit. In contrast to various other configuration used for colour printing, since the GSPRs resonance does not depend on diffraction phenomena, the colour print is not angle-dependent or dependent on the illumination conditions. Moreover, since the plasmonic mode resides mainly in the dielectric between the metallic layers, one can cover the colour print with a protective layer of e.g. polymer, leading to touch-resistant colour print with excellent chemical stability.

Figure 4.1 shows the use of GSPR for colour printing onto a gold substrate. As seen on the schematic (4.1a), a dielectric spacer of SiO_2 is used and a rectangular lattice of circular resonators.

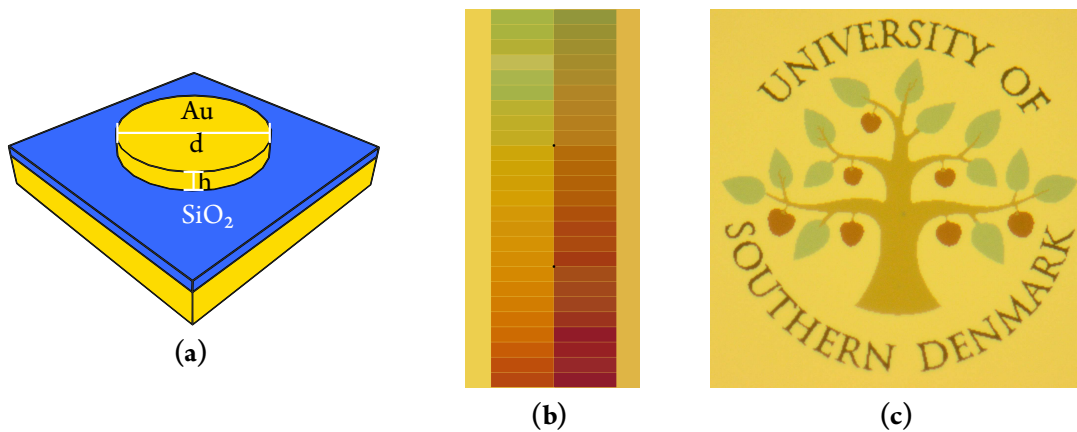


Figure 4.1: (a) Schematic of a gap surface plasmon resonator consisting of a continuous bottom gold layer, a continuous intermediate dielectric layer consisting of SiO_2 and a top layer which is structured by electron-beam lithography into circular discs. The diameter of the discs determines the resonance wavelength of the resonator. (b) The range of colours that available from GSP resonators with 20 nm dielectric layer thickness (left) and 40 nm dielectric thickness (right) through simple variation of the disc diameter. The colour of the respective gold-dielectric interface can be seen to the sides. (c) Colour print of the logo of the university of Southern Denmark. The logo is approximately $80 \mu\text{m}$ in diameter and is printed with a subwavelength pixel pitch of 340 nm.

By variation of the resonator diameter a variety of colours are obtained (fig. 4.1b), which can be fed into a library that can subsequently be used to print a colour image. For an illustration of the resolution, an image of the logo of the University of Southern Denmark is printed (Figure 4.1c) with a diameter of 80 nm, corresponding to approximately the width a human hair or two dot widths on a laser printer with a resolution of 600 dpi. More details are found in [49] which is attached in appendix A.

4.2 Trench gap surface plasmon resonators

While gold-based GSPR are ideal for the design of spectrally selective surfaces, the combination of the low melting point of gold and the need for a top layer of gold nanodiscs makes gold-based GSPRs in the above configuration less than ideally suited for thermal emission. Another related configuration is highly preferable: a high aspect ratio trench, drilled (or otherwise fabricated) directly into a metallic substrate. Such a configuration has the advantage of consisting of only one material, which should minimise melting point depression and eliminate problems arising from different expansion coefficients and bad adhesion between layers of different materials. This motivated investigations into the properties and fabrication of such trenches at an early stage in the project, resulting in paper [50] which can be found in appendix C, in which a comprehensive analysis of the scattering, absorption and extinction properties of single trench gap surface plasmon resonators (tGSPRs) and arrays of tGSPRs is carried out. In the paper, a Fabry-Pérot model is

established, based on the simplified expression for GSP dispersion from eq. (2.57), and reflection phases at the terminations of the tGSPR derived elsewhere. The model allows for the accurate and efficient calculation of scattering, absorption and extinction properties of the tGSPR, which is verified by comparison with numerical simulation of both single and arrays of trenches. The model reveals several interesting fundamental properties of the tGSPR, most notably that the scattering cross-section $\sigma_{sca.}$ in the lossless limit approaches the unitary scattering cross section for a dipolar scatterer $\sigma_{sca.} = 4\lambda/\pi$. Experimental verification of result from the model and numerical simulations are provided by measuring scattering spectra from trenches fabricated into a monocrystalline gold substrate.

There are several ways to fabricate a tGSPR, such as focussed ion-beam (FIB) which is discussed in the publication enclosed in appendix B. However, FIB yields a tapering V-shaped profile which is detrimental to the quality of the resonance supported by the trench structure. Another possibility of fabrication of to fabricate the inverse structure into a silicon substrate. Subsequently, a gold film (or any other material for that matter) can be deposited onto the substrate and subsequently stripped from silicon template in a process known as template stripping. Attempts to fabricate tGSPRs by template stripping proved unsuccessful, despite devoting significant efforts and time towards it. The fabrication of a suitable template is rather straightforward, using KOH wet-etching, that can yield virtually perfect vertically-walled trenches (see fig. 4.2a). However, the gold film must be firmly attached to a substrate prior to template stripping in order to overcome adhesive forces between the gold layer and the template. This requirement becomes very hard to satisfy for a vertically-walled template, and it was not possible to solve the problem of reliably attaching the obtained gold films to a substrate. Figure 4.2b shows an example of a resulting gold surface still loosely attached to the template after an unsuccessful template stripping attempt.

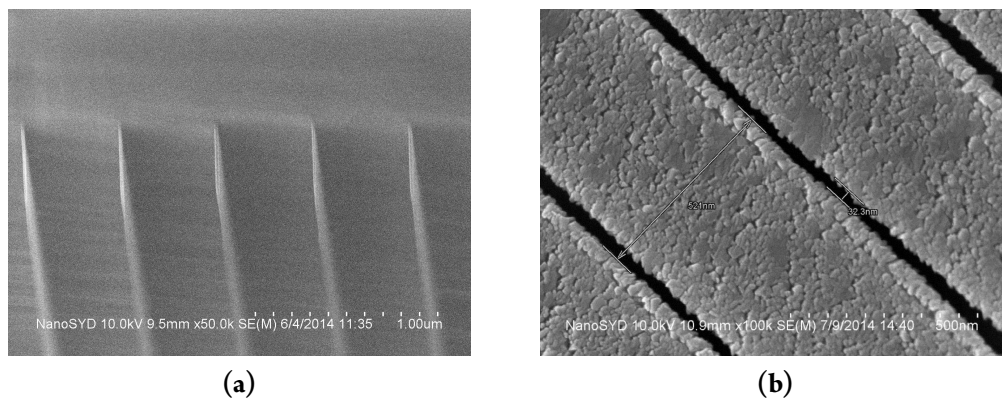


Figure 4.2: (a) SEM image of a template fabricated from anisotropic wet-etching in KOH (template is seen below). (b) Image of an array of gold tGSPRs obtained by template stripping from a silicon template similar to (a). The width of the obtained trenches is approximately 30 nm with an array period of 520 nm.

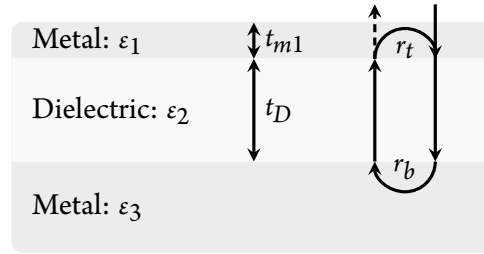


Figure 4.3: Schematic of a continuous-layer Fabry-Pérot resonator (cl-FPR), consisting of an optically thick metallic layer or substrate, a dielectric layer of thickness t_D , and a top metal layer of thickness t_{m1} on the order of the optical skin depth. Complex reflection amplitudes r_t and r_b are associated with reflection from top and bottom metallic layers, respectively. The relative thinness of the top layer enables the confined mode to couple to radiating modes.

4.3 Continuous-layer Fabry-Pérot Resonators

In recent years, significant attention has been paid to the absorption of multilayer structures incorporating nm-thick metallic films for the design of optical and near-infrared absorbers [51–59]. As opposed to absorption in plasmonic resonators, thin films can be used to form an optical which does not require any in-plane structuring of the surface but relies solely on control over the thickness and material choice of each layer. The absence of surface structuring comes with the advantage of greatly simplifying the fabrication of the resonators, making them both more economical and easier to scale up in size. Another advantage is that the melting point is significantly less affected for ultra-thin films, compared to nanoparticles of the same dimension, enabling the use at temperatures closer to the melting point of the bulk material. An increased operating temperature is an important feature for absorbers in both solar thermal and TPV applications since, in both cases, it is important to maximise the absorber temperature resulting in the requirements to the thermal stability of the absorber or emitter.

A simple photonic resonator can be constructed on a metallic substrate by deposition of only two layers onto a metallic substrate; a dielectric layer, in which light can propagate back and forth, and a thin metallic top layer with a thickness on the order of the skin depth, which acts a semi-transparent mirror (fig. 4.3). An intuitive picture of the physics involved in the relatively simple geometry can be understood in terms of the round trip phase of such a plane-wave travelling between the metallic layers. Resonance occurs when the round-trip phase for the plane wave equals 2π . The round-trip phase, which comprises phases for reflections at the top and bottom metallic layers, φ_r and φ_t , respectively, and a propagation phase, which is given by the optical path length between the two mirrors:

$$\varphi_r + \varphi_t + 2\frac{t_D n_D}{\lambda_0} = m \cdot 2\pi, \quad (4.1)$$

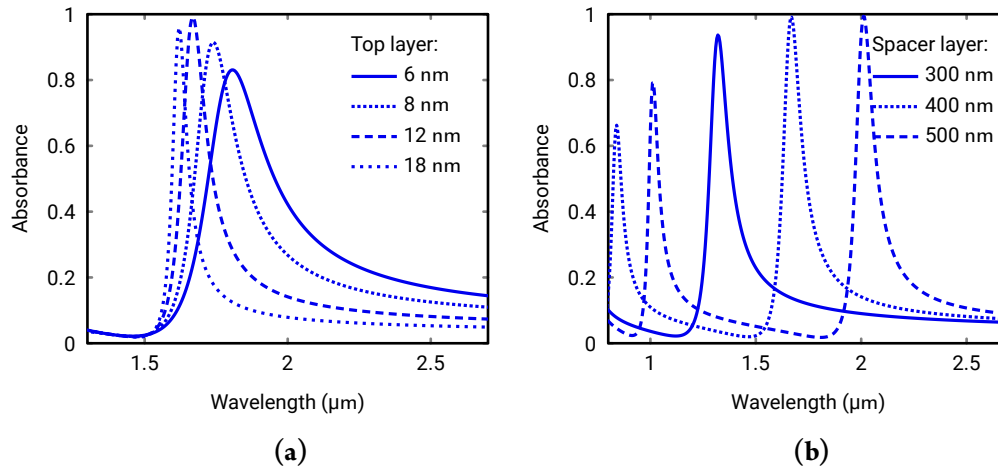


Figure 4.4: (a) Influence of variation of continuous-layer Fabry-Pérot resonator (cl-FPR) top layer thickness on the absorption at room temperature, calculated by the transfer-matrix method (TMM) method. The simulated structure consists of a substrate of a bottom layer of 80 nm gold, a dielectric layer of 400 nm thickness, and a metallic top layer thickness as indicated. The optical properties of gold are taken from [61]. (b) Influence of variation of the dielectric spacer layer on the absorbance of the cl-FPR. The simulated geometry is a gold top and bottom layer of 12 nm and 80 nm, respectively. The dielectric spacer thickness is as indicated.

where n_D and t_D are the refractive indices and the thickness of the dielectric, respectively, and m is the order of the resonance. A more general and rigorous treatment of the structure can be obtained by the impedance transformation method [57], or by the exact TMM method presented in chapter 2. The TMM is used to calculate the influence of varying the layer thicknesses of the dielectric /top metal on the absorption of an Au-SiO₂-Au cl-FPR fig. 4.4. It is clear that the resonator exhibits a distinct absorption peak in the vicinity of 1.7 μm, the height and Q-factor of which are influenced by the thickness of the top metal layer (see fig. 4.4a). Since full absorption only occurs when the optical mode couples with equal strength to radiative modes and intrinsic dissipative loss mechanisms [60], complete absorption requires the fine tuning of the thin top layer to within a single nanometre or so. Maximum absorption occurs around a thickness of 12 nm, with the maximum absorption decreasing for both thicker and thinner films. As one would expect, the Q-factor of the resonator increases with increasing top layer thickness as the metallic film becomes an increasingly ideal mirror. Conversely, thinner films have significantly wider resonances. For the variation of the dielectric thickness, the resonance shifts linearly to longer wavelengths with increasing thickness (see fig. 4.4b). Additionally, a minor change in the maximum absorption is observable, which can be explained by the dispersion of gold leading to slightly modified ideal top layer thickness. Overall, eq. (4.1) captures the essential physics of the resonator rather well.

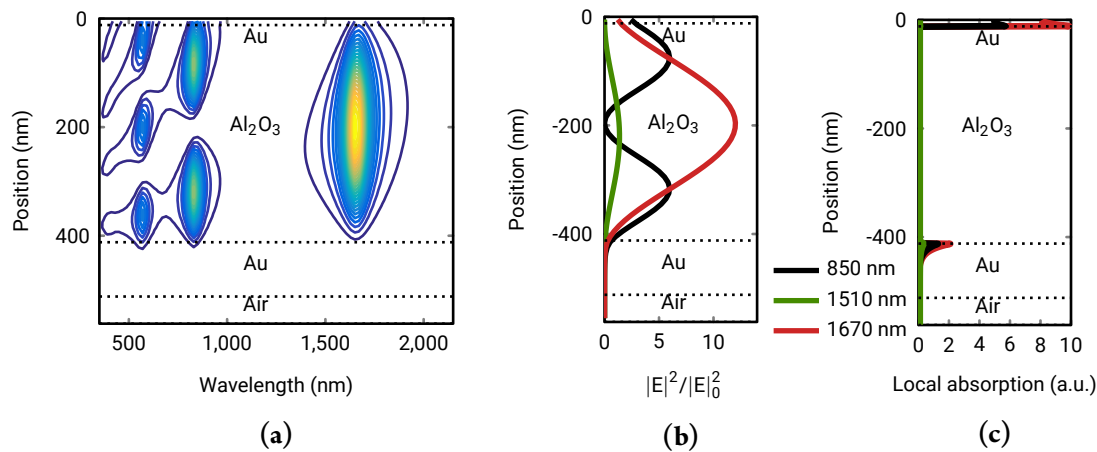


Figure 4.5: Results obtained by the transfer matrix method for a continuous-layer Fabry-Pérot resonator (cl-FPR) consisting of 12 nm Au on 400 nm Al₂O₃ on 100 nm Au at normal incidence. (a) The electric field intensity within the multilayer structure at the fundamental mode (1670 nm, red), slightly detuned from the fundamental mode (1510 nm, green) and at the second harmonic (850 nm, black). (b) The electric field intensity distribution as a function of wavelength. (c) Local absorption.

The TMM is used to calculate the spectral field distribution for the cl-FPR consisting of 12 nm Au / 400 nm Al₂O₃ / 100 nm Au to evaluate the spectral field distribution (see fig. 4.5a). It emerges that the modes at 1.7 μm and 0.8 μm correspond to fundamental and first harmonic mode of the cl-FPR. From the graph, another interesting feature emerges: the mode resides in a slightly asymmetric manner in the resonator, reflecting the geometric asymmetry of the mirrors. Whereas at the bottom of the dielectric layer the mode only penetrates to a small extent into the thick gold film, the top layer is, as indeed intended, not sufficiently thick to guarantee confinement to the cavity, thus allowing for the desired coupling to plane waves outside of the cl-FPR. This means that a relatively strong field resides within the top layer of the structure. It is worth briefly looking at the field intensity enhancement of the cl-FPR (fig. 4.5b), defined as the local intensity $|E|^2$ normalised to the incoming intensity $|E_0|^2$. At the resonance (1670 nm) the intensity enhancement of the resonator reaches a value of 12, corresponding to a field enhancement of 3.5. At a slightly detuned wavelength (1510 nm) the intensity enhancement does not exceed 3, corresponding to only very weak field enhancement. The strong field in the top layer leads to a local absorption profile which is strongly dominated by the top layer of the resonator at resonance (see fig. 4.5a). The locally absorbed power density in the thin top gold layer is larger than the local absorption in the substrate film by a factor of five. This is not a major issue for applications such as solar thermal or TPV, for the generation of hot electrons, it might be preferential to have absorption taking place in the bottom layer. The use of gold limits the wavelength range to wavelength clear of interband transitions, i.e. to wavelengths larger than 500 nm, covering the requirements of most likely TPV scenarios. The optical response is calculated with an air layer beneath the bottom gold layer to ensure that the transmission through the sample is negligible, which is the case at all wavelengths over 450 nm.

Thermal stability

Nanostructured surfaces are prone to enhanced degradation mechanisms, based mainly on two phenomena inherent to the surface of any material. Firstly, the fact that the surface atoms of a solid see an entirely different lattice energy. Hence, the energy of an occupied lattice site near the surface differs significantly from a lattice site in the bulk structure, affecting all material properties which are dependent on the lattice energy, such as the melting point, the evaporation of atoms/molecules from the surfaces and diffusion, to name a few. Since the lattice energy is less for atoms in close vicinity to the surface, these will melt at a lower temperature than atoms in the bulk [62–64]. In addition to the distance to the closest surface, the number of dimensions in which the material is confined strongly affect the magnitude of the melting point depression. Films, wires and particles experience different melting point depression by a ratio of 1 : 2 : 3 [65, 66]. Therefore, films experience the lowest amount of melting point depression for any given temperature and feature size, when compared to wire or particle based selective emitters, a fact that becomes increasingly important for few-nm ultra-films. Secondly, since the surface is the boundary to the surrounding media, chemical reactions are to a large extent confined to the surface. In an ambient atmosphere, the principal mechanism of degradation is often oxidation, especially at elevated temperatures. It is worth noting that other degrading effects are also occurring at the surface, such as e.g. oxidation or the evaporation of molecules.

Optimisation potential of multi-layer structures

One advantage of the cl-FPR is that it generalises to a multilayer stack in a straightforward fashion both in terms of the fabrication and the theoretic treatment. Multilayer stacks allow for powerful optimisation techniques, based on the needle optimisation techniques. While multilayer stacks of made out of dielectrics can approach any desired spectral reflectance within a given bandwidth, the inclusion of metallic nanometre scale layers yields a powerful tool to tailor the absorption or thermal emission. The feasibility of such emitters is, however, limited by the thermal stability of the metallic thin-film.

4.4 Gold-based cl-FPRs

Due to the advantages outlined in the preceding section, and the mentioned difficulties in the fabrication of plasmonic resonators of the tGSPR type, a decision was made to investigate a the cl-FPR structure which exhibits most of the advantages of the tGSPR, besides those being derived from consisting of a monomaterial. Despite gold not being considered suitable for high-temperature application due to its low melting point, it can sustain sufficiently high temperatures for a proof-of-concept investigation.

To investigate the thermal emission from selective emitters, a measurement setup based on a heated microscope stage (Linkam, TS-1000), with a temperature range of 25 °C to 1050 °C, a mi-

croscope equipped with long working-distance objectives, and a fibre-coupled visible and near-infrared CCD-spectrometers. Additionally, a blackbody reference is capable of providing a reference spectrum for the calculations of emissivity. Gold cl-FPRs are investigated at wavelengths near the GaSb band gap ($1.7\ \mu\text{m}$) spectral selectivity in accordance with Kirchhoff's law is shown. A detailed description of the obtained results and the setup can be found in appendix B.

The results obtained for gold cl-FPRs, were especially encouraging, as such thin-film structures provide a flexible platform for high-temperature spectrally selective surfaces, with a large degree of flexibility in the choice of materials, straightforward large-area fabrication and the potential to optimise emitter and absorber FOMs by the inclusion of additional layers application of numerical optimisation tools. The positive results thus encouraged the search for metallic films which could satisfy the needs of SEs and SSAs, i.e. excellent thermal stability and yielding a comparatively high-Q resonance for a narrow emission spectrum, in the case of SEs. Conversely, for SSAs, a broad resonance is needed, ideally one covering the entire solar spectrum. The former requirement translates to the necessity of a low-loss metal while the latter requirement necessitates the use of heavily lossy metals.

4.5 Titanium nitride-based cl-FPRs

In the search for high-temperature alternatives to gold, one material has recently garnered attention; Titanium Nitride (TiN). Titanium nitride is a ceramic with metallic optical properties and exceptional thermal and chemical stability. A bulk melting point exceeding $2900\ ^\circ\text{C}$ promises a comparatively high melting point even for nanostructures subjected to melting point depression. Moreover, since the optical properties of high-quality Titanium Nitride closely resemble those of gold, it can be used as a replacement for gold, where the thermal stability of gold is insufficient, or where gold is otherwise unsuited, such as e.g. for complementary metal-oxide-semiconductor (CMOS) compatible applications and the fabrication in CMOS compatible facilities.

However, despite its chemical inertness, Titanium nitride (TiN) is prone to oxidise at temperatures above $800\ ^\circ\text{C}$, which prompts the use of a dielectric protection layer. A further potential advantage of a protection layer is that the convective cooling of the SE takes place at the upper interface of the protection layer, as opposed to at the ultra-thin metallic layer, consisting of TiN in this case.

Figure 4.6a shows a schematic of a TiN- Al_2O_3 -TiN-MgO structure optimised for maximum emission at the GaSb bandgap wavelength of $1.7\ \mu\text{m}$. The bottom TiN layer is $80\ \text{nm}$ which is sufficient to guarantee negligible transmission through the emitter. A dielectric spacer thickness of approximately $400\ \text{nm}$ yields analytically fitting spectra. A top TiN thickness of $12\ \text{nm}$ yields a maximum absorption of over $80\ \%$ (see fig. 4.6b). The TiN films are obtained through reactive radio-frequency (RF)-sputtering, the Al_2O_3 film through conventional (non-reactive) sputtering while the protection layer is obtained by chemical vapour deposition (CVD) which provides a higher

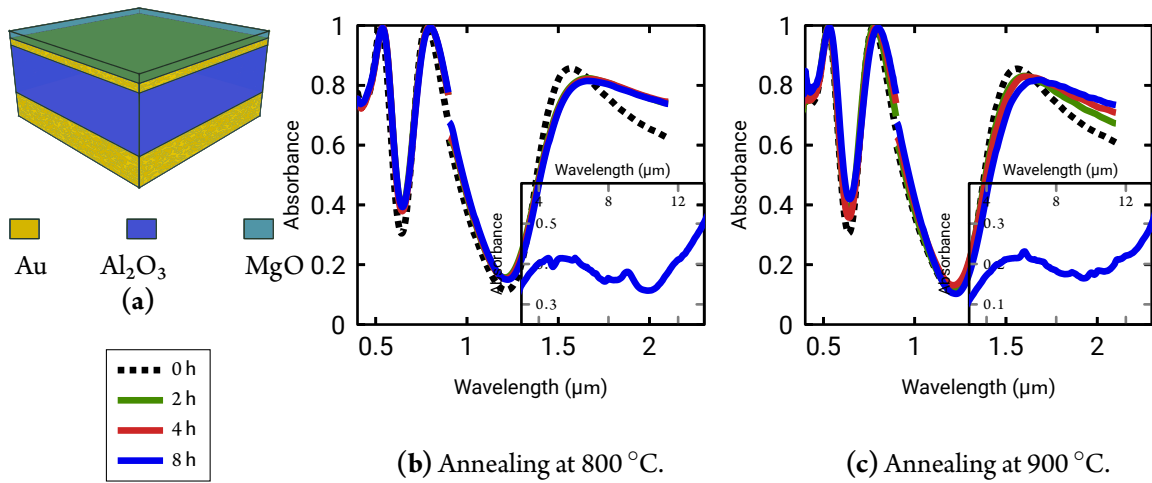


Figure 4.6: (a) Schematic representation of the continuous-layer Fabry-Pérot resonator based on Titanium Nitride. Comparison of absorbance spectra from non-annealed (dotted) MDMD selective emitters and identical emitters annealed in nitrogen under atmospheric pressure at temperatures of 800 °C (b) and 900 °C (c) for a total duration of 2, 4 and 8 hours, respectively (solid lines). All anneals lead to a significant initial change occurring at a time scale of minutes. Subsequent annealing reveals the excellent optical stability of the emitter under extended operation at temperatures up to 800 °C. At 900 °C an initial spectral change comparable to (c), but with a slow but continuous degradation of the optical properties. A mid-infrared absorption of 20 % is observed for all annealed samples, with the notable exception of (c) which exhibits a roughly 40 % absorbance. Insets: FTIR absorption spectra of the annealed samples after 8 hours. (Note different y-axes of insets in ((b) and (c).)

degree of conformal surface coverage, which is important for the use as a diffusion barrier against traces of oxygen, amongst others.

The thermal emitters are subjected to annealing cycles of increasing length to gain insight into the resistance towards repeated thermal cycling. A sequence of 1, 1, 2 and 4 hours is used, which allows for investigation of the structures after 1, 2, 4 and 8 hours. The increase in annealing duration enables the judging of the long-term behaviour of the TiN SE. It emerges from annealing at 800 °C that the emitter has excellent thermal stability, experiencing an only minor drop in the maximum absorption of a few percent, accompanied by a broadening of the resonance. No changes are observed when comparing the absorption after two hours with the absorption after 8 hours, which indicates that after an initial change during the first anneal, the selective emitter has stabilised into a stable configuration. Annealing results at 900 °C show an initially similar behaviour: In fact, the initial change observed is smaller than for 800 °C, most likely due to better fabrication quality or better purity of the TiN surface (see fig. 4.6b). However, at 900 °C, the emitter does not stabilise, and a minor change continues to occur, albeit at a relatively slow rate. The continued degradation of the SE indicated that the maximum operating temperature for the emitter exceeds 800 °C and lies somewhere in the range of 800 °C to 900 °C for the examined configuration in nitrogen. This

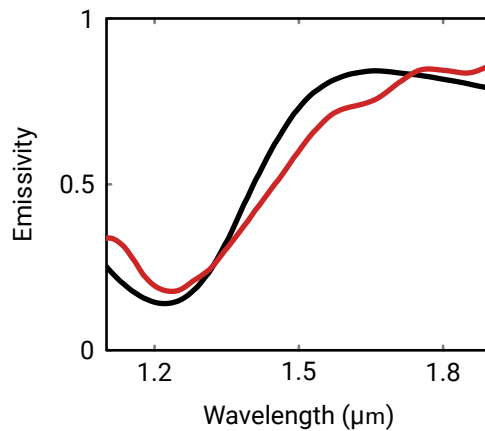


Figure 4.7: TiN cl-FPR reflectivity at room temperature (black) and emissivity measured at 700 °C (red) showing reasonable correspondence.

corresponds to the high end of reported oxidation mechanisms for TiN [67, 68], which is a likely explanation since the nitrogen atmosphere used has not been purified, and the partial oxygen pressure might, therefore, not be negligible.

The thermal emission of the SE is compared to its reflectance at room temperature in fig. 4.7, in order to actually confirm the spectral selectivity in emission. As can be seen, there is correspondence between the two curves, in most of the spectrum.

The above results provide confirmation that the excellent refractory properties of TiN enables cl-FPR-type SEs with optical properties similar to gold while exhibiting drastically improved thermal resistance exceeding in excess of 800 °C. Aforementioned advantages in the potential for geometric scaling, optimisation and ease of fabrication of thin-film structures apply equally to the TiN cl-FPRs and are, additionally, accompanied by the considerably more economical choice of materials and high-temperature applicability. Most notably, the quality of the spectral selectivity is, to a large extent, preserved. Thus, it was conclusively shown that the cl-FPR structure based on TiN, Al₂O₃ and MgO is a highly flexible, scalable, economical selective emitter with at temperature of over 800 °C or 1073 K. (Manuscript is currently under preparation, cf. list of publication for the intended title.)

4.6 Multilayer tungsten solar absorbers

The design of a selective solar absorber based on a resonant thin-film structure is greatly facilitated by the use of metals with high losses in the near-infrared, which broaden the resonances of the resonator, leading to absorption over an enhanced wavelength range. Matching the solar spectrum with a cl-FPR made of low-loss materials, such as gold or TiN yield resonators with too narrow resonances to cover the entire solar spectrum (cf. sections 4.4 and 4.5). Regarding the thermal

stability, the requirements to a solar absorber for TPV are similar to those of an emitter, as these are in thermal contact with an (ideally) small thermal gradient. As such, refractory materials with good chemical stability are of crucial importance. One material simultaneously satisfying the requirements to the optical properties and the thermal stability is Tungsten. It has a bulk melting point of over 3400 °C and high absorption losses at optical and near-infrared wavelengths which decrease drastically between 2 μm to 2.5 μm . Therefore, an investigation into a cl-FPR with a related geometry to previously outlined publication, however with Tungsten as the metal, is carried out. The resulting publication (enclosed in appendix D), resulted in highly efficient absorbers with a near-unity absorption band which is tunable throughout the entire solar spectrum. By appropriate design, wideband absorbance better than 95 % at wavelength from 650 nm to 1750 nm was achieved. Low re-emission of absorbed heat and thus high thermal efficiency of the absorber is guaranteed through a low absorption beyond 3 μm . From 3 μm to 7 μm absorbances could be minimised to under 5 % in the entire wavelength range; with no absorber exhibiting above 25 % average absorption in the range and typical values of roughly 10 % (average).

The thermal range of application is examined both vacuum and air, and good stability is found in vacuum at up to 800 °C and in ambient air at up to 600 °C. Higher temperatures in air are shown to oxidise the tungsten film in the absorber by use of secondary-ion mass spectroscopy (SIMS), while higher temperatures in vacuum lead to diffusion into the adjacent dielectric layers, facilitated by the cracking of the dielectric layers. As such, the thermal stability in vacuum was found to mainly attributable to the quality of dielectrics, which were obtained by e-beam deposition. As such the use of atomic layer deposition (ALD) could help improve the thermal stability, or CVD, as could the choice of other dielectric materials, less prone to percolation by cracking.

Chapter 5

Prototype evaluation of selective emitters

With the aim of demonstrating the potential for efficient TPV operation using cl-FPR-type selective emitters, an accessible, hands-on prototype TPV system was constructed, based on a GaSb PVC in a coplanar arrangement with an electrical heater. The all-electrical setup allows for both input and generated output power to be measured with relative ease and without any ambiguity. Moreover, since the geometry is well-defined and straightforward, view-factors can be evaluated accurately. This allows for geometric scaling potential to be judged. The prototype uses a cm-scale emitter area which is detrimental to the efficiency, but was a necessary design choice based on available PVCs. Selective emitters are compared to the greybody of the rough emitter surface composed of a rough high-pressure silicon nitride. The cell is furthermore evaluated for its potential for increased efficiency due to geometric scaling to assess the power outputs one could expect from a realistically sized application.

5.1 Prototype description

The TPV prototype consists conceptually of three distinct parts that can be operated separately and produce separate readouts needed for the calculation of the efficiency (see fig. 5.1). The first part is responsible for controlling the heater temperature, a second part for cooling the PVC and the third part measures the electrical power generated by the prototype under different load conditions (current-voltage (IV)-characterisation). Each part is fitted with probes allowing for calculation of the consumed powers for heating the emitter / and cooling the PVC and the power output generated.

Central design choice in the design of TPV prototype is the choice of PVC, more specifically the band gap of the semiconductor material used. Since the efficient operation of a PVCs depends on the matching of the maximum of the BB radiation to the band gap, lower band gap PVCs facilitate the design of TPV systems, since a lower band gap relaxes requirements on the emitter temperature. The lowest band gap PVCs which were commercially available at the time of sourcing (in lab-scale quantities and sizes), were GaSb cells with a band gap of 0.72 eV. The prototype is therefore for practical reasons based on GaSb, despite the existence of lower band gap materials which

promise higher efficiencies at comparable temperatures [69–71]. The heater is a commercial resistive glow igniter (*Bach Resistor Ceramics GmbH*), which consists of hot-pressed silicon nitride with an embedded tungsten heating element. Silicon nitride fabricated under high pressure is chemically highly inert and resistant to thermal shocks and thermal cycling at temperatures of over 1000 °C. It has a 12-by-15 mm rectangular hot area, enabling the fabrication of precisely fitting samples. The heater can be seen under operation in fig. 5.2a.

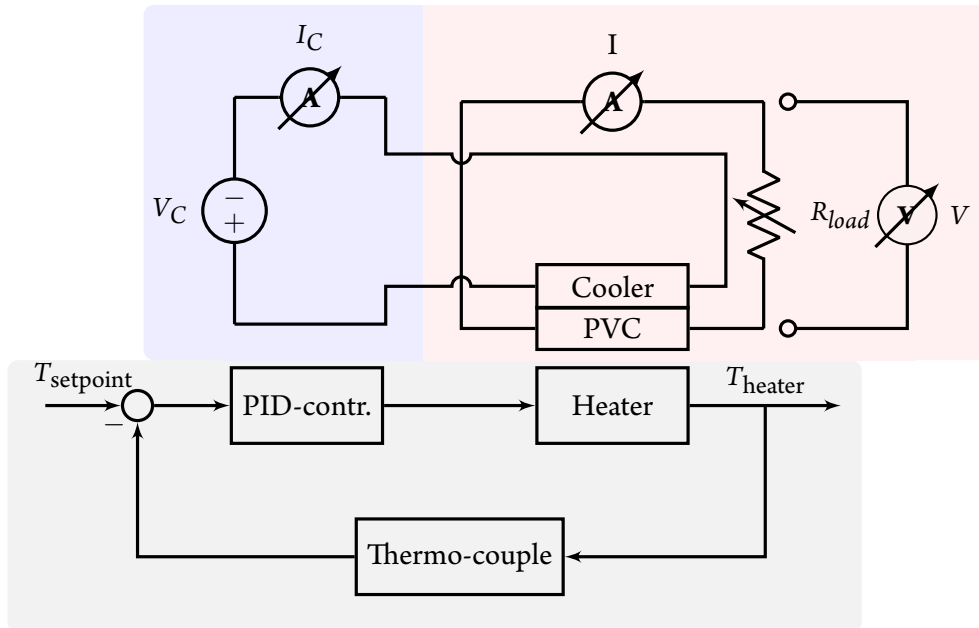


Figure 5.1: A simplified schematic of control and acquisition in the TPV prototype. A cooling circuit (blue) supplies and monitors the current I_C and voltage V_C provided to an active cooler. The temperature control circuit (grey) consists of a PID controller that switches a solid-state relay. The SSR switches on and off the variable AC voltage to the heater. PID duty cycle, heater voltage and heater current are monitored separately (not shown) to determine the power supplied to the heater. An IV characteristic is obtained by an impedance spectrometer, here (somewhat inaccurately) indicated by a variable load resistor, as well as current and voltage probes (red).

The temperature of the heater onto which the emitter is placed, is controlled by an on-off PID feedback (fig. 5.1). It reads out the signal from a K-type thermocouple which is inserted into a hole drilled into the heater and controls as solid-state relay (SSR) that switches the voltage supplied to the heater. The feedback electronics are based on a commercial tool (ELK 38 tempatron), which regulates the temperature to a given set-point with an accuracy better than 0.5 °C, based on a PID on-off algorithm. The heater input voltage is monitored along with the logic state of the SSR and the current running through the heater. Figure 5.3a shows an example of the logic state of the SSR overlaid with the voltage at the heater under operation. Furthermore, the heater power is supplied from a *Brüel & Kjaer* amplifier which is substantially less prone to distortion during switching than a

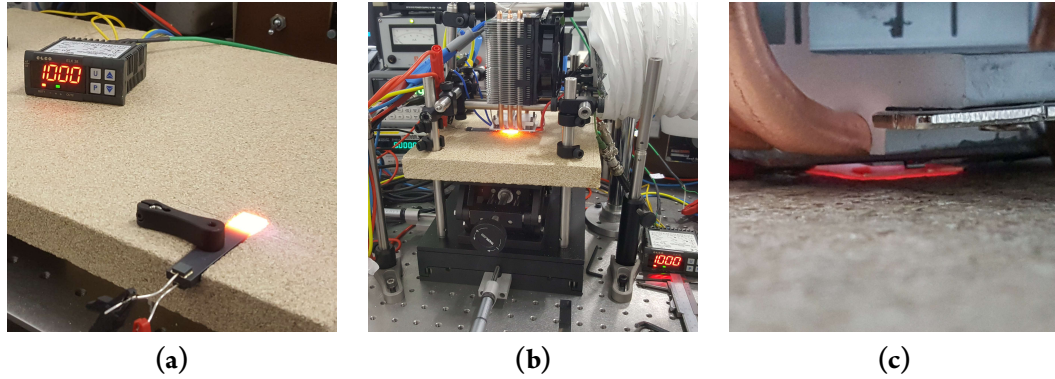


Figure 5.2: (a) Silicon nitride heater at 1000 °C mounted independently. The heater is recessed into a thermal isolator. A thermocouple is inserted from the bottom into the center of the hot area for temperature feedback (not shown). (b) TPV cell prototype under operation at 1000 °C at increased emitter-PVC distance. Copper heat conductors, cooling fins and fan can be seen above the emitter. (c) Close-up of the emitter and cooling assembly at distance used under operation. The edge of the PVC can be seen directly above the selective emitter.

regular variable alternating current (AC) power supply, thus preserving the sinusoidal shape of the AC voltage, which is assumed in further calculations. The power supplied to the heater can straightforwardly be retrieved from the duty cycle of the PID controller and the root mean square (RMS) voltage and RMS current provided to the heater when the SSR is in the on-state. Care is taken to ensure that switching times significantly exceed the integration times of all electrical measurements. The cooling electronics are simple, consisting only of a variable direct current (DC)-power supply and measurements probes for current and voltage supplied to commercial cpu cooler. Significant cooling is achievable with a few hundreds of milliwatts, which is utterly insignificant relative to the heater power and therefore not a critical input parameter. The cooling power is obtained directly by the DC current I_C and voltage V_C , respectively and included in all input powers.

The IV characteristics of the TPVC under operation are obtained via a commercial impedance spectrometer (*Zahner Zennium*), which can be operated in DC scanning potentiostat. The output power is determined after an initial settling time of five minutes, by an IV characterisation of the PVC under operation and determination of the point of maximum useful power output, P_{MP} , while the cooling and heating powers, P_C and P_H , are determined simultaneously. An example of an obtained IV curve from the prototype is seen in fig. 5.3b, together with the resulting power curve, obtained from the product of I and V . The output power is defined as the maximum power, P_{MP} . From these three powers, cooling power P_C , heating power P_H and maximum output power P_{MP} , the efficiency η_{TPV} is calculated as the ratio between the total input power and useful output power:

$$\eta_{TPV} = \frac{P_{out,useful}}{P_{in,total}} = \frac{P_{MP}}{P_H + P_C}. \quad (5.1)$$

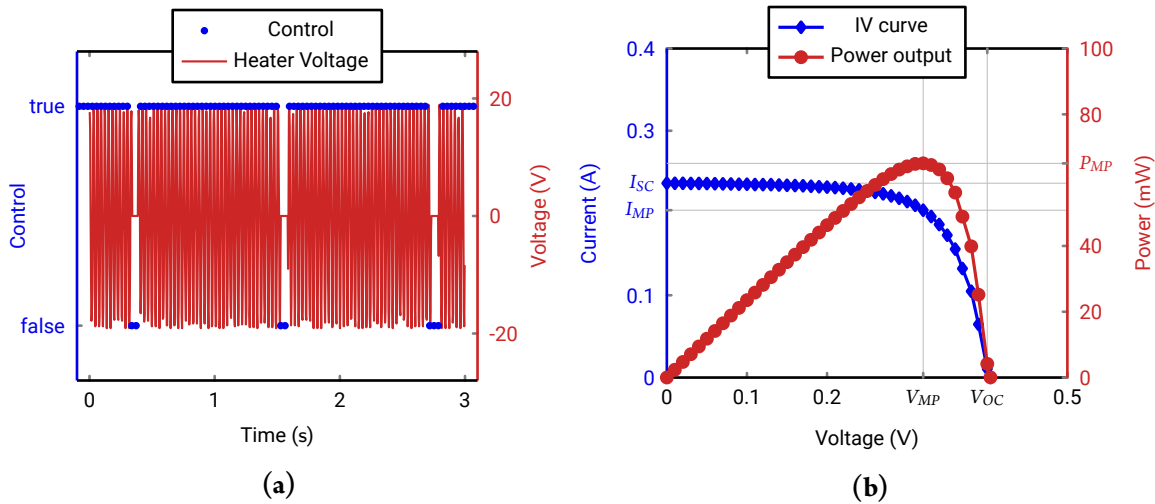


Figure 5.3: (a) Logic signal (blue) of the PID controller and resulting voltage on the heater (red) during operation of the prototype at 650 °C. The current supplied to the heater is measured separately and combined with the above-shown measurement to calculate the power consumptions. (Apparent fluctuations in the voltage are due to down-sampling of the data set for plotting.) (b) The current-voltage (IV) characteristic (blue) and power output (red) measured from a 0.72 eV GaSb PV-cell under halogen illumination. Included are indications of the short-circuit current (I_{SC}), the open-circuit voltage (V_{OC}) and the maximum power (P_{MP}), as well as the voltage at maximum power (V_{MP}) and the current at maximum power (I_{MP}).

Evaluation of photovoltaic cell configurations

Two distinct configurations of PVC assemblies are investigated, incorporating one and two photovoltaic cells, respectively, to determine the degree, if any, to which the increase in view-factor can increase the output power and efficiency of the prototype. The two configurations can be seen in side-by-side fig. 5.4. The single-cell configuration consists of a cell mechanically mounted and spot-welded to a solid copper by clamps and is a commercial testing assembly supplied by the manufacturer of the cells *JX Crystals*. The two-cell versions of the cell mounts are manufactured in-house, each of which offers an increased view factor at the cost of increasing complexity.

Figure 5.5a shows the comparison between the single cell and the dual cell configurations. For the dual-cell, the cells are mounted in series. Comparing the input power, it emerges that the single-cell configuration requires an almost identical power input to hold a given temperature, increasing from roughly 30 W to 60 W in the temperature interval from 500 °C to 800 °C, while the output power is approximately double that of the two-cell configuration, despite subtending a significantly smaller area. The reason is most likely found in the mounting process, specifically the soldering of connecting electrodes to the cell and board. Clearly, this results in lower efficiency by approximately 50 % (fig. 5.5b). Since, for cooling purposes, the board is made of solid aluminium, it conducts heat so efficiently that a high-power soldering (300 W) is needed complete the soldering process with good electrical connections. Thus one runs the risk of overheating the PVCs, particularly in

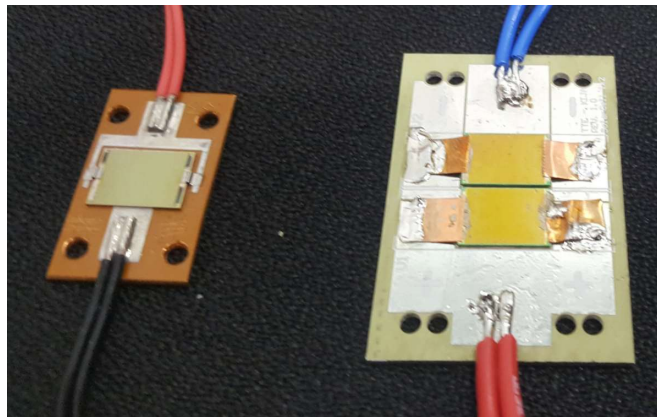


Figure 5.4: Configuration of photovoltaic cell mounts. (left) mechanically clamped and spot-welded to a solid copper board, (right) PVCs soldered to an aluminium board. The soldering process leads to visibly discolouration in the PVCs which subsequently exhibit a reduced power output.

areas near to the cell bus to which the connecting electrodes are attached. Overheating of the PVC leads to irreversible changes in the cell, which, apart from decreasing the efficiency also alter the impedance matching conditions of the cells. Since two serially (or parallel) connected cells are only automatically impedance matched if they are identical in their characteristics, any differences can potentially lead to drastic changes in output power. All further operation of the TPV prototype is carried out using the single-cell configuration.

5.2 TPV efficiency with a bi-layer Tungsten-dielectric emitter

A good choice of emitter used for the prototype TPV is heavily dependent on the specific TPV system. The TPVC presented here has a low level of radiation shielding and operated at normal pressure, the former leading to relatively large losses caused by both (useful) thermal radiation not hitting the PVC and the latter to convection and conduction losses. Therefore, a highly selective emitter is not desirable since spectral selectivity comes at the cost of power throughput, as outlined in chapter 3. Since the useful radiation from the emitter competes with the losses, it becomes increasingly important to maximise the radiated energy above the bandgap with increasing losses. For this reason, a bi-layer structure consisting of 200 nm Tungsten with an anti-reflective (and protective) layer of 145 nm MgO (estimated, under determination) is optimised for high near infrared (NIR) absorption. As noted in section 4.6, Tungsten has the desirable property of being a lossy metal in the visible and NIR while exhibiting increasingly good metallic (ϵ negative and real) behaviour at longer wavelengths, suppressing thermal re-emission.

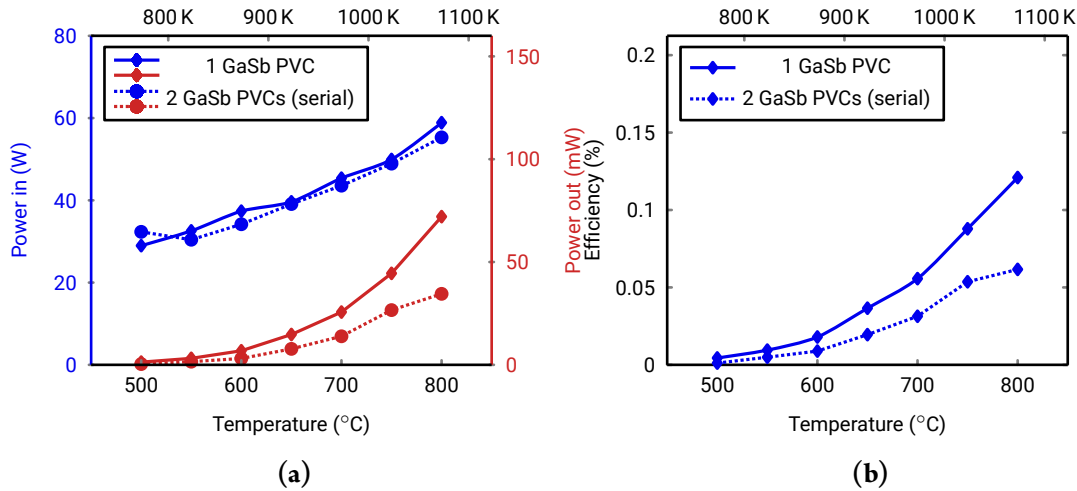


Figure 5.5: (a) Power consumption (blue) and power generated (red) by the TPV prototype under operated with a highly rough silicon nitride surface as the emitter. Single and double PV-cell configurations are investigated (solid and dotted lines, respectively). The single cell configuration is superior in terms of generated output while requiring only insignificantly more power under operation. (b) Total TPV prototype efficiency resulting from data in (a). The power used for active cooling (700 mW) is included in the efficiency. Despite having a larger view factor, the 2-cell configuration does not convert more energy than the single cell.

Emitter stability

An initial idea of the range of acceptable thermal stability is obtained by annealing the emitters in the TPV setup. This is necessary to ensure that the samples is stable during measurement and to determine the temperature range of use for efficiency measurements. Figure 5.6 shows spectra reflectance and bright-field microscopy images of Tungsten bi-layer emitters before and after annealing at 500 °C, 600 °C and 700 °C in the TPV prototype. From a comparison of the spectra before and after the annealing process, it emerges that all emitters undergo a significant change, after which the emitters still have virtually identical spectra, despite the relatively large difference in annealing temperature. Optical bright-field microscopy images show that the ten minute anneal at 500 °C and 600 °C does not degrade the emitter by an optically appreciable amount (figs. 5.6b to 5.6d). Annealing at 700 °C reveals the onset of degradation that is strongly dependant on the spatial position of the emitter (fig. 5.6e). Since the majority of the sample area is not affected, which could explain the absence of noticeable differences between the spectra of emitters annealed at 600 °C and 700 °C.

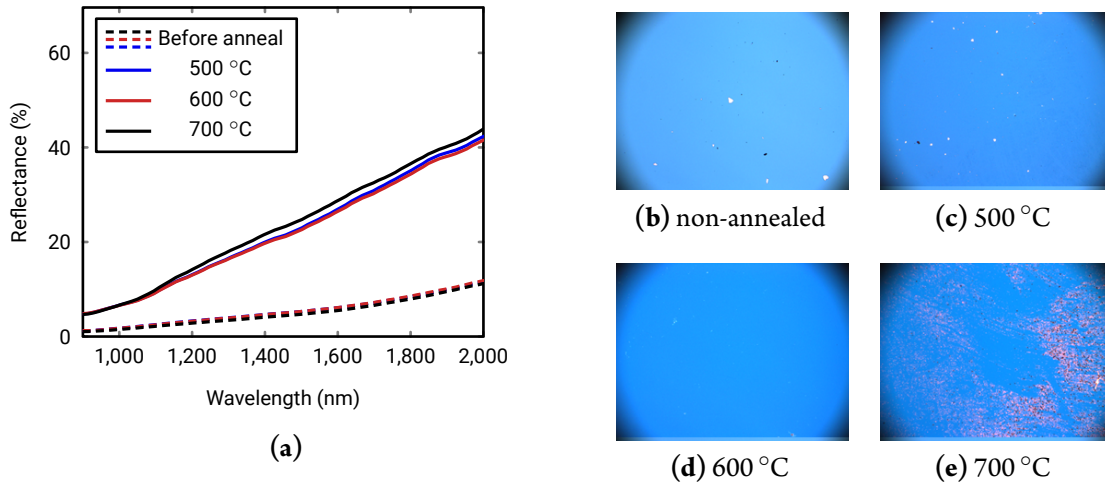


Figure 5.6: (a) Reflectance spectra from Tungsten bilayer samples before and after annealing in an ambient atmosphere for 10 min at 500 °C, 600 °C and 700 °C. (b)–(e) Bright-field reflectance microscopy images of the bilayer selective emitter surface before (b) and after annealing at 500 °C, 600 °C and 700 °C; (c), (d) and (e), respectively.

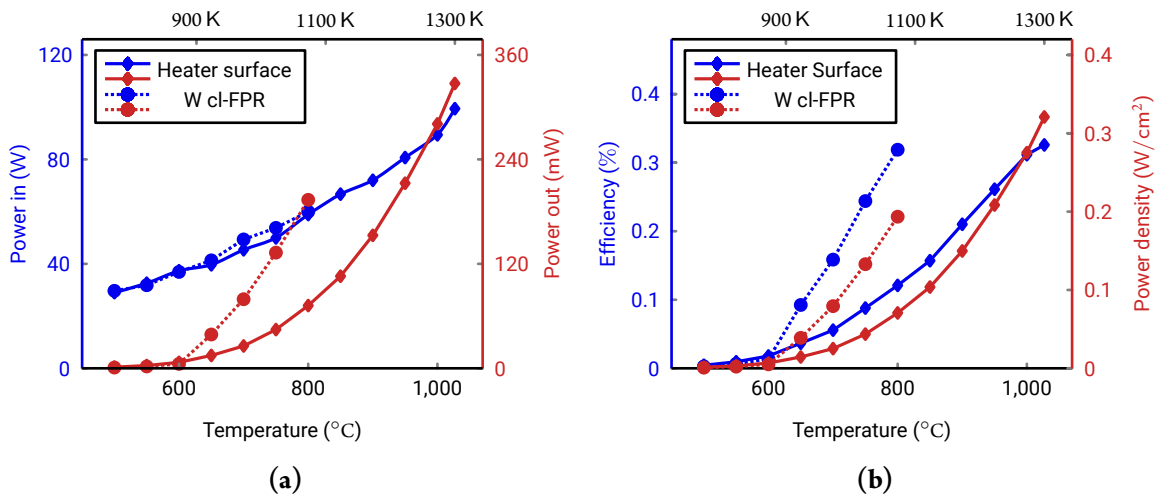


Figure 5.7: (a) Power consumption (blue) and useful power output (red) by the TPV prototype, under operation with a tungsten continuous-layer Fabry-Pérot resonator (cl-FPR) emitter (dotted), compared to the plane silicon nitride surface of the heater (solid). While consumption and output are comparable at temperatures up to 600 °C, the tungsten cl-FPR exhibits a significant increase in power output above 600 °C, approaching threefold relative power output at 800 °C. (b) Efficiencies (blue), calculated from the data in (a) taking into account active cooling power, and converted power density (red). A clear efficiency advantage for the W cl-FPR emerges from 650 °C which increases with temperature. A maximum efficiency of 0.32 % is observed at 800 °C for the W cl-FPR while similar efficiency (0.33 %) is observed for the heater nitride surface at 1027 °C, the maximum investigated temperature.

TPV efficiency Tungsten bi-layer emitter

For the testing of the efficiency attainable with the TPV prototype and the Tungsten bi-layer emitter presented above, the emitter annealed at 500 °C is mounted into the setup and efficiencies are obtained by the procedure outlined in section 5.1. The results regarding in- and output power, efficiency and power density are presented in fig. 5.7. It emerges clearly (fig. 5.7a) that the emitter increases the input power by a few percent, which is likely due to the increased area of the emitter which can be expected to increase all heat loss mechanisms (radiative, conductive & convective). Nonetheless, the behaviour of the input power need to sustain a given temperature are very similar up to 800 °C. At 800 °C only a subset of the emitters are stable, which possibly points to either differences in the samples, or differences in the thermal contact with the heater.

In contrast, the output is drastically increased: over the entire temperature range supported by the emitter, 500 °C to 800 °C, the output power is roughly threefold increased. The efficiency reaches a maximum value of 0.32 % at 800 °C, corresponding to a power density of roughly 0.2 W/cm² fig. 5.7b. To investigate at which temperature an equivalent efficiency occurs for the greybody surface, the efficiency measurement presented in fig. 5.5a is extended to the maximum temperature that can be held by the prototype: 1027 °C or 1300 K. It is seen that the input power continues to rise in a close-to-linear fashion. Similarly, the output power rises exponentially, approaching 360 mW at 1027 °C. At this temperature, the efficiency reaches 0.33 % at a power density of over 0.3 W/cm². This is a sufficiently high power density to obtain useful power output from practically sized TPVCs. A wood fired heating furnace, or a gas-fired water boiler could very realistically have hundreds to thousands of cm² of TPV-active surface. Based on the assumption of a TPVC with above power densities, an output power of 20 W per 10-by-10cm² can be extracted, *without* taking into account the increase that would result from the geometric scaling alone. Staying briefly with the thought experiment, this power could conceivably be used to construct a self-powered wood furnace with built-in thermostat/timer/remote control, a fire alarm, power outlets or other useful functionalities, especially in regions where no grid-based power is available.

While these are not high efficiencies in their own right, these are nonetheless highly promising results, which becomes clear when considering a CHP application, as above. Furthermore, since the scaling does not affect the distance between the PVC and the emitter, the view-factor for a scaled geometry increases. VF calculations are carried out based on the scaling of emitter and/or heater to a 10-by-10 cm² area and for the geometry as is (fig. 5.7). From fig. 5.7b, it is seen that at a emitter-PVC separation of 4 mm, the view-factor of the prototype slightly exceeds 0.4. Note that zero separation the prototype geometry does not give a unity view factor since the emitter is slightly larger than the heater (see fig. 5.7a). However, decreasing the separation does have some potential for improved efficiency, which would, however, necessitate a redesign of the PVC mounting. More importantly, the simultaneous scaling of the emitter and PVC would result in more than a twofold increase in efficiency.

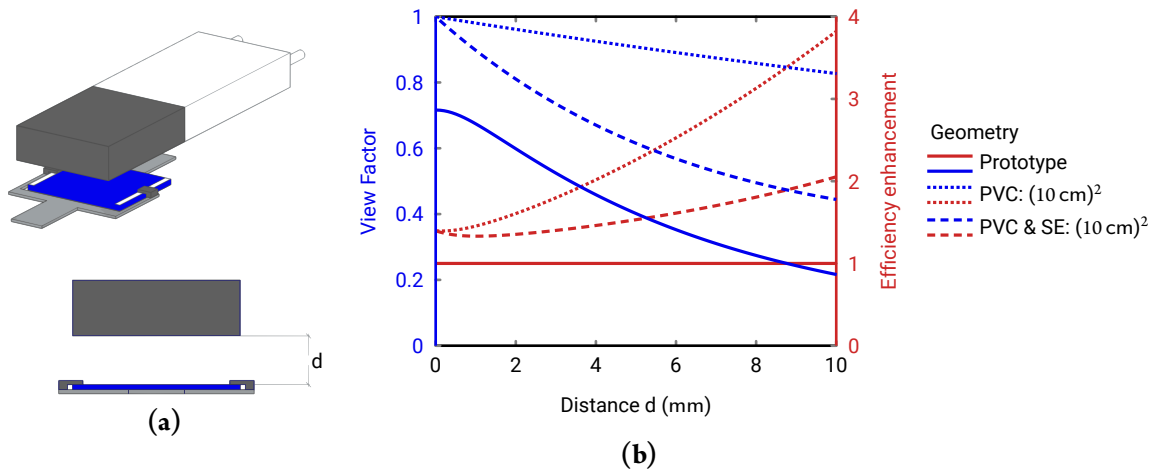


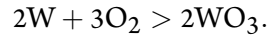
Figure 5.8: (a) Schematic of the prototype geometry and distance d between the heater (grey) and the photovoltaic cell (blue) used for view factor calculations, in isometric (top) and front view (bottom). (b) Prototype geometry (solid) and view factors after scaling the emitter area to $(10 \text{ cm})^2$ (dashed) and scaling both emitter and photovoltaic cell to $(10 \text{ cm})^2$ (dotted). The calculations are based on the exact method in [74] and coparallel rectangular geometry with dimensions and relative positions as measured.

It thus stands clear that a square TPVC with a side length of 10 cm yields a power output of over 40 W based solely on the efficiency enhancement from geometric scaling and the observed temperature stability at 800°C at an efficiency of 0.64 %. This is indeed very close to the criterion of Palfinger et al. for economic TPV operation. Several modifications conceivably have the ability to provide the relatively modest enhancements necessary for the 1 % limit to be breached; a radiation shield reflecting photons not emitted towards the emitter, a decrease of emitter-PVC distance, or slightly improved temperature resistance of the emitter, for example. Finally, roughly 20 % of the cell front face is covered in aluminium electrodes, which reflect the incoming radiation. This is not taken into account in the view-factor calculations (fig. 5.8b), but essentially acts to diminish the view-factor by a factor of 0.8, while electrodes can be made of DC-conductive, but optically transparent materials, such as conducting doped metals oxides [e.g. indium tin oxide (ITO)] [72], conducting polymers or two-dimensional (2d) materials [e.g. graphene or carbon nano-tubes (CNTs)] [73].

Increasing the cl-FPRs temperature range

Despite Tungsten being a refractory metal with a bulk melting point of $3422(15) \text{ K}$ [75], the temperatures that Tungsten can sustain in a given application, strongly depends on the surroundings in which it is heated. As previously discussed, melting point depression will lower the melting point near the surface of structures. However, in reactive surroundings the temperature limiting effect is often the chemical degradation that occurs due to oxidisation, with several possible resulting ox-

ides, depending on the temperature at which the process occurs. For temperatures up to 500 K, the oxide formed is purely WO_3 , with the rate of oxidisation increasing with temperature and with relative humidity [76]:



Other oxides such WO_2 , $\text{W}_{18}\text{O}_{49}$ (commonly called $\text{WO}_{2.72}$ in literature) and $\text{WO}_{2.9}$ do exist, but are occur mainly at higher temperatures and are created at lower rates than WO_3 .

For pure tungsten being oxidised at 600 K, a $\text{W}_{18}\text{O}_{49}$ scale is formed, which limits the oxidation rate providing natural protection from further oxidation. However, at 700 K and 800 K the film is reported to be prone to cracking leading again to enhanced oxidisation [77]. A protective layer of Tungsten oxide could explain why emitters that show first sign of oxidation at 700 °C can hold up to 800 °C. With increasing temperature, the gas pressure of tungsten trioxide increases, forming a gaseous phase at 1300 °C, suggesting that this is the upper limit to long-term use in any situation in which Tungsten surface does not essentially see zero O_2 -partial pressure. Since the rate of oxidisation is limited by the diffusion of oxygen to the surface (along with the volatility of WO_3 and the diffusion of W_3O_9) [78], the control of oxygen diffusion becomes a critical parameter in determining the feasibility of tungsten based emitters for oxygen atmospheres.

For Tungsten in a water saturated oxygen atmosphere, oxidisation occurs even at room temperature [79], however, no changes to the reflectivity are seen in the spectra despite storage in regular sample containers, without atmospheric control. Under the operation of the prototype, the air in contact with SE is heated significantly from room temperature before coming in contact with the SE. This help to reduce the relative humidity of the air which is in direct contact with the emitter.

Regardless of the exact mechanism behind the degradation of Tungsten in the W-SEs, Tungsten must be protected from oxidation by physically preventing oxygen molecules from directly contacting the metallic layers. Since this is true for both Tungsten and TIN, it is worth briefly commenting on recent progress within diffusion barriers and their application to high-T application. Recent developments in protective coatings for refractories have shown promising results in the protection of refractories and cermets, preventing the oxidation of Tungsten surfaces at temperatures of up to 1400 K [80, 81]. These protective layers, however, depend on the complex interdiffusion between silicide layers of molybdenum and tungsten and an aluminoborosilicate layer. Since the materials used for this oxidation barrier are fixed and, equally important, optically thick, the (optical) metallic surface properties of the refractory metal that make the cl-FPR possible in the first place are lost.

Another class of oxygen diffusion barriers have recently garnered attention, namely 2d materials, most prominently graphene. Graphene consists of a monolayer of sp^2 -bonded carbon atoms which have rather remarkable properties in various respects. It is known to be transparent, electrically and thermally conducting, and elastic amongst others, while providing an excellent barrier against diffusion of many kinds of gaseous atoms [82–84]. While graphene can be stable at temperatures comparable to bulk refractories – stability up to a minimum temperature of 2600 K were reported in [85] under ultra high vacuum (UHV) conditions – it is found that under atmospheric

conditions and when bound to a substrate multiple layers of graphene can provide effective oxidation protection at temperatures up to 750 °C [86]. This is not currently enough to cover the needs of high-temperature TPV, but further development of graphene-based barrier systems seem likely and for intermediate-temperature applications 750 °C can be an acceptable operating temperature. Certainly, it covers temperature requirements for many solar-thermal applications.

Any further research aiming at elevating of the temperature range of cl-FPR platform should therefore have the development of efficient diffusion barriers at its center.

Chapter 6

Outlook

The primary motivation behind this PhD study was the investigation of resonant surface structures for spectrally selective surfaces for thermophotovoltaic use with an emphasis on plasmonic resonant structures. Plasmonic resonators were demonstrated to be highly versatile in their use as spectrally selective surfaces, as is shown by subwavelength plasmonic colour printing and by the comprehensive theoretic treatment of (vertical) trench gap plasmon resonators, demonstrating that these can exhibit strongly enhanced cross sections for scattering, absorption and extinction. Continuous-layer Fabry-Pérot resonators are shown to exhibit most properties that make plasmonic resonators ideal selective emitters for thermophotovoltaics, while benefiting from additional advantages where ease of fabrication, potential for optimisation, cost and scalability are concerned. These resonators can indeed act as a substitution for plasmonic (amplitude) selective surfaces, where these are unsuitable, or simpler geometries are desired for practical reasons. Efficient selective solar absorbers and selective thermal emitters aimed at the GaSb band gap are demonstrated. Temperature limits for all thin-film structures are established, and it is shown for Tungsten-based selective solar absorber that the main degrading mechanism is oxidation. Finally, a TPV prototype was constructed which has so far successfully underlined the efficacy of simple but powerful thin-film structures based on few-nm metallic films.

A continuation of this research would be particularly interesting in at least two ways: First, the emergence of two-dimensional materials such as graphene can provide an efficient class of diffusion barriers, for higher thermal resistance in air. Secondly, the implementation of a prototype into a real world scenario under consideration of the economy seems distinctly valuable when considering the results presented in this thesis in the light of recent work (on the economy of thermophotovoltaic cogeneration) by others

Appendix A

Subwavelength Plasmonic Color Printing Protected for Ambient Use

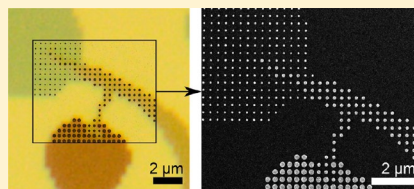
Subwavelength Plasmonic Color Printing Protected for Ambient Use

Alexander S. Roberts,* Anders Pors, Ole Albrektsen, and Sergey I. Bozhevolnyi*

Department of Technology and Innovation (ITI), University of Southern Denmark, Niels Bohrs Allé 1, DK-5230 Odense M, Denmark

Supporting Information

ABSTRACT: We demonstrate plasmonic color printing with subwavelength resolution using circular gap-plasmon resonators (GPRs) arranged in 340 nm period arrays of square unit cells and fabricated with single-step electron-beam lithography. We develop a printing procedure resulting in correct single-pixel color reproduction, high color uniformity of colored areas, and high reproduction fidelity. Furthermore, we demonstrate that, due to inherent stability of GPRs with respect to surfactants, the fabricated color print can be protected with a transparent dielectric overlay for ambient use without destroying its coloring. Using finite-element simulations, we uncover the physical mechanisms responsible for color printing with GPR arrays and suggest the appropriate design procedure minimizing the influence of the protection layer.



KEYWORDS: Plasmonics, color printing, subwavelength optics, metasurfaces, gap surface plasmons

The manipulation of electromagnetic waves by plasmonic structures, in which propagating light couples to electromagnetic excitations associated with metallic nanostructures (i.e., surface plasmons), has been the subject of extensive studies at wavelengths spanning from microwave^{1–3} and terahertz radiation^{4,5} to infrared⁶ and visible light.^{7,8} Plasmonic structures potentially exhibit strong enhancement and confinement of electromagnetic fields. These properties enable the fabrication of efficient optical elements with subwavelength dimensions featuring unique properties such as, for example, facilitating light confinement beyond the (far-field) diffraction limit determined by the light wavelength.⁹

Plasmonic nanostructures with closely controlled sizes and geometries have long been recognized as a means to tailoring absorption spectra, by locally controlling resonator dimensions on which the resonance frequency depends. This has been utilized, among others, to create meta-surfaces acting as color filters and absorbers in transmission,^{10–16} reflection,^{17–20} and, more recently, for phase-critical optical elements, such as waveplates.^{21–23} Using this approach, color printing at the diffraction limit has recently been demonstrated.¹⁷

However, the practicality of previously reported approaches to plasmonic color printing is limited, among others, by several factors. Configurations that have significant dependence of positions of spectral features on periodicity^{10–14,16,19} are expected to exhibit strong angular dependence, which is a major disadvantage for printing purposes, as colors are desired to be stable under variations in the viewing angle. Some configurations feature strongly polarization-dependent spectra,^{10,16} while others are not supposed to be covered with commonly available dielectrics, either due to the absorption mechanism being dependent on the contrast in the refractive index between vacuum and incorporated dielectric structures¹⁷ or due to large shifts of spectral features.¹⁸ While being of

major advantage for sensing applications,^{24,25} surface sensitivity is an obvious disadvantage for printing and filtering applications where color stability is of paramount importance and application-specific mechanical protection layers may be desired. Finally, printing techniques utilizing complex structures do not easily transfer to large-scale production techniques, such as nanoimprint lithography.

In this work we develop plasmonic color printing with subwavelength resolution that is based on the metal–insulator–metal (MIM) configuration capable of supporting gap-surface plasmons (GSPs). The uppermost metal layer is lithographically structured in a one-step process to consist of two-dimensional (2D) square arrays of circular gold nanodiscs (NDs). If desired, the sample can be protected with a transparent dielectric overlay without significantly influencing resonances, providing the sample with the chemical and mechanical stability necessary for use in exposed ambient color printing applications such as, for example, security certificates. This important feature is a direct result of the GSP field distribution that is almost entirely contained within the MIM structure itself.

It is well established that the Fabry–Perot (FP) resonance condition for the fundamental mode of a circular GSP-based resonator of diameter D is^{26,27}

$$D \frac{2\pi}{\lambda} n_{\text{GSP}} = \pi - \phi \quad (1)$$

where n_{GSP} is the effective mode index for the GSP, λ is the vacuum wavelength, and ϕ is the phase acquired upon reflection at the boundary of the ND. The spectral position

Received: November 6, 2013

Revised: December 23, 2013

Published: January 6, 2014

Nano Letters

Letter

of the resonance can thereby be controlled by changing the diameter of the gold NDs. Note that material and geometric choices also influence the effective index and the reflection phase.²⁶

The investigated samples consist of arrays of square unit cells of gold NDs, fabricated with EBL, on an insulator-on-metal structure consisting of continuous gold and SiO₂-layers (Figure 1), deposited by electron beam (e-beam) evaporation of 100

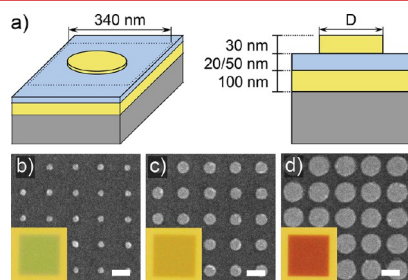


Figure 1. (a) Schematic views of the 340 nm unit cell of a rectangular array of circular gold NDs and continuous gold layer (yellow) and SiO₂ layer (blue) forming a MIM structure. (b–d) Example SEM images of NDs with average sizes of 80, 120, and 270 nm, respectively. Insets: Optical reflection microscopy images of the entire $27 \times 27 \mu\text{m}^2$ arrays. It is seen that the colors produced are visually highly uniform. Edge roughness can be seen on several gold NDs. Scale bars: 250 nm (b–d).

nm gold and subsequent radio frequency (RF) Ar⁺-sputtering of an SiO₂-insulator layer onto a Si-substrate. Adhesion layers (not shown in Figure 1) of 3 nm titanium are deposited by e-beam evaporation prior to each layer. The e-beam lithographic process of the top gold layer consists of spin-coating a 100 nm thick layer of positive tone 950 kDa PMMA resist onto the sample and exposing the design in a scanning electron microscope (SEM, model: JEOL JSM-6490LV) with an acceleration voltage of 30 kV, a working distance of 6 mm and an area dose of $350 \mu\text{C}/\text{cm}^2$. The writefield size is $100 \times 100 \mu\text{m}^2$ with a step size of 2.0 nm. After exposure the resist is developed for 30 s in a 3:1 mixture of 2-propanol/methyl

isobutyl ketone (MIBK) and subsequently rinsed in 2-propanol. Three nanometer titanium and 30 nm gold is then deposited by thermal evaporation, and lift-off is performed in a 10 h acetone bath without ultrasonic activation, yielding ND structures of which representative optical and SEM images can be seen in Figure 1b–d. The SEM images reveal arrays with well-defined circular discs and periodicity with a small amount of edge roughness while the optical images reveal a high degree of color homogeneity. In order to achieve independence of individual pixels it is necessary to minimize diffraction close to normal incidence. A subwavelength unit cell periodicity of 340 nm is chosen, with NDs ranging in diameter from 80 to 270 nm.

We characterize the reflection of the sample arrays by means of optical bright-field reflection spectroscopy in the visible range (400–800 nm). Reflection spectra are measured with an optical microscope (Olympus, BX-51 Research System) with halogen illumination through a $\times 50$ objective (numerical aperture 0.75). Reflected light is collected by the objective and collimated by a pinhole allowing for definition of the circular area from which light is collected, and subsequently directed to a fiber-coupled spectrometer (Ocean Optics QE65000), with sensitivity in the visible and near-infrared. Reflection spectra measured on the samples are normalized against the reflection (R_{ref}) of the homogeneous MI-surface, i.e., before the fabrication of gold ND-arrays. It has previously been established that the geometry chosen in the present work does not exhibit polarization dependence.²⁷ Size measurements, geometry, and quality inspection are performed in-system on the SEM used for fabrication.

We produce quadratic gold ND arrays with a periodicity of 340 nm and disc diameters that increase from bottom to top, as seen in Figure 2a. The ND arrays are produced on samples with SiO₂ spacer layer thicknesses of 20 nm (Figure 2a, left) and 50 nm (Figure 2a, right). All array geometries exhibit bright colors. CCD images are captured with a $\times 20$ objective and a color average over a square area of $10 \times 10 \mu\text{m}^2$ is performed, the result of which is seen in Figure 2a. The arrays on 20 nm SiO₂ are examined in bright-field reflection spectroscopy, as described above, yielding the selection of spectra shown in Figure 2b. We perform finite-element simulations of the

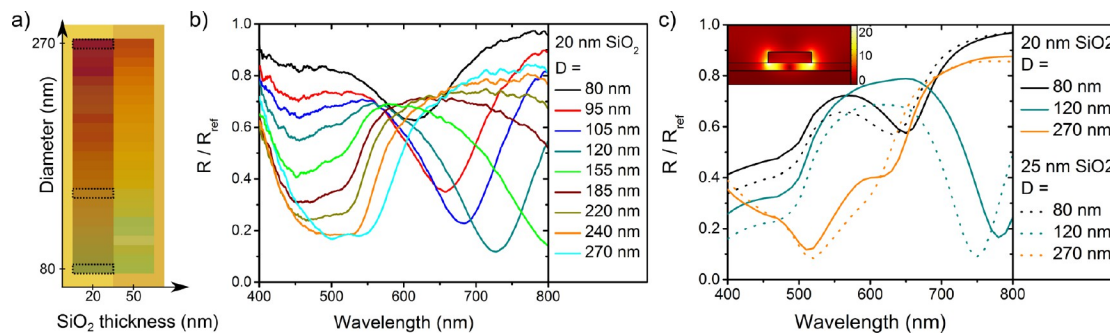


Figure 2. (a) Colors of rectangular arrays of gold CL-GPR arrays fabricated on an MI-structure with a 20 nm (left) and 50 nm (right) SiO₂ insulator layer against the color of the MI-surface itself. Colors used for color printing (Figure 3a) are marked with dotted boxes and correspond to ND diameters of 80, 120, and 270 nm. (b) Reflection spectra from NDs with increasing diameters on 20 nm SiO₂, collected with a $\times 50$ objective (NA = 0.75) and normalized against the reflection from SiO₂-on-gold. (c) Finite-element simulation of the reflection spectrum normalized against the SiO₂-on-gold surface, shown for SiO₂ thicknesses 20 and 25 nm. Inset: Electric field enhancement normalized against the incoming field amplitude for a 120 nm ND illuminated at its first order FP resonance at 780 nm.

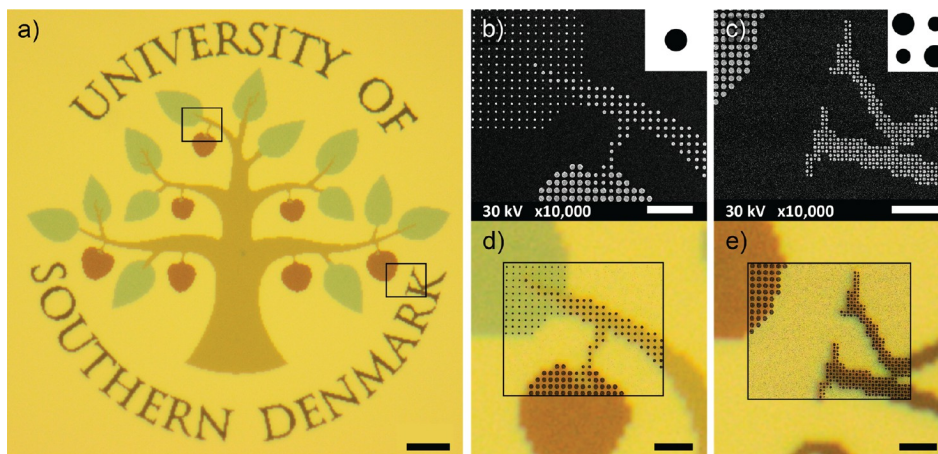


Figure 3. (a) Optical microscopy image ($\times 50$ magnification, $NA = 0.75$) of a color print exhibiting bright colors with high contrast. The monotonically colored areas are visually uniform, indicating a high degree of accuracy in the fabrication process. (b,c) SEM images of the areas outlined in panel a for (b) green, brown, and red pixels and (c) black pixels. Insets: schematic pixel geometry. (d,e) Overlay of optical and SEM images showing how even single pixel details are colored and discernible. Scale bars: $10\ \mu\text{m}$ (a); $2\ \mu\text{m}$ (b–e).

reflection spectra of ND arrays in COMSOL Multiphysics, with a Floquet-bounded unit cell and plane wave, normal incidence.

The simulated spectra (Figure 2c) are normalized against the analytically calculated reflection of the SiO_2 -on-gold surface. We use interpolated optical properties from tabular values²⁸ for gold. For the gold nanodiscs we multiply the imaginary part of the dielectric function with a factor of 4, so as to take into account the increased grain boundary and surface effects for thin films and the additional losses due to the titanium layer.^{29,30} The influence of different factors multiplied onto the imaginary part of the dielectric function can be seen in Figure S1 in the Supporting Information. The dielectric refractive indexes used for SiO_2 and air are $n_{\text{SiO}_2} = 1.45$ and $n_{\text{air}} = 1$, respectively.

For the practical usability of the proposed plasmonic color printing, a weak angular dependence of the reflection spectra is necessary. Furthermore, spectra collected as described above are the result of weighted average of the response of the structures at the incidence angles in question (angles up to 49° in Figure 2b). We have performed finite-element simulations of the reflection spectra for varied angles of incidence (Figure S2 in the Supporting Information) and optical measurements with different magnifications (Figure S3), both showing that the influence of incidence angle is indeed negligible.

All measured reflection spectra (Figure 2b) exhibit at least one of two distinct absorption features. One absorption feature occurs at $610\ \text{nm}$ for $80\ \text{nm}$ diameter discs. This dip in reflectance red-shifts almost linearly with regard to the disc diameter and has a near constant fwhm width of approximately $110\ \text{nm}$, which is consistent with a FP type resonance. Simulations of the electric field distribution support this assumption regarding the resonance type (Figure 2c, inset). Returning to Figure 2b, it can furthermore be seen that the resonant absorption increases rapidly for disc diameters up to approximately $120\ \text{nm}$, after which it is saturating and red-shifting out of the visible part of the spectrum. For small diameters, the increase in absorption for increasing diameters can simply be related to an increase in the filling factor, i.e., to an increase of the ND area resulting in stronger absorption by a

unit cell. At larger diameters, however, the GSP excitation efficiency becomes weaker due to stronger overlap of neighboring GSP mode fields, resulting in a reduced cross-section per GPR.²⁷ A second absorption feature, located at $500\ \text{nm}$ wavelength, exhibits a fundamentally different behavior: this absorption is very broad and its location is insensitive to the GPR diameter. The absorption strength is weak for discs up to $120\ \text{nm}$ in diameter but grows in strength with growing disc size. For disc diameters up to $220\ \text{nm}$, the position of the feature is largely constant, while spectra obtained from the two largest discs show an additional higher order mode located at a wavelength of $540\ \text{nm}$ for $D = 270\ \text{nm}$ diameter GPRs. The invariance of the spectral position to D and the position of the absorption feature indicate nonresonant absorption, due to the interband-transitions in gold at short visible wavelengths,²⁸ leading to increased skin depth and nonresonant Ohmic losses within the gold. Below $450\ \text{nm}$ the reflection increases for decreasing diameter, presumably the result of scattering on the ND surface and edge irregularities acting as Rayleigh scatterers with a scattering cross-section that scales with k^4 , where $k = 2\pi/\lambda$ is the vacuum wavenumber. As is immediately clear from the spectra, the GSP-based absorption feature lies outside the visible spectrum for $D > 150\ \text{nm}$, making nonresonant Ohmic absorption the fundamental feature determining the color of the largest disc arrays. With higher resolution of fabrication, however, eq 1 allows for resonant absorption in a larger part of the spectrum. The decreasing absorption strength of the resonance (with decreasing diameter) can readily be compensated for by increasing the number of NDs per unit cell.²⁷

Comparison of the simulated and measured spectra gives qualitatively good correspondence (Figure 2b,c). One should keep in mind that ND edge and surface irregularities are not included in the simulations, and therefore, the steep increase in the reflection at low wavelengths cannot be expected to show in the simulated spectra. However, quantitative analysis reveals that the position of the simulated resonance features are red-shifted by $50\ \text{nm}$ with regard to the observed spectra. This is presumably due to inaccuracies in the thickness of the RF-

Nano Letters

Letter

sputtered SiO₂ layers. The effect of changing the spacer layer thickness on the effective refractive index is demonstrated in Figure 2c, where simulations of the reflection spectra have been performed for an SiO₂ thickness of 25 nm for otherwise equal parameters. Finally, the adhesion layers of 3 nm titanium, which are not included in the finite-element simulation, potentially contribute to further deviation from measured reflection spectra.

To demonstrate the suitability of the presented technique for use in color prints and related applications, we prepare a colored bitmap of the University of Southern Denmark logo with a resolution of 287 × 290 pixels. Each pixel is represented by a quadratic unit cell with 340 nm periodicity, yielding an exposure pattern approximately 98 × 99 μm in size (Figure 3). Color pixels are represented by a unit cell comprising one ND (Figure 3d), while black pixels are represented by a composite unit cell containing four NDs of two different sizes (Figure 3e), drawing inspiration from previous work.²⁷ We chose colors that correspond to disc diameters of 80, 120, and 270 nm (Figure 2a). For each pixel the most appropriate disc size and geometry is found by matching the desired pixel color with the three chosen colors, using a computerized script.

The fabrication steps are as described above for periodic square arrays. The resulting print is displayed in Figure 3. The optical image (Figure 3a) reveals a high quality color print with several desirable properties. First, the colors are bright and stand out well against each other and the background due to high color saturation. Second, colored areas exhibit a high degree of visual homogeneity, attributable to limited proximity-effect in conjunction with a high contrast development procedure. Furthermore, color can be encoded into a pixel containing only one GPR as can be seen from Figure 3b–d. Note especially the areas in which the tree branch tapers off into single-pixel width (Figure 3d). After optimization of the exposure parameters, we observed that there were no missing pixels or other significant deviations from the design file, indicating that the fabrication procedure has a very high degree of fidelity and reproducibility.

To demonstrate how this color printing procedure can be passivated for ambient use, opening the door toward practical applications, we mechanically and chemically protect the sample by spin-coating a 100 nm thick PMMA layer, using the EBL recipe described above. Figure 4 shows a direct comparison between an uncoated sample (left) and the resulting PMMA-coated sample (right). The extra layer of PMMA does have limited influence on the resulting colors, effectively reducing the red content of all the colors. This is due to weakening of the nonresonant absorption caused by a lower contrast in refractive indexes at the Au/PMMA interface compared to an Au/air interface, resulting in a larger part of the field situated in the (near lossless) dielectric. It should be noted that the resonant behavior is largely unchanged and that both sample geometry and color values were originally designed for use in air. It should therefore be possible to achieve better color production by designing the GSP structures specifically for use with PMMA coverage.

Several improvements to the geometry can be made. The influence of the dielectric protection layer can be further minimized by using NDs with increased film thickness and thereby confining the GSP modes within the intermediate dielectric to an even larger extent. Furthermore, the use of smaller discs in smaller unit cells (which can be achieved with thinner spacer layers) would also increase the GSP mode

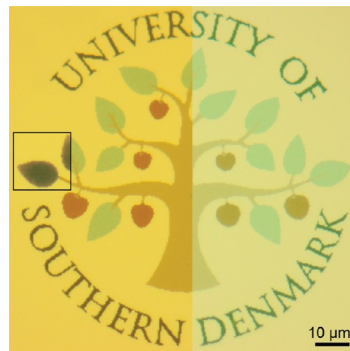


Figure 4. Optical microscopy images (×50 magnification, NA = 0.75) comparing an uncovered color print (left) and the same print (right) after covering the sample with 100 nm of PMMA. It is seen that while the PMMA layer does have an influence on the perceived colors, color printing is still very much feasible, mainly influencing the red content of the image. Inset (left): The unit cells used for printing the green leaf is exchanged with a unit cell of double periodicity (170 nm) and equal nominal disc diameter. Scale bar: 10 μm.

confinement and could make the FP resonances available in the entire visible spectrum, while at the same time increasing the angle at which diffraction begins to occur. A rough estimate using eq 1 for the spacer thickness of 15 nm, gives the range of ND diameters with first order FP resonances in the visible regime as approximately 45 nm < D < 155 nm, which is well within the resolution range of current EBL and NIL procedures. This would allow a reduction in unit cell size to roughly 200 nm, further reducing the influence of diffraction and allowing for wider viewing angles.

The flexibility in terms of unit cell geometry is demonstrated in the inset of Figure 4, where we have used a periodicity of 170 nm instead of 340 nm, which leads to highly increased absorption in the long wavelength range and colors with very high saturation, in this case yielding a dark blue.

We would like to point out that the color printing demonstrated above is very well suited for practical applications, such as security marking, as several requirements are simultaneously met. The design is flexible and can easily be reprogrammed, while fabrication incorporates expensive and specialized equipment (as well as knowledge). Furthermore, the print can readily be inspected with standard low-magnification microscopes while being small enough to hide from plain view. Finally, the security stamp should be stable under mechanical and chemical influence from the environment. As demonstrated, a transparent dielectric cover layer provides aforementioned protection, with negligible influence on the plasmonic resonances.

Summarizing, we have demonstrated that, using continuous-layer gap surface plasmon resonators, in which only the top layer is structured, it is possible to produce clear color prints with subwavelength resolution that exhibit low dependence on incidence angle and surface coverage (by dielectric materials). We demonstrate this by fabricating effectively an MIMI structure that to a large extent produces the same colors as the uncovered (MIM) sample. Furthermore, it should be noted that the developed approach can easily be implemented using fabrication with scalable techniques, such as nanoimprint lithography.

Nano Letters

Letter

■ ASSOCIATED CONTENT

📄 Supporting Information

Finite element simulations and reflection spectra. This material is available free of charge via the Internet at <http://pubs.acs.org>.

■ AUTHOR INFORMATION

Corresponding Authors

*(A.S.R.) E-mail: asro@iti.sdu.dk.

*(S.I.B.) E-mail: seib@iti.sdu.dk.

Notes

The authors declare no competing financial interest.

■ ACKNOWLEDGMENTS

We thank René Lynge Eriksen for advice with regard to optical measurements. We acknowledge financial support from the Danish Council for Independent Research (the FTP project PlasTPV, contract no. 1335-00104).

■ REFERENCES

- (1) Jiang, T.; Shen, L.; Wu, J.-J.; Yang, T.-J.; Ruan, Z.; Ran, L. *Appl. Phys. Lett.* **2011**, *99*, 261103.
- (2) Shen, X.; Cui, T. J.; Martin-Cano, D.; Garcia-Vidal, F. J. *Proc. Natl. Acad. Sci. U.S.A.* **2013**, *110*, 40.
- (3) Song, Z.; Li, X.; Hao, J.; Xiao, S.; Qiu, M.; He, Q.; Ma, S.; Zhou, L. *Opt. Express* **2013**, *21*, 18178.
- (4) Gay-Balmaz, P.; Maccio, C.; Martin, O. J. F. *Appl. Phys. Lett.* **2002**, *81*, 2896.
- (5) Pradarutti, B.; Rau, C.; Torosyan, G.; Beigang, R.; Kawase, K. *Appl. Phys. Lett.* **2005**, *87*, 204105.
- (6) Li, X.; Jiang, T.; Shen, L.; Deng, X. *Appl. Phys. Lett.* **2013**, *102*, 031606.
- (7) Klein Koerkamp, K. J.; Enoch, S.; Segerink, F. B.; van Hulst, N. F.; Kuipers, L. *Phys. Rev. Lett.* **2004**, *92*, 183901.
- (8) Pors, A.; Albrektsen, O.; Radko, I. P.; Bozhevolnyi, S. I. *Sci. Rep.* **2013**, *3*, 2155.
- (9) Schuller, J. A.; Barnard, E. S.; Cai, W.; Jun, Y. C.; White, J. S.; Brongersma, M. L. *Nat. Mater.* **2010**, *9*, 193.
- (10) Xu, T.; Wu, Y.-K.; Luo, X.; Guo, L. J. *Nat. Commun.* **2010**, *1*, 59.
- (11) Chen, Q.; Cumming, D. R. *Opt. Express* **2010**, *18*, 14056.
- (12) Kaplan, A. F.; Xu, T.; Guo, L. J. *Appl. Phys. Lett.* **2011**, *99*, 143111.
- (13) Chen, Q.; Chitnis, D.; Walls, K.; Drysdale, T. D.; Collins, S.; Cumming, D. R. *IEEE Photonics Technol. Lett.* **2012**, *24*, 197.
- (14) Yokogawa, S.; Burgos, S. P.; Atwater, H. A. *Nano Lett.* **2012**, *12*, 4349.
- (15) Ye, F.; Burns, M. J.; Naughton, M. J. *Nano Lett.* **2013**, *13*, 519.
- (16) Zeng, B.; Gao, Y.; Bartoli, F. J. *Sci. Rep.* **2013**, *3*, 2840.
- (17) Kumar, K.; Duan, H.; Hegde, R. S.; Koh, S. C.; Wei, J. N.; Yang, J. K. *Nat. Nanotechnol.* **2012**, *7*, 557.
- (18) Zhang, J.; Ou, J.; MacDonald, K.; Zheludev, N. J. *Opt.* **2012**, *14*, 114002.
- (19) Zhu, P.; Guo, L. J. *Appl. Phys. Lett.* **2012**, *101*, 241116.
- (20) Aydin, K.; Ferry, V. E.; Briggs, R. M.; Atwater, H. A. *Nat. Commun.* **2011**, *3*, 517.
- (21) Roberts, A.; Lin, L. *Opt. Lett.* **2012**, *37*, 1820.
- (22) Pors, A.; Nielsen, M. G.; Valle, G. D.; Willatzen, M.; Albrektsen, O.; Bozhevolnyi, S. I. *Opt. Lett.* **2011**, *36*, 1626.
- (23) Chimento, P. F.; Kuzmin, N. V.; Bosman, J.; Alkemade, P. F. A.; 't Hooft, G. W.; Eliel, E. R. *Opt. Express* **2011**, *19*, 24219.
- (24) Stewart, M. E.; Anderton, C. R.; Thompson, L. B.; Maria, J.; Gray, S. K.; Rogers, J. A.; Nuzzo, R. G. *Chem. Rev.* **2008**, *108*, 494.
- (25) Anker, J. N.; Hall, W. P.; Lyandres, O.; Shah, N. C.; Zhao, J.; Van Duyne, R. P. *Nat. Mater.* **2008**, *7*, 442.
- (26) Nielsen, M. G.; Gramotnev, D. K.; Pors, A.; Albrektsen, O.; Bozhevolnyi, S. I. *Opt. Express* **2011**, *19*, 19310.

(27) Nielsen, M. G.; Pors, A.; Albrektsen, O.; Bozhevolnyi, S. I. *Opt. Express* **2012**, *20*, 13311.

(28) Johnson, P. B.; Christy, R. W. *Phys. Rev. B* **1972**, *6*, 4370.

(29) Pors, A.; Nielsen, M. G.; Bozhevolnyi, S. I. *Opt. Lett.* **2013**, *38*, 513.

(30) Liu, N.; Mesch, M.; Weiss, T.; Hentschel, M.; Giessen, H. *Nano Lett.* **2010**, *10*, 2342.

Supporting information for:
“Subwavelength Plasmonic Color Printing
Protected for Ambient Use”

Alexander S. Roberts,* Anders Pors, Ole Albrektsen, and Sergey I.

Bozhevolnyi*

Department of Technology and Innovation (ITI), University of Southern Denmark, Niels

Bohrs Allé 1, DK-5230 Odense M, Denmark

E-mail: asro@iti.sdu.dk; seib@iti.sdu.dk

*To whom correspondence should be addressed

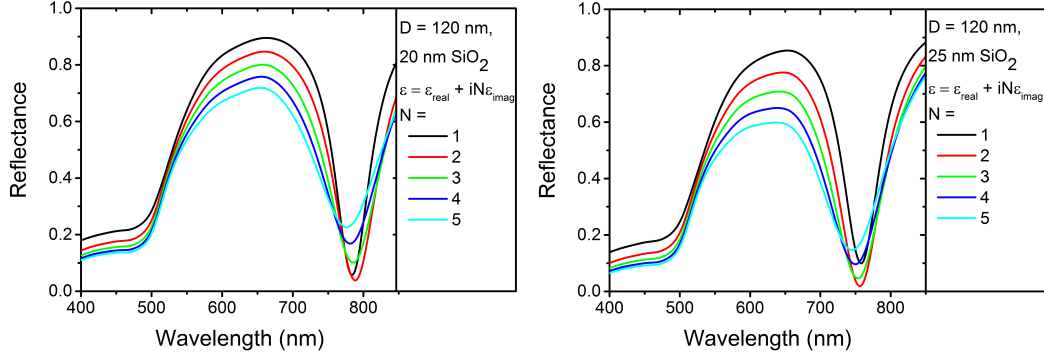


Figure S1: left: Finite-element simulations of the absolute reflection spectra at normal incidence of a 120 nm ND with a factor N multiplied onto the imaginary parts of the dielectric functions: $\epsilon = \epsilon_{real} + iN\epsilon_{imag}$. As expected an increase in N reduces the strength of the resonance feature while increasing the width and red-shifting the position. This red-shift, which is on the order of 2 nm per unit increase in N , is negligible with regard to printing.

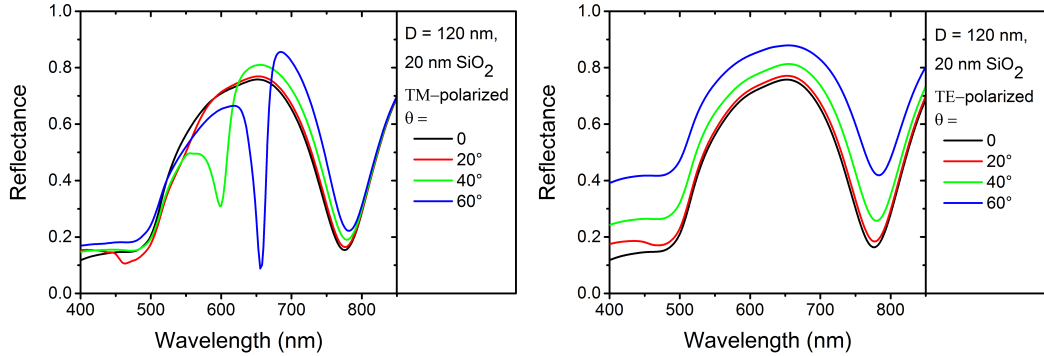


Figure S2: left: Absolute reflection spectra showing the absolute reflection of a 120nm gold nanodisc illuminated in TM polarisation as a function of the angle of incidence, θ . The most noteworthy change is the appearance of reflection dips due to diffraction into SPP modes. These peaks are not visible in measurements, due to the averaging over many angles (see figure S3). The plasmonic features and non-resonant power absorption are largely unchanged. right: Absolute reflection spectra for a ND of diameter 120 nm in TE-polarisation. The reflection for oblique incidence generally increases with increasing angle of incidence. However, all relevant features of the spectra are unchanged with regard to their spectral position.

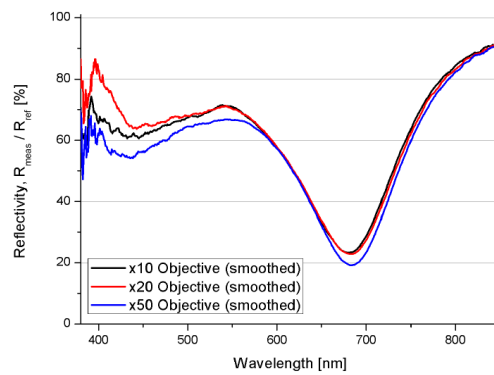


Figure S3: Measured reflection spectra of an array of NDs with diameters of 105 nm, normalized against the SiO_2 -on-gold surface. It is seen that the reflection does not change significantly with the magnification and the resulting change of angles of incidence. The angles from which light is collected for the different objectives, are $\times 10$: $\pm 14^\circ$; $\times 20$: $\pm 23^\circ$ and $\times 50$: $\pm 49^\circ$.

Appendix B

Near-infrared tailored thermal emission from wafer-scale continuous-film resonators

Near-infrared tailored thermal emission from wafer-scale continuous-film resonators

**Alexander S. Roberts,^{1,*} Manohar Chirumamilla,² Kasper
Thilsing-Hansen,³ Kjeld Pedersen,² and Sergey I. Bozhevolnyi¹**

¹*University of Southern Denmark, Institute of Technology & Innovation, Niels Bohrs Alle 1,
5230 Odense, Denmark*

²*University of Aalborg, Department of Physics and Nanotechnology, Skjernvej 4, 9220
Aalborg, Denmark*

³*University of Southern Denmark, Mads Clausens Institute, Alsion 2, 6400 Sønderborg,
Denmark*

[*asro@iti.sdu.dk](mailto:asro@iti.sdu.dk)

Abstract: We experimentally investigate the near-infrared emission from simple-to-fabricate, continuous-film Fabry-Perot-type resonators, consisting only of unstructured dielectric and metallic films. We show that the proposed configuration is suitable for realization of narrowband emitters, tunable in ranges from mid- to near-infrared, and demonstrate emission centered at the wavelength of 1.7 μm , which corresponds to the band gap energy of GaSb-based photodetectors. The emission is measured at 748 K and follows well the emissivity as predicted from reflection measurements and Kirchhoff's reciprocity. The considered emitter configuration is spectrally highly tunable and, consisting of only few unstructured layers, is amenable to wafer-scale fabrication at low cost by use of standard deposition procedures.

© 2015 Optical Society of America

OCIS codes: (260.3060) Infrared; (290.6815) Thermal emission; (230.5750) Resonators; (310.6845) Thin film devices and applications.

References and links

1. J.-J. Greffet, R. Carminati, K. Joulain, J.-P. Mulet, S. Mainguy, and Y. Chen, "Coherent spontaneous emission of light by thermal sources," *Nature* **416**, 61 (2002).
2. F. Marquier, K. Joulain, J.-P. Mulet, R. Carminati, J.-J. Greffet, and Y. Chen, "Coherent spontaneous emission of light by thermal sources," *Phys. Rev. B* **69**, 155412 (2004).
3. Y. Shuai, H. Tan, and Y. Liang, "Polariton-enhanced emittance of metallic-dielectric multilayer structures for selective thermal emitters," *J. Quant. Spectrosc. Radiat. Transfer* **135**, 50 (2014).
4. M. Florescu, K. Busch, and J. P. Dowling, "Thermal radiation in photonic crystals," *Phys. Rev. B* **75**, 201101 (2007).
5. S.-Y. Lin, J.G. Flemming, and I. El-Kady, "Experimental observation of photonic-crystal emission near a photonic band edge," *Appl. Phys. Lett.* **83**, 593 (2003).
6. B.J. Lee, C.J. Fu, and Z.M. Zhang, "Coherent thermal emission from one-dimensional photonic crystals," *Appl. Phys. Lett.* **87**, 071904 (2005).
7. P. Ben-Abdallah and B. Ni, "Single-defect Bragg stacks for high-power narrow-band thermal emission," *J. Appl. Phys.* **97**, 104910 (2005).
8. I. Celanovic, N. Jovanovic, and J. Kassakian, "Two-dimensional tungsten photonic crystals as selective thermal emitters," *Appl. Phys. Lett.* **92**, 193101 (2008).
9. C.-M. Wang, Y.-C. Chang, M.-W. Tsai, Y.-H. Ye, C.-Y. Chen, Y.-W. Jiang, Y.-T. Chang, S.-C. Lee, and D. P. Tsai, "Reflection and emission properties of an infrared emitter," *Opt. Express* **15**, 14673 (2007).

10. H. Miyazaki, K. Ikeda, T. Kasaya, K. Yamamoto, Y. Inoue, K. Fujimura, T. Kanakugi, M. Okada, K. Hatade, and S. Kitagawa, "Thermal emission of two-color polarized infrared waves from integrated plasmon cavities," *Appl. Phys. Lett.* **92**, 141114 (2008).
11. X. Liu, T. Tyler, T. Starr, A. F. Starr, N. M. Jokerst, and W. J. Padilla, "Taming the blackbody with infrared metamaterials as selective thermal emitters," *Phys. Rev. Lett.* **107**, 045901 (2011).
12. H. G. Jones, "Application of thermal imaging and infrared sensing in plant physiology and ecophysiology," in *Incorporating Advances in Plant Pathology*, J. A. Callow, ed., vol. 41 of *Advances in Botanical Research*, pp. 107–163 (Academic, 2004).
13. W. Turner, S. Spector, N. Gardiner, M. Fladeland, E. Sterling, and M. Steininger, "Remote sensing for biodiversity science and conservation," *Trends Ecol. Evol.* **18**(6), 306–314 (2003).
14. A. Hayden, E. Niple, and B. Boyce, "Determination of trace-gas amounts in plumes by the use of orthogonal digital filtering of thermal-emission spectra," *Appl. Opt.* **35**, 2802 (1996).
15. A. Lenert, D. M. Bierman, Y. Nam, W. R. Chan, I. Celanović, M. Soljačić, and E. N. Wang, "A nanophotonic solar thermophotovoltaic device," *Nat. Nanotechnol.* **9**, 126 (2014).
16. S. Molesky, C.J. Dewalt, and Z. Jacob, "High temperature epsilon-near-zero and epsilon-near-pole metamaterial emitters for thermophotovoltaics," *Opt. Express* **21**, A96 (2013).
17. B. Zhao, L. Wang, Y. Shuai, and Z.M. Zhang, "Thermophotovoltaic emitters based on a two-dimensional grating/thin-film nanostructure," *Int. J. Heat Mass Transfer* **67**, 637 (2013).
18. M. Yan, "Metal-insulator-metal light absorber: a continuous structure," *J. Opt.* **15**, 025006 (2013).
19. D. Zhao, L. Meng, H. Gong, X. Chen, Y. Chen, M. Yan, Q. Li, and M. Qiu, "Ultra-narrow-band light dissipation by a stack of lamellar silver and alumina," *Appl. Phys. Lett.* **104**, 221107 (2014).
20. I. Celanovic, D. Perreault, and J. Kassakian, "Resonant-cavity enhanced thermal emission," *Phys. Rev. B* **72**, 075127 (2005).
21. L. Wang, S. Basu, and Z. Zhang, "Direct measurement of thermal emission from a Fabry–Perot Cavity resonator," *J. Heat Transfer* **134**, 072701 (2012).
22. M. Planck, "Ueber das Gesetz der Energieverteilung im Normalspectrum," *Ann. Phys.* **309**, 553 (1901).
23. A.S. Gawarekar, R.P. Shea, and J.J. Talghader "Radiation efficiency of narrowband coherent thermal emitters," *AIP Adv.* **2**, 032113 (2012).
24. F. E. Nicodemus, "Directional reflectance and emissivity of an opaque surface," *Appl. Opt.* **4**, 767 (1965).
25. J.-J. Greffet and M. Nieto-Vesperinas, "Field theory for generalized bidirectional reflectivity: derivation of Helmholtz's reciprocity principle and Kirchhoff's law," *J. Opt. Soc. Am. A* **15**, 2735 (1998).
26. K. Ujihara, "Reflectivity of metals at high temperatures," *J. Appl. Phys.* **43**, 2376 (1972).
27. M. Brückner, J.H. Schäfer, C. Schiffer, and J. Uhlenbusch, "Measurements of the optical constants of solid and molten gold and tin at $\lambda = 10.6\mu\text{m}$," *J. Appl. Phys.* **70**, 1642 (1991).
28. S. Tripura Sundari, K. Srinivasu, S. Dash, and A.K. Tyagi, "Temperature evolution of optical constants and their tuning in silver," *Solid State Commun.* **167**, 36 (2013).
29. Y.-J. Chen, M.-C. Lee, and C.-M. Wang, "Dielectric function dependence on temperature for Au and Ag," *Jpn. J. Appl. Phys.* **53**, 08MG02 (2014).
30. M. Zhang, M.Y. Efremov, F. Schiettekatte, E. A. Olson, A. T. Kwan, S. L. Lai, T. Wisleder, J. E. Greene, and L. H. Allen, "Size-dependent melting point depression of nanostructures: Nanocalorimetric measurements," *Phys. Rev. B* **62**, 10548 (2000).
31. G. Allen, R. Bayles, W. Gile, and W. Jesser, "Small particle melting of pure metals," *Thin Solid Films* **144**, 297 (1986).
32. Y. G. Chushak and L. S. Bartell, "Melting and Freezing of Gold Nanoclusters," *J. Phys. Chem. B* **105**, 11605 (2001).
33. U. Guler, A. Boltasseva, and V. M. Shalaev, "Refractory plasmonics," *Science* **344**(6181), 263 (2014).
34. C. Jeppesen, N. A. Mortensen, and A. Kristensen, "The effect of Ti and ITO adhesion layers on gold split-ring resonators," *Appl. Phys. Lett.* **97**, 263103 (2010).
35. B. Lahiri, R. Dylewicz, R. M. De La Rue, and N. P. Johnson, "Impact of titanium adhesion layers on the response of arrays of metallic split-ring resonators (SRRs)," *Opt. Express* **18**, 11202 (2010).

1. Introduction

Progress in the tailoring of thermal emission spectra in the infrared by both nano-structured surfaces and thin-film stacks serving as gratings [1–3], photonic crystals [4–8] or resonators [9–11], has been widely reported in recent years. As thermal emission is a process inherent to all ordinary matter, it provides an energy transfer and loss mechanism available in most conceivable system, allowing for sensing, spectroscopic analysis or energy transport as such. The fields of actual and potential application of thermal radiation emission and detection are therefore correspondingly diverse, spanning from industrial and botanical control [12–14] to

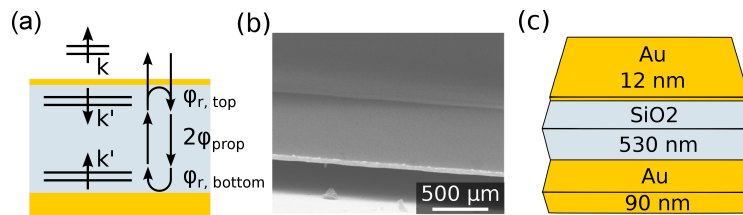


Fig. 1. (a) Working principle of the continuous resonator. Freely propagating waves can couple to the resonator through the optically thin top layer. Inside the resonator, photonic modes are confined in the vertical direction, acquiring reflection and propagation phases, $\phi_{r, top}$, $\phi_{r, bottom}$ and ϕ_{prop} , respectively, as indicated in the right part of (a), creating a resonance when the round-trip phases equal multiples of 2π . (b) Scanning electron micrograph (side view) of a continuous-film Fabry-Perot emitter detached and elevated above its substrate. Note that the 12 nm top gold layer is not well-resolved. (c) The structure of (b), showing the amorphous SiO₂-layer (blue), the optically thick bottom gold layer and the optically thin top gold layer (yellow). Not shown are adhesion-promoting layers of 3 nm Ti at the SiO₂-gold interfaces.

thermophotovoltaic energy conversion [15–17], amongst others. While nanostructuring of surfaces constitutes a very powerful tool for the tailoring of optical properties, it often requires expensive and slow fabrication techniques, hence calling for simpler structures with which to tailor the optical properties of surfaces. In this work, we present tailored thermal emission from an unstructured few-layer resonator, that is both easily fabricated and suited for the controlled tailoring of thermal near- and mid-infrared narrowband emission, see Fig. 1. The emitter conceptually consists of two gold films of different thicknesses, which are spaced by an amorphous silicon dioxide layer. The thicknesses of the gold films are such that the bottom film is fully reflecting while the top film is semitransparent and so ensures that the resonator modes couple to freely propagating waves. We design the emissivity to coincide with the band gap energy of GaSb, a low band gap semiconductor material often used for thermophotovoltaic (TPV) conversion. Its band gap energy is 0.7 eV for an unstrained material, corresponding to a vacuum wavelength of roughly 1.7 μm .

The structure was recently investigated by Yan [18], at a resonance wavelength of 1 μm , and by Zhao et al. [19] in the visible, with regard to its cold optical properties and was found to exhibit sharp resonances that are tunable in resonant wavelength, through variation of the spacer thickness. The line width and maximum absorption are determined primarily by the thickness of the top gold layer. A conceptually closely related structure, where a Bragg reflector acts as the top reflector, can be found in [20]. Previously, Wang et al. have measured thermal emission from a very similar structure, however at energies too small for photovoltaic conversion [21]. Here, we investigate the thermal emission from this structure at 1.72 μm - that is at wavelengths with direct relevance in thermophotovoltaic conversion. As the emitter requires no layer-structuring and, moreover, can be fabricated in a variety of metals and dielectrics, it has the potential for cost-effective production scaling of thermal emitters for large-scale illumination of photovoltaic cells in TPV applications.

2. Thermal emission and Kirchhoff's reciprocity

In thermodynamic equilibrium, the thermal emission of a totally absorbing and opaque object, a blackbody, is described by the radiation law first derived by Planck [22], that relates wavelength and temperature of a blackbody to its spectral radiance, I , which quantifies the emitted power

per unit area, wavelength, and solid angle. A blackbody is an idealized object; the emission of any real object is further described by their emissive power or emissivity, $\epsilon_\lambda(T)$, which quantifies the spectral radiance of an object, relative to that of a blackbody. The spectral radiance of an object with emissivity $\epsilon_\lambda(T)$, can thus be expressed as

$$I(\lambda, T) = \epsilon_\lambda(T)B(\lambda, T) = \epsilon_\lambda(T) \cdot \frac{2hc^2}{\lambda^5} \frac{1}{e^{\frac{hc}{\lambda k_B T}} - 1}, \quad (1)$$

where λ is the vacuum wavelength, T is the temperature of the object, h is Planck's constant, c is the vacuum speed of light and k_B is Boltzmann's constant. The wavelength of maximum spectral radiance of the blackbody spectrum λ_{\max} , is given by Wien's displacement law, which can be expressed in the following reciprocal relationship between T and λ_{\max} :

$$\lambda_{\max}(T) = b/T = 2898 \mu\text{mK}/T, \quad (2)$$

where b is Wien's displacement constant. Optimizing the efficiency of the emitter, defined as the power emitted around the design wavelength divided by the total power emitted by a blackbody at the same temperature, therefore, requires heating the sample to a temperature where λ_{\max} and the resonance wavelength become comparable [23].

Due to the broad spectrum of the blackbody radiation, efficient technological utilization of thermally generated emission is often challenging, apart from the rather obvious case of radiative cooling. However, for many other applications, it is desirable to emit or detect radiation only within a particular frequency band, determined by the characteristic energies of the processes involved. As the blackbody spectrum depends only on temperature and is inherently broadband, the emissivity must be tightly controlled to achieve narrowband thermal emission. Through Kirchhoff's reciprocity, which equates emissivity and absorptivity, $\alpha_\lambda = \epsilon_\lambda = 1 - R_\lambda - T_\lambda$, thereby relating absorptivity α_λ and emissivity ϵ_λ to transmissivity T_λ and reflectivity R_λ [24, 25]. The relation $\epsilon_\lambda = 1 - R_\lambda$ is readily derived for non-transmitting objects (Temperature dependence is suppressed for readability). Consequently, a narrowband absorbing surface functions as a thermal narrowband emitter with a relatively high degree of temporal coherence, when heated to sufficient temperatures.

3. Fabrication and tunability of spectral properties

The emitter is fabricated on a polished silicon (p-type, c-Si (100)) substrate by electron-beam evaporation of 90 nm of gold at an evaporation rate of 0.3 Å/s, subsequent radio-frequency sputtering of the spacer layer consisting of amorphous SiO₂ at a rate of 0.5 Å/s and finally by electron-beam evaporation of a 12 nm gold top layer at 0.3 Å/s. Adhesion-promoting titanium layers of 3 nm thickness are evaporated between all layers at 0.3 Å/s. All deposition steps are performed in a continuously evacuated chamber at pressures of 10⁻⁵ mbar or less. The thickness of the stacked layers is characterized independently by spectroscopic ellipsometry. Figure 1(a) shows a schematic and a scanning electron micrograph of the resulting continuous-film Fabry-Perot resonator. In contrast to the optically thick bottom layer of gold acting as a reflector, the top gold layer functions as a semi-transparent mirror by choosing its thickness to be comparable to the skin depth of light. The partially reflecting film allows for coupling of the lossy resonator modes to freely propagating waves, leading to absorption at wavelengths near resonance. The spectral position of the resonance is determined by the condition that the round-trip phase equals integer multiples of 2π at resonance:

$$\phi_{r, \text{bottom}} + \phi_{r, \text{top}} + 2 \cdot \phi_{\text{prop}} = 2m\pi, \quad (3)$$

for integer m . Appropriate geometric parameters are found by reflectivity measurements, see Fig. 2. As a result of Eq. (3), the resonance frequency can be tuned over most of the infrared

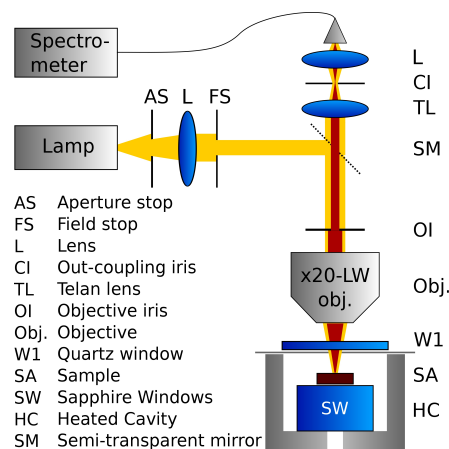


Fig. 2. Schematic of the setup used for emission and reflection measurements. The sample is heated in a temperature-controlled microscope stage (HC). For the measurement of blackbody reference spectra, the heated sample cavity (HC) is replaced with a reference blackbody cavity with W1 mounted to the cavity opening. Reflection of sample and silver mirror reference is measured outside of the HC to avoid reflections from window W1, while the frequency shift is monitored inside HC. The numerical aperture (NA) of illumination is controlled with irises AS and FS, while in emission the NA and the area from which light is picked up, are controlled by irises CI and OI.

spectrum, see Fig. 3. The depth of the resonance is determined mainly by the thickness of the top gold layer which, to a lesser extent, also modifies the resonance position, as the reflection phase ϕ_r , top depends on the thickness of the top layer. Moreover, the structure is flexible in terms of material choices, allowing for use in a much broader range of both temperatures and wavelengths than presented here.

4. Thermal emission measurements

Thermal emission is measured by heating the sample in a microscope heating stage (Linkam TS-1000) while picking up the generated thermal radiation through a long-working distance objective which is fibre-coupled to a near-infrared spectrometer (OceanOptics, NirSpec), see Fig. 2 for details. For the calculation of the emissivity, it is necessary to divide the thermal emission spectrum by the blackbody spectrum at the same temperature, which simultaneously eliminates the setup dispersion from the resulting emissivity spectrum. The blackbody in use is a high absorptivity cavity-type (Electro-Optical Industries, with a surface extinction specified at 0.97 – 0.99 at wavelengths from 500 nm to 20 μm), and spectra are taken after allowing thermal stabilization for at least 30 min. Temperatures are ramped with 0.5 K/s under both heating and cooling. A quartz window identical to W1 (Fig. 2) is mounted to the reference cavity to guarantee identical optical paths and dispersion. Reflection measurements are referenced against a silver mirror with a reflectivity of at least 97.5 % in the wavelength range investigated (Thorlabs, PF10-03-P01). Frequency shifts occurring during heating are evaluated by measuring the reflection spectra at each temperature point (also comprising thermal emission that unrelated to the reflected light), from which we subtract the generated emission. This procedure allows for the tracking of the shift in resonance frequency, as shown Fig. 4, inset. It can be seen that

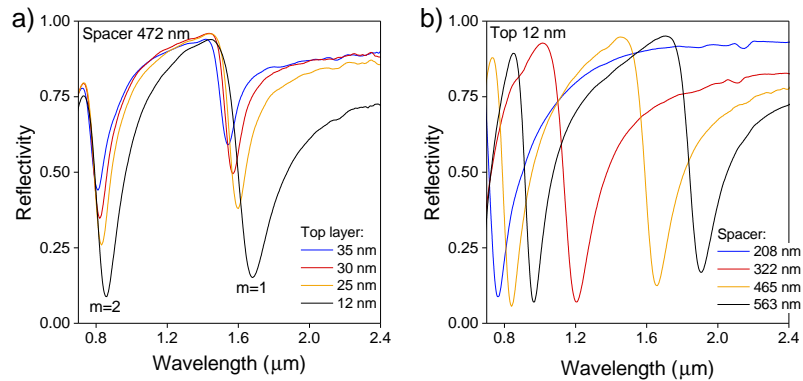


Fig. 3. (a) Dependence of the reflectivity on the top gold layer thickness, for a spacer thickness of 472 nm. (b) Dependence of the reflectivity on spacer layer thickness for a top layer thickness of 12 nm. It is obvious that the emitter offers a high degree of tunability. Variation of the spacer thickness influences mainly on the position of the resonance and, to a lesser extent, also the position of the resonance through modification of the reflection phase ϕ_r , top.

the observed reflectivity wavelength shift corresponds exactly to the wavelength shift observed between peaks in room temperature reflectivity and heated emissivity. It should be noted that ambient thermal emission that is reflected by the sample into the setup is not taken into account; it is negligible at the temperatures investigated here, as is clear from Eq. (1).

Figure 4 shows emission spectra taken at 673, 723 and 748 K from an emitter fabricated with a resonance at 1.72 μm at room temperature. As seen in Fig. 4(a), the emission rises rapidly with increasing temperature, which, assuming temperature-independent optical properties, is wholly attributable to the change of the blackbody spectrum. At 723 K and 748 K the emission from the emitter exhibits a clear peak at the resonance, where the blackbody emission, in contrast, continues to increase. The resulting emissivity ϵ_λ is shown in Fig. 4(b). Clearly, the emissivity closely matches the absorption, approximated as the measured extinction, $1 - R_\lambda$. The observed emissivity peak is somewhat broader than the extinction peak and slightly lower in maximum emissivity. Both broadening and redshift might be explained by material temperature dependent behavior, since it is known the dielectric function ϵ of gold (and other metals) is temperature dependent with the imaginary part of ϵ increasing with increasing temperature, while at the same time, the reflectivity decreases [26–29], leading to a lower Q-factor and broader peak. Furthermore, thermal expansion might explain the red-shift. However, experimental factors could also play a role such as illumination conditions and emission measurement conditions not being perfectly matched (Fig. 2 illustrates such a situation where neither NA or illuminated sample area are matched) or scattering caused by surface roughness which can cause extinction in reflection measurements that is not associated with absorption, but with light being scattered out of the observed solid angle. Consequently, to minimize extinction in reflection measurements arising from scattering, it is necessary to pick up light with the largest NA possible. Thus, the extinction is not exclusively dominated by absorption as assumed by $\epsilon_\lambda = \alpha_\lambda \approx 1 - R_\lambda$. The inset in Fig. 4 shows the temperature dependence of the resonance to be very low, amounting to a maximum shift of the resonance of less than 7 nm at 748 K, when compared to room tem-

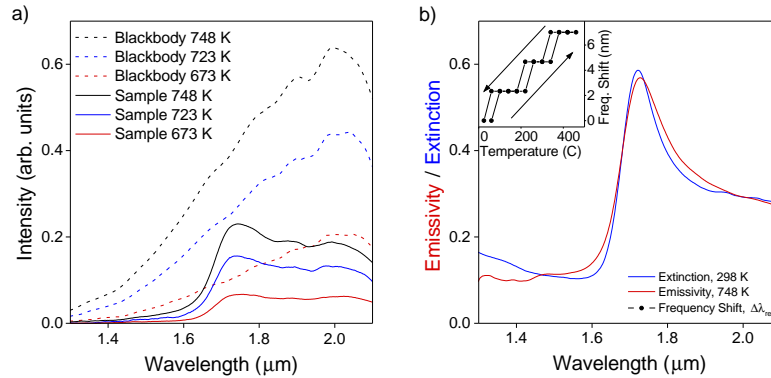


Fig. 4. Thermal emission measurements. (a) Emission from sample (solid) and blackbody (dashed) at temperatures 673, 723 and 748 K, respectively. It should be noted that intensity measurements incorporate the setup dispersion, leading to an apparent peak at 2 μm . (b) Emissivity calculated from spectra in (a) and extinction measurements (estimated as 1-R) showing an excellent match, in agreement with Kirchhoff's reciprocity. Inset: The total frequency shift of the resonance is roughly 6 nm and has a low degree of hysteresis.

perature. The resonance position shows a very low degree of hysteresis, indicating that changes to the sample that have an influence on the emissivity are reversible to a large extent. Note that the initial annealing procedure can cause a more substantial, permanent shift to occur, presumably associated with increases in gold grain size but possibly also related to inter-diffusion of titanium and gold and oxidation of titanium.

5. Thermal stability

Degradation of the structure plays no role for short-term heating procedures at 748 K but starts to set in at even slightly higher temperatures. This degradation cannot be expected from inspection of material properties, with the bulk melting point of all materials being at least several hundred degrees Celsius higher than the temperatures investigated in this context. However, the melting point of finite materials with dimensions on the order of the grain sizes or impure materials, is known to be influenced by melting point depression [30–32], which arises both due to diffusion of impurities and due to the presence of surface lattice-sites. Both effects induce local variations in the lattice energy, causing melting to set in at lower temperatures than for the corresponding bulk material. Furthermore, the phase change occurs gradually over a range of temperatures that corresponds directly to the spread in lattice energies. As a result, temperature instability of the sample sets in well below the bulk melting point of Au. The degradation of the sample under excessive heating is shown in Fig. 5, where samples heated to 823 and 923 K are seen. The temperatures are ramped as in the emission measurements (0.5 K/s), while samples are annealed for 60 minutes. The extent of the damage caused by heating varies heavily, depending on the homogeneity of the layers. For a relatively smooth sample, only the thin top layer is damaged at 823 K (Fig. 5(d)), in marked contrast to samples with considerable surface roughness, in which case all layers are damaged, (Fig. 5(b)). It should be noted that for a combination of sufficiently high temperatures and a high degree of roughness, no equilibrium or metastable state is reached. The effect of further annealing is then to drive further changes to

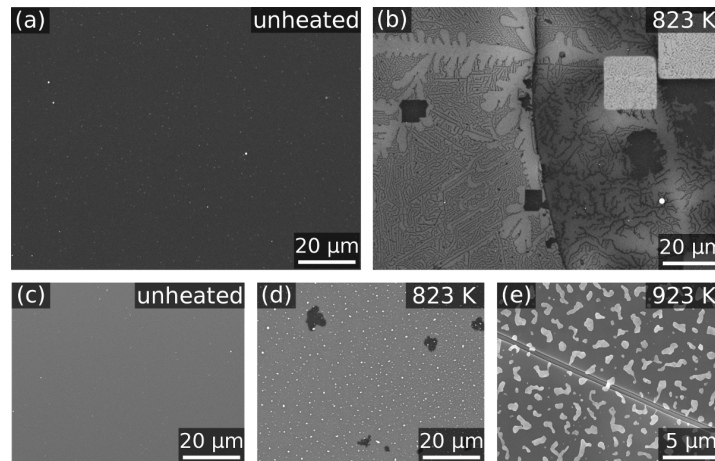


Fig. 5. Scanning electron micrographs of heated samples after cooling. (a)-(b) and (c)-(e) show different sample batches, respectively, highlighting the influence of fabrication imperfections. (a) Sample A before heating. Several imperfections can be seen on the sample surface. (b) Sample A heated to 823 K, showing a complicated multitude of phase changes, cracks in the spacer layer and wrinkling of the bottom gold layer. (c), (d) Heated emitter of a fabrication batch with improved surface roughness. (c) The number of imperfections in the unheated sample are visibly reduced compared to (a). (d) Identical to c, heated to 823 K. This sample shows degradation of the top layer only, which has transformed into distinct particles. (e) Identical sample to (c), heated to 923 K, where the SiO_2 -layer starts to fracture.

structure - this is the case in Fig. 5(b), while samples similar to Figs. 5(c)-5(e) mostly show little to no obvious structural changes after initial degradation has occurred. We anticipate that the presented structure will be further optimized for the TPV use at temperatures given by Wien's Law, by using combinations of refractory materials [33]. This would also eliminate the need for adhesion layers and thus decrease the potential for inter-diffusion and the entailing changes in optical properties, such as increased losses [34, 35], and melting point depression. For use in the mid-infrared, however, no further modifications are necessary; an inspection of Wien's law (Eq. (2)) reveals that α_{\max} lies at a wavelength of $\lambda_{\max} \approx 3.9 \mu\text{m}$ at a working temperature of 748 K.

6. Conclusion

In conclusion, we have demonstrated tunable thermal narrowband emission from a simple, unstructured few-layer structure, exhibiting a resonance at the band gap energy of GaSb. The spectral properties can be modified in terms width, depth and resonance frequency through straightforward variation of fabrication parameters. The emitter is suitable for scaling to large-area fabrication and transferable to other combinations of materials, as the emitter is unstructured and relies only on standard film deposition procedures. Given the thermal stability of the sample, highly efficient emission can be achieved at wavelength of $3.9 \mu\text{m}$, or longer, and owing to the simple physical principles of the resonance, there are large degrees of freedom concerning material combinations and geometry, which can be chosen to suit specific applications.

Acknowledgments

We acknowledge financial support from the Danish Council for Independent Research (the FTP project PlasTPV, contract no. 1335-00104).

Appendix C

Light extinction and scattering from individual and arrayed high-aspect-ratio trenches in metal

PHYSICAL REVIEW B 93, 075413 (2016)

Light extinction and scattering from individual and arrayed high-aspect-ratio trenches in metalsAlexander S. Roberts,¹ Thomas Søndergaard,² Manohar Chirumamilla,² Anders Pors,¹ Jonas Beermann,¹ Kjeld Pedersen,² and Sergey I. Bozhevolnyi¹¹*Centre for Nano Optics, University of Southern Denmark, Campusvej 55, 5230 Odense M, Denmark*²*Department of Physics and Nanotechnology, University of Aalborg, Skjernvej 4, 9220 Aalborg, Denmark*

(Received 23 October 2015; revised manuscript received 15 January 2016; published 4 February 2016)

We investigate the scattering properties of two-dimensional high-aspect-ratio metal trenches acting as resonators for gap-surface plasmons and show that these resonators are highly efficient scatterers of free waves, reaching at resonance in the perfect-conductor limit the unitary dipolar limit for a two-dimensional scatterer. We construct a simple resonator model which predicts the wavelength-dependent extinction, scattering, and absorption cross section of the trench and compare the model findings with full numerical simulations. Both extinction and scattering cross sections are mainly determined by the wavelength and can reach highly supergeometric values. At wavelengths where the metal exhibits near perfect electrical conductor behavior, such trenches lend themselves to be used as self-normalizing scatterers, as their scattering cross section is independent of their geometry and depend only on the resonance wavelength. For real metals with nonzero absorption, efficient monomaterial absorbers and emitters can be fabricated. We extend the analysis to tapering trenches that can be readily fabricated employing common milling or etching techniques and verify by reflection spectroscopy and two-photon luminescence that the resonant behavior of the vertical trenches is preserved.

DOI: [10.1103/PhysRevB.93.075413](https://doi.org/10.1103/PhysRevB.93.075413)**I. INTRODUCTION**

The study of the coupling between electron gas oscillations inherent to metallic surfaces and freely propagating electromagnetic waves forms the basis of the field of plasmonics, and has led to the investigation of numerous novel applied [1–3] and exploratory concepts [4–7]. Plasmonics has been a highly active research area in recent years, especially since the discovery of extraordinary optical transmission by Ebbesen and co-workers [8]. Optical and infrared absorption, scattering, and transmission of corrugation structures in metallic surfaces has been at the center of attention for many years and continues to be the subject of extensive numerical and experimental research [9,10]. One structure of particular interest is the trench with vertical sidewalls and high aspect ratios, in the sense that its depth greatly exceeds its width. This trend is driven, amongst others, by the emergence of fabrication capabilities allowing for the fabrication of trenches with a high degree of precision and with sizes necessary for resonances in the visible and near infrared. Such capabilities enable the use of gratings of various types for sensing [11–13], thermal emission [14,15], etc. While the mechanism has been elucidated from several angles, the scattering strength of an ideal or perfect metallic slit possesses several characteristics that, under certain circumstances, make it an ideal dipolar scatterer for the scattering of freely propagating waves.

In this work, we investigate a high-aspect-ratio trench in terms of its extinction, scattering, and absorption properties. We present experimental, analytical, and numerical investigations and show that narrow-band absorption stems from the coupling of free-space propagating modes to gap-surface plasmon (GSP) modes propagating in the trench. We develop an analytical model predicting the extinction and scattering cross section on the basis of a GSP mode propagating in the trench and being reflected at the top and bottom terminations, while being excited by an incoming plane-wave field. Resonance occurs due to the Fabry-Perot condition that

the round-trip phase accumulation equals an integer multiple of 2π . The developed model shows good correspondence with numerical simulations while being very rapid in terms of computation time, in marked contrast to the full simulations. High-aspect-ratio vertical trenches reach the electric dipolar unitary scattering limit (DUSL) in the perfect-conductor limit at the first-order resonance. For a full theoretical treatment of the maximization of scattering and absorption cross sections, the reader is referred to [16]. Here, we will focus on a vertical trench and a trench with a tapering profile, which is more easily producible employing common milling or etching fabrication techniques.

We thereby build on work by other groups which have previously investigated trenchlike corrugation structures in metals, in either high-aspect-ratio trenches [17,18] or similar configurations [19–23].

II. THEORY

We study a metallic trench with vertical sidewalls, depth d , and width w [Fig. 1(a)] and consider the fundamental GSP mode that can propagate along the trench and reflect at its terminations, forming a simple Fabry-Perot resonator [24].

We assume a strongly subwavelength width $w \ll \lambda_0$, where λ_0 is the vacuum wavelength of the illuminating light. Illumination is at normal incidence by a \hat{x} -polarized plane wave of amplitude E_0 . This geometry is particularly interesting as it supports one antisymmetric GSP mode (with respect to E_y), for which no cutoff in terms of trench width exists.

A. Gap-surface plasmon single-mode model**1. Resonator formalism**

Within the trench, GSPs propagate with a propagation constant β and complex-valued reflection coefficients r_b and r_t at the bottom and top terminations, respectively. In the course of one round trip, the plasmon is subjected to both

ALEXANDER S. ROBERTS *et al.*

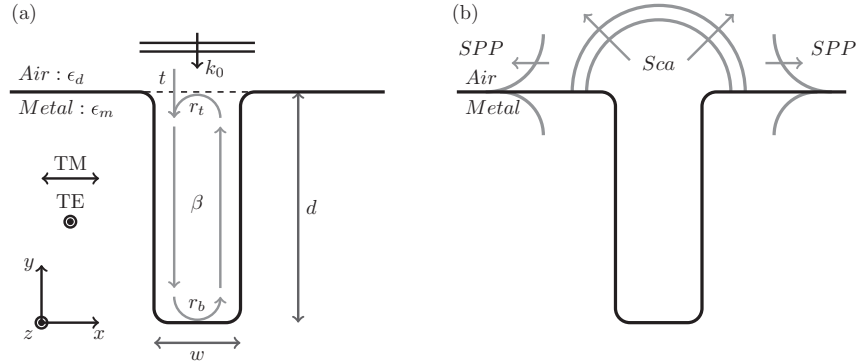
 PHYSICAL REVIEW B **93**, 075413 (2016)


FIG. 1. (a) Schematic of the vertical trench, showing (complex) reflection coefficients and amplitudes as defined in the resonator model. k_0 and β are the wave vectors of the incoming plane wave and the gap-surface plasmon mode supported in the trench, respectively. r_t and r_b are reflection coefficients at the top and bottom terminations, respectively. (b) Definition of the calculated scattering contributions in the GFSI method. The method yields the extinction cross section σ_{ext} , the cross section for scattering to SPPs σ_{spp} , and the cross section for scattering to plane waves σ_{sca} , of which the two latter are indicated in the schematic.

phase accumulation and amplitude attenuation, described by the complex round-trip modulation τ :

$$\tau \equiv r_b r_t e^{2i\beta d}.$$

In steady state, the amplitude of the downward propagating GSP at the open termination of the trench can be written as an infinite geometric series, due to the summation of an infinite number of contributions with increasing powers of τ :

$$E_d = E_0 t (1 + \tau + \tau^2 + \dots) = \frac{E_0 t}{1 - \tau}. \quad (1)$$

Furthermore, at the open termination, the amplitude of the downward-propagating GSP is related to the two incoming fields, that is, the incoming plane wave and the reflected GSP field, both of which contribute to the downward-propagating amplitude with amplitudes tE_0 and $r_t E_u$, respectively. E_d is, therefore, related to these fields by

$$E_d = r_t E_u + t E_0. \quad (2)$$

The amplitude of the excited field in the aperture E_x is given by the sum of the up- and down-going partial amplitudes

$$E_x = E_d + E_u = E_d (1 + \tau/r_t). \quad (3)$$

Equation (3) follows directly from use of Eqs. (1) and (2). Further elementary manipulation of these three identities leads to the desired expression for the norm-square of the field enhancement (FE) in the trench Γ given by the squared norm of the ratio of the field amplitude in the trench E_x to the amplitude of the incoming field E_0 :

$$\Gamma \equiv \left| \frac{E_x}{E_0} \right|^2 = \left| \frac{E_d + E_u}{E_0} \right|^2 = \left| t \frac{1 + \tau/r_t}{1 - \tau} \right|^2. \quad (4)$$

It can be shown (Appendix A) that the radiated and extincted power (P_{sca} and P_{ext}) by a two-dimensional aperture with a constant electrical field E_x , oriented orthogonally across the

gap, is given by

$$P_{\text{sca}} = \frac{k_0 w^2 |E_x|^2}{4\eta_0}, \quad (5a)$$

$$P_{\text{ext}} = \frac{E_0 w}{\eta_0} \text{Re}\{E_x\}, \quad (5b)$$

where $\eta_0 = \sqrt{\mu_0/\epsilon_0}$ is the impedance of free space and w is the width of the trench. Above expressions for the radiated and extincted power enable the calculation of the corresponding cross sections σ_{sca} and σ_{ext} , defined by the ratio of scattered or extincted power to the incident intensity $I = |E_0|^2/2\eta_0$:

$$\sigma_{\text{sca}} = \frac{P_{\text{sca}}}{I} = \frac{k_0 w^2}{2} \left| \frac{E_x}{E_0} \right|^2, \quad (6a)$$

$$\sigma_{\text{ext}} = \frac{P_{\text{ext}}}{I} = 2w \frac{\text{Re}\{E_x\}}{E_0}. \quad (6b)$$

We have now derived the scattering and extinction cross sections, assuming a constant field across the trench opening, in terms of the propagation constant β , transmission and reflection coefficients t , r_b , and r_t , and geometric parameters d and w . The absorption cross section is calculated as $\sigma_{\text{ext}} - \sigma_{\text{sca}}$.

2. Transmission and reflection coefficients

The reflection of the downward-propagating GSP mode being reflected at the closed end of the trench is characterized by the fact the GSP mode in the trench has components along the x direction, predominantly. As a consequence, the reflection coefficients can be approximated well by simple Fresnel theory describing the reflection of a plane wave, with appropriate use of mode parameters for the GSP mode. The reflection coefficient is then given by

$$r_b = \frac{1 - F}{1 + F} \quad \text{with} \quad (7a)$$

$$F = \frac{n_m}{n_{\text{GSP}}} \approx \frac{\sqrt{\epsilon_m}}{\sqrt{\epsilon_d + \frac{2\epsilon_d \sqrt{\epsilon_d - \epsilon_m}}{-k_0 w \epsilon_m}}}, \quad (7b)$$

where n_{GSP} is the effective index for the GSP, for which we use the approximation seen in the denominator of Eq. (7b) [24]. $n_m = \sqrt{\varepsilon_m}$ is the refractive index of the metal, and an air or vacuum gap is assumed with $\varepsilon_d = 1$.

For the reflection at the open termination, we use the reflectivity as derived in Ref. [25] through use of tangential field continuity and energy conservation at the interface:

$$r_t = \frac{1 - G}{1 + G} \quad \text{with} \quad (8a)$$

$$G = \frac{1}{2\pi} \frac{\int_{-\infty}^{\infty} \frac{k_0}{\eta_0 \sqrt{k_0^2 - k_x^2}} [\mathcal{F}\{E_x^{\text{tr}}(x, 0)\}]^2 dk_x}{\int_{-\infty}^{\infty} E_x^{\text{tr}}(x, 0) H_z^{\text{tr}}(x, 0) dx}, \quad (8b)$$

where k_0 and k_x are the scalar values of total and x component of the wave vector, respectively. \mathcal{F} denotes the unitary Fourier transform and $E_x^{\text{tr}}(x, 0)$ and $H_z^{\text{tr}}(x, 0)$ describe the fields across the open trench termination, which are related as $H_z^{\text{tr}}(x, 0) = E_x^{\text{tr}}(x, 0)/\eta_0$. The reflection coefficient is calculated for an assumed constant field across the trench and zero field outside, so that $E_x^{\text{tr}}(x, 0)$ and $H_z^{\text{tr}}(x, 0)$ reduce to rectangular functions.

The transmission coefficient t , governing the transmission of the free-space plane wave to the GSP mode of the trench, is derived in Ref. [26] as

$$t = \left(\frac{2I_1(0) \sqrt{\frac{\varepsilon_0}{\mu_0}}}{\frac{1}{\lambda} \sqrt{\frac{\varepsilon}{\mu_0}} \int_{-\infty}^{\infty} \frac{|I_1(u)|^2}{\sqrt{1-u^2}} du - \int_{-\infty}^{\infty} E_x^{\text{tr}} H_z^{\text{tr}*} dx} \right)^* \quad \text{with} \quad (9a)$$

$$I_1(u) = \int_{-\infty}^{\infty} E_x^{\text{tr}} e^{-ik_0 u x} dx, \quad (9b)$$

where u denotes spatial frequencies and $*$ denotes the complex conjugate. The approximation of the fields as rectangular functions greatly simplifies the calculations outlined in Eqs. (8b)–(9b).

Without going into details of the derivation of Eq. (9a) given in Ref. [26], it should be mentioned that the implicit assumption of zero field at metal surfaces away from the slit is only strictly valid in the perfect conductor limit. It is thus expected that Eq. (9a) will work best for long wavelengths, at which metals approach the perfect conductor limit.

Equation (6a), in conjunction with Eqs. (7a), (8a), and (9a), constitutes a full, closed description of the scattering power of the trench resonator. As will be shown, this fairly simple model accounts accurately for the extinction and scattering behavior of the resonator, provided that the cross section for scattering into surface plasmon polaritons (SPPs) is small. The fields around the top terminations can excite SPPs propagating away from the trench [27], a behavior not accounted for by the model. Furthermore, evanescent modes inside the resonator can lead to behavior that is unaccounted for in this model. We therefore limit the present considerations to trenches that are deep enough to ensure that the evanescent modes at the terminations do not couple significantly, that is, $d \gg w$.

B. Unitary scattering limits in two and three dimensions

1. Unitary scattering limit in three dimensions

When solving the wave equation in spherical coordinates, the scattering of a sphere can be expressed in terms of the expansion coefficients $|a|$ and $|b|$ in the Riccati-Bessel basis as [28]

$$\sigma_{\text{sca}} = \frac{2\pi}{k^2} \sum_{n=1}^{\infty} (2n+1)(|a_n|^2 + |b_n|^2), \quad (10)$$

where a_n and b_n are coefficients for expansion into Riccati-Bessel functions of the first (a_n) and second (b_n) kinds of order n . The outgoing dipolar field is represented by coefficient a_1 , so in an electric dipolar scattering event, only coefficient a_1 representing an outgoing wave can be nonzero. In the limit of $a_1 \rightarrow 1$, one obtains the dipolar unitary scattering limit describing a scattering event in which the scattered power is entirely scattered into the dipolar channel [29]

$$\sigma_{\text{sca}}^{\text{unitary}} = \frac{3\lambda^2}{2\pi}. \quad (11)$$

Equation (11) is thus the unitary scattering cross section for a dipolar scatterer in three dimensions.

2. Unitary scattering limits in two dimensions

A corresponding expression suitable for describing the unitary, dipolar scattering event in two dimensions can be derived by considering the multipole expansion of the scattering cross section in a cylindrical geometry. In this case, two types of polarizations exist, transverse electric (TE) and transverse magnetic (TM). The scattering cross sections for TE and TM incident light may be formulated in terms of expansion coefficients into cylindrical harmonics, as outlined in [28]. Here, we are only interested in the TM case:

$$\sigma_{\text{sca}}^{\text{TM}} = \frac{4}{k} \left[|a_0|^2 + 2 \sum_{n=1}^{\infty} (|a_n|^2 + |b_n|^2) \right], \quad (12)$$

which in the unitary limit gives

$$\sigma_{\text{sca}}^{\text{TM, unitary}} = \frac{4}{\pi} \lambda. \quad (13)$$

This cross section poses the limit for a dipolar, unitary scattering process, thereby providing the maximum scattering cross section for a lossless scatterer that exhibits purely dipolar behavior. It should be noted that this is not a fundamental upper limit on the total scattering cross section, merely the upper limit for the dipolar scattering channel. Scattering contributions from several channels can increase the cross section arbitrarily (see Ref. [30]).

In the absence of all resonator losses apart from reradiation to the far field, the extincted and the scattered power must be identical. This situation is realized for a trench in a perfect electrical conductor (PEC) material (note that a lossless metal with finite $|\varepsilon|$ still supports SPPs capable of transporting energy away from the trench). It follows directly from the equality of the expressions for σ_{sca} and σ_{ext} that the trench, at strict resonance in the PEC limit, scatters with a cross section

ALEXANDER S. ROBERTS *et al.*

 PHYSICAL REVIEW B **93**, 075413 (2016)

exactly at the DUSL:

$$\sigma_{\text{sca,pec}} = \frac{\sigma_{\text{ext,PEC}}^2}{\sigma_{\text{sca,ext}}} = \frac{\left(2w \frac{\text{Re}(E_x)}{E_0}\right)^2}{\frac{\pi w^2}{\lambda_0} \left|\frac{E_x}{E_0}\right|^2} = \frac{4}{\pi} \lambda_0. \quad (14)$$

In the visible regime, losses are unavoidable at room temperatures. However, the trenches retain substantial scattering power, even with losses.

III. METHODS

We employ two different numerical methods for the calculation of the optical properties of a single trench and a one-dimensional trench array, respectively. All optical properties are calculated using linear interpolations on the data in Ref. [31]. The trench under consideration is of depth d , width w [Fig. 2(a)], and, in the periodic case, period p .

A. Numerical methods

We employ Green's function surface integral method (GFSI) to calculate cross sections for total extinction σ_{ext} , scattering to SPPs propagating away from the trench σ_{SPP} , and scattering to freely propagating light σ_{sca} for illumination at normal incidence. The geometry is fully defined in Fig. 2 for both tapered and vertical side walls, while SPP and free-wave scattering contributions are indicated in Fig. 1(b). A corner rounding radius (s_r) of 4 nm is used in all calculations. For details on the GFSI method, the reader is referred to Appendix B and Refs. [32–34]. The total extinction cross section is defined as the power reduction in the specularly reflected beam due to the trench, normalized to the intensity of the incident beam. In the GFSI simulations, since all scattering contributions are taken into account, any energy loss is associated with material absorption in the trench. As calculations are performed in two dimensions, the validity of the obtained results is limited to cases in which the trench dimension in the z direction is infinite or very large compared to other trench dimensions. We investigate the structure in transverse magnetic (TM) and transverse-electric polarization

(TE) with the incident wave vector being antiparallel with the y axis (Fig. 1).

For investigations of arrays of trenches, we implement finite-element simulations in the numerical simulations software COMSOL. The trench geometry is identical to the GFSI simulations, however, with exact plane-wave excitation and Floquet-periodic boundary condition in the x direction. Diffraction orders are handled with additional ports, allowing for the simulation of angled incidence at arbitrary periodicity.

Perfectly periodic arrays of trenches may in some cases support spoof plasmons [35,36], but these cannot be excited by illuminating the surface with a source placed at far-field distances from the surface, which is similar to ordinary SPPs at flat metal surfaces not being excited by such a source. Spoof plasmons are thus not considered here.

B. Fabrication

The investigated trenches are milled into a monocrystalline (100)-gold crystal using focused gallium ion beam milling (FIB). We optimize the tapering trenches for the most vertical side walls while still retaining a nonvanishing radius of curvature at the bottom termination of the trench. Achieving a nonzero width at the bottom termination is crucial to obtain appreciable reflection, i.e., $|r_b| \gg 0$. Conversely, a vanishing radius of curvature will lead to adiabatic focusing of the trench mode, with increasing losses as the plasmon approaches the termination [37]. However, at widths at which the mode is GSP like, the feature sizes approach the resolution of the milling instrument. Hence, the most ideal achievable trenches still divert significantly from vertical walls as convolution with the resolution function and material redeposition alter the desired trench shape and lead to a self-tapering trench profile [38,39]. It should be noted that with the available milling equipment, trenches with such a geometry were not obtainable with smooth side walls. This motivated the use of a gold monocrystal, which is known to improve the smoothness of FIB-milled structures, as well as increase the scattering intensity of resonant structures [40,41].

C. Experimental methods

1. Reflection spectroscopy

We measure linear reflection spectra of the fabricated samples with an Olympus BX-51 microscope and a 50 \times -magnifying objective with a numerical aperture of 0.75. Linear reflection spectroscopy on single trenches is performed with an Olympus IX-71 microscope and a 50 \times -magnifying objective with numerical aperture of 0.5. In both cases we illuminate with a white laser (NKT Photonic, SuperK) at normal incidence. Since this type of laser gives close to circularly polarized light at the power used (roughly 1 W output power), a Glan-Taylor polarizer is used to ensure transverse incident polarization in all discussed measurements. The laser is heavily attenuated with reflective neutral density filters before reaching the microscope to prevent heat damage to the sample and saturation of the fiber-coupled spectrometer. Several spectra taken in succession are used to verify that no observable heat damage is caused. It should be pointed out that the used gold sample is extremely efficient at dissipating heat,

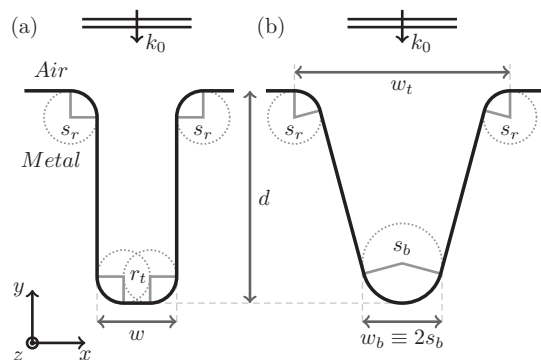


FIG. 2. Definition of the geometry of the vertical trench (a) and tapered trench (b) considered in the numerical calculations. Both vertical and tapering trenches consist entirely of circular sectors and tangentially connected lines. Rounding radii s_r are unchanged at 4 nm. Rotations around z and x define angles θ and ϕ , respectively.

due to its monocrystalline nature and large thickness of 1 mm. Reference spectra are taken on the plane sample surface.

2. Scanning two-photon luminescence microscopy

One well-established experimental technique for the evaluation of field enhancement in nanostructures is two-photon luminescence (TPL) from metals, which was earlier described [42,43] with spatially resolved TPL studies [44,45] and near-field imaging [46] used for characterization of local FEs. We have recently employed diffraction-limited TPL scanning microscopy for direct estimations, and detailed mapping, of FE at the bottom of V grooves [47] and one-dimensional plasmonic black gold [48], both revealing very selective polarization properties of excitation and TPL emission at the narrow groove bottom.

Our experimental setup for TPL microscopy is essentially the same as that described in detail previously [49]. It consists of a scanning optical microscope in reflection geometry built on the base of a commercial microscope and a computer-controlled two-dimensional (2D) piezoelectric translation stage. The linearly polarized light from a mode-locked pulsed (pulse duration 200 fs, repetition rate 80 MHz) Ti:sapphire laser ($\lambda = 740$ nm, $\delta\lambda \approx 10$ nm) is used for sample

illumination at the fundamental harmonic (FH) frequency. The illumination power is kept constant at 5 mW and focused with a Mitutoyo infinity-corrected long working distance $\times 100$ objective (N.A. = 0.7) at normal incidence. The TPL radiation generated in reflection and the reflected FH beam are collected with the same objective, separated by a wavelength selective beam splitter, directed through appropriate filters and detected with two photomultiplier tubes, the tube for TPL photons being connected with a photon counter obtaining usually less than 10 dark counts per seconds. The integration time for all discussed measurements is 100 ms.

IV. RESULTS

A. Model and numerical results

1. Extinction and scattering of a single trench

Cross-section spectra for total extinction, SPP scattering, and scattering to freely propagating waves for a two-dimensional vertical trench with the geometry defined above [Fig. 2(a)] are obtained using the GFSI method [Figs. 3(a), 3(b), 3(d), and 3(e)]. The considered trench has width $w = 56$ nm and depth $d = 640$ nm. These parameters correspond to those used for trench arrays with a period of

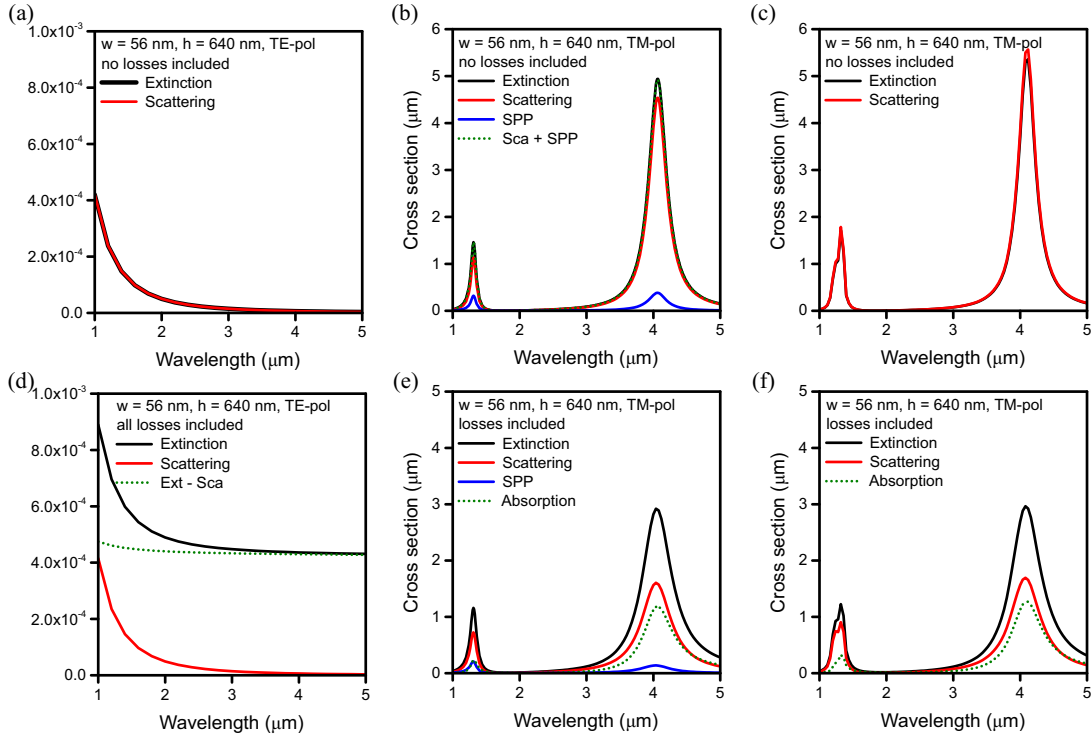


FIG. 3. Comparison between the analytical model and GFSI simulations of an individual trench of width 56 nm and 640 nm depth under normally incident illumination. (a), (d) Show spectra obtained by GFSI simulations for TE-polarized light for omitted and included losses, respectively. (b), (e) Show corresponding spectra for TM polarization while (c) and (f) show spectra obtained by use of the GSP model (for TM polarization). Linear interpolation on the optical data from [31] has been used in all six cases, while neglected losses have been implemented by setting the imaginary part of the dielectric function to zero.

ALEXANDER S. ROBERTS *et al.*PHYSICAL REVIEW B **93**, 075413 (2016)

2.472 μm in Ref. [10]. Spectra for TE- and TM-polarized illumination are shown, with and without material losses, respectively. We implement omitted losses by setting the imaginary part of the dielectric constant to zero.

The cross sections for TE-polarized light [Figs. 3(a) and 3(d)] show no resonance and are roughly four orders of magnitude smaller than the corresponding cross sections for TM-polarized light [Figs. 3(b) and 3(e)]. Since TE-polarized light can excite neither propagating SPPs nor modes localized to the resonator, it acts merely as a highly subwavelength, nonresonant surface roughness with correspondingly low cross sections. A slight decrease in the cross section for increasing wavelengths is expected as the disparity between wavelength and trench dimensions becomes larger.

In the lossless case with TM-polarized illumination [Fig. 3(b)], the sum of σ_{SPP} and σ_{sca} is plotted. The correspondence between the total extinction and the sum of scattering and SPP contribution is very good. Since, without Ohmic losses in the metal, there are no other loss channels, this behavior is expected from a physical point of view. Nonetheless, the correspondence indicates a good quality of the partition of the total cross section into parts responsible for scattering into SPPs and out-of-plane propagating waves. It is immediately apparent that σ_{sca} and σ_{ext} have values that exceed the width of the trench substantially (values of 4.4 and 4.9 μm , by factors of 79 and 87, respectively). While the cross section for the excitation of SPP is significantly lower at 0.37 μm , the trench retains a supergeometric cross section of almost 7 w .

The extinction spectra for the lossy trench, under TM-polarized illumination [Fig. 3(e)], show that material losses reduce the scattering cross section to roughly one-third of the DUSL, or $\sigma_{\text{sca}} = 1.6 \mu\text{m}$ at a wavelength of 4.04 μm . In other words, the GSP trench is a highly efficient scatterer, with a scattering cross section 28 times larger than its geometrical width. The cross sections for SPP excitation amount to 0.37 μm (lossless) and 0.14 μm (lossy). These results encourage the use of vertical trench scatterers as an alternative to scatterers deposited onto a metallic substrate, providing good geometric scattering enhancements for scattering of plane waves to both surface plasmon polaritons and free waves.

The analytical model is used to calculate extinction, scattering, and absorption cross sections for identical trenches ($w = 56 \text{ nm}$ and $h = 640 \text{ nm}$), for lossless and lossy gold [Figs. 3(c) and 3(f)]. Considering first the lossless case, it is apparent that, at strict resonance, the scattering cross section exceeds the extinction cross section. This is presumably due to the different sets of approximations on which the calculations of σ_{ext} and σ_{sca} are based (cf. Appendix A). Specifically, the assumption of a point dipole emitter in Eq. (A4) does not enter in the calculation of the extinction cross section. Nonetheless, the model gives very good correspondence in terms of resonance wavelength and satisfactory correspondence in terms of scattering and extinction cross sections at resonance, when compared to GFSI simulations of the same trench [Figs. 3(b) and 3(c)]. It is seen that the model also reliably predicts the second-order resonance of the trench. The asymmetric shape of the second-order resonance around 1.3 μm is due a kink in the optical data [31] to which the model is significantly more sensitive than the GFSI calculation.

When including losses, the correspondence between model and GFSI becomes even more pronounced, and extinction, scattering, and absorption are predicted with high accuracy [Figs. 3(e) and 3(f)]. While this is only possible as long as the SPP cross section is small, it is further facilitated by the fact that the metal at a wavelength of 4 μm behaves close to the PEC limit, which, as pointed out above, enters the model in the form of field-free metals (e.g., in the derivation of t). In the following, we will compare the model predictions to GFSI simulation over a wider range of wavelengths (and material properties) to clarify in which regimes the model is valid.

2. Model and numerical predictions of scattering of a metallic trench

In the following, we compare results obtained with the analytical model with GFSI results, focusing on the magnitude of the scattering to clarify the conditions under which one can expect σ_{sca} to approach or reach the DUSL from a vertical trench. While the GFSI method yields the more precise results, the model allows for an investigation of the degree to which an isolated GSP mode is responsible for the scattering predicted.

We calculate a comparison between scattering cross section obtained by the analytical GSP model [Eq. (6a)] and the GFSI method, for 40-nm-wide trenches and depths of 100, 200, 300, 400, 500, and 600 nm, corresponding to resonances ranging from approximately 1 to 4 μm [Fig. 4(a)]. Clearly, the resonance wavelength is well predicted, albeit with an approximate red-shift of 45 nm for all resonances. This

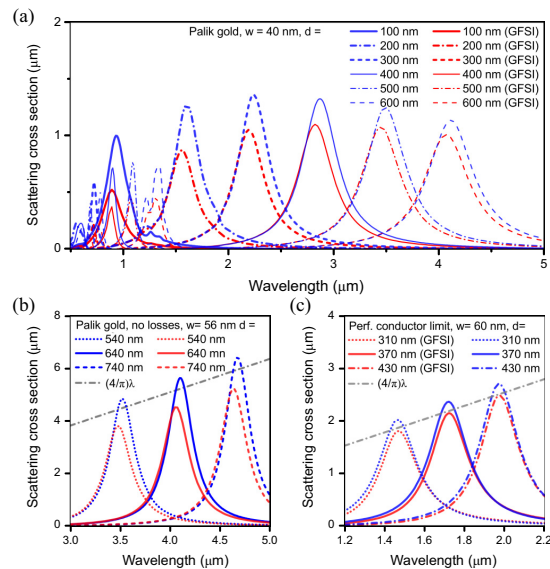


FIG. 4. Comparison between scattering to freely propagating waves spectra obtained from the resonator model (blue curves) and the GFSI method (red curves). (a) Scattering spectra for Palik gold, in the near infrared. (b) Comparison of the unitary scattering limit with scattering spectra obtained for a (Palik) gold trench with neglected losses, i.e., $\text{Im}(\epsilon) = 0$. (c) Scattering spectra for a trench in the perfect conductor limit $\epsilon \rightarrow -\infty$.

behavior is most likely due to the reflection phase of the GSP at the bottom of the trench $\arg(r_b)$ being different from the Fresnel phase by a few percent. The accuracy of the model in terms of the value of the scattering cross section is less pronounced at short wavelengths, where the model increasingly overestimates the scattering cross section σ_{sca} . However, for resonances at longer wavelengths, the correspondence between model and full GFSI simulation is satisfying with a mismatch of only a few percent. This trend can be explained by the fact that the SPP cross section is comparatively large at short wavelengths (not shown). Since SPPs pose an additional loss channel to the resonator, it reduces the amplitude available for scattering to free waves [Eq. (5a)]. Therefore, the field amplitude is overestimated, leading, in turn, to an overestimation of the scattering cross section σ_{sca} . Furthermore, the assumptions for which the transmission t is derived hold poorly at short wavelengths.

For the lossless resonator [Fig. 4(b)], two points are worth noticing. First, the model rather accurately matches GFSI results to within 60 nm in wavelength. Second, despite being less accurate in terms of the size of the scattering cross section, it does correctly predict a strongly scattering trench with a cross section almost two orders of magnitude larger than the width. In fact, the model predicts a cross section slightly above the unitary limit at $4\lambda/\pi$ for all three resonances.

Moving onto the perfect conductor limit ($\epsilon = -10^9$ is used in the model) for which three resonances are shown in Fig. 4(c), the scattering is predicted by the exact calculations to lie perfectly at the DUSL. Since the effective index of the mode is now equal to one, the resonances are strongly blue-shifted, due to a reduced round-trip phase accumulation. The resonances for the perfect conductor resonator are extremely well reproduced by the GSP model. Since the highly efficient scattering is derived purely from the idealized GSP field at the opening of the trench, one can draw the conclusion that an aperture supporting a GSP mode is an ideal choice for maximizing the dipolar scattering cross section from a resonator.

We now simulate a lossless, vertical trench with metallic properties (ϵ_m entirely real and negative) approaching the perfect electrical conductor (PEC) limit, to investigate closer the trench behavior in the limit in which no SPPs are launched (Fig. 5). Since a change in the dielectric function leads to a change in the resonance wavelength, the trench depth is adjusted to keep the resonances at (roughly) unchanging wavelengths. For a trench in an $\epsilon = -10$ material, σ_{SPP} is comparable to the scattering cross section σ_{sca} , amounting to 17 widths, or 680 nm. It is clear that the rise in σ_{sca} with $|\epsilon|$ is not fully compensated by a corresponding decrease in σ_{SPP} [Figs. 5(a) and 5(c)], wherefore an increased overall extinction is observed [Fig. 5(b)]. Most interestingly, however, the scattering cross section increases to the unitary limit when the metal is near the PEC limit. At resonance ($\lambda_0 = 1620$ nm), the scattering cross section is 2080 nm compared to the DUSL of $4\lambda/\pi = 2070$ nm. Scattering near the DUSL is seen for a dielectric function of $\epsilon = -200$ or greater (in magnitude). This range of dielectric functions is available for gold at wavelengths $2 \mu\text{m}$ and longer. However, as has been seen in Fig. 4(a), the scattering is also limited by propagation losses of the GSP mode. The introduction of losses leads to a red-shift

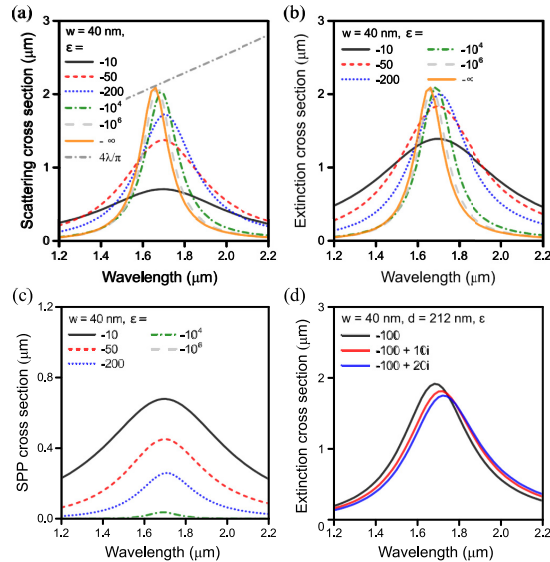


FIG. 5. Cross sections for scattering to (a) freely propagating waves, (b) total extinction, and (c) scattering to SPPs for vertical trenches of width 40 nm, indicated depth h , and ideal metallic properties approaching the perfect electrical conductor limit, i.e., $\epsilon \rightarrow -\infty$. The depths of the trenches have been adjusted to keep the resonance roughly stationary and allow for direct comparison. The depths are 84 ($\epsilon = -10$), 178, 246, 350, 370, and 370 nm (PEC) for decreasing dielectric values. In the PEC limit, SPP excitation is suppressed and the scattering cross section reaches the unitary limit. (d) Shows the influence of introduced losses.

and slight broadening of the resonance while lowering the maximum extinction cross section [Fig. 5(d)].

B. Focused ion-beam milled gold trenches

We have fabricated single trenches and arrays of trenches with a period of 600 nm into a monocrystalline gold sample, as described under Methods. Due to the inherently self-tapering profile of narrow FIB-milled features, ideal vertical trenches are not attainable using this procedure. For this reason, the produced trenches have a tapered profile, which we numerically approximate by a linearly tapering geometry [Fig. 2(b)]. The defined trench geometry is comprised of linear and circular sections, merged into a continuous, smooth curve. The trench is thus fully characterized by its top width w_t , a bottom width w_b , and depth d . We investigate eight different trenches (and arrays), all with top width 200 nm and with depths ranging from 200 to 390 nm [Fig. 6(a)].

1. Extinction analysis

Reflectance spectra from fabricated trench arrays are measured with TM-polarized illumination at normal incidence [Fig. 6(b)]. The resonances lie at wavelengths from 1.1 to 1.6 μm with a clear red-shift of the resonance with increasing depth and a distinct line shape with nearly linear slopes. It is seen that the strength of the resonance as judged by the dip

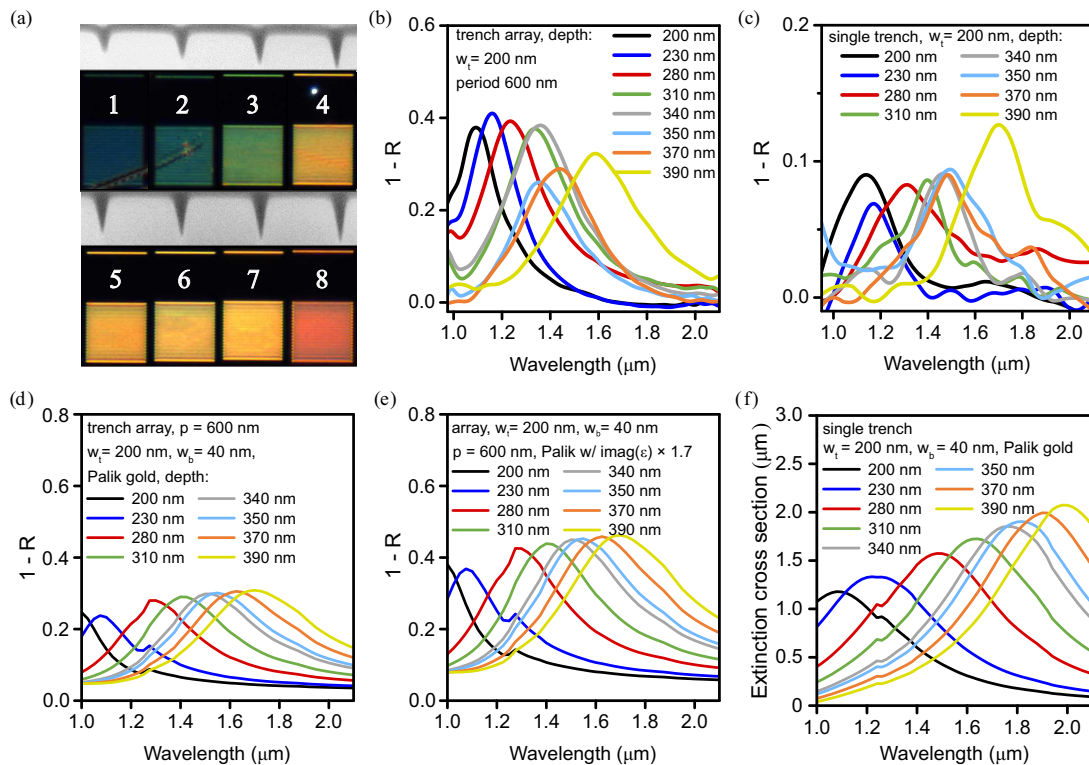
ALEXANDER S. ROBERTS *et al.*PHYSICAL REVIEW B **93**, 075413 (2016)

FIG. 6. (a) SEM imaged cross sections of single trenches of increasing depth in a gold monocrystal, obtained by milling away a solid area and dark field microscopy images, showing the scattering of single and arrayed trenches in the visible, due to the second-order resonance. Trench depths: 1: 200 nm, 2: 230 nm, 3: 280 nm, 4: 310 nm, 5: 340 nm, 6: 350 nm, 7: 370 nm, 8: 390 nm. (b) Experimental extinction spectra of first-order resonances of FIB-milled, tapered trench arrays with a top width $w_t = 200$ nm for TM polarization. (c) Experimental single trench extinction spectra for TM polarization. (d) FEM extinction spectra of tapered trenches with $w_t = 200$ nm, $w_b = 40$ nm, and period $p = 600$ nm for a TM-polarized, normal incidence plane wave. (e) FEM simulations of $w_t = 200$ nm, $w_b = 40$ nm, $p = 600$ nm trench arrays with the imaginary part of the dielectric function increased by a factor of 1.7, leading to an improved agreement with the measured spectra. (f) GFSI simulations of single grooves with $w_t = 200$ nm and $w_b = 40$ nm.

in reflectance (i.e., a peak in $1-R$) decreases with increasing resonance wavelength.

Reflectance measurements of single trenches for TM polarization and a spot size of roughly $3.0 \mu\text{m}$ are obtained [Fig. 6(c)]. Clear resonances ranging from 1.15 to $1.7 \mu\text{m}$ are seen for all trench depths and exhibit a red-shift with increasing depth and an accompanying slight increase in the reflectance dip: all trenches cause a reduction in reflection close to 0.1. This is in contrast to the tendency seen for trench arrays where the reflectance dip decreases with increasing wavelength. Finally, comparing single and arrayed trenches, the resonance wavelength of trench arrays is blue-shifted compared to the single trenches of corresponding depths. It should be noted that the measured reflectance cannot be related exclusively to either absorption or extinction cross section. This can be understood by considering the definitions of extinction cross section (power removed from specular reflection of plane wave, normalized to incident power) and absorption cross section (scattered power for incident plane wave normalized to incident power). It is clear from our measurements with

intermediate numerical apertures (0.7 and 0.9) that neither of these conditions are fulfilled.

Using FEM simulation, we calculate reflectance spectra for periodic trench arrays with geometrical parameters corresponding to the parameters measured from the SEM scans [Fig. 6(a)] and an array period of $p = 600$ nm for gold with optical properties as described by Palik [Fig. 6(d)], and with the imaginary part of the dielectric function increased by a factor of 1.7. While the use of a gold monocrystal eliminates conduction losses associated with grain boundaries, due to the FIB-milling process, damage occurs to the gold lattice, in addition to Ga^+ -ion implantation. Moreover, the presence of the surface inherently increases the electron scattering rate beyond the bulk rate. Both effects increase the optical losses of the gold comprising the trench resonators. We aim to take these effects into account by increasing the imaginary part of the gold permittivity until the best correspondence is reached. This is the case for a factor of 1.7 [Fig. 6(e)]. For thermally evaporated gold, where the scattering on grain boundaries additionally is of importance, values of 3–4 yield

good correspondence [50–52]. It is worth noticing that the observed Q factor of the trenches is actually higher than predicted, which could indicate differences between real and assumed tapering geometries.

Extinction cross-section spectra of single tapered trenches with the measured depths and with the geometry indicated in Fig. 2(b) are calculated using the GFSI method [Fig. 6(f)]. Compared to vertical trenches, the extinction cross section at resonance is reduced by the tapering profile, as well as being subject to considerable broadening. These changes are expected since the GSP mode is reflected less efficiently by a wider top termination, leading to a lower Q factor and, thereby, a broader resonance. The extinction cross section scales almost one-to-one with the wavelength.

The resonance wavelength of the simulations for arrayed trenches shows reasonable correspondence with measurements, for both simulations with altered and unaltered Palik gold. However, this correspondence does not apply for the strength of the reflectance dip, with opposite trends emerging for simulation and measurement. Nonetheless, the overall level can be seen to match for simulations in which above-mentioned alterations to take into account increased losses have been included. Comparing simulations of trench arrays and single trenches, it is obvious that the resonance of single trenches is red-shifted when compared to trench arrays. This behavior is also seen clearly in the measurements when comparing trench arrays and single trench resonances [Figs. 6(b) and 6(c)]. The coupling of plasmonic modes with diffraction orders leads to surface-lattice resonances (see Refs. [53–55]) which have asymmetric line shapes with pronounced (and loss-independent) diffraction features.

The resonance wavelength is somewhat sensitive to the array period, even for periods below the wavelength, where diffraction to free-space waves does not take place. We exemplify this by a goldlike metal with decreasing losses for period of 600 nm in Fig. 7(a) and a period of 1000 nm in Fig. 7(b). In the latter case, the trench resonance is seen at $1.7 \mu\text{m}$, with diffraction orders appearing at $p = m\lambda$ for integer m at normal incidence. In both cases, the line shapes are asymmetric due to the coupling with the first diffraction order. It is furthermore seen that the resonance red-shifts with increasing period and the trenches in consequence become increasingly isolated and, therefore, closer to their single isolated behavior. Finally, the extinction can be tuned by appropriate choice of periodicity, making unity absorption attainable even for very low single trench losses. However, as is seen in the insets, a larger period gives a stronger angular dependence of the extinction at resonance. A reflectivity color map of the λ - p parameter space shows the full evolution of the spectrum for increasing periods [Fig. 7(c)]. A corresponding plot for a vertical trench [Fig. 7(d)] highlights that the vertical trench array possesses narrower resonances and is influenced to a lesser extent by diffraction coupling.

2. TPL analysis

An indication of the validity of the scattering mechanism outlined in the theory, by which the scattering power is directly related to the intensity enhancement Γ , as indicated by Eq. (5a), can be obtained by measuring the TPL signal from the trenches

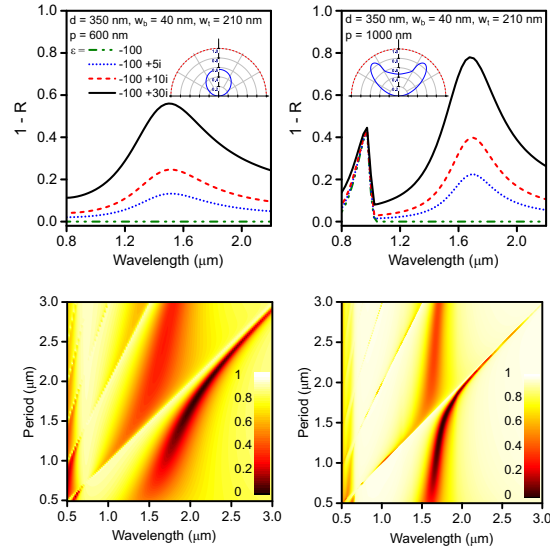


FIG. 7. Spectra of $1 - R$ of tapered trenches with a top width of 210 nm, bottom width 40 nm, and depth 350 nm, indicating the influence of losses at periodicities of (a) 600 nm and (b) 1000 nm. Insets: $1 - R$ dependence on the angle of incidence for in-plane angle for the $\epsilon = -100 + 30i$ material at a wavelength of $1.5 \mu\text{m}$. As an aid to the eye, unity is indicated with a red line. (c) Color map of the reflectivity R of tapered trenches for normal incidence, showing the interplay between the plasmonic mode and the diffraction orders at different wavelengths and periods. The trench geometry is identical to (a). (d) Identical to (c), but with a vertical trench of width 40 nm.

and observing the degree to which it is proportional to the scattering power. According to previous characterizations of narrow grooves [47,48], the TPL mainly originates from the bottom of the trench where the only emission channel is through GSPs.

Under TM-polarized illumination, the intensity enhancement Γ and scattering power show good correspondence. We interpret this as an indication that tapered trenches, while being resonators of lower quality in terms of Q factors, still retain the scattering mechanism of the vertical trench, where excitation of a single GSP mode leads to reradiation into the far field.

The TPL signal, the intensity enhancement, and the scattering power is obtained at 740 nm, which is the excitation wavelength, or fundamental harmonic (FH), of the TPL measurement (Fig. 8). The intensity enhancement Γ and the field enhancement are calculated by the procedure outlined in [56–58], through the relation

$$\Gamma = FE^2 = \left(\frac{\text{TPL}_{\text{trench}} \langle P_{\text{ref}} \rangle^2 A_{\text{ref}}}{\text{TPL}_{\text{ref}} \langle P_{\text{trench}} \rangle^2 A_{\text{trench}}} \right)^{1/2}, \quad (15)$$

where TPL is the observed TPL signal, $\langle P \rangle$ is the (time-averaged) illumination power, and A is the area from which the TPL signal stems. While there is certainly some degree of freedom in the choice of A_{trench} , we are interested in observing a common trend between the intensity enhancement Γ and the scattering power divided by the wavelength, as opposed

ALEXANDER S. ROBERTS *et al.*

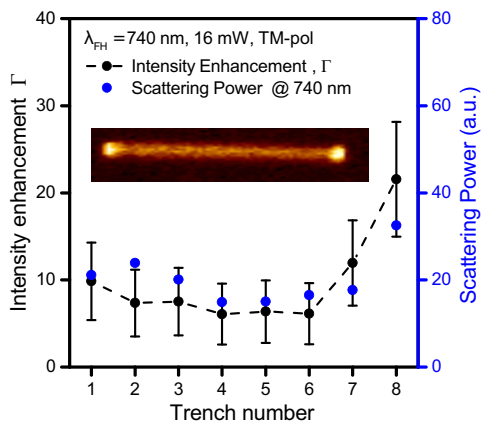
 PHYSICAL REVIEW B **93**, 075413 (2016)


FIG. 8. Intensity enhancement (black dots), calculated from TPL enhancements [Eq. (15)] for an assumed width of 100 nm, and dark-field signal at 740 nm (blue circles). As predicted by the simple model, field enhancement and scattering power follow the same trend. Inset: TPL image of a $14 \times 3 \mu\text{m}^2$ area containing trench 1. (Trench depths: 1: 200 nm, 2: 230 nm, 3: 280 nm, 4: 310 nm, 5: 340 nm, 6: 350 nm, 7: 370 nm, 8: 390 nm.)

to the numerical value of Γ . We estimate that the TPL stems from a 100-nm-wide area and that the beam is tightly focused. A typical TPL image obtained for the 200-nm-deep trench is seen in the inset of Fig. 8. All the TPL images of the different depths obtained at 740 nm appear similar, but the strength of the TPL signal, the intensity enhancement, and the scattering power significantly depend on the trench depth (Fig. 8).

V. CONCLUSION

In conclusion, we have presented a simple resonator model based on gap surface plasmons, which is capable of accurately predicting the extinction, scattering, and absorption cross sections of a high-aspect-ratio metallic trench. A Green's function surface integral method has been presented and used to verify the model findings and identify that mainly SPP excitation at short wavelength is the main reason for deviation from rigorous theory. We have shown that such trenches can exhibit scattering and extinction cross section that are highly supergeometric and that the two-dimensional unitary scattering limit is reached for metals near the perfect conductor limit. The possibility of highly enhanced extinction cross section encourages the utilization of trench arrays for strong, wavelength selective absorption or thermal emission from a metallic surface. We expand the considerations to tapering trench geometries that are more easily attainable with widespread FIB equipment and fabricate such tapered trenches into a monocrystalline gold substrate. It is verified by reflection spectroscopy that strong resonances exist in tapered trenches and we show, by two-photon luminescence measurements, that tapered trenches exhibit strong field enhancements. Strongly supergeometric cross sections are numerically shown to exist for these trenches. The influence of increasing losses and periodicity is investigated by numerical simulations.

ACKNOWLEDGMENT

We acknowledge financial support from the Danish Council for Independent Research (the FTP project PlasTPV, Contract No. 1335-00104).

APPENDIX A: RADIATION FROM A ONE-DIMENSIONAL APERTURE

In this appendix, we derive expressions for the power extinguished and scattered by a subwavelength-wide trench in a PEC film. In principle, these two quantities are equivalent for the PEC case, but for real metals, featuring a complex permittivity with a large negative real part, the extinction also includes the power lost to Ohmic heating. The configuration is depicted in Fig. 1, with the incident light propagating along the $-y$ axis and being TM polarized. The metal interface is assumed to be at $y = 0$, while the surrounding medium is chosen to be air. It is evident that for $w \ll \lambda$ and far away from any trench resonance, the electromagnetic field in the upper half-space can be approximated by the incident and specularly reflected wave, hereby giving rise to the standing-wave pattern

$$E_x^{(+)} = -2i E_0 \sin(k_0 y), \quad H_z^{(+)} = 2E_0/\eta_0 \cos(k_0 y), \quad (\text{A1})$$

where E_0 is a real-valued positive constant representing the amplitude of the incident wave, k_0 is the free-space wave number, and η_0 is the vacuum impedance. We note that it is the above field that can be considered as the driving field when exciting trench resonances. Moreover, it is clear that $E_x^{(+)} = 0$ and $H_z^{(+)} = 2E_0/\eta_0$ at the metal boundary ($y = 0$). Since extinction is related to the interference between the driving and scattered fields, the power extinguished by the trench can, in general, be written as [28]

$$P_{\text{ext}} = -\frac{1}{2} \int_{-w/2}^{w/2} \text{Re}\{\mathbf{E}^{(+)} \times \mathbf{H}^{\text{sc},*} + \mathbf{E}^{\text{sc}} \times \mathbf{H}^{(+),*}\} \cdot \hat{\mathbf{y}} dx, \quad (\text{A2})$$

where $(\mathbf{E}^{\text{sc}}, \mathbf{H}^{\text{sc}})$ are the scattered fields evaluated at the trench aperture, and $*$ means complex conjugate. The above expression can be easily simplified, yielding

$$P_{\text{ext}} = \frac{E_0 w}{\eta_0} \text{Re}\{\langle E_x \rangle\}. \quad (\text{A3})$$

Here, $\langle \dots \rangle$ means average value, and we have used the fact that the total electric field at the trench aperture $E_x = E_x^{\text{sc}}$. It should be noted that in the resonator model presented in the main text, E_x is assumed constant across the aperture and, hence, also represents the average value. Furthermore, it is important to realize that Eq. (A3) implies that $\text{Re}\{\langle E_x \rangle\}$ is always positive. The physical origin of this property derives from the fact that light scattered from any resonator changes from being in phase to out of phase with the driving field as one crosses the resonance from the low-frequency side. As Eq. (A1) represents the driving field for the trench, it naturally follows that the phase of the electric field changes from $-\pi/2$ to $\pi/2$ when crossing the resonance from the low-frequency side, thus entailing that $\langle E_x \rangle$ is purely real at the resonance and $\text{Re}\{\langle E_x \rangle\} \geq 0$ at any wavelength.

In the remainder of the appendix, we calculate the power scattered by the trench. From the field equivalence principle

and image theory, it is possible to show that radiation from an aperture in a PEC film corresponds to radiation of a magnetic surface current defined by [59]

$$\mathbf{J}_m = -2(\hat{\mathbf{n}}_a \times \mathbf{E}_a), \quad (\text{A4})$$

where \mathbf{E}_a is the electric field in the plane of the aperture and $\hat{\mathbf{n}}_a$ is the surface normal. In this work, the scattering from the subwavelength trench can in the far-field zone be approximated by the radiation from the point source

$$\mathbf{J}_m = 2\langle E_x \rangle w \hat{\mathbf{z}}, \quad (\text{A5})$$

which is assumed to be positioned at the center of the coordinate system. The associated far-field magnetic vector potential is given by

$$\mathbf{A}_m^{\text{far}}(\mathbf{r}) = \varepsilon_0 \mathbf{J}_m g_0^{\text{far}}(\mathbf{r}, 0), \quad (\text{A6})$$

where

$$g_0^{\text{far}}(\mathbf{r}, 0) = \frac{i}{\sqrt{8\pi k_0 r}} e^{i(k_0 r - \pi/4)} \quad (\text{A7})$$

is the asymptotic expression of the free-space Green's function for large arguments, ε_0 is the free-space permittivity, $\mathbf{r} = x\hat{\mathbf{x}} + y\hat{\mathbf{y}}$ is the position vector in the xy plane, and $r = |\mathbf{r}|$. The electric far field is defined by $\mathbf{E}^{\text{far}} = -ik_0/\varepsilon_0(\hat{\mathbf{r}} \times \mathbf{A}_m^{\text{far}})$, corresponding to

$$\mathbf{E}^{\text{far}}(\mathbf{r}) = -\frac{w\sqrt{k_0}\langle E_x \rangle}{\sqrt{2\pi r}} e^{i(k_0 r - \pi/4)} \hat{\phi}, \quad (\text{A8})$$

where $\hat{\phi} = \hat{\mathbf{z}} \times \hat{\mathbf{r}}$. As the far field from any current source locally behaves as a plane wave, the time-averaged Poynting vector in the direction $\hat{\mathbf{r}}$ can be written as $\mathbf{S}^{\text{far}} = \frac{1}{2\eta_0} |\mathbf{E}^{\text{far}}|^2 \hat{\mathbf{r}}$. The total power radiated into the upper half-space can now be found by direct integration of the power flowing through the circular line segments $rd\theta$, i.e.,

$$P_{\text{sc}} = \int_0^\pi \mathbf{S}^{\text{far}} \cdot \hat{\mathbf{r}} r d\theta = \frac{k_0 w^2}{4\eta_0} |\langle E_x \rangle|^2. \quad (\text{A9})$$

APPENDIX B: CALCULATION OF EXTINCTION FROM A SINGLE TRENCH IN A METAL SURFACE

In this appendix, we will present briefly the integral equation method used in this paper to calculate scattering from a single trench in a metal surface. In this method, the field at all positions is related to the field and its normal derivative at the surface of a scattering object through integral equations. It is sufficient to reduce the numerical problem at first to only the surface of the scattering object, and the radiating boundary condition is automatically taken care of via the choice of Green's function.

We will describe the structure following the procedure shown in Fig. 9. Here, a region shaped as the trench (the scattering object) is buried inside the metal of a two-layer air-metal reference geometry. In the limit where the trench-shaped region is moved upwards until it touches the air-metal interface ($\delta \rightarrow 0$), the resulting structure is a trench in an air-metal surface.

We will assume that the incident light is p polarized and propagating in the xy plane, and the magnetic field will thus

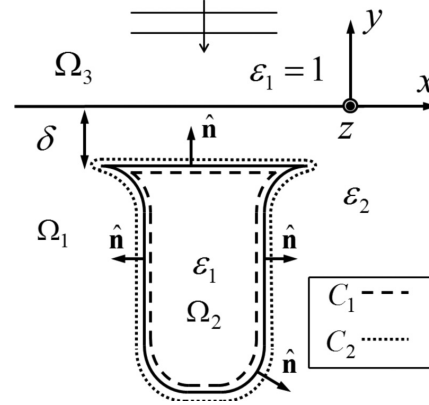


FIG. 9. Schematic of obtaining a trench in a metal surface by adding an air scatterer in the metal region, and then taking the limit of moving the scatterer upwards ($\delta \rightarrow 0$) until it is no longer buried inside the metal.

be of the form

$$\mathbf{H}(\mathbf{r}) = \hat{\mathbf{z}} H(\mathbf{r}), \quad (\text{B1})$$

where $\mathbf{r} = \hat{\mathbf{x}}x + \hat{\mathbf{y}}y$ is a position in the xy plane.

The field at any position inside the trench (Ω_2 in Fig. 9) can be expressed in terms of the field and its normal derivative at the boundary C_1 (see Fig. 9) by the following surface integral equation [60]:

$$H(\mathbf{r}) = \int_{C_1} \{g_2(\mathbf{r}, \mathbf{r}') \hat{\mathbf{n}}' \cdot \nabla' H(\mathbf{r}') - H(\mathbf{r}') \hat{\mathbf{n}}' \cdot \nabla' g_2(\mathbf{r}, \mathbf{r}')\} dl', \quad (\text{B2})$$

where $\hat{\mathbf{n}}$ is the outward normal vector (see Fig. 9), and g_2 can be chosen as the free-space Green's function

$$g_2(\mathbf{r}, \mathbf{r}') = \frac{i}{4} H_0^{(1)}(k_0 n_1 |\mathbf{r} - \mathbf{r}'|). \quad (\text{B3})$$

Here, k_0 is the free-space wave number, n_1 is the refractive index inside the trench ($n_1 = 1$), and $H_0^{(1)}$ is the Hankel function of zero order and first kind.

For positions outside the trench (Ω_1 and Ω_3), the field must be described as the sum of the reference field, which is a solution for the case where the trench is absent, and field components propagating away from the trench. This can be expressed by the integral equation

$$H(\mathbf{r}) = H_{\text{ref}}(\mathbf{r}) - \int_{C_2} \{g_1(\mathbf{r}, \mathbf{r}') \hat{\mathbf{n}}' \cdot \nabla' H(\mathbf{r}') - H(\mathbf{r}') \hat{\mathbf{n}}' \cdot \nabla' g_1(\mathbf{r}, \mathbf{r}')\} dl'. \quad (\text{B4})$$

Two cases must be considered for the air-metal reference structure Green's function g_1 . If both $y < 0$ and $y' < 0$, then

$$g_1(\mathbf{r}, \mathbf{r}') = \frac{i}{2\pi} \int_{\kappa_x=0}^{\infty} \frac{\cos(\kappa_x [x - x'])}{\kappa_{y2}} \times \frac{(e^{i\kappa_{y2}|y-y'|} + r_{13}^{(p)}(\kappa_x) e^{-i\kappa_{y2}(y+y')})}{\kappa_{y2}} d\kappa_x, \quad (\text{B5})$$

ALEXANDER S. ROBERTS *et al.*PHYSICAL REVIEW B **93**, 075413 (2016)

where the reflection coefficient is given by

$$r_{13}^{(p)}(\kappa_x) = \frac{\varepsilon_1 \kappa_{y2} - \varepsilon_2 \kappa_{y1}}{\varepsilon_1 \kappa_{y2} + \varepsilon_2 \kappa_{y1}}, \quad (\text{B6})$$

with $\kappa_{yi} = \sqrt{k_0^2 \varepsilon_i - \kappa_x^2}$ and $\text{Im}\{\kappa_{yi}\} \geq 0$. On the other hand, if $y' < 0$ and $y > 0$, then

$$g_1(\mathbf{r}, \mathbf{r}') = \frac{i}{2\pi} \int_{\kappa_x=0}^{\infty} \frac{\cos(\kappa_x [x - x']) e^{-i\kappa_{y2} y' + i\kappa_{y1} y} t_{13}^{(p)}(\kappa_x)}{\kappa_{y2}} d\kappa_x, \quad (\text{B7})$$

where the transmission coefficient is given by

$$t_{13}^{(p)}(\kappa_x) = 1 + r_{13}^{(p)}(\kappa_x). \quad (\text{B8})$$

For calculating the field and normal derivative at the boundary C_1 we only need Eq. (B5).

For the reference structure magnetic field entering the integral equation we choose the solution for the reference geometry in the case of a normally incident plane wave:

$$H_{\text{ref}}(\mathbf{r}) = H_i \begin{cases} e^{-i k_0 n_1 y} + r_{31}^{(p)}(\kappa_x = 0) e^{+i k_0 n_1 y}, & y > 0 \\ t_{31}^{(p)}(\kappa_x = 0) e^{-i k_0 n_2 y}, & y < 0. \end{cases} \quad (\text{B9})$$

Here, $r_{31}^{(p)} = -r_{13}^{(p)}$ and $t_{31}^{(p)} = 1 + r_{31}^{(p)}$.

The scatterer surface is now subdivided into small discrete elements on which the field and normal derivative are assumed to vary linearly from one end to the other. The field and its normal derivative at the end of one element can be directly related to their counterpart at the beginning of another neighbor element through boundary conditions, and thus the right-hand sides of Eqs. (B2) and (B4) can be cast in parameters for the beginning of elements only. By now letting \mathbf{r} approach the position of the beginning of an element from either side (Ω_1 or Ω_2) self-consistent equations are obtained for the parameters that can be cast on matrix form. This must, in addition, be combined with boundary conditions relating the field and normal derivative just outside the scatterer boundary with their counterparts just inside the boundary.

After solving the resulting matrix equation, we are now ready to calculate the extinction and scattering cross sections. The scattered field can be obtained using Eq. (B4) and the calculated fields at C_2 :

$$H_{\text{scat}}(\mathbf{r}) = - \int_{C_2} \{ g_1(\mathbf{r}, \mathbf{r}') \hat{\mathbf{n}}' \cdot \nabla' H(\mathbf{r}') - H(\mathbf{r}') \hat{\mathbf{n}}' \cdot \nabla' g_1(\mathbf{r}, \mathbf{r}') \} dl'. \quad (\text{B10})$$

If we now use $\mathbf{r} = \hat{\mathbf{x}}r \cos \theta + \hat{\mathbf{y}}r \sin \theta$ with $\theta \in]0; \pi[$, and consider large distances r ($k_0 r \gg 1$), and in principle also large distances to the surface, then we can replace the Green's function (B7) with the corresponding far-field approximation given by [60]

$$g_1^{ff}(\mathbf{r}, \mathbf{r}') = \frac{e^{i k_0 n_1 r}}{\sqrt{r}} e^{i\pi/4} \frac{1}{2} \frac{1}{\sqrt{2\pi}} \frac{1}{\sqrt{k_0 n_1}} \times \left[\frac{\kappa_{y1}}{\kappa_{y2}} t_{13}^{(p)}(\kappa_x) e^{-i\kappa_x x'} e^{-i\kappa_{y2} y'} \right], \quad (\text{B11})$$

where here $\kappa_x = k_0 n_1 \cos \theta$, $\kappa_{y1} = k_0 n_1 \sin \theta$, and $\kappa_{y2} = \sqrt{k_0^2 \varepsilon_2 - \kappa_x^2}$ with $\text{Im}\{\kappa_{y2}\} \geq 0$. Note that here κ_x can assume

negative values for $\pi/2 < \theta < \pi$. With this expression it is straightforward to evaluate the field at large distances r , and the scattering cross section for scattering into the upper half-plane can now be obtained using

$$\sigma_{\text{scat}} = \lim_{r \rightarrow \infty} \frac{1}{|H_i|^2} \int_{\theta=0}^{\pi} |H_{\text{scat}}(r, \theta)|^2 r d\theta. \quad (\text{B12})$$

In order to evaluate the extinction cross section, we need only to consider the scattered field for a single direction but all phase information must be maintained. We consider a case of a wide Gaussian beam being incident on the scatterer, where the Gaussian beam width must be so large that the incident field is plane-wave-like. In that case, the power removed from the reflected beam due to the presence of the scatterer can be calculated and will be independent of the width of the incident Gaussian beam. If this power is then normalized by the incident power per unit area of the incident plane wave, we obtain the extinction cross section

$$\sigma_{\text{ext}} = - \frac{2\sqrt{\frac{2\pi}{k_0}}}{|H_i|^2} \text{Re} \{ r_{31}^{(p)}(\theta = \pi/2) [H_{\text{scat}}(r, \theta = \pi/2)]^* \times \sqrt{r} e^{i k_0 r} e^{-i\pi/4} H_i(\mathbf{r} = \mathbf{0}) \}. \quad (\text{B13})$$

Here, $r^{(p)} = r_{31}^{(p)} = -r_{13}^{(p)}$.

For positions close to the air-metal interface ($y = 0$) it is also relevant to consider the contribution to g_1 from the pole of $t_{13}^{(p)}(\kappa_x)$, which here leads to

$$g_1^{(\text{SPP})}(\mathbf{r}, \mathbf{r}') = - \frac{1}{2} e^{i\kappa_x \text{SPP} |x - x'|} e^{-i\kappa_{y2, \text{SPP}} y'} \frac{A}{\kappa_{y2, \text{SPP}}} \times \begin{cases} \exp(i\kappa_{y1, \text{SPP}} y), & y > 0 \\ \exp(-i\kappa_{y2, \text{SPP}} y), & y < 0 \end{cases} \quad (\text{B14})$$

where

$$\kappa_{x, \text{SPP}} = k_0 \sqrt{\frac{\varepsilon_1 \varepsilon_2}{\varepsilon_1 + \varepsilon_2}}, \quad (\text{B15})$$

$$A = \lim_{\kappa_x \rightarrow \kappa_{x, \text{SPP}}} (t_{13}^{(p)}(\kappa_x) (\kappa_x - \kappa_{x, \text{SPP}})) = - \frac{2\varepsilon_1 \kappa_{y2, \text{SPP}}}{\kappa_{x, \text{SPP}} \left(\frac{\varepsilon_1}{\kappa_{y2, \text{SPP}}} + \frac{\varepsilon_2}{\kappa_{y1, \text{SPP}}} \right)}, \quad (\text{B16})$$

and $\kappa_{yi, \text{SPP}} = \sqrt{k_0^2 \varepsilon_i - \kappa_{x, \text{SPP}}^2}$ with $\text{Im}\{\kappa_{yi, \text{SPP}}\} \geq 0$.

The excitation of the SPP left- and right-propagating guided modes can then be calculated by inserting $g_1^{(\text{SPP})}$ into Eq. (B10). For a position x located to the right of the trench ($x > x'$ for all relevant x' of the curve C_2), we find

$$H_{\text{SPP}}(\mathbf{r}) = H_{\text{SPP}, 0} e^{i\kappa_x \text{SPP} x} \begin{cases} \exp(i\kappa_{y1, \text{SPP}} y), & y > 0 \\ \exp(-i\kappa_{y2, \text{SPP}} y), & y < 0 \end{cases} \quad (\text{B17})$$

where

$$H_{\text{SPP}, 0} = \frac{\varepsilon_1 \kappa_{y1, \text{SPP}} \kappa_{y2, \text{SPP}}}{\kappa_{x, \text{SPP}} (\varepsilon_1 \kappa_{y1, \text{SPP}} + \varepsilon_2 \kappa_{y2, \text{SPP}})} \int_{C_2} e^{-i\kappa_x \text{SPP} x'} e^{-i\kappa_{y2, \text{SPP}} y'} \times [\hat{\mathbf{n}}' \cdot \nabla' H(\mathbf{r}') - H(\mathbf{r}') \hat{\mathbf{n}}' \cdot (\hat{\mathbf{x}}(-i\kappa_{x, \text{SPP}}) + \hat{\mathbf{y}}(-i\kappa_{y2, \text{SPP}}))] dl'. \quad (\text{B18})$$

A similar expression can be obtained for the left-propagating SPP ($x < x'$). In the case of normally incident light, it is sufficient to consider the power carried by the right-propagating SPP and then multiplying by a factor of 2 to obtain the total power scattered into SPP waves. Scattering into guided modes of a geometry supporting many guided modes was recently considered in [61].

The total time-averaged power carried by the right-propagating SPP wave at a given x is given by

$$P_{\text{SPP},r} = \frac{1}{2} \text{Re} \int_y \{ \mathbf{E}^{(\text{SPP})}(\mathbf{r}) \times (\mathbf{H}^{(\text{SPP})}(\mathbf{r}))^* \cdot \hat{\mathbf{x}} \} dy. \quad (\text{B19})$$

By normalizing with the incident power per unit area and rewriting in terms of the magnetic field only, we find the scattering cross section related to the excitation of right-propagating SPP waves

$$\sigma_{\text{SPP},r} = \frac{|H_{\text{SPP},0}|^2}{|H_i|^2} e^{-2\kappa_{x,\text{SPP},i}x} \left(\text{Re} \left\{ \frac{\kappa_{x,\text{SPP}}}{k_0 n_1} \right\} \frac{1}{2\kappa_{y1,\text{SPP},i}} + \text{Re} \left\{ \frac{\kappa_{x,\text{SPP}} \varepsilon_1}{k_0 n_1 \varepsilon_2} \right\} \frac{1}{2\kappa_{y2,\text{SPP},i}} \right), \quad (\text{B20})$$

where $\kappa_{x,\text{SPP},i} = \text{Im}\{\kappa_{x,\text{SPP}}\}$, and $\kappa_{yi,\text{SPP},i} = \text{Im}\{\kappa_{yi,\text{SPP}}\}$.

It should be noted that in the case of no absorption losses then $\sigma_{\text{ext}} = \sigma_{\text{scat}} + \sigma_{\text{SPP},r} + \sigma_{\text{SPP},l}$ identically, where $\sigma_{\text{SPP},l}$ is the cross section related to left-propagating SPP waves, while in the case of absorption losses we expect $\sigma_{\text{ext}} > \sigma_{\text{scat}} + \sigma_{\text{SPP},r} + \sigma_{\text{SPP},l}$ due to excess absorption losses related to the trench. The case of absorption losses is tricky though since clearly the SPP scattering cross sections depend on the value of x where the SPP field is evaluated.

We have also considered scattering for s -polarized light. In that case, the calculations were done by replacing in the above expressions the magnetic field H with the electric field E , and replacing Fresnel reflection and transmission coefficients with their s -polarized counterparts. In this case, the Green's function g_1 is then different, and also the boundary condition relating the normal derivative of the field on one and the other side of the scatterer surface is different. Note that for s polarization, the air-metal geometry does not support guided modes, and also the Fresnel reflection and transmission coefficients no longer have a pole. Thus, no scattering of light into guided modes should be considered for this polarization (for this particular geometry).

-
- [1] W. Turner *et al.*, *Trends Ecol. Evol.* **18**, 306 (2003).
 [2] A. Kabashin *et al.*, *Nat. Mater.* **8**, 867 (2009).
 [3] N. Liu, M. Mesch, T. Weiss, M. Hentschel, and H. Giessen, *Nano Lett.* **10**, 2342 (2010).
 [4] S. V. Yalunin, M. Gulde, and C. Ropers, *Phys. Rev. B* **84**, 195426 (2011).
 [5] X. Ni, N. Emani, A. Kildishev, A. Boltasseva, and V. Shalaev, *Science* **335**, 427 (2012).
 [6] M. G. G. Herink, D. R. Solli, and C. Ropers, *Nature (London)* **483**, 190 (2012).
 [7] A. Väkeväinen *et al.*, *Nano Lett.* **14**, 1721 (2013).
 [8] T. W. Ebbesen, H. Lezec, H. Ghaemi, T. Thio, and P. Wolff, *Nature (London)* **391**, 667 (1998).
 [9] F. J. Garcia-Vidal, L. Martin-Moreno, T. W. Ebbesen, and L. Kuipers, *Rev. Mod. Phys.* **82**, 729 (2010).
 [10] R. H. F. Pardo, P. Bouchon, R. Haider, and J.-L. Pelouard, *Phys. Rev. Lett.* **107**, 093902 (2011).
 [11] S. Lal, S. Link, and N. J. Halas, *Nat. Photon.* **1**, 641 (2007).
 [12] F. Hao *et al.*, *Nano Lett.* **8**, 3983 (2008).
 [13] R. Gordon, D. Sinton, K. L. Kavanagh, and A. G. Brolo, *Acc. Chem. Res.* **41**, 1049 (2008).
 [14] M.-W. Tsai, T.-H. Chuang, C.-Y. Meng, Y.-T. Chang, and S.-C. Lee, *Appl. Phys. Lett.* **89**, 173116 (2006).
 [15] R. Stanley, *Nat. Photon.* **6**, 409 (2012).
 [16] J.-P. Hugonin, M. Besbes, and P. Ben-Abdallah, *Phys. Rev. B* **91**, 180202 (2015).
 [17] A. Polyakov *et al.*, *Sci. Rep.* **2**, 933 (2012).
 [18] S. Kim *et al.*, *Opt. Express* **21**, 15081 (2013).
 [19] A. Polyakov *et al.*, *Appl. Phys. Lett.* **98**, 203104 (2011).
 [20] A. Polyakov *et al.*, *J. Vac. Sci. Technol. B* **29**, 06FF01 (2011).
 [21] L. Meng, D. Zhao, Q. Li, and M. Qiu, *Opt. Express* **21**, A111 (2013).
 [22] J. Le Perchec, P. Quemerais, A. Barbara, and T. Lopez-Rios, *Phys. Rev. Lett.* **100**, 066408 (2008).
 [23] M. Melli *et al.*, *Nano Lett.* **13**, 2687 (2013).
 [24] S. I. Bozhevolnyi and J. Jung, *Opt. Express* **16**, 2676 (2008).
 [25] R. Gordon, *Phys. Rev. B* **73**, 153405 (2006).
 [26] A. Chandran, E. S. Barnard, J. S. White, and M. L. Brongersma, *Phys. Rev. B* **85**, 085416 (2012).
 [27] P. Lalanne, J.-P. Hugonin, and J.-C. Rodier, *J. Opt. Soc. Am. A* **23**, 1608 (2006).
 [28] C. F. Bohren and D. R. Huffman, *Absorption and Scattering of Light by Small Particles* (Wiley, Hoboken, NJ, 2008).
 [29] R. G. Newton, *Scattering Theory of Waves and Particles* (Springer, New York, 1982).
 [30] Z. Ruan and S. Fan, *Phys. Rev. Lett.* **105**, 013901 (2010).
 [31] E. Palik and E. Prucha, *Handbook of Optical Constants of Solids* (Academic Press, Boston, MA, 1997).
 [32] T. Søndergaard, *Phys. Status Solidi B* **244**, 3448 (2007).
 [33] J. Jung and T. Søndergaard, *Phys. Rev. B* **77**, 245310 (2008).
 [34] V. Siahpoush, T. Søndergaard, and J. Jung, *Phys. Rev. B* **85**, 075305 (2012).
 [35] J. Pendry, L. Martin-Moreno, and F. Garcia-Vidal, *Science* **305**, 847 (2004).
 [36] A. Pors, E. Moreno, L. Martin-Moreno, J. B. Pendry, and F. J. Garcia-Vidal, *Phys. Rev. Lett.* **108**, 223905 (2012).
 [37] T. Søndergaard *et al.*, *Nat. Commun.* **3**, 969 (2012).
 [38] M. Vasile, Z. Niu, R. Nassar, W. Zhang, and S. Liu, *J. Vac. Sci. Technol. B* **15**, 2350 (1997).
 [39] D. De Winter and J. Mulders, *J. Vac. Sci. Technol. B* **25**, 2215 (2007).
 [40] J.-S. Huang *et al.*, *Nat. Commun.* **1**, 150 (2010).
 [41] H.-W. Liu *et al.*, *ACS Nano* **9**, 3875 (2015).
 [42] A. Mooradian, *Phys. Rev. Lett.* **22**, 185 (1969).

ALEXANDER S. ROBERTS *et al.*PHYSICAL REVIEW B **93**, 075413 (2016)

- [43] G. T. Boyd, Z. H. Yu, and Y. R. Shen, *Phys. Rev. B* **33**, 7923 (1986).
- [44] M. R. Beversluis, A. Bouhelier, and L. Novotny, *Phys. Rev. B* **68**, 115433 (2003).
- [45] P. Ghenuche, S. Cherukulappurath, T. H. Taminiau, N. F. van Hulst, and R. Quidant, *Phys. Rev. Lett.* **101**, 116805 (2008).
- [46] A. Bouhelier, M. R. Beversluis, and L. Novotny, *Appl. Phys. Lett.* **83**, 5041 (2003).
- [47] J. Beermann *et al.*, *Opt. Express* **20**, 654 (2012).
- [48] J. Beermann *et al.*, *New J. Phys.* **15**, 073007 (2013).
- [49] J. Beermann and S. I. Bozhevolnyi, *Phys. Rev. B* **69**, 155429 (2004).
- [50] A. Pors, O. Albrektsen, I. P. Radko, and S. I. Bozhevolnyi, *Sci. Rep.* **3**, 2155 (2013).
- [51] A. S. Roberts, A. Pors, O. Albrektsen, and S. I. Bozhevolnyi, *Nano Lett.* **14**, 783 (2014).
- [52] S. K. Andersen, A. Pors, and S. I. Bozhevolnyi, *ACS Photon.* **2**, 432 (2015).
- [53] V. G. Kravets, F. Schedin, and A. N. Grigorenko, *Phys. Rev. Lett.* **101**, 087403 (2008).
- [54] B. Auguié and W. L. Barnes, *Phys. Rev. Lett.* **101**, 143902 (2008).
- [55] A. D. Humphrey and W. L. Barnes, *Phys. Rev. B* **90**, 075404 (2014).
- [56] A. Hohenau, J. R. Krenn, F. J. Garcia-Vidal, S. G. Rodrigo, L. Martin-Moreno, J. Beermann, and S. I. Bozhevolnyi, *Phys. Rev. B* **75**, 085104 (2007).
- [57] J. Beermann, S. M. Novikov, T. Søndergaard, A. Boltasseva, and S. I. Bozhevolnyi, *Opt. Express* **16**, 17302 (2008).
- [58] J. Beermann *et al.*, *J. Opt. Soc. Am. B* **28**, 372 (2011).
- [59] S. A. Schelkunoff, *Phys. Rev.* **56**, 308 (1939).
- [60] A. V. Lavrinenko, J. Lægsgaard, N. Gregersen, F. Schmidt, and T. Søndergaard, *Numerical Methods in Photonics* (CRC Press, Boca Raton, FL, 2014).
- [61] T. Søndergaard, Y.-C. Tsao, P. K. Kristensen, T. G. Pedersen, and K. Pedersen, *J. Opt. Soc. Am. B* **31**, 2036 (2014).

Appendix D

Multilayer tungsten-alumina-based broadband light absorbers for high temperature applications

Multilayer tungsten-alumina-based broadband light absorbers for high-temperature applications

MANOHAR CHIRUMAMILLA,^{1,*} ALEXANDER S. ROBERTS,² FEI DING,² DEYONG WANG,¹ PETER KJÆR KRISTENSEN,¹ SERGEY I. BOZHEVOLNYI,² AND KJELD PEDERSEN¹

¹Department of Physics and Nanotechnology, University of Aalborg, Skjernvej 4A, Aalborg, 9220, Denmark

²Institute of Technology & Innovation, University of Southern Denmark, Niels Bohrs Allé 1, Odense, 5230, Denmark

*mch@nano.aau.dk

Abstract: Efficient broadband absorption of visible and near-infrared light by low quality-factor metal-insulator-metal (MIM) resonators using refractory materials is reported. Omnidirectional absorption of incident light for broad angles of incidence and polarization insensitivity are observed for the fabricated MIM resonator. Excellent thermal stability of the absorber is demonstrated at high operating temperatures (800 °C). The experimental broadband absorption spectra show good agreement with simulations. The resonator with 12 nm top tungsten and 100 nm alumina spacer film shows absorbance above 95% in the range of 650 to 1750 nm. The absorption window is tunable in terms of the center wavelength, bandwidth, and the value of maximum absorbance (~98%) by simple variation of appropriate layer thicknesses. Owing to their flexibility, ease of fabrication and low cost, the presented absorbers have the potential for a wide range of applications, including the use in commonly used infrared bands or absorbers for (solar) thermo-photovoltaic energy conversion, where high absorbance and simultaneously low (thermal) re-radiation is of paramount importance.

©2016 Optical Society of America

OCIS codes: (310.6860) Thin films, optical properties; (230.5750) Resonators; (230.4170) Multilayers; (260.3060) Infrared.

References and links

- J.-J. Greffet, R. Carminati, K. Joulain, J.-P. Mulet, S. Mainguy, and Y. Chen, "Coherent emission of light by thermal sources," *Nature* **416**(6876), 61–64 (2002).
- Y. Cui, Y. He, Y. Jin, F. Ding, L. Yang, Y. Ye, S. Zhong, Y. Lin, and S. He, "Plasmonic and metamaterial structures as electromagnetic absorbers," *Laser Photonics Rev.* **8**(4), 495–520 (2014).
- C. M. Watts, X. Liu, and W. J. Padilla, "Metamaterial Electromagnetic Wave Absorbers," *Adv. Mater.* **24**(23), OP98–OP120 (2012).
- D. Kraemer, B. Poudel, H.-P. Feng, J. C. Caylor, B. Yu, X. Yan, Y. Ma, X. Wang, D. Wang, A. Muto, K. McEnaney, M. Chiesa, Z. Ren, and G. Chen, "High-performance flat-panel solar thermoelectric generators with high thermal concentration," *Nat. Mater.* **10**(7), 532–538 (2011).
- W. Li and J. Valentine, "Metamaterial perfect absorber based hot electron photodetection," *Nano Lett.* **14**(6), 3510–3514 (2014).
- P. Zhu and L. Jay Guo, "High performance broadband absorber in the visible band by engineered dispersion and geometry of a metal-dielectric-metal stack," *Appl. Phys. Lett.* **101**(24), 241116 (2012).
- R. Walter, A. Tittl, A. Berrier, F. Sterl, T. Weiss, and H. Giessen, "Large-area low-cost tunable plasmonic perfect absorber in the near infrared by colloidal etching lithography," *Adv. Opt. Mater.* **3**(3), 398–403 (2015).
- V. Steenhoff, M. Theuring, M. Vehse, K. von Maydell, and C. Agert, "Ultrathin resonant-cavity-enhanced solar cells with amorphous germanium absorbers," *Advanced Optical Materials* **3**(2), 182–186 (2015).
- M. Yan, "Metal-insulator-metal light absorber: a continuous structure," *J. Opt.* **15**(2), 025006 (2013).
- G. Kajtar, M. Kafesaki, E. N. Economou, and C. M. Soukoulis, "Theoretical model of homogeneous metal-insulator-metal perfect multi-band absorbers for the visible spectrum," *J. Phys. D Appl. Phys.* **49**(5), 055104 (2016).
- T. Søndergaard, S. M. Novikov, T. Holmgaard, R. L. Eriksen, J. Beermann, Z. Han, K. Pedersen, and S. I. Bozhevolnyi, "Plasmonic black gold by adiabatic nanofocusing and absorption of light in ultra-sharp convex grooves," *Nat. Commun.* **3**, 969 (2012).
- Y. Cui, K. H. Fung, J. Xu, H. Ma, Y. Jin, S. He, and N. X. Fang, "Ultrabroadband Light Absorption by a Sawtooth Anisotropic Metamaterial Slab," *Nano Lett.* **12**(3), 1443–1447 (2012).

13. F. Ding, Y. Jin, B. Li, H. Cheng, L. Mo, and S. He, "Ultrabroadband strong light absorption based on thin multilayered metamaterials," *Laser Photonics Rev.* **8**(6), 946–953 (2014).
14. S. He, F. Ding, L. Mo, and F. Bao, "Light absorber with an ultra-broad flat band on multi-sized slow-wave hyperbolic metamaterial thin-films," *Prog. Electromagnetics Res.* **147**, 10 (2014).
15. F. Ding, L. Mo, J. Zhu, and S. He, "Lithography-free, broadband, omnidirectional, and polarization-insensitive thin optical absorber," *Appl. Phys. Lett.* **106**(6), 061108 (2015).
16. Z. Li, E. Palacios, S. Butun, H. Kocer, and K. Aydin, "Omnidirectional, broadband light absorption using large-area, ultrathin lossy metallic film coatings," *Sci. Rep.* **5**, 15137 (2015).
17. H. Deng, Z. Li, L. Stan, D. Rosenmann, D. Czaplowski, J. Gao, and X. Yang, "Broadband perfect absorber based on one ultrathin layer of refractory metal," *Opt. Lett.* **40**(11), 2592–2595 (2015).
18. Y. G. Chushak and L. S. Bartell, "Melting and freezing of gold nanoclusters," *J. Phys. Chem. B* **105**(47), 11605–11614 (2001).
19. M. Zhang, M. Y. Efremov, F. Schiettekatte, E. A. Olson, A. T. Kwan, S. L. Lai, T. Wisleder, J. E. Greene, and L. H. Allen, "Size-dependent melting point depression of nanostructures: Nanocalorimetric measurements," *Phys. Rev. B* **62**(15), 10548–10557 (2000).
20. M. Sarrazin and J.-P. Vigneron, "Optical properties of tungsten thin films perforated with a bidimensional array of subwavelength holes," *Phys. Rev. E Stat. Nonlin. Soft Matter Phys.* **68**(1 Pt 2), 016603 (2003).
21. S. Roberts, "Optical Properties of Nickel and Tungsten and Their Interpretation According to Drude's Formula," *Phys. Rev.* **114**(1), 104–115 (1959).
22. A. D. Rakić, A. B. Djurić, J. M. Elazar, and M. L. Majewski, "Optical properties of metallic films for vertical-cavity optoelectronic devices," *Appl. Opt.* **37**(22), 5271–5283 (1998).
23. E. Rephaeli and S. Fan, "Tungsten black absorber for solar light with wide angular operation range," *Appl. Phys. Lett.* **92**(21), 211107 (2008).
24. Z. J. Coppens, I. I. Kravchenko, and J. G. Valentine, "Lithography-Free Large-Area Metamaterials for Stable Thermophotovoltaic Energy Conversion," *Advanced Optical Materials*, 1–6 (2016, in press).
25. N. I. Landy, S. Sajuyigbe, J. J. Mock, D. R. Smith, and W. J. Padilla, "Perfect Metamaterial Absorber," *Phys. Rev. Lett.* **100**(20), 207402 (2008).
26. Y. Avitzour, Y. A. Urzhumov, and G. Shvets, "Wide-angle infrared absorber based on a negative-index plasmonic metamaterial," *Phys. Rev. B* **79**(4), 045131 (2009).
27. I. H. Malitson and M. J. Dodge, "Refractive-index and birefringence of synthetic sapphire," *J. Opt. Soc. Am.* **62**, 1405 (1972).
28. L. A. A. Pettersson, L. S. Roman, and O. Inganäs, "Modeling photocurrent action spectra of photovoltaic devices based on organic thin films," *J. Appl. Phys.* **86**(1), 487–496 (1999).
29. D. Zhao, L. Meng, H. Gong, X. Chen, Y. Chen, M. Yan, Q. Li, and M. Qiu, "Ultra-narrow-band light dissipation by a stack of lamellar silver and alumina," *Appl. Phys. Lett.* **104**(22), 221107 (2014).
30. S. Fan, "Photovoltaics: an alternative 'Sun' for solar cells," *Nat. Nanotechnol.* **9**(2), 92–93 (2014).
31. I. E. Khodasevych, L. Wang, A. Mitchell, and G. Rosengarten, "Micro- and Nanostructured Surfaces for Selective Solar Absorption," *Advanced Optical Materials* **3**(7), 852–881 (2015).
32. A. Lenert, D. M. Bierman, Y. Nam, W. R. Chan, I. Celanović, M. Soljačić, and E. N. Wang, "A nanophotonic solar thermophotovoltaic device," *Nat. Nanotechnol.* **9**(2), 126–130 (2014).
33. P. Bermel, M. Ghebrebrhan, W. Chan, Y. X. Yeng, M. Araghchini, R. Hamam, C. H. Marton, K. F. Jensen, M. Soljačić, J. D. Joannopoulos, S. G. Johnson, and I. Celanovic, "Design and global optimization of high-efficiency thermophotovoltaic systems," *Opt. Express* **18**(S3), A314–A334 (2010).
34. Z. Liu, X. Liu, S. Huang, P. Pan, J. Chen, G. Liu, and G. Gu, "Automatically Acquired Broadband Plasmonic-Metamaterial Black Absorber during the Metallic Film-Formation," *ACS Appl. Mater. Interfaces* **7**(8), 4962–4968 (2015).
35. C. Hägglund, S. P. Apell, and B. Kasemo, "Maximized Optical Absorption In Ultrathin Films and Its Application to Plasmon-Based Two-Dimensional Photovoltaics," *Nano Lett.* **10**(8), 3135–3141 (2010).
36. C. Hägglund and S. P. Apell, "Resource efficient plasmon-based 2D-photovoltaics with reflective support," *Opt. Express* **18**(S3 Suppl 3), A343–A356 (2010).
37. M. Esfandyarpour, E. C. Garnett, Y. Cui, M. D. McGehee, and M. L. Brongersma, "Metamaterial mirrors in optoelectronic devices," *Nat. Nanotechnol.* **9**(7), 542–547 (2014).
38. C. Qu, S. Ma, J. Hao, M. Qiu, X. Li, S. Xiao, Z. Miao, N. Dai, Q. He, S. Sun, and L. Zhou, "Tailor the Functionalities of Metasurfaces Based on a Complete Phase Diagram," *Phys. Rev. Lett.* **115**(23), 235503 (2015).
39. H. A. Haus, *Waves and Fields in Optoelectronics* (Prentice-Hall, 1984).
40. D. L. C. Chan, I. Celanovic, J. D. Joannopoulos, and M. Soljačić, "Emulating one-dimensional resonant Q-matching behavior in a two-dimensional system via Fano resonances," *Phys. Rev. A* **74**(6), 064901 (2006).
41. M. A. Kats, R. Blanchard, P. Genevet, and F. Capasso, "Nanometre optical coatings based on strong interference effects in highly absorbing media," *Nat. Mater.* **12**(1), 20–24 (2013).
42. A. S. Roberts, M. Chirumamilla, K. Thilsing-Hansen, K. Pedersen, and S. I. Bozhevolnyi, "Near-infrared tailored thermal emission from wafer-scale continuous-film resonators," *Opt. Express* **23**(19), A1111–A1119 (2015).
43. A. S. Roberts, T. Søndergaard, M. Chirumamilla, A. Pors, J. Beermann, K. Pedersen, and S. I. Bozhevolnyi, "Light extinction and scattering from individual and arrayed high-aspect-ratio trenches in metals," *Phys. Rev. B* **93**(7), 075413 (2016).
44. P. N. Dyachenko, J. J. do Rosário, E. W. Leib, A. Y. Petrov, M. Störmer, H. Weller, T. Vossmeier, G. A. Schneider, and M. Eich, "Tungsten band edge absorber/emitter based on a monolayer of ceramic microspheres," *Opt. Express* **23**(19), A1236–A1244 (2015).

1. Introduction

Recent development in the fields of thermo-photovoltaic (TPV) energy conversion, solar energy harvesting, photo-detectors, and thermal imaging and emission has highlighted the significance of broadband absorbers [1–8]. The ideal blackbody absorber possesses an absorption magnitude equal to unity and omnidirectional, polarization-independent nature [9, 10]. Several methods have been developed to obtain broadband absorption, such as lattice-scattering effects, excitation of slow-light modes, impedance matching, multiple resonances and adiabatic nano-focusing of gap surface plasmon modes [11–14]. However, the fabrication process of these absorbers includes electron beam lithography or focused ion beam milling that is expensive, time-consuming and only feasible for fabricating over a few $100 \mu\text{m}^2$ area, which limits their applicability. Significant progress has been made over the last years in achieving broadband absorption with continuous metal-insulator-metal (MIM) resonators based on chromium, gold, titanium and silicon dioxide materials, by simple, cost-effective wafer-scale fabrication methods [15–17]. The broadband absorption window of these resonators can be improved further by increasing the number of metal and dielectric film layers; however, there is a severe trade-off between omni-directionality and absorbance. Moreover, multilayered resonators require increased fabrication cost and time, while leading to a decrease in the high-temperature stability. It is worth pointing out that the geometry and entailing physics of the resonators described in this work differ substantially from equally named MIM resonators supporting so-called gap-surface plasmons.

Although the MIM resonators provide broadband absorption, their melting points (for thin metal layers) are rather low because of the relatively low melting points of the bulk materials combined with the grain sizes of the thin metal layer causing melting point depression [18, 19]. In particular, the efficient application in TPV/solar TPV energy conversion requires that the absorber is capable of withstanding high operating temperatures. Achieving both angular and polarization insensitivity in a broadband absorber with high-temperature stability by an MIM resonator remains a challenge. In this regard, refractory materials can improve the limiting temperature instability of thin films. Therefore, tungsten and alumina [with bulk melting points of 3422 and 2072 °C, and low thermal expansion coefficients of 4.2×10^{-6} and 5.4×10^{-6} m/(m·K) at room temperature, respectively] are used in the present study to fabricate the MIM resonator. Tungsten is a good radiation absorber in the visible range since the real part of the dielectric permittivity is positive below 900 nm, while the imaginary part is significant. A rather large imaginary part (in comparison with the real part) of the dielectric function of tungsten results directly in efficient light absorption by metallic layers of the resonator, which allows one to minimize the reflection from the (opaque) resonator as well as usually occurred near-infrared heat radiation (thermal re-radiation) at high temperatures [20–22]. The absorption spectrum of a 100 nm thick tungsten film exhibits a substantial drop in absorption from 47% to 18% when tuning the wavelength from the visible to near-infrared [Fig. 1(c)] due to impedance mismatching between free space and tungsten (that becomes progressively a better metal for longer wavelengths).

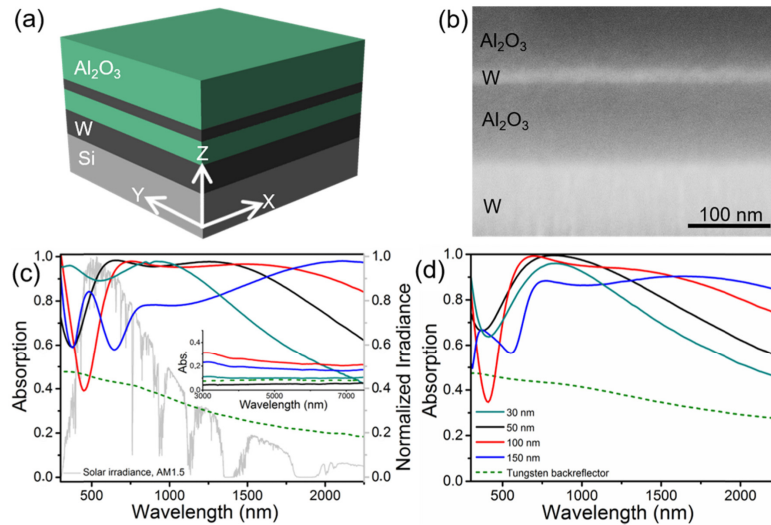


Fig. 1. (a) Schematic of an MIM resonator with a protective coating layer. (b) Cross-sectional SEM image of the MIMPC resonator for 100 nm spacer film and 12 nm top W film (the substrate is not seen). (c) Experimental absorption spectra of an MIMPC structure using UV-vis-NIR spectrometer and FTIR spectrometer with a 100 nm top protection layer of Al₂O₃, a semi-transparent layer consisting of 12 nm W, a 30, 50, 100 and 150 nm Al₂O₃ spacer layer, and a 100 nm bottom layer of W. The substrate is a piece of Si wafer. Normalized AM1.5 solar spectrum is shown in (c), gray line. Simulated absorption spectra up to near-infrared region are shown in (d).

A high melting point in conjunction with a low thermal expansion coefficient makes tungsten a promising material for broadband absorption at high temperatures [23]. In addition, a protective coating (PC) of alumina can be deposited over the MIM structure to stabilize the film at high temperatures and to widen the absorption band [24–26]. Herein, we report fabrication and characterization of a tungsten and alumina based MIM resonator as a broadband absorber working in the visible and near-infrared. The absorption window can be tuned in the visible and near-infrared spectral regions by varying the dielectric layer thickness, and - to a significantly lesser extent - by varying the top metal layer thickness, which influences the reflection phase of the mode propagating inside the dielectric layer. The maximum absorbance of the resonator is optimized by variation of the top metal and protective coating film thicknesses. Experimental absorption spectra show good agreement with theoretical calculations. The broadband absorption for both transverse electric (TE) and transverse magnetic (TM) polarizations is high at normal incidence light, and remains to be high at angles of incidence of up to 50°. The high-temperature stability of the substrate is examined by annealing the resonator for 4 hours at 600 °C in air and 800 °C in vacuum. A secondary-ion mass spectrometer is used for compositional analysis of the resonator interfacial layers. It should be pointed out, that the absorber could straightforwardly be adapted to function in commonly used infrared bands, such as e.g. the 3–5 μm band.

2. Method

2.1. Fabrication

The broadband absorbers are fabricated on a polished silicon [p-type, C-Si(100)] substrate using e-beam deposition (for alumina) and DC sputtering (for tungsten) at a rate of 0.3 Å/s. First, a 30 nm alumina followed by a 100 nm thick tungsten layer are deposited on a silicon substrate, where alumina works as an adhesion promotor between the silicon substrate and a tungsten layer. Subsequently, tungsten and alumina layers of

desired thicknesses are deposited. Cross-sectional SEM images are taken by a Zeiss 1540 XB machine.

2.2 Optical measurements

Reflection measurements in the visible and near-infrared regions are performed on a PerkinElmer Lambda 1050 spectrometer with a 150 mm integrating sphere. Reflection measurements are taken with a wavelength scan step of 3 nm and normalized to a lab-sphere spectralon reflectance standard. The oblique angle of incidence spectra are measured with a variable angle reflectance center mount holder, which is attached to the integrating sphere. For mid-infrared measurements, a PerkinElmer Spectrum One FTIR spectrometer is used. Spectroscopic, variable angle ellipsometry is used (J.A. Woollam, V-VASE ellipsometer) to obtain the optical data (300-2200 nm) for the deposited Tungsten film, while the optical data used for aluminum oxide is interpolated from data presented in [27].

2.3 Simulations

The shown simulation of spectral absorption, field intensity ($|E|^2$) and local absorption are obtained analytically by use of the thin-film transfer-matrix method [28]. The local field intensity and local absorption are renormalized to their respective maximum values.

2.4 SIMS

A Hiden analytical SIMS workstation is used to analyze the MIMPC resonator. Cesium ions (at 5 keV and 100 nA) are used to sputter the thin film layers and secondary cesium tungsten clusters are detected from an area of $0.3 \mu\text{m}^2$ using an EQS quadrupole analyzer.

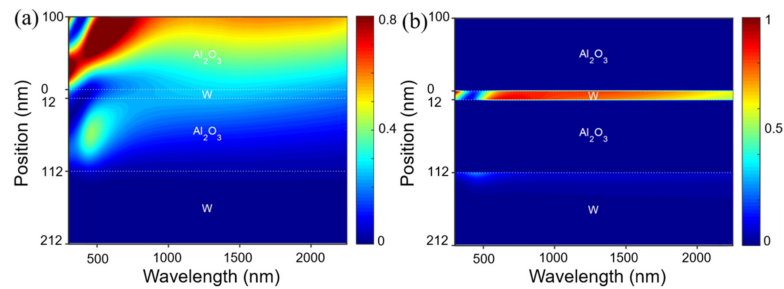


Fig. 2. The calculated contour plots of electric field intensity (a) and absorbed power (b) for the resonator (spacer and protective films of a 100 nm Al_2O_3 , and a 12 nm top tungsten film) as a function of wavelength and depth into the sample.

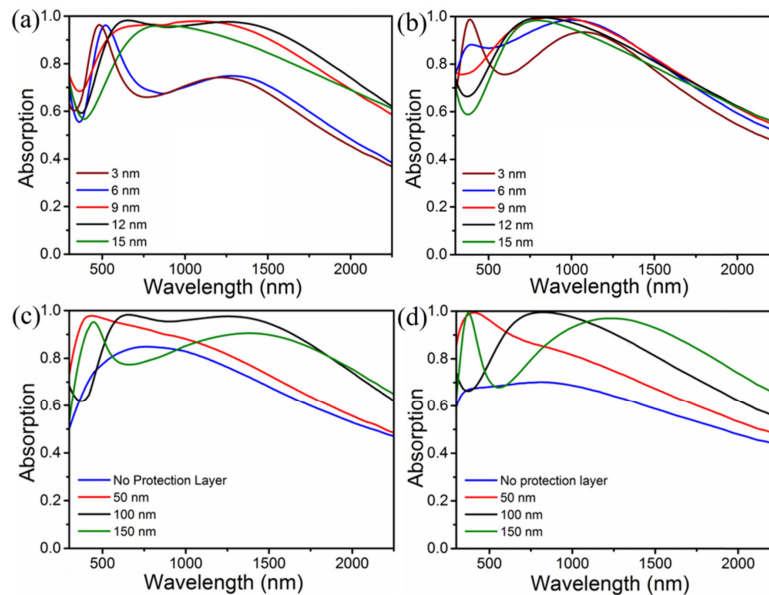


Fig. 3. Broadband absorption spectra for 50 nm alumina spacer resonator with various (a) top tungsten layer, (c) PC layer film thicknesses. (b and d) Simulation spectra of (a) and (c), respectively. Dimension, unless otherwise specified: Al_2O_3 Protection layer thickness: 100 nm, W semi-transparent film 12 nm, Al_2O_3 dielectric spacer 50 nm, W bottom tungsten layer: 100 nm.

3. Results and discussions

The investigated configuration of an MIM (tungsten-alumina-tungsten) resonator with a protective coating layer of alumina is shown in Fig. 1(a). A 30-nm-thin alumina layer (not shown) is used as an adhesion layer between the silicon substrate and a thick tungsten layer. The resonator consists of a 100-nm-thick tungsten layer that works as a mirror (back reflector) and a 12-nm-thin top tungsten layer, acting as a semi-transparent mirror, with the lossless dielectric layer (alumina) functioning as a spacer between the thick and thin tungsten layers. This configuration forms thereby a low-quality factor asymmetric Fabry-Perot (FP) resonator [29]. A cross-sectional scanning electron microscope (SEM) image of an MIM resonator with a protective layer (MIMPC) and a 100 nm alumina spacer layer is shown in Fig. 1(b). The normal-incidence absorption spectra for MIMPC resonators with 30-, 50-, 100- and 150-nm-thick alumina spacer films and 12-nm-thin and 100-nm-thick top tungsten and PC films, respectively, are measured by a UV-Vis-NIR spectrometer [Fig. 1(c)]. The optical absorption is deduced by $A = I - R - T$, where A , R and T are absorbance, reflectance and transmittance. Since $T = 0$ for an optically thick (100 nm) tungsten layer, the absorption is directly related to the reflection: $A = I - R$. Corresponding simulated spectra are calculated analytically using the transfer-matrix method, Fig. 1(d) [28]. For a 100-nm-thick alumina spacer, the resonator exhibits above 95% absorbance in the wavelength range from 650 to 1750 nm and 90% from 625 to 2030 nm, with a maximum absorbance reaching 98% at 750 nm. Broadband spectral tunability across the visible and near-infrared with unchanged high absorbance is demonstrated as the alumina spacer thickness is varied. When de- or increasing the alumina spacer thicknesses to 30 and 50, and 150 nm, a respective blue- or red-shift in the absorption window occurs due to changes in the FP cavity length. Theoretical spectra show good correspondence with experimental spectra, Fig. 1(d).

The absorbance of MIMPC resonators in the mid-infrared region, as measured by an FTIR spectrometer is shown in the inset of Fig. 1(c). The spectral region between 2200

and 3000 nm is not accessible by our experimental setup. The suppression of absorbance (to 0.06 for 50 nm alumina layer) at wavelengths from 3 to 7.5 μm , means that low radiative losses are to be expected when operating at high temperatures. In (solar) TPV systems absorbers are thermally coupled to the emitters. The absorber transmits the absorbed power conductively to a narrow-band emitter, which then emits selectively at a wavelength matched to the bandgap energy of a photovoltaic cell [30, 31]. This scheme does require the MIMPC absorber to have high thermal conductance, which restricts the choice of dielectrics. Re-radiative losses from the absorber are a major limiting factor in TPV efficiency [32, 33], therefore it is necessary to minimize the emission in the spectral range, where the blackbody radiance at the working temperature attains significant values; at 600 °C and 800 °C the blackbody radiation is most intense at 3320 nm and 2700 nm, respectively. Due to the broadband nature of Planckian radiation, it is advantageous to have low absorbance at all wavelengths that do not significantly contribute to the absorption of solar radiation – ideally at all wavelengths larger than the desired absorption window. As such, the low absorbance of the MIMPC resonator at wavelengths between 3 and 7.5 μm strongly underlines its potential for TPV applications. The MIMPC absorbers show a remarkable degree of tunability. For a resonator with a 30 nm alumina spacer film, the absorption window spans from the UV to infrared regions, which can be directly employed to the solar TPV/solar thermal systems. The normalized AM1.5 solar spectrum is shown in the Fig. 1(c) for reference. Since elevated working temperatures are required for solar TPV, the low emittance at a wavelength where significant thermal emission can occur, and high absorption covering most of the solar spectrum of the 30 nm alumina spacer resonator, makes it an ideal candidate for solar TPV applications. Moreover, due to a high absorption of the 150 nm resonator around 2 μm region, it can be used as a blackbody radiator. By varying the spacer film thickness, it is possible to tailor the absorption window for TPV/solar TPV applications or other application where high absorption(emission) is desired in a broad spectral band.

The simulated contour plots of total electric field intensity and absorbed power as a function of wavelength and thickness for a typical resonator with a 100-nm-thick spacer film are shown in Figs. 2(a) and 2(b), respectively. A decrement in field intensity inside the spacer layer confirms the low-quality factor of the resonator; see Fig. 2(a). As seen in Fig. 2(b) the top W layer absorbs most of the incident power in a broad range of wavelengths (above a wavelength of 500 nm), while less dissipation of power occurs in the thick W layer that acts as a mirror reflecting the incident light. The effects of varied top metal and PC film thicknesses on the absorption spectrum are examined experimentally, Figs. 3(a) and 3(c), and by transfer matrix calculations, Figs. 3(b) and 3(d). The broadband absorption spectra are shown for top tungsten film thicknesses of 3, 6, 9, 12 and 15 nm while keeping constant thicknesses (100 and 50 nm, respectively) of PC and alumina spacer films, Fig. 3(a). For 3- and 6-nm-thin top tungsten films, a narrow band around 480 nm with an absorbance of 96% and a wide band around 1220 nm with 76% absorbance are clearly seen. The narrowband absorption around 480 nm is due to the formation of discontinuities in the tungsten film at ultra-low metal thicknesses [34]. In the case of a 9-nm-thin top tungsten layer, absorption lies above 90% at wavelengths from 530 to 1510 nm, with a maximum absorbance of 97%. The absorbance reaches its maximum value (98% at 650 nm) for a 12-nm-thick top tungsten layer, and absorption above 90% is attained in the wavelength range spanning from 530 nm to 1640 nm. In the case of 15-nm-thick and thicker top tungsten films, the bandwidth of high absorption reduces due to the fact that light can no longer penetrate the top layer with sufficient amplitude to be couple critically to the resonator.

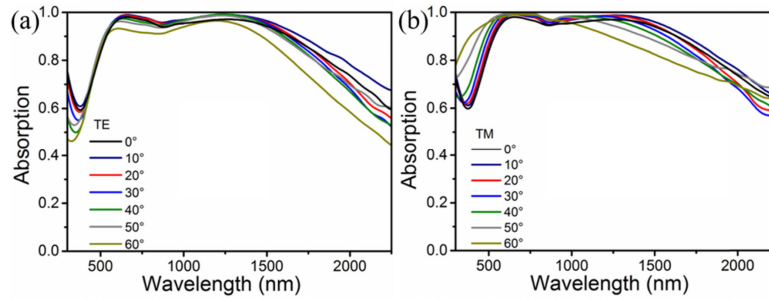


Fig. 4. Absorption spectra of the MIMPC resonator for 50 nm alumina spacer film with the different oblique angles of incident light (0° - 60°) for TE (a) and TM (b) polarization.

For the resonator without a PC layer, Fig. 3(c), wide-band absorption around 800 nm with a maximum absorption of 84% is observed. In the case of a 50-nm-thick PC film, a blue-shift in the absorption band along with a decrement in the bandwidth is seen. For a 100-nm-thick PC film, a maximum absorbance of 98% around 650 nm is obtained, with the broadband absorption above 90% occurring in the wavelength range from 530 to 1640 nm. A change in the absorption bandwidth, as well as absorbance, is seen for the PC layer thickness of 150 nm. In general, unitary absorption can be obtained only when the optical impedance of the absorber is matched with the impedance of the medium from which the light is incident on the absorber [17, 35–37]. When the impedance matching condition is fulfilled, all reflections from the resonator cancel out, and the resonator completely absorbs incident light. This amounts to the condition that the decay of the mode in the resonator has equal rates for Ohmic decay and decay to freely propagating modes, respectively [38–40]. The optimal thicknesses of the top tungsten and PC layer for maximum absorbance in the visible and near-infrared spectral regions are 12 and 100 nm, respectively.

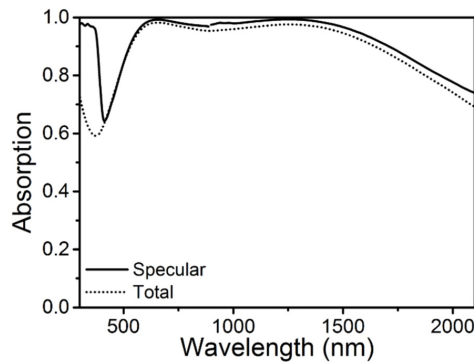


Fig. 5. Broadband absorption spectra due to specular and specular plus diffusive (total) reflections, taken from a resonator with spacer, top tungsten and PC layer thicknesses of 50, 12 and 100 nm, respectively.

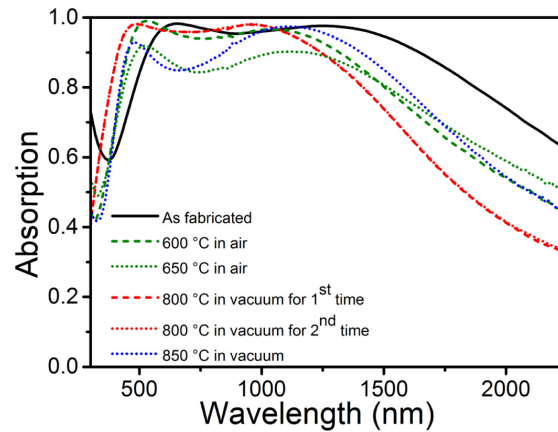


Fig. 6. Absorption spectra of an MIMPC resonator with a 50 nm alumina spacer film as fabricated, annealed in air at 600 and 650 °C, and annealed in vacuum at 800 and 850 °C.

To demonstrate the angle and polarization-insensitive absorption of the MIMPC resonator, we perform absorption measurements on the resonator with both TE and TM polarization, Figs. 4(a) and 4(b), respectively, for oblique angles of incidence. The angle of incidence is varied up to 60° in steps of 10° for the MIMPC resonator with a 50-nm-thick alumina spacer, 12-nm-thin top tungsten and 100-nm-thick PC films. In the case of TE polarization, Fig. 4(a), the MIMPC resonator exhibits a maximum absorption of 98% at angles of incidence of up to 50°. The broadband absorption starts decreasing at the angle of 60°, but remains above 90% over a broad spectral range with a maximum absorbance of 96%. Since the total thickness of the resonator is on the sub-wavelength scale, the accumulated phase change in the resonator due to propagation is small and depends to a large extent on the reflection and transmission phases [41]. Thus, the MIMPC resonator exhibits absorption over visible and near-infrared regions of the spectrum in a broad range of angles of incidence. The absorption loss at higher incident angles is due to the change in the increased path length of the incident light. The angle-dependent absorption spectra of the MIMPC resonator for TM polarization is shown in Fig. 4(b). The spectra show broadband absorption response similar to the TE polarization except for angles of 50° and 60°, where a significant change in absorption bandwidth and a decrease in absorbance in the near-infrared is observed. The absorption spectra were taken by a Perkin Elmer UV-vis-NIR spectrometer equipped with an integrating sphere, which has a minimum angle of incidence of 8° for the reflection measurements. Thus, the total absorption spectra contain both specular and diffuse reflections. A custom-made setup is used to measure the absorption spectrum due to specular reflection [42, 43]. The absorption spectra taken on an MIMPC resonator with a 50 nm alumina spacer, 12 nm top tungsten and 100 nm PC films for specular and, specular plus diffusive reflections are shown in Fig. 5. A good correspondence is observed between the absorption spectra obtained from the specular and total reflection measurements, which indicates that the layer quality is good and does not lead to significant scattering of the specularly incident beam.

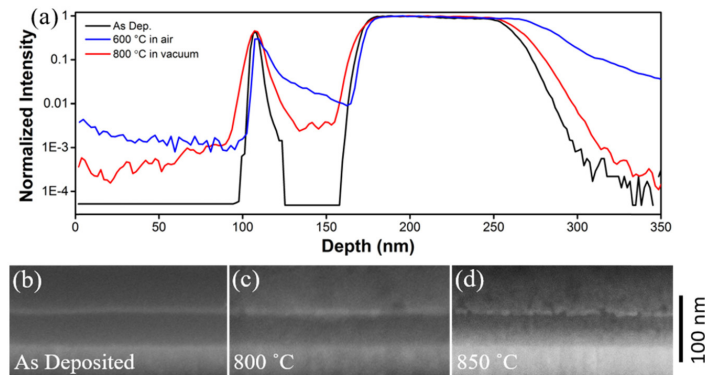


Fig. 7. (a) Secondary ion intensity of W for the depth profile of the MIMPC resonators (as fabricated, annealed at 600 and 800 °C in air and vacuum, respectively) with 50 nm alumina spacer and 100 nm PC films. Cross-sectional images of the resonator cavity as fabricated (b) and, after annealing at 800 °C (c) and 850 °C (d) for 4 hours, where each micrograph shares the same scale bar.

The thermal stability of the MIMPC resonator is examined by annealing a resonator with a 50 nm alumina spacer, 12 nm top tungsten, and 100 nm PC films up to 650 °C in air and 850 °C in vacuum, both for a duration of 4 hours. The temperature is ramped at a rate of 8 °C min⁻¹. A blue-shift in the absorption band is observed for the substrate annealed in air at 600 °C in comparison to the non-annealed substrate, see Fig. 6. Since the tungsten and alumina films are deposited at room temperatures, annealing at 600 °C can induce intrusive stresses in the thin layers that can lead to minor degradation of the resonator, which, however, maintains high absorbance over a broad spectral region which is comparable in width, and maximum absorbance to the non-annealed absorber. After annealing at 650 °C in air, a noticeable change in the absorption is seen due to the structural change of the resonator due to oxidation, which is avoided by use of the resonators in vacuum or surrounded by inert gas. Since, solar TPV systems operate in vacuum [32], the upper limit of working temperature of MIMPC resonators are tested with vacuum annealing procedure. Similar to the substrate annealed in air, a comparable blue shift in the absorbance band is observed for the substrate annealed at 800 °C in vacuum. In order to test the thermal cycling stress, the substrate is annealed second time at 800 °C which leaves the absorption spectrum entirely unchanged (Fig. 6), confirming the stability and durability of the absorber against thermal cycling stress at high working temperatures. Substrate degradation starts appearing at 850 °C, resulting in changes to the absorbance and bandwidth of the resonator. In order to investigate the structural changes of annealed substrates, a secondary-ion mass spectrometer is used. A typical compositional analysis of secondary ions of W plotted against the depth of the MIMPC resonator as fabricated, annealed in air at 600 °C and in vacuum at 800 °C, is shown in Fig. 7(a). In the case of vacuum annealing at 800 °C, a very low intensity of secondary ions of W throughout the spacer film confirms a low diffusion rate of tungsten into the adjacent alumina layers, whereas the air-annealed substrate at 600 °C shows a higher percentage of tungsten into the alumina layers due to oxidation. A comparison of samples that were annealed at 800 °C and 850 °C by SEM [Figs. 7(c) and 7(d)] shows a degradation of top W film due to the onset of percolation of the film, when raising the temperature significantly above 800 °C. This may be minimized by using other refractory dielectric materials (with higher melting points), such as magnesium oxide, hafnium oxide, etc., deposited by atomic layer deposition [44] which could be the focus of future work.

4. Conclusions

In conclusion, we have demonstrated an omnidirectional and polarization-insensitive broadband absorber, which is based on the refractory materials tungsten and alumina allowing for high-temperature applications. We show that the structure is stable at 800 °C, in terms of both optical properties and composition. The MIMPC resonator is fabricated using inexpensive and widely available film-deposition techniques, which allows wafer-scale processing of practical broadband absorbers. The development of broadband absorbers suitable for operation at temperatures of up to 800 °C and above has a significant positive impact on a range of practical applications, including TPV systems, solar TPV and solar thermal energy conversion. The tunable bandwidth, variable center wavelength, high absorbance, omnidirectionality, polarization-insensitivity and thermal stability of the resonator makes it an ideal absorber for, amongst others, (solar) TPV applications or as an absorber in commonly used infrared bands. Our findings will help accelerate the adoption of specifically tailored broadband absorbers in efficient thermal systems.

Acknowledgments

We acknowledge financial support from the Danish Council for Independent Research (the FTP project PlasTPV, contract no. 1335-00104), Det Obelske Familiefond, and Direktor Ib Henriksens Fond.

Appendix E

Hot-spot Engineering in 3D Multi-branched Nanostructures: Ultrasensitive Substrates for Surface Enhanced Raman Spec- troscopy

Hot-Spot Engineering in 3D Multi-Branched Nanostructures: Ultrasensitive Substrates for Surface-Enhanced Raman Spectroscopy

Manohar Chirumamilla,* Anisha Chirumamilla, Alexander S. Roberts, Remo Proietti Zaccaria, Francesco De Angelis, Peter Kjær Kristensen, Roman Krahne, Sergey I. Bozhevolnyi, Kjeld Pedersen, and Andrea Toma*

The detection of probe molecules at ultralow concentrations, even at the single-molecule level, can be addressed with the breakthrough concept of plasmonic hot-spot engineering. In view of that, the fabrication of nanostructures endowed with sub-10 nm gaps and extremely large near-field enhancement has gained increasing attention, becoming a key-condition for improved sensitivity. The present work demonstrates a new perspective in ultrasensitive detection by engineering every individual plasmonic nanostructure with a giant electric field confinement and superior hot-spot densities, thus eliminating the need for extremely narrow interparticle separations.

1. Introduction

The manipulation of strongly enhanced and localized electromagnetic (EM) fields, i.e., hot-spot engineering, is a consolidated concept in plasmon-based molecular sensing.^[1] Among them, surface enhanced Raman spectroscopy (SERS) provides label-free detection of analytes down to the single-molecule level by making use of hot-spots with high sensitivity and specificity.^[2–5] In SERS, the weak Raman signals are enhanced by many orders of magnitude (up to 10^7 or higher) due to the interaction between molecules and optical near-fields confined to and enhanced by plasmonic nanostructures. In view of that, positioning probe molecules in the vicinity of hot-spots is crucial for improving the SERS enhancement factor and therefore the detection limit.^[2,6,7] For instance, Le Ru et al.^[8] have shown that, for a system of silver particle dimers, 98% of the

SERS signal is provided by only 2% of the molecules adsorbed at positions with strongly enhanced EM fields. It is therefore imperative for sensing applications at ultralow molecule concentrations to design and fabricate nanostructures featuring sufficiently high hot-spot densities. So far, nanostructures arranged in the form of dimers, arrays or clusters with separations of few nanometers have been used to engineer single/multiple hot-spots.^[9,10] However, the fabrication methods employed, whether bottom-up or top-down, suffer from irreproducibility and nonuniformity, due to practical limitations such as gap diffusion, proximity effect, agglomeration, etc.^[11] These difficulties call for alternative platforms in order to develop ultrasensitive SERS substrates, among which single plasmonic nanostructures with multiple branches and sharp protrusions are ideal candidates. In fact, the present architectures can sustain large hot-spot densities with precisely defined spatial locations, thus eliminating the need for sub-10 nm gaps in single/few molecules detection.^[12]

Multi-branched nanostructures can be realized by various methods, including colloidal and top-down approaches.^[7,13] Colloidal techniques provide metal nanoparticles with sharp tips but are still of limited capabilities with respect to the number of branches, spatial control of their placement, and uniformity, all of which hamper reproducible SERS applications. The poor spatial control over the formation of hot-spots can significantly be improved by fabricating multibranched nanostructures with lithographic methods and thereby realizing uniformly patterned (in terms of morphology and interparticle separation, IPS) periodic nanostructures.^[14]

Furthermore, the substrate supporting the nanostructures plays a key factor in determining the hot-spot strength.^[15,16] The vast majority of plasmonic nanostructures are fabricated on conventional bulk dielectric substrates. This causes strong EM field interactions between the nanostructure and the underlying material, thus reducing the near-field enhancement. In recent works, it has been demonstrated that nanostructures residing on nanopillars (3D nanostructures) can enhance the strength of optical near-fields by orders of magnitude as compared to the corresponding planar (2D) counterparts (Scheme 1a).^[3,17,18] Therefore, in the present work, 3D multi-branched nanostructures (3D MBNS) with number of arms

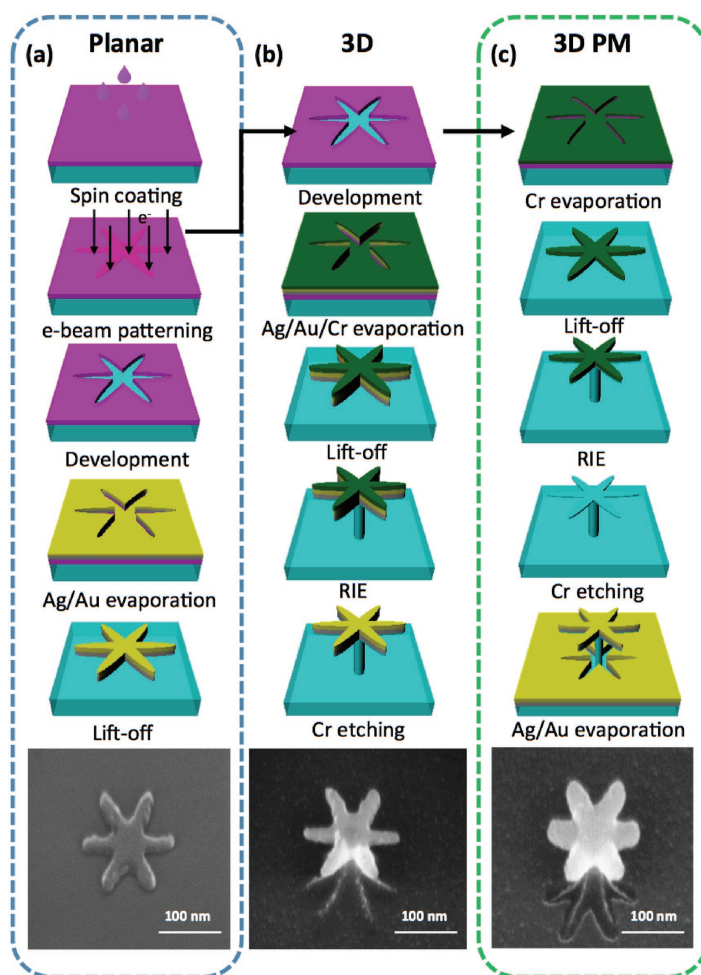
Dr. M. Chirumamilla, Dr. P. Kjær Kristensen, Prof. K. Pedersen
Department of Physics and Nanotechnology
University of Aalborg
Skjernvej 4A, Aalborg 9220, Denmark
E-mail: mch@nano.aau.dk

Dr. A. Chirumamilla, Prof. R. Proietti Zaccaria, Dr. F. De Angelis, Dr. R. Krahne, Dr. A. Toma
Istituto Italiano di Tecnologia
Via Morego 30, Genova 16163, Italy
E-mail: andrea.toma@iit.it

A. S. Roberts, Prof. S. I. Bozhevolnyi
Centre for Nano Optics
University of Southern Denmark
Campusvej 55, Odense 5230, Denmark

DOI: 10.1002/adom.201600836





Scheme 1. a–c) Schematic representation of the fabrication protocol for six branch nanostructures with planar, 3D, and 3D PM topologies. The corresponding fabricated nanostructures are shown in the SEM images.

from four to ten (in the following named S4 to S10) detached from dielectric substrates, and/or perforated metal (PM) layers were systematically engineered for achieving the best combination of hot-spot density and optical near-field enhancement. The corresponding topologies have been schematically illustrated in Scheme 1b,c. To this end, planar and 3D bimetallic (Au/Ag) plasmonic nanostructures with multiple-branches were fabricated by electron-beam lithography (EBL) and reactive ion etching (RIE) techniques. The advantage of double-layer Au/Ag nanostructures is the combination of high chemical stability and high field enhancement that cannot be provided by the single metal components.^[4,19] The far-field and near-field optical responses of the nanostructures were experimentally evaluated by reflection and Raman spectroscopy. In particular, the formation of multiple hot-spots with strongly enhanced local EM

fields and the subsequent detection of analyte molecules at ultralow concentrations (p-Aminothiophenol (p-MA) and Rhodamine-6G (R6G) down to 1×10^{-15} M) have been demonstrated through SERS measurements.

2. Results and Discussion

The detailed protocol for the fabrication of planar, 3D and 3D PM structures with multibranch geometry is presented in Scheme 1a–c and described in the Experimental Section. The corresponding scanning electron microscope (SEM) images (54° tilted view) of the fabricated nanostructures have been placed at the bottom of each panel, highlighting the difference between the various topologies. For 3D PM nanostructures, metallic perforations are clearly visible in the SEM image (Scheme 1c). To avoid strong near-field coupling between the individual unit of the array, a 200 nm IPS was chosen. In order to explore the effect of topology on the plasmon resonances, the height (H), size (S), and tip radius (T_t) for all nanostructures have been fixed to 150, 140, and 10 nm, respectively (see the schematic illustration reported in Figure 1a,c). A typical SEM image of 3D MBNS structures for S8 geometry with 200 nm IPS and 340 nm array periodicity is displayed in Figure S11 in the Supporting Information, demonstrating their structural uniformity and spatial homogeneity. The morphology of nanostars with four to ten branches is depicted in Figure 1b. The corresponding surface area has been extracted from the SEM images, obtaining a value of 4400, 5500, 6400, 7300, 9500, 10 100, and 10 700 nm², for the structures S4, S5, S6, S7, S8, S9, and S10, respectively. We notice that more than ten branches are not feasible for 140 nm sized structures, since the individual protrusions are no longer well defined.

Figure 1d illustrates a typical SERS spectrum of p-MA at 1×10^{-15} M concentration deposited by chemisorption (see the Experimental section) on the 3D MBNS with S8 geometry. The characteristic Raman modes at 1077 and 1590 cm⁻¹ are clearly visible and highlight the viability of the device for ultrasensitive Raman applications. Here the incident laser wavelength, accumulation time, and power were set to 785 nm, 3 s, and 1 mW, respectively, while the incident light polarization was fixed parallel to the x -direction.

In order to assess the number of branches effect on the hot-spot formation and plasmonic behavior, the near-field distribution (computer simulation technology-microwave, CST-MW) and far-field response (Synopsis' Optical Solutions, RSoft) of MBNS were numerically simulated. In particular, the near-field behavior has been evaluated through finite integration

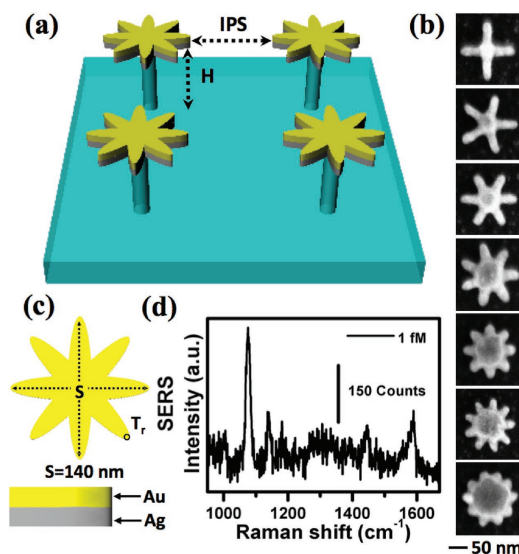


Figure 1. a,c) Schematic of bimetallic 3D MBNS structures for S8 layout, illustrating the geometrical parameters: silicon pillar height H , interparticle separation IPS , tip radius T_r , and structure size S . b) Representative SEM images (top view) of 3D MBNS with four to ten branches (S4–S10 from top to bottom); every micrograph shares the same scale bar. d) SERS spectrum recorded from p-MA (chemisorbed from 1×10^{-15} M concentrated solution) on 3D MBNS structure with S8 geometry.

technique (FIT) while far-field response was determined through rigorous coupled wave analysis (RCWA). Indeed, while the former approach is very suitable for determining the electromagnetic field distribution within sub-wavelength structures, the latter one is particularly convenient for evaluating the transmission/reflection/absorption spectra of periodic structures. **Figure 2a–g** shows the electric field enhancement ($|E/E_0|$) distribution of S4–S10 planar nanostructures in correspondence of their localized surface plasmon resonance (LSPR). The relative wavelengths have been reported in **Figure 2h** (blue triangles). Two hot-spots along the incident polarization direction (x -axis) are clearly visible for the S4 configuration (**Figure 2a**). An increase in the hot-spot density is observed when raising the number of branches, accompanied by a strong blue-shift in the LSPR position (**Figure 2h**).^[20]

Reflectance measurements have been performed on MBNS (S4–S10) with planar and 3D architectures. **Figure 3a** shows the typical experimental results from planar, 3D and 3D with PM layer (for schematics, see **Figure 3b–d**) for S8 geometry. The reflectance spectra have been normalized with respect to the unpatterned area of the corresponding substrate. The experimental results match the theoretical calculations, reported in **Figure 3e**. For planar architectures (**Figure 3a**, black trace, resonating around 1165 nm), the local near-fields are confined at the interface between metal and bulk silicon substrate (**Figure 3f**), weakening the local EM field enhancement $|E/E_0| = 20$, and limiting the accessible regions (hot-spot volume) for molecule detection. Surface plasmon resonances in high refractive index materials (such as silicon) are tightly confined within

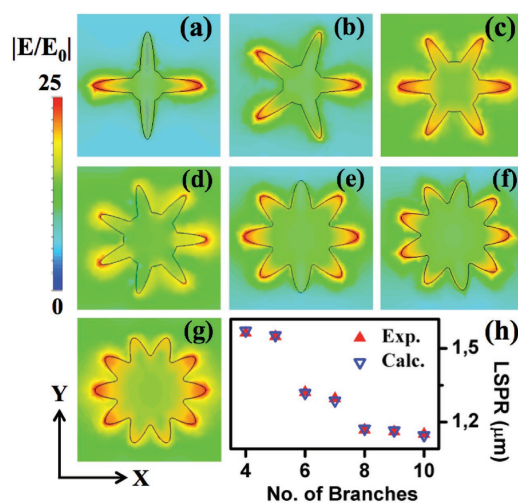


Figure 2. a–g) The total electric field distribution of planar MBNS for S4–S10 architectures obtained at a distance of 1 nm above the nanostructure for their characteristics LSPRs (h) in the x - y plane. The illuminating EM field is polarized along the x -direction.

the substrate, resulting in low optical near-field strengths, low extinction-cross sections, large propagation losses, and strong red-shifts with the broadening of resonances when compared to low refractive index materials (e.g., glass).^[15,21] In order to avoid the confinement of the hot-spots into the bulk substrate and to create an effective low index medium, it is essential to engineer further the present layout. The contact area of the metallic nanostructure interacting with the dielectric substrate can be decreased by introducing a dielectric nanopedestal, which decouples the strong optical-near fields localized at the metal surface from the bulk substrate. Here RIE has been used to carve out the dielectric medium underneath the metallic nanostructures, thus promoting the formation of a thin, pedestal-like support structure (**Figure 3c,d**).

For 3D MBNS structures, a significant blue shift of LSPR (**Figure 3a,e**—green band in the olive trace) has been observed with a resonance maximum at around 680 nm. Numerical calculations show that the separation of the metal nanostructures from the bulk substrate leads to a significant EM field enhancement, $|E/E_0| = 80$ (**Figure 3g**). Furthermore, the nanopedestal introduction causes a huge blue-shift (around 485 nm) in the LSPR spectral position, since the plasmon resonance is very sensitive to the dielectric environment.^[17,22,23] The elevated 3D design has additional advantages in comparison with other works:^[22] the regions of enhanced EM fields are completely accessible to the probe molecules used in analytical techniques, and it offers a low effective dielectric medium along with the high chemical and structural stability of silicon. For 3D MBNS with PM layer structures, multiple resonances are observed in the reflection spectrum (**Figure 3a,e**, red trace). To elucidate the origin of these modes, near-field distributions were calculated and analyzed in **Figures S12** and **S13** in the Supporting Information. It is worth noticing that the electric field (**Figure 3h**) and the surface current distributions (**Figure S12**, Supporting

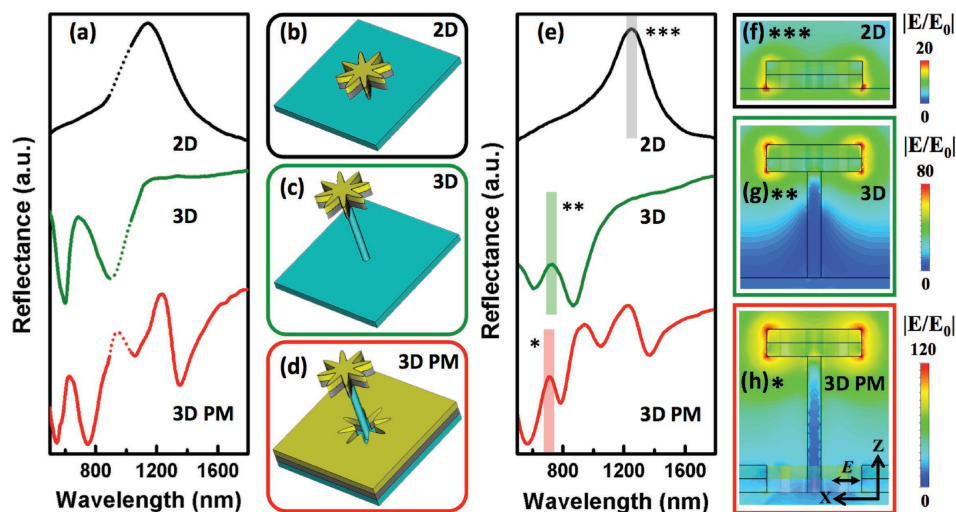


Figure 3. a) Experimental reflectance spectra for S8 architectures with planar, 3D, and 3D PM topologies depicted by black, olive, and red traces, respectively. The dotted lines are a guide to the eye bridging the spectral region not accessible by our experimental setup. b–d) Schematic representation of the different topologies. e) Simulated reflectance spectra of periodic S8 nanostructures with planar, 3D, and 3D PM layouts. f–h) Electric near-field distribution in the x – z plane for S8 nanostructures shown in (a,e) at their characteristic LSPR position, 1165 nm (***, gray band), 680 nm (**, green band), and 650 nm (*, red band) for planar, 3D, and 3D PM layouts, respectively.

Information) at 650 nm show a dipolar behavior with strong electric field localization at the nanostructure ends, thus confirming the LSP nature of this resonance. A slight variation in the nanostructure LSPR position (i.e., a blue-shift of 30 nm) with respect to the 3D configurations without PM layer is observed.^[24] To illustrate the PM role on the far-field response of the 3D MBNS PM nanostructure, numerical calculations were performed on the PM layer alone, without taking into account the complete 3D layout (Figure S12c black trace, and Figure S13, Supporting Information). The star-shaped hole in the PM layer behaves like a plasmonic cavity and allows the excitation of LSPR as well as surface plasmon polarizations (SPPs) propagating at the metal/air and metal/substrate interfaces.^[25] A complete description of the modes supported by the structures is analyzed in Figure S12 and S13 in the Supporting Information, where the near- and far-field responses have been investigated. Turning back to the 3D MBNS PM structures, we find that for the S8 architecture the resonances of the isolated PM layer and 3D structure can be clearly recognized (Figure 3a,e, red trace). SPP modes propagating at the two interfaces of the PM layer can be associated to the spectral features at 543 and 1050 nm, while the resonances at 620 and 1350 nm can be attributed to the LSPRs supported by MBNS and PM holes, respectively (a deeper investigation has been carried out in Figure S13 in the Supporting Information). Reflection spectra for morphological changes (from four to ten branches) of 3D MBNS PM in the visible region are shown in Figure S14 in the Supporting Information.

The sensing performances of MBNS structures were evaluated by SERS measurements on the S8 geometry with p-MA molecules chemisorbed from 1×10^{-6} M solution concentration. Since the Raman enhancement scales with the fourth power of

the field, 3D MBNS PM with an EM field enhancement factor of 120 can increase the Raman signals up to a factor of 10^8 .^[26] Figure 4a shows the SERS spectra from the S8 architectures with planar, 3D, and 3D PM layer topologies (black, olive, and red traces, respectively). The laser excitation wavelength, power, and accumulation time were set to 785 nm, 1 mW, and 30 s, respectively, while the incident light was polarized along the x -axis. Strong and well-resolved characteristic Raman modes of p-MA centered at 1077, 1140, 1179, 1390, 1440, and 1590 cm^{-1} , corresponding to the molecular vibrations of C–S-stretching, C–H-bending, C–H-bending, C–H-bending + C–C-stretching, C–C-stretching + C–H-bending, and C–C-stretching, respectively, are clearly visible for the 3D MBNS PM (red trace) structures.^[3,4] For planar nanostructures, a low signal-to-noise ratio SERS spectrum (black trace) is observed. Two peaks centered at 1077 and 1590 cm^{-1} are identified in the spectrum with intensity just above the noise level while the other bands are buried in the background noise. When the metal nanostructures are elevated from the bulk substrate by a nanopedestal, the SERS signal intensity increases significantly and the presence of characteristic Raman modes of p-MA in the full spectral range is clearly observable in the olive trace. A further rise in the SERS signal intensity has been obtained for 3D MBNS PM structures (red trace), owing to the coupling of reflected light from the PM back-plane with the metallic nanostructures. The observed SERS signal enhancement is in accordance with the rise in the electric field enhancement, as confirmed by numerical calculations (Figure 3g,h).

The 3D MBNS PM structures show an average enhancement of 5×10^6 , obtained by evaluating the peak at 1077 cm^{-1} recorded from p-MA on substrates with S8 geometry (an unpatterned area of the AgAu film has been used as a

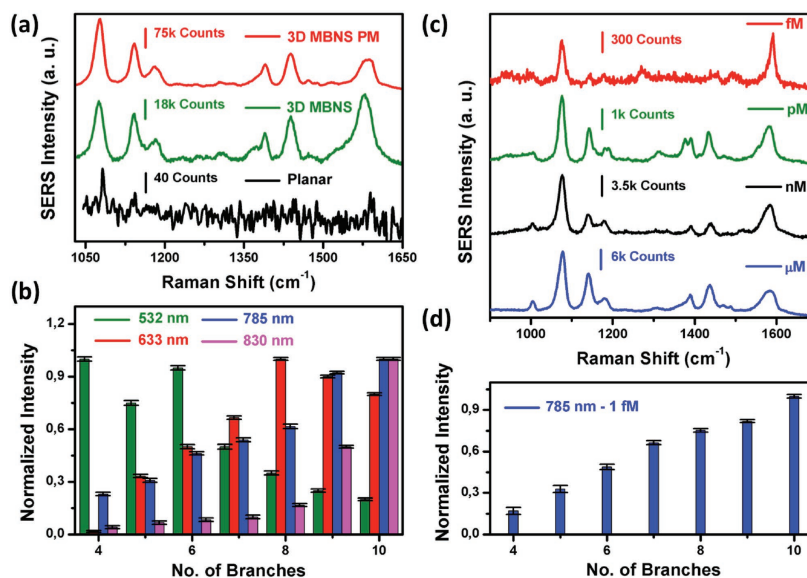


Figure 4. a) SERS spectra of p-MA chemisorbed at 1×10^{-6} M concentration obtained from S8 MBNS on planar, 3D, and 3D PM topologies, black, green, and red traces, respectively. b) SERS intensity variation of 1077 cm^{-1} band as a function of a number of branches for 532, 633, 785, and 830 nm laser excitation wavelengths. c) SERS spectra recorded from p-MA molecules chemisorbed on 3D MBNS PM structures with S8 geometry at 1×10^{-6} M, 1×10^{-9} M, 1×10^{-12} M and 1×10^{-15} M concentrations represented by red, blue, green, and orange traces, respectively. d) SERS signal intensity versus a number of branches at 1×10^{-15} M concentration for 785 nm laser excitation.

reference). The detailed method adopted for the enhancement factor calculation has been reported in Supporting Information. We underpin that the planar AgAu film itself acts as SERS enhancing substrate and provides an enhancement factor in the order of 10^4 (Supporting information),^[27] hence the absolute enhancement factor of the MBNS structures are estimated to be in the order of 10^{11} . The uniformity of the substrate, reproducibility of the SERS signals and homogeneity of the molecular deposition have been evaluated by taking SERS measurements (around 70 spectra) on 3D MBNS PM structures with S8 geometry laid on the same substrate at different spatial positions. A 3D waterfall SERS spectrum shows uniform signal intensity for each characteristic band position (Figure S15, Supporting Information); the maximum standard deviation of SERS intensity at 1077 cm^{-1} is less than 5%, which highlights the substrate reproducibility in terms of uniform hot-spot density, and homogeneity of molecular chemisorption. To further understand the influence of the hot-spots on the SERS intensity, Raman measurements were performed on 3D MBNS PM structures (from S4 to S10) with four different excitation sources. In order to get the same molecular surface absorption properties, nanostructures with four to ten branches were fabricated on the same substrate. Figure 4b shows the SERS intensity of the 1077 cm^{-1} band recorded with laser sources at 532, 633, 785, and 830 nm, depicted by green, red, blue, and magenta bars, respectively. The SERS intensities have been independently normalized for each laser source with respect to the highest peak intensity obtained in the series. For 830 and 785 nm laser excitations, a monotonic increment in SERS signal intensity with increasing branch number can be observed, where the excitation source

is out of resonance with the LSPRs (Figure S14, Supporting Information). In this case, the SERS signal intensity increases with the number of hot-spots. In the case of 633 nm excitation, the S8 architecture shows a significantly higher SERS signal intensity compared to other nanostructures, because the excitation wavelength approaches the LSPR of the S8 nanostructure. Similarly, the variations in the SERS signal intensity for 532 nm excitation can be understood in terms of closeness to the LSPR. SERS spectra of 3D MBNS PM structures with S8 geometry for different excitation sources demonstrate that such nanostructures enable fine-tuning of the SERS performance that can be adapted to a broadband of excitation wavelengths, which is of great advantage for practical SERS applications (Figure S16, Supporting Information).

Figure 4c presents the SERS spectra of p-MA molecules on the 3D MBNS PM structures with S8 geometry for concentrations ranging from 1×10^{-6} M to 1×10^{-15} M. The excitation wavelength, power and accumulation time are set to 785 nm, 1 mW, and 3 s, respectively. The SERS spectra show clearly distinguishable characteristic peaks of p-MA with good signal to noise ratio. We note that for low concentrations only a limited number of molecules are available for adsorption on the metal nanostructures and therefore the SERS signal intensity decreases. The SERS spectrum from 1×10^{-15} M concentration (orange trace) clearly shows two characteristic bands of p-MA at 1077 and 1590 cm^{-1} ; other modes are slightly above the noise level. Detection of p-MA molecules at 1×10^{-15} M concentration highlights the capabilities of the proposed substrate toward single/few molecule detection. Similarly, typical SERS spectra of R6G at different molecular coverage density are shown in

Figure S17 in the Supporting Information. At 1×10^{-15} M concentration, the prominent peaks of R6G at 1364 and 1610 cm^{-1} are clearly distinguishable in the spectrum.^[4,10] Figure 4d shows the SERS intensity (normalized with respect to 3D MBNS PM structures with S10 geometry for 1077 cm^{-1} band position) versus the number of branches for 785 nm laser excitation at 1×10^{-15} M concentration. A monotonic rise in the SERS intensity is observed with an increasing in the number of branches from four to ten, due to a corresponding growth of the hot-spot density. Therefore, the number of branches and 3D topology play a key role in the SERS signal enhancement. The increased hot-spot density successfully boosts the SERS signal intensity at extremely low concentrations, and the detection of analyte molecules at 1×10^{-15} M firmly establishes the ultrasensitive capability of the proposed 3D multibranched nanostructures.

3. Conclusion

In summary, 3D multibranched nanostars with perforated metal layers have been conceived and proposed as ideal platforms for high density hot-spot generation, particularly suitable for detection at extremely low concentration (1×10^{-15} M), as demonstrated by SERS measurements on p-MA and R6G molecules. Our systematic study elucidates the influence of the number of branches on hot-spot generation, and the effect of dielectric substrate and underlying perforated metal layer on the far-field and near-field response. Tuning and optimization of the multibranched nanostar structures with respect to the excitation sources enable average enhancement factors of 5×10^6 with good homogeneity over the entire device. These engineered SERS substrates pave the way toward the commercialization of ultrasensitive SERS devices through economically scalable manufacturing methods and cost-effective approaches.^[4] Moreover, the unique properties offered by multibranched architectures, i.e., the realization of multiple hot-spots on a single nanostructure, envision clear-cut perspectives in hyperspectral Raman imaging, miniaturized Raman-on-chip biomolecule detection, and more in general for the development a new-era of sensing technology.

4. Experimental Section

Fabrication of Multi-Branched Nanostructures: All presented MBNS structures were fabricated by EBL (Raith 150-Two) and subsequent RIE (SENTECH) techniques. A detailed protocol of the fabrication procedure along with SEM images is shown in the Scheme 1. Planar, 3D and 3D PM nanostructures had the EBL step in common. A 250 nm polymethyl methacrylate (PMMA) layer was formed by spin coating an anisole based PMMA solution (PMMA-A2, average molecular weight 950 kDa, Micro Chem Corp.) at 3000 rpm for 60 s onto a p-type c-Si (100) wafer and subsequent baking (180 °C for 9 min on a hot plate). The PMMA was exposed (Raith 150-Two, operated with an acceleration voltage of 30 kV and a beam current of 130 pA) with an area dose of 1 mC cm^{-2} . The PMMA layer was then developed in a 1:3 mixture of methyl isobutyl ketone and isopropanol ratio at 4 °C for 180 s.

To obtain planar nanostructures, a 36 nm thick bi-layer of 18 nm Au on 18 nm Ag was deposited. Excess resist and metal layers were removed by ultrasonically assisted lift-off in acetone. 3D nanostructures were fabricated by a first evaporating a bi-layer of Au-on-Ag (18 nm + 18 nm) and a subsequent thermal deposition of a 20 nm chromium

layer. Ultrasonically assisted lift-off was then performed. Subsequently, the samples were reactive-ion etched in an atmosphere of SF_6 (30 Standard Cubic Centimeters per Minute - SCCM) + C_4F_8 (32 SCCM) at 1 mTorr. The process parameters temperature, power, and etching time were held at 4 °C, 18 W, and 25 s, respectively, which yielded an etch rate of $\approx 100 \text{ nm min}^{-1}$. The excess chromium film was then removed by a commercially available chromium etch (Sigma-Aldrich). 3D MBNS PM structures were obtained by depositing 20 nm of chromium after developing the EBL-patterned substrates. After the deposition of chromium, acetone lift-off left behind star-shaped chromium patterns on silicon, serving as etching masks. RIE then shaped the pedestals supporting the stars, and subsequently, the chromium mask was etched away, leaving behind silicon stars on poles. Finally, an Au-on-Ag (18/18 nm) bi-layer was evaporated at a deposition rate of 0.3 \AA s^{-1} to form the resonators as well as the perforated film.

Numerical Calculations: The near-field behavior has been evaluated through FIT (CST-MW) while far-field response was determined through rigorous coupled wave analysis (Synopsys' Optical Solutions, RSoft). The former approach was very suitable for determining the electromagnetic field distribution within sub-wavelength structures; the latter one was more specific for providing the transmission/reflection/absorption spectra of periodic structures.

Optical Characterization: The authors measured linear spectra of the nanostructures under normal incidence, in an Olympus IX-73 research microscope. Broadband illumination of the sample was performed with a 100 W halogen lamp (Olympus) which gave intensity in the visible and near-infrared spectral range. The polarization state was controlled with a Glan-Taylor polarizer, giving linearly polarized light. The authors measured the reflection spectra with a 50x objective of numerical aperture 0.5. The collected light was fiber-coupled to a spectrometer with a Peltier-cooled charge-coupled-device from Ocean Optics (QE65000 and NIRquest512 for visible and near-infrared measurements, respectively).

Surface Enhanced Raman Spectroscopy: SERS spectra were recorded with a Renishaw inVia micro-Raman spectrometer equipped with 150x LEICA HCX PL APO objective (numerical aperture 0.95), laser excitations at 830, 785, 633, 532 nm, and a thermo-electrically cooled charge-coupled device (CCD) as a detector. Consequently, the laser spot diameter was around 680 nm, 800 nm, 1 μm , and 1.07 μm for excitation wavelengths of 532, 633, 785, and 830 nm, respectively. The instrument was calibrated with respect to the first order silicon peak at 520 cm^{-1} , and all the spectra were recorded in backscattering geometry at room temperature. The spectra were baseline corrected with a third order polynomial by using Wire 3.0 software. The probe molecules (p-MA and Rhodamine) employed in this study were purchased from Sigma-Aldrich.

Analyte Preparation: A stock solution of p-MA at 1×10^{-3} M concentration was prepared by dissolving an appropriate amount of the solid analyte (Sigma-Aldrich) into 15 mL of ethanol. Afterward, 1×10^{-6} M to 1×10^{-15} M solutions were prepared by a further dilution. For SERS measurements, molecules were deposited on to the substrate by chemisorption process. The samples were dipped for 20 min, and then washed in ethanol to remove excess molecules that were not covalently bound to the metallic surface, and finally purged with nitrogen gas. In the case of R6G, the stock solution was prepared by diluting the molecules into deionized water.

Supporting Information

Supporting Information is available from the Wiley Online Library or from the author.

Acknowledgements

The authors acknowledge financial support from the Danish Council for Independent Research (the FTP project PlasTPV, contract no.

1335-00104). A.T. acknowledges support by Compagnia di San Paolo under grant agreement ID ROL 10262.

Received: October 11, 2016

Published online:

- [1] a) M. Moskovits, *Nature* **2011**, 469, 307; b) R. Zhang, Y. Zhang, Z. C. Dong, S. Jiang, C. Zhang, L. G. Chen, L. Zhang, Y. Liao, J. Aizpurua, Y. Luo, J. L. Yang, J. G. Hou, *Nature* **2013**, 498, 82; c) D. Punj, M. Mivelle, S. B. Moparthi, T. S. van Zanten, H. Rigneault, N. F. van Hulst, M. F. Garcia-Parajo, J. Wenger, *Nat. Nanotechnol.* **2013**, 8, 512; d) A. Ahmed, R. Gordon, *Nano Lett.* **2011**, 11, 1800.
- [2] P. G. Etchegoin, E. C. Le Ru, *Phys. Chem. Chem. Phys.* **2008**, 10, 6079.
- [3] M. Chirumamilla, A. Toma, A. Gopalakrishnan, G. Das, R. P. Zaccaria, R. Krahn, E. Rondanina, M. Leoncini, C. Liberale, F. De Angelis, E. Di Fabrizio, *Adv. Mater.* **2014**, 26, 2353.
- [4] A. Gopalakrishnan, M. Chirumamilla, F. De Angelis, A. Toma, R. P. Zaccaria, R. Krahn, *ACS Nano* **2014**, 8, 7986.
- [5] a) S. Harmsen, R. Huang, M. A. Wall, H. Karabeber, J. M. Samii, M. Spaliviero, J. R. White, S. Monette, R. O'Connor, K. L. Pitter, S. A. Sastra, M. Saborowski, E. C. Holland, S. Singer, K. P. Olive, S. W. Lowe, R. G. Blasberg, M. F. Kircher, *Sci. Transl. Med.* **2015**, 7, 271ra7; b) A. Gopalakrishnan, M. Malerba, S. Tuccio, S. Panaro, E. Miele, M. Chirumamilla, S. Santoriello, C. Dorigoni, A. Giugni, R. Proietti Zaccaria, C. Liberale, F. De Angelis, L. Razzari, R. Krahn, A. Toma, G. Das, E. Di Fabrizio, *Ann. Phys.* **2012**, 524, 620.
- [6] a) H. Xu, J. Aizpurua, M. Käll, P. Apell, *Phys. Rev. E* **2000**, 62, 4318; b) J. M. McLellan, Z.-Y. Li, A. R. Siekkinen, Y. Xia, *Nano Lett.* **2007**, 7, 1013; c) E. M. Perassi, E. A. Coronado, *J. Phys. Chem. C* **2013**, 117, 7744.
- [7] F. S. Ou, M. Hu, I. Naumov, A. Kim, W. Wu, A. M. Bratkovsky, X. Li, R. S. Williams, Z. Li, *Nano Lett.* **2011**, 11, 2538.
- [8] E. C. Le Ru, P. G. Etchegoin, M. Meyer, *J. Chem. Phys.* **2006**, 125, 204701.
- [9] a) R. Schreiber, J. Do, E.-M. Roller, T. Zhang, V. J. Schuller, P. C. Nickels, J. Feldmann, T. Liedl, *Nat. Nanotechnol.* **2014**, 9, 74; b) A. Hakonen, M. Svedendahl, R. Ogier, Z.-J. Yang, K. Lodewijks, R. Verre, T. Shegai, P. O. Andersson, M. Käll, *Nanoscale* **2015**, 7, 9405; c) A. Toma, G. Das, M. Chirumamilla, A. Saeed, R. Proietti Zaccaria, L. Razzari, M. Leoncini, C. Liberale, F. De Angelis, E. Di Fabrizio, *Microelectron. Eng.* **2012**, 98, 424.
- [10] M. Chirumamilla, G. Das, A. Toma, A. Gopalakrishnan, R. P. Zaccaria, C. Liberale, F. De Angelis, E. Di Fabrizio, *Microelectron. Eng.* **2012**, 97, 189.
- [11] a) M. Hu, F. S. Ou, W. Wu, I. Naumov, X. Li, A. M. Bratkovsky, R. S. Williams, Z. Li, *J. Am. Chem. Soc.* **2010**, 132, 12820; b) M. S. Schmidt, J. Hübner, A. Boisen, *Adv. Mater.* **2012**, 24, OP11; c) X. Xu, K. Kim, H. Li, D. L. Fan, *Adv. Mater.* **2012**, 24, 5457.
- [12] D. Radziuk, H. Moehwald, *Phys. Chem. Chem. Phys.* **2015**, 17, 21072.
- [13] a) K. Jung, J. Hahn, S. In, Y. Bae, H. Lee, P. V. Pikhitsa, K. Ahn, K. Ha, J.-K. Lee, N. Park, M. Choi, *Adv. Mater.* **2014**, 26, 5924; b) C. Forestiere, A. J. Pasquale, A. Capretti, G. Miano, A. Tamburrino, S. Y. Lee, B. M. Reinhard, L. Dal Negro, *Nano Lett.* **2012**, 12, 2037; c) B. Yan, A. Thubagere, W. R. Premasiri, L. D. Ziegler, L. Dal Negro, B. r. M. Reinhard, *ACS Nano* **2009**, 3, 1190; d) S. L. Kleinman, R. R. Frontiera, A.-I. Henry, J. A. Dieringer, R. P. Van Duyne, *Phys. Chem. Chem. Phys.* **2013**, 15, 21; e) L. Fabris, *Chem. Commun.* **2012**, 48, 9346; f) M. Chirumamilla, A. Gopalakrishnan, A. Toma, R. P. Zaccaria, R. Krahn, *Nanotechnology* **2014**, 25, 235303; g) H. Yuan, C. M. Wilson, J. Xia, S. L. Doyle, S. Li, A. M. Fales, Y. Liu, E. Ozaki, K. Mulfaul, G. Hanna, G. M. Palmer, L. V. Wang, G. A. Grant, T. Vo-Dinh, *Nanoscale* **2014**, 6, 4078.
- [14] A. Shiohara, Y. Wang, L. M. Liz-Marzán, *J. Photochem. Photobiol. C: Photochem. Rev.* **2014**, 21, 2.
- [15] M. Valamanesh, Y. Borensztein, C. Langlois, E. Lacaze, *J. Phys. Chem. C* **2011**, 115, 2914.
- [16] M. W. Knight, Y. Wu, J. B. Lassiter, P. Nordlander, N. J. Halas, *Nano Lett.* **2009**, 9, 2188.
- [17] C. Huck, A. Toma, F. Neubrech, M. Chirumamilla, J. Vogt, F. De Angelis, A. Pucci, *ACS Photonics* **2015**, 2, 497.
- [18] a) A. E. Cetin, D. Etezadi, H. Altug, *Adv. Mater.* **2014**, 2, 866; b) H. Chen, A. M. Bhuiya, R. Liu, D. M. Wasserman, K. C. Toussaint, *J. Phys. Chem. C* **2014**, 118, 20553.
- [19] a) L. Rivas, S. Sanchez-Cortes, J. V. García-Ramos, G. Morcillo, *Langmuir* **2000**, 16, 9722; b) W. Zhang, M. Rahmani, W. Niu, S. Ravaine, M. Hong, X. Lu, *Sci. Rep.* **2015**, 5, 8382.
- [20] W. Rechberger, A. Hohenau, A. Leitner, J. R. Krenn, B. Lamprecht, F. R. Aussenegg, *Opt. Commun.* **2003**, 220, 137.
- [21] A. Curry, G. Nusz, A. Chilkoti, A. Wax, *Opt. Express* **2005**, 13, 2668.
- [22] a) Y. Shen, J. Zhou, T. Liu, Y. Tao, R. Jiang, M. Liu, G. Xiao, J. Zhu, Z.-K. Zhou, X. Wang, C. Jin, J. Wang, *Nat. Commun.* **2013**, 4, 2381; b) K. Kumar, H. Duan, R. S. Hegde, S. C. W. Koh, J. N. Wei, J. K. W. Yang, *Nat. Nanotechnol.* **2012**, 7, 557.
- [23] a) A. Dmitriev, C. Häggglund, S. Chen, H. Fredriksson, T. Pakizeh, M. Käll, D. S. Sutherland, *Nano Lett.* **2008**, 8, 3893; b) K. C. Vernon, A. M. Funston, C. Novo, D. E. Gómez, P. Mulvaney, T. J. Davis, *Nano Lett.* **2010**, 10, 2080.
- [24] A. Tittl, P. Mai, R. Taubert, D. Dregely, N. Liu, H. Giessen, *Nano Lett.* **2011**, 11, 4366.
- [25] a) T. W. Ebbesen, H. J. Lezec, H. F. Ghaemi, T. Thio, P. A. Wolff, *Nature* **1998**, 391, 667; b) J. Li, J. Ye, C. Chen, L. Hermans, N. Verellen, J. Ryken, H. Jans, W. Van Roy, V. V. Moshchalkov, L. Lagae, P. Van Dorpe, *Adv. Opt. Mat.* **2015**, 3, 176.
- [26] K. Katrin, K. Harald, I. Irving, R. D. Ramachandra, S. F. Michael, *J. Phys.: Condens. Matter* **2002**, 14, R597.
- [27] S. M. Mahurin, J. John, M. J. Sepaniak, S. Dai, *Appl. Spectrosc.* **2011**, 65, 417.

Copyright WILEY-VCH Verlag GmbH & Co. KGaA, 69469 Weinheim, Germany, 2017.

ADVANCED OPTICAL MATERIALS

Supporting Information

for *Adv. Optical Mater.*, DOI: 10.1002/adom.201600836

Hot-Spot Engineering in 3D Multi-Branched Nanostructures:
Ultrasensitive Substrates for Surface-Enhanced Raman
Spectroscopy

Manohar Chirumamilla, Anisha Chirumamilla, Alexander S. Roberts, Remo Proietti Zaccaria, Francesco De Angelis, Peter Kjær Kristensen, Roman Krahné, Sergey I. Bozhevolnyi, Kjeld Pedersen, and Andrea Toma**

WILEY-VCH

Supporting Information

DOI: 10.1002/ (adom.201600836)

Article type: Full Paper

Hot-spot Engineering in 3D Multi-branched Nanostructures: Ultrasensitive Substrates for Surface Enhanced Raman Spectroscopy

Manohar Chirumamilla, Anisha Chirumamilla, Alexander S. Roberts, Remo Proietti Zaccaria, Francesco De Angelis, Peter Kjær Kristensen, Roman Krahné, Sergey I. Bozhevolnyi, Kjeld Pedersen and Andrea Toma**

Dr. M. Chirumamilla, Dr. P. Kjær Kristensen, Prof. K. Pedersen
Department of Physics and Nanotechnology, University of Aalborg, Skjernvej 4A, Aalborg, 9220, Denmark

E-mail: mch@nano.aau.dk

Dr. A. Chirumamilla, Prof. R. Proietti Zaccaria, Dr. F. De Angelis, Dr. R. Krahné, Dr. A. Toma,

Istituto Italiano di Tecnologia, Via Morego 30, Genova, 16163, Italy

E-mail: andrea.toma@iit.it

A. S. Roberts, Prof. S. I. Bozhevolnyi

Centre for Nano Optics, University of Southern Denmark, Campusvej 55, Odense, 5230, Denmark

Keywords: Hotspot engineering, 3D multibranch nanostar structures, plasmonics, electron beam lithography, Single Molecule Surface enhanced Raman scattering

WILEY-VCH

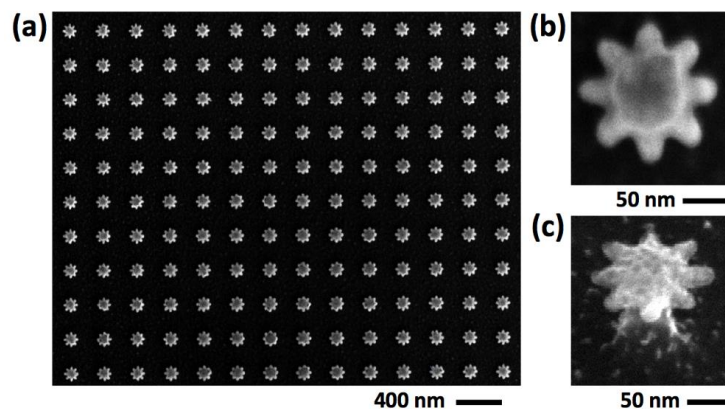


Figure S11. SEM images of 3D MBNS, S8 layout: In order to perform far-field spectroscopy, we fabricated $25\ \mu\text{m} \times 25\ \mu\text{m}$ size matrices of planar, 3D MBNS and 3D MBNS PM nanostars, each of them at a mutual distance of 340 nm in both directions. The homogeneity and uniformity of the fabricated nanostructures is highlighted by the SEM micrograph reported in (a). b, c) represent the magnified view of a single S8 nanostructure, top and tilted view, respectively.

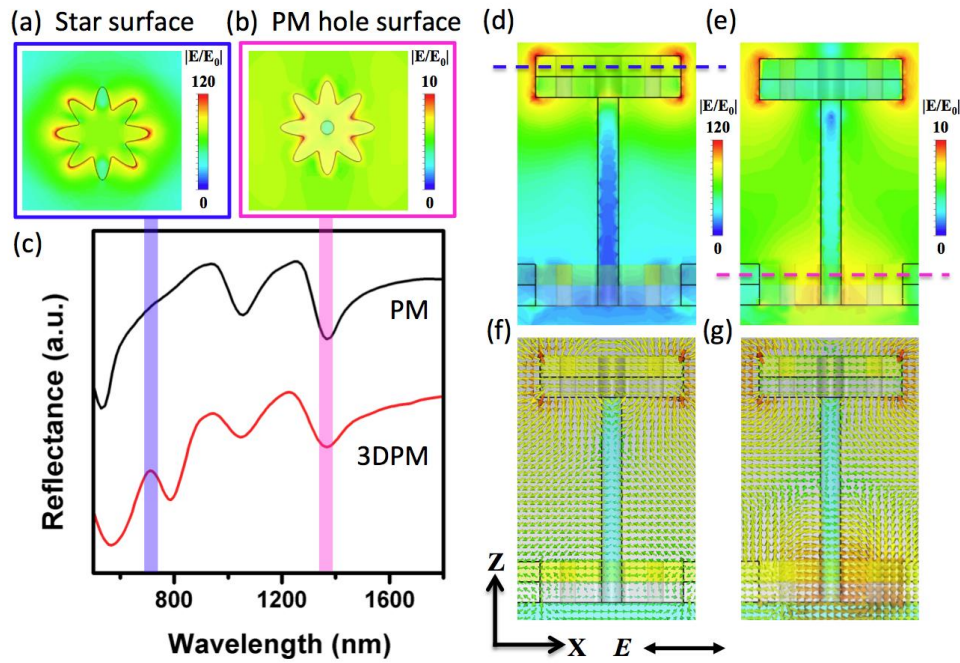


Figure SI2. Comparison between 3D MBNS PM and PM hole topologies: the optical response of the S8 architecture with PM hole and 3D MBNS PM topologies has been numerically evaluated. For 3D MBNS with PM layer, the electric field (Figure SI2a – top view and Figure SI2d – side view) and the surface current distributions (Figure SI2f) at 650 nm show a dipolar behavior with strong electric field localization at the nanostructure ends. As clearly highlighted by the far-field spectral behavior (Figure SI2c black and red traces), the peak at 650 nm appears only in the MBNS layout. Therefore, the present mode can be associated to the localized surface plasmon resonance of the 3D nanostar. On the contrary, for the reflection minimum at 1350 nm, the electric field (Figure SI2b – top view and Figure SI2e – side view) and the surface current distributions (Figure SI2g) are strongly localized at the sharp inward edges of the PM holes. This configuration can be ascribed to the localized surface plasmon resonance supported by the PM cavity. The blue and purple dashed lines in Figure SI2d and SI2e indicate the regions where the top view cut-outs (Figure SI2a and SI2b, respectively) have been evaluated.

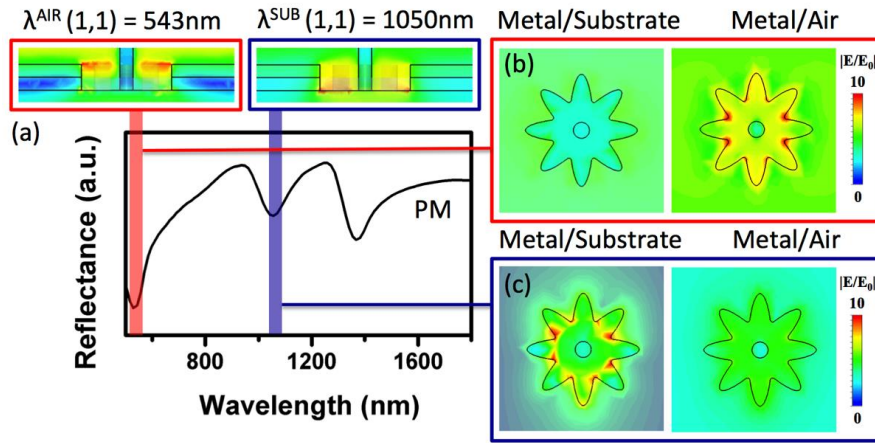


Figure SI3. Resonant Modes supported by PM structures: the star-shaped hole in the PM layer behaves like a plasmonic cavity and allows the excitation of LSPR as well as surface plasmon polaritons (SPPs) propagating at the metal/air and metal/substrate interfaces. The origin of the observed modes can be explained by calculating the near- and far-field responses of a PM layer alone (without 3D MBNS structures). By taking into account the momentum matching condition for perforated metallic holes (*i.e.* the Bragg's equation) we can obtain for a two-dimensional lattice:

$$k_0 \sin \theta \pm iG_x \pm jG_y = k_{mode}$$

and accordingly the SPP mode can be described by:

$$\lambda_{SPP} \cong \frac{p}{\sqrt{i^2 + j^2}} \sqrt{\frac{\epsilon_m \epsilon_d}{\epsilon_m + \epsilon_d}}$$

Where G_x and G_y are the reciprocal lattice vectors, i and j the grating orders, θ and k_0 the angle and the wavenumber of the incident light, p is the periodicity of the hole array and ϵ_m , ϵ_d are the dielectric functions of the metal and the surrounding medium. For a periodicity of 340 nm, SPPs excited at the metal/substrate interface show a reflection minimum at 1050 nm (Blue boxes in Figure SI3), which can be ascribed to the mode $\lambda_{(1,1)}^{SUB}$. On the contrary, SPPs propagating at the metal/air interface $\lambda_{(1,0)}^{AIR}$ and $\lambda_{(1,1)}^{AIR}$ can be seen at 750 nm and 543 nm (Red boxes in Figure SI3), respectively. The physical origin of $\lambda_{(1,1)}^{AIR}$ and $\lambda_{(1,1)}^{SUB}$ modes is depicted by the near-field distributions presented in Figure. For instance at the $\lambda_{(1,1)}^{AIR}$ resonance, the electric field distribution at the metal/substrate and metal/air interfaces (Figure SI3b) confirm that there is strong field localization to the metal/air interface (Figure SI3a, b). Similarly, for the $\lambda_{(1,1)}^{SUB}$ resonance, the field is localized to the metal/substrate interface (Figure SI3a, c).

WILEY-VCH

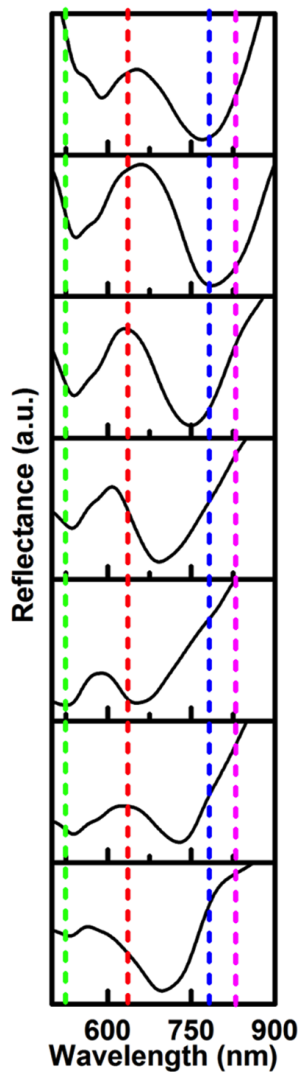


Figure SI4. Reflection spectra of 3D MBNS PM structures with different number of branches: the optical response of 3D nanostars with 4 to 10 branches (bottom to top, respectively) is reported in Figure SI4. Dashed lines (green, red, blue and magenta) indicate the excitation laser lines (532, 633, 785 and 830 nm) available for SERS measurements. In 3D nanostructures, the plasmon resonance strongly depends on the Si nanopiedestal. Therefore, the anisotropic etching of the Si pillar, due to the different nanostructure geometries, leads to an irregular trend, contrary to what is observed for 2D nanostructures.

WILEY-VCH

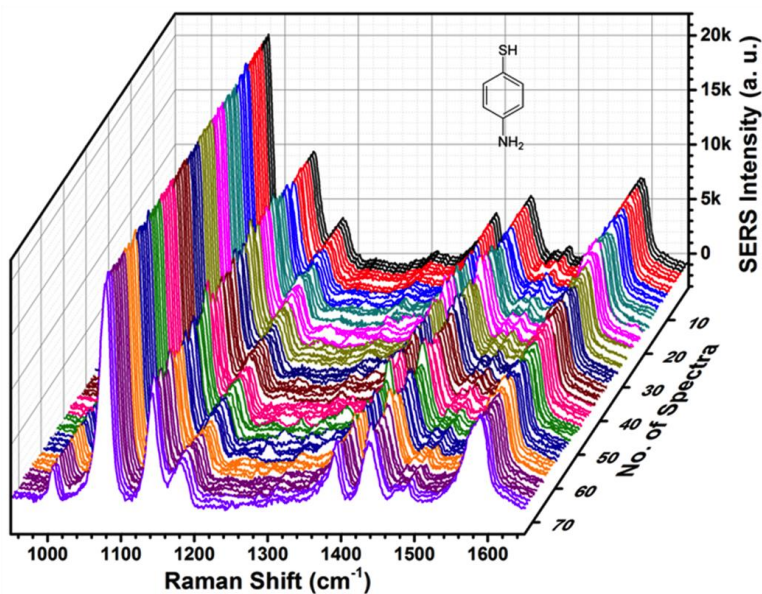


Figure SI5. SERS spectra of p-MA molecules: 3D waterfall spectra of p-MA (1 μ M concentration) on 3D MBNS PM with S8 geometry have been recorded from around 70 different spatial positions of the same sample. The incident laser, accumulation time and power are set to 785 nm, 1 mW and 3 s, respectively.

WILEY-VCH

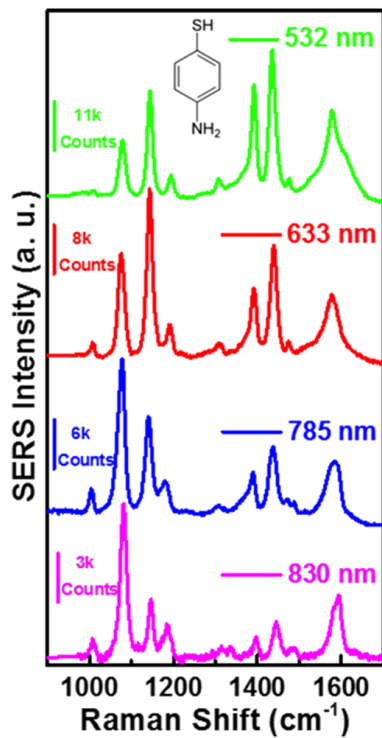


Figure SI6. SERS spectra acquired with different excitation sources: typical SERS spectra of p-MA (1 μM concentration) taken on 3D MBNS PM structures with S8 geometry for 532, 633, 785 and 830 nm excitation laser lines, represented by green, red, blue and magenta traces, respectively. The accumulation time is set to 3 s.

WILEY-VCH

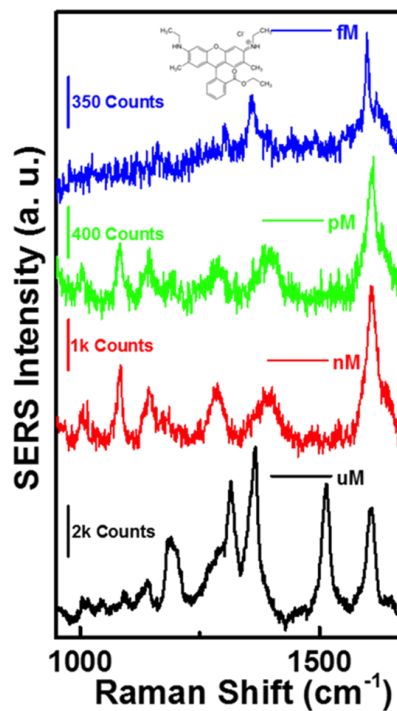


Figure SI7. SERS spectra of R6G molecules: typical SERS spectra of R6G recorded on 3D MBNS PM structures with S8 geometry at molecular concentrations of 1 μM , 1 nM, 1 pM and 1 fM, depicted by black, red, green and blue traces, respectively. The laser excitation, power and accumulation time are set to 830 nm, 10 mW and 3 s, respectively.

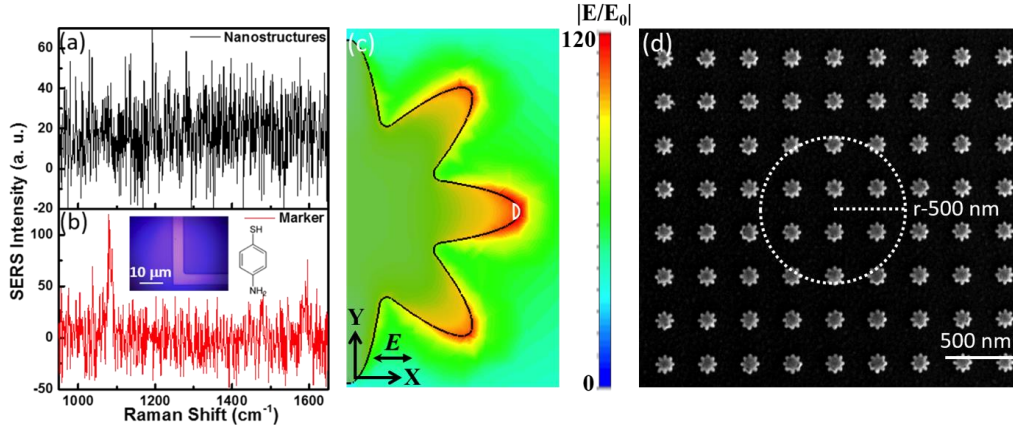


Figure SI8. SERS enhancement factor calculation: a) Background Raman spectrum was taken on 3D MBNS PM with S8 architectures before chemisorption of p-MA molecules. b) Reference Raman spectrum of p-MA (1 μ M concentration) recorded on an L-shaped marker. The laser excitation, power and accumulation time are set to 785 nm, 1 mW and 30 s, respectively.

SERS enhancement factor calculation

The SERS enhancement factor (EF), has been calculated using the following expression,

$$EF = \left(\frac{I_{SERS}}{I_{Raman}} \times \frac{A_{Raman}}{A_{SERS}} \times \frac{P_{Raman}}{P_{SERS}} \times \frac{t_{Raman}}{t_{SERS}} \right) \quad (\text{eq. S1})$$

where I , A , P and t are the peak height, the area of the structure, the laser power and the accumulation time. The subscripts *Raman* and *SERS* stand for measurements performed on planar metal films and MBNS nanostructures, respectively. In each case, incident power and accumulation time were kept constant.

According to Le Ru et al.^[1] the SERS signal is essentially provided by the molecules adsorbed at positions with strongly enhanced EM fields. For such a reason, in order to evaluate A_{SERS} we have considered the local surface area^[2] of every hot spots (see Figure SI8c, half-circle surrounded by white line $\sim 14 \text{ nm}^2$ for each protrusion). From the Figure 2e and SI8c, it is clear that only 6 tips contribute to the SERS signal (for an 8-branched MBNS under linear polarization along x-axis). Moreover, the average field enhancement along the branches placed at an angle of 45° is decreased by a factor of 2. In view of that, the effective area for a single nanostar is $\sim 56 \text{ nm}^2$. By considering 7 nanostars excited under the laser spot (Figure SI8d - incident laser beam with 500 nm radius), we can obtain $A_{SERS} = 7 \times 56 \text{ nm}^2 = 3.92 \times 10^{-16} \text{ m}^2$,

For the reference spectrum A_{Raman} corresponds to the illumination spot size:

$$A_{Raman} = 3.14 \times (500 \text{ nm})^2 = 7.85 \times 10^{-13} \text{ m}^2$$

The experimental values of I , P and t for SERS and Raman are taken from Figure 4a and Figure SI8, respectively:

$I_{SERS} = 260100$ (counts) and $I_{Raman} = 100$ (counts). Therefore, $EF = 5.2 \times 10^6$

It is worth to be noticed that the planar AgAu films are acting as SERS substrates with an enhancement factor EF' (evaluated by considering a non-enhancing Raman substrate) which can be calculated as:

$$G' = \left(\frac{I_{Raman}}{I_{Bulk}} \times \frac{N_{Bulk}}{N_{Raman}} \times \frac{P_{Bulk}}{P_{Raman}} \times \frac{t_{Bulk}}{t_{Raman}} \right) \quad (\text{eq. S2})$$

where I , N , P and t represent the peak height, the number of molecules, the laser power and the accumulation time. The subscripts *Bulk* and *Raman* indicate measurements performed on a

WILEY-VCH

non-enhancing Raman substrate and a planar metal film, respectively. $N_{Bulk} = 3.3 \times 10^{10}$ has been estimated by considering the focusing volume of the laser spot and the density of p-MA (1.06 g/cm^3).^[3] N_{Raman} has been calculated by considering the same active area employed in eq. S1 (A_{Raman}) and a packing density of $0.2 \text{ nm}^2/\text{molecule}$ for the p-MA.^[3] The estimated absolute enhancement factor is $EF' = EF \times G' = 1.6 \times 10^{11}$.

References

- [1] E. C. Le Ru, P. G. Etchegoin, M. Meyer, *The Journal of Chemical Physics* 2006, 125, 204701.
- [2] C. Hrelescu, T. K. Sau, A. L. Rogach, F. Jackel, J. Feldmann, *Applied Physics Letters* 2009, 94, 153113; M. Chirumamilla, A. Toma, A. Gopalakrishnan, G. Das, R. P. Zaccaria, R. Krahne, E. Rondanina, M. Leoncini, C. Liberale, F. De Angelis and E. Di Fabrizio, *Advanced Materials* 2014, 26, 2353.
- [3] N. A. Hatab, C.-H. Hsueh, A. L. Gaddis, S. T. Retterer, J.-H. Li, G. Eres, Z. Zhang, B. Gu, *Nano Letters* 2010, 10, 4952; J. B. Jackson, N. J. Halas, *Proceedings of the National Academy of Sciences* 2004, 101, 17930.

Appendix F

Excitation of surface plasmon polariton modes with multiple nitrogen vacancy centers in single nanodiamonds

Excitation of surface plasmon polariton modes with multiple nitrogen vacancy centers in single nanodiamonds

Shailesh Kumar^{1,4}, Jens L Lausen^{1,4}, Cesar E Garcia-Ortiz²,
Sebastian K H Andersen¹, Alexander S Roberts¹, Ilya P Radko¹,
Cameron L C Smith³, Anders Kristensen³ and Sergey I Bozhevolnyi¹

¹ Centre for Nano Optics, University of Southern Denmark, DK-5230 Odense M, Denmark

² CONACYT Research Fellow—CICESE, Unidad Monterrey, Alianza Centro 504, PIIT Apodaca, Nuevo Leon, 66629, Mexico

³ Department of Micro- and Nanotechnology, Technical University of Denmark, DK-2800 Kgs. Lyngby, Denmark

E-mail: shku@iti.sdu.dk

Received 15 September 2015, revised 4 November 2015

Accepted for publication 11 November 2015

Published 21 December 2015



CrossMark

Abstract

Nitrogen-vacancy (NV) centers in diamonds are interesting due to their remarkable characteristics that are well suited to applications in quantum-information processing and magnetic field sensing, as well as representing stable fluorescent sources. Multiple NV centers in nanodiamonds (NDs) are especially useful as biological fluorophores due to their chemical neutrality, brightness and room-temperature photostability. Furthermore, NDs containing multiple NV centers also have potential in high-precision magnetic field and temperature sensing. Coupling NV centers to propagating surface plasmon polariton (SPP) modes gives a base for lab-on-a-chip sensing devices, allows enhanced fluorescence emission and collection which can further enhance the precision of NV-based sensors. Here, we investigate coupling of multiple NV centers in individual NDs to the SPP modes supported by silver surfaces protected by thin dielectric layers and by gold V-grooves (VGs) produced via the self-terminated silicon etching. In the first case, we concentrate on monitoring differences in fluorescence spectra obtained from a source ND, which is illuminated by a pump laser, and from a scattering ND illuminated only by the fluorescence-excited SPP radiation. In the second case, we observe changes in the average NV lifetime when the same ND is characterized outside and inside a VG. Fluorescence emission from the VG terminations is also observed, which confirms the NV coupling to the VG-supported SPP modes.

Keywords: NV center, nanodiamond, surface plasmon polariton, channel plasmon polariton, V-groove, quantum plasmonics

(Some figures may appear in colour only in the online journal)

1. Introduction

Nitrogen-vacancy (NV) centers in diamonds have attracted much attention as a possible candidate for solid-state quantum bits (qubits) [1, 2]. Their ground-state electron-spin coherence time is sufficiently longer than the time it takes to perform a

qubit operation in such qubits. The electronic qubit state can be initialized and read out optically and, importantly, even at room temperatures [3–6]. The fluorescence from NV centers is stable, and a single NV center is a stable source of single photons [7]. NV centers are also a promising candidate for a high-precision magnetic field, electric field and temperature sensors [8–14]. It is argued that high densities of NV centers are needed for achieving the best performance of NV centers

⁴ These authors contributed equally to this work.

in magnetic field sensors. Multiple NV centers in nanodiamonds (NDs) can provide high sensitivity (depending on number of NV centers in the ND) as well as high resolution (determined by the size of the ND) for the magnetic field sensors [11, 12]. In addition, NDs with multiple NV centers are also useful as a stable fluorophore in biological applications due to their chemical neutrality and brightness [15]. In general, the applications potentially enabled by NV centers stand to benefit from the enhancement of the fluorescence rate as well as the efficient collection of the fluorescence from the NV centers. There are several methods that have been proposed and investigated in this direction, such as coupling NV centers to diamond pillars [16], dielectric waveguides [17], dielectric cavities [18–20], plasmonic nanostructures [21, 22] and plasmonic waveguides [23–28].

Waveguide configurations supporting the SPP propagation, i.e., plasmonic waveguides, exhibit (at least, in some cases) a unique feature of guiding SPP modes with extreme confinement, far beyond the diffraction limit [29]. This opens a way to realize a very efficient coupling of emitters to these SPP guided modes [30–32]. Channel plasmon polariton (CPP) modes supported by VGs cut into metal are especially suited for efficient coupling to emitters due to their strong confinement and relatively long propagation lengths [28, 33, 34]. The so-called β -factor, defined as the probability of a spontaneous decay of an emitter leading to excitation of the plasmonic waveguide mode, is not only high for CPP modes but also distributed more uniformly in space (within a VG), compared to other plasmonic waveguides such as cylindrical and wedge waveguides [33]. VGs have been proposed for realization of long-distance resonant energy transfer and super-radiance effects [33] as well as long-distance entanglement of two quantum emitters [34]. In addition, a wide range of devices, including plasmonic circuit components and nanofocussing elements formed by VGs, have also been demonstrated [35–37]. With nano-mirrors fabricated at the VG terminations, the efficient in- and out-coupling of far-field propagating radiation and CPP modes is demonstrated to be feasible [38, 39].

In this work, we investigate the possibility of exploiting multiple NV centers in individual NDs for coupling to the surface plasmon polariton (SPP) modes supported by silver surfaces (protected by thin dielectric layers) and by gold V-grooves (VGs) produced via the self-terminated silicon etching. This article is organized as follows: We first consider, in section 2.1, the coupling of multiple NV centers in NDs to the SPP modes supported by a silver–dielectric interface. The SPPs propagating along the interface are scattered by another ND. We conduct measurements of the fluorescence spectra obtained from a source ND, which is illuminated by a pump laser, and from a scattering ND illuminated only by the fluorescence-excited SPP radiation. The normalized fluorescence spectrum (by the source spectrum) measured from the scattering ND shows short-wavelength attenuation, which we explain by using an analytic expression based on the point-dipole approximation. Next, in section 2.2, we consider the coupling of multiple NV centers in an ND to the CPP mode supported by a gold VG, which is fabricated

using UV lithography and self-terminated silicon etching [39]. The investigated ND is pushed from the gold–air interface outside the VG to inside the VG using an atomic force microscope (AFM) [22, 24–28]. Fluorescence lifetimes are measured before and after movement of the ND, revealing a noticeable change in the average lifetime that we associate with the NV–CPP coupling. Emission from the VG termination mirrors, when the ND is excited, further confirms this coupling. We terminate our paper with section 3, in which we summarize the results obtained and offer our conclusions.

2. Experiments and results

The experiments are performed using NDs with an average diameter of 100 nm and containing ~ 400 NV centers each (Adamas Nanotechnologies). To characterize our systems, we use a scanning confocal microscope. A 532 nm linearly polarized pulsed laser with pulsewidth of ~ 50 ps and a repetition rate varying between 2.5 and 80 MHz is used as the excitation source for NV centers in NDs. The laser beam is focused with a $100\times$ objective (NA 0.9) onto the sample to a spot size of ~ 500 nm. The same objective is used for collection of the fluorescence signal. A long pass filter at 550 nm filters out the signal from the excitation source. The fluorescence is either temporally resolved with an avalanche photo diode (APD) and counting electronics, or spectrally resolved with an electron-multiplying charge-coupled device (EMCCD) camera mounted on a spectrometer. A schematic of the set-up is presented in figure 1(a).

2.1. Coupling of NV centers in an ND to SPPs at a silver–dielectric interface

The sample for studying the excitation of SPPs propagating along a silver–dielectric interface is prepared by thermal evaporation of an optically thick 150 nm silver film on a silicon wafer. Subsequently, a 20 nm amorphous SiO_2 film is sputtered on top of the silver film while it remains in vacuum in order to minimize its reaction with atmospheric sulphur and oxygen. NDs are deposited on the sample using a technique that has been described in [40]. Briefly, spin coating of PMMA (Poly(methyl methacrylate)), electron-beam lithography and development is used to fabricate an array of holes in PMMA. A suspension of NDs in water is then applied, is left to dry out under ambient conditions, thereafter a lift-off is used to remove the PMMA and obtain an array of NDs on the sample surface. The process ensures that the NDs are placed periodically at a controllable distance. The experiments are performed for two different distances between NDs: 7 and 9 μm .

The excitation polarization is changed between polarization parallel to the straight line connecting the source and the scattering ND (referred to as p polarization) and that perpendicular to the line (referred to as s polarization), as indicated in figure 1(c). Likewise, the signal from the NDs is analyzed in these two different orientations (p and s) and also

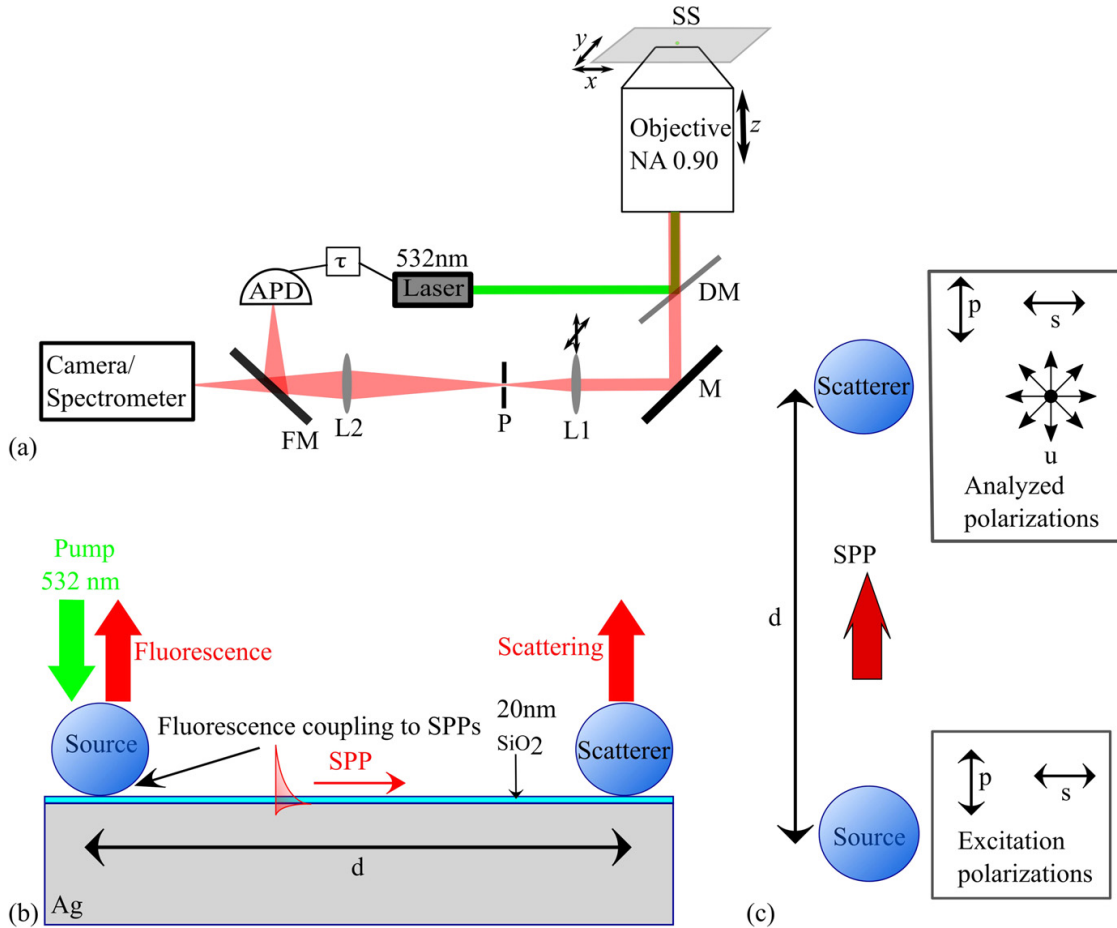


Figure 1. (a) Schematic of our experimental set-up. SS: sample stage, DM: dichroic mirror, M: mirror, L1 and L2: lenses, P:pinhole, FM: flip mirror, APD: avalanche photodiode, and τ denotes the timing electronics. The arrows indicate the possibility of moving the corresponding components. (b) side view and (c) top view of the experimental set-up for the NDs on a silver/glass surface. A pump laser excites NV centers in the source ND, where some of the fluorescence couples to the SPP mode and the scatterer ND scatters the SPPs to the far field. The source ND is excited by polarizations parallel to the line joining the source and the scatterer NDs (p) and perpendicular to the line (s). The signal is analyzed in these two polarization directions as well as unpolarized (u).

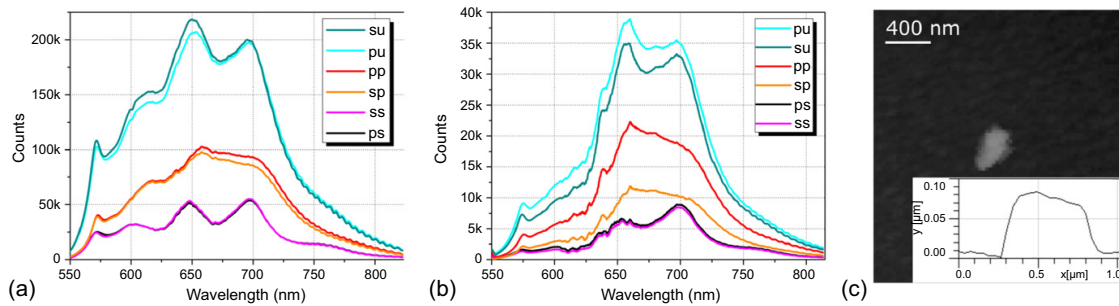


Figure 2. Typical spectra measured at the source (a) and scatterer (b) ND with different combinations of excitation and analyzed polarizations. In the graphs, the first letter denotes excitation polarization, whereas the second letter denotes analyzed polarization. (c) Shape of a single ND imaged with an AFM. The inset shows a cross-section of the ND.

in the absence of analyzer (u), which is also indicated in figure 1(c).

When an ND is excited, its fluorescence couples to SPPs at the silver–dielectric interface, propagates along the interface and is scattered by a separate ND. In figures 2(a) and (b), we present the source and the scattering spectra collected from the NDs, which are separated by 7 μm . Different configurations of polarization orientations for excitation radiation and analyzed signal are indicated in the insets in the respective figures. No significant difference in the strengths of signals collected from the source ND for the two orthogonal excitation polarizations is observed, a feature that can be explained by a high number and arbitrary orientation of NV centers inside the ND. The spectrum is found to depend only on the analyzed polarization, which we attribute to an irregular shape and relatively large size of the source ND (figure 2(c)) resulting in complicated Mie scattering spectra. For other source scatterer ND combinations, we have observed fluorescence dependence on excitation polarization (data not shown).

The signal from the scatterer ND is found dependent on the excitation polarization (figure 2(b)). The unpolarized collected signal for the s-polarized excitation (su) is lower compared to the unpolarized collected signal for the p-polarized excitation (pu). The same is observed when an analyzer is present: excitation by the p-polarized light consistently gives higher signals from the scatterer ND (the difference is small for the s-analyzed orientation). The dipoles excited by p polarization couple preferentially to the SPP propagating in the direction along the electric field of excitation [40]. A signal is still observed for the s polarization excitation, because many of the excited NV dipoles have a nonzero projection on the line connecting the source and scatterer NDs and can therefore couple to the SPPs propagating in that direction. In general, the relative strength of ND-excited SPP radiation depends on the distribution of dipoles inside the source ND [41]. Note that, similarly to the source ND spectra, the shape of the scatterer ND spectra is determined by the analyzed polarization (figure 2(b)), a feature that can again be related to the ND shape and size influence on the scattering spectra.

The signal strength collected from the scatterer ND is, in general, significantly lower compared to that collected from the source ND. Comparing the overall (over the whole spectrum) photon counts from the scatterer ND with that from the source ND, we found that their ratio varies substantially from one pair of NDs to another. It cannot be explained merely by variations in ND separation due to imperfect fabrication. The largest ratio observed is 1:2850 and the lowest is 1:4 (data not shown), where these two different pairs of NDs have the same separation of 7 μm . The decrease in signal strength when changing the detection from the source to scatterer ND is therefore not only related to the SPP propagation loss (as conjectured previously [40]) but also to the excitation polarization state, SPP coupling and scattering efficiencies, ND shape, and NV dipole-to-interface distance. We note that the ratio of scattered intensities pp:ps and sp:ss should, in principle, be the same (as observed for a distance

24 μm between source and scatterer [40]). When the distance is smaller (7 and 9 μm), a small background due to the direct illumination of scatterer (by pump or fluorescence, which affect the ps and ss spectra the most) changes these ratios.

We use two different analytical models to fit the ratio of spectra measured from the source and the scatterer NDs. In the first model suggested previously [40], it is assumed that the ratio of spectra can be expressed as follows:

$$\frac{P_{\text{scat}}(\lambda)}{P_{\text{source}}(\lambda)} = f(\lambda) \exp[-d/L_{\text{spp}}(\lambda)] \quad \text{with} \quad (1)$$

$$f(\lambda) = \frac{\eta_{\text{spp}}(\lambda) \sigma_{\text{sc}}}{2\pi\eta_{\text{rad}}(\lambda) da_s},$$

where d is the distance between the NDs, $L_{\text{spp}}(\lambda)$ is the SPP propagation length for a given wavelength λ , $\eta_{\text{spp}}(\lambda)$ is the photon to SPP coupling efficiency for the source ND, σ_{sc} is the scattering cross-section of the scatterer ND, $\eta_{\text{rad}}(\lambda)$ is the photon emission efficiency of the source ND, and a_s is the in-plane angular dependence of the SPP intensity. In this rather simple model, the term $f(\lambda)$ is assumed to be wavelength-independent, i.e., taken as a constant, which is the fitting parameter for the model. Since $f(\lambda)$ is used as a multiplication factor, all spectra are normalized to their own maximum. In the second model, we have attempted to develop a more accurate and yet analytic description by using the expression for the SPP contribution to Green's dyadic constructed for evaluating SPP-mediated interaction between small particles located close to a metal surface [42]. When applied to our configuration, one arrives at the following expression:

$$G_{\text{spp}}^{zz}(d, \lambda) = \frac{k_{\text{spp}}}{2\sqrt{\varepsilon}} \sqrt{\frac{2}{\pi k_{\text{spp}} d}} e^{-2r\sqrt{k_{\text{ND}}^2 - k_0^2}} e^{-(d/L_{\text{spp}}(\lambda))}, \quad (2)$$

where k_{spp} is the magnitude of the wave vector for the SPP at the silver–dielectric interface, k_{ND} is the magnitude of the wave vector at the silver–diamond interface, r is an average radius of NDs, ε is the dielectric constant of silver, $L_{\text{spp}}(\lambda)$ is the SPP propagation length at the silver–dielectric interface, and d is the distance between the two NDs. The first exponential term accounts for the SPP excitation (by a dipole source, such as an NV center) and out-coupling (by a dipole scatterer) to free propagating radiation, and the second exponential term describes the SPP propagation loss. The square root term describes the angular divergence of the propagating SPP. Using the expression for Green dyadic above (source and scatterer dipole are assumed to have z-orientation), we write the ratio of detected intensities as $P_{\text{scat}}(\lambda)/P_{\text{source}}(\lambda) = \alpha |G_{\text{spp}}^{zz}(\lambda, d)|^2$, where α is a fitting parameter constant for the second model (together with the ND radius r). The value of k_{spp} in equation (2) for a three-layer structure (air/glass/silver), and k_{ND} for a diamond–silver interface (the air above and the glass beneath the ND are neglected) are obtained analytically. The normalized scattering spectra for 7 and 9 μm of separation between NDs (figure 3) appear shifted to longer wavelengths relative to the fluorescence spectra measured from the source NDs. The SPP attenuation is larger for shorter wavelengths, which contributes to the spectral shape of the scattered spectrum. The

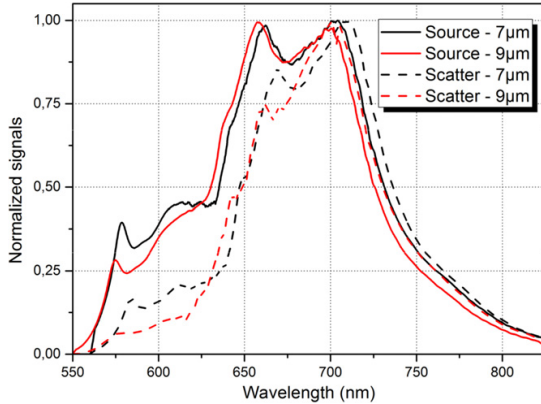


Figure 3. Source and scatterer spectra, shown for two different distances (7 and 9 μm) between the NDs. All signals are normalized to their own maximum value.

coupling efficiency of fluorescence to SPPs and angular divergence of the SPP beam depend on the wavelength, both of which also influence the shape of the scattered spectrum. This is readily seen in figure 4, where the extended model provides better fitting. The best fit for the extended model has the coefficient of determination (R^2) of 0.90 and 0.97 for the distances of 7 and 9 μm , respectively. The ND radii obtained from fits, $r = 36.38$ nm for the distance of 7 μm and $r = 45.44$ nm for the distance of 9 μm , correspond well with the NDs that are actually deposited (an average diameter of 100 nm).

2.2. Coupling of NV centers in a ND to CPP modes in a VG

The VGs used in these experiments are fabricated with the same procedure as described in [39] which consists of UV lithography, crystallographic etching of silicon and a thermally grown silicon dioxide (SiO_2) layer on the silicon to modify the V-shape geometry. Initially, a 200 nm SiO_2 layer

on the silicon substrate is patterned by both UV lithography and reactive-ion etching to define the perimeter of the VG devices. It is necessary that the patterning of the SiO_2 layer is well-aligned with the crystal $\langle 100 \rangle$ planes of the silicon substrate. The VGs and termination mirrors are formed by anisotropic wet etching of the exposed silicon in a potassium hydroxide (KOH) bath at 80 $^\circ\text{C}$. The KOH etch yields smooth $\langle 111 \rangle$ VG sidewalls and termination mirrors with a fixed inclination of 55 $^\circ$ from the surface plane. The nature of the crystallographic etching yields excellent mirror formation at the ends of the VG perimeter. Tailoring of the V-shape geometry is performed by thermal wet oxidation of the silicon VGs (1150 $^\circ\text{C}$ for 9 h, resulting in a 2320 nm SiO_2 layer at flat sections of the substrate) which sharpens the interior angle of the groove in order to support a CPP mode. The metal is deposited by electron-beam evaporation: first a 5 nm layer of chromium to promote adhesion before a 70 nm layer of gold. The gold layer is chosen to be sufficiently thick to eliminate interaction of air–interface plasmons with the underlying SiO_2 layer and also to minimize self-aggregation.

To couple NDs to the VGs, a water suspension containing NDs is spin coated on the sample with VGs. For this experiment, the concentration of NDs in water is adjusted so that the density of NDs on the surface after spin-coating is less than 1 per $10 \times 10 \mu\text{m}^2$. An AFM image of a VG together with an NDs is presented in figure 5(a). As can be observed from the figure, the depth of the VG structure is more than 2 μm . Figures 5(b) and (c) show images of the areas containing the NDs, which are also indicated in 5(a). A confocal raster scan image of the area with the ND presented in figure 5(d), shows that the fluorescence from the ND on the flat gold–air interface at an excitation of 100 μW is ~ 700 kcounts/s. Confocal scan images taken at an excitation power of 100 μW and two orthogonal polarizations show (figures 5(e)–(f)) that fluorescence from the VG is higher in case of excitation polarization across the VG (s polarization in figure 5(e)) due to the contribution from gap plasmons [43]. In figure 5(f), termination mirror A can be seen to fluoresce

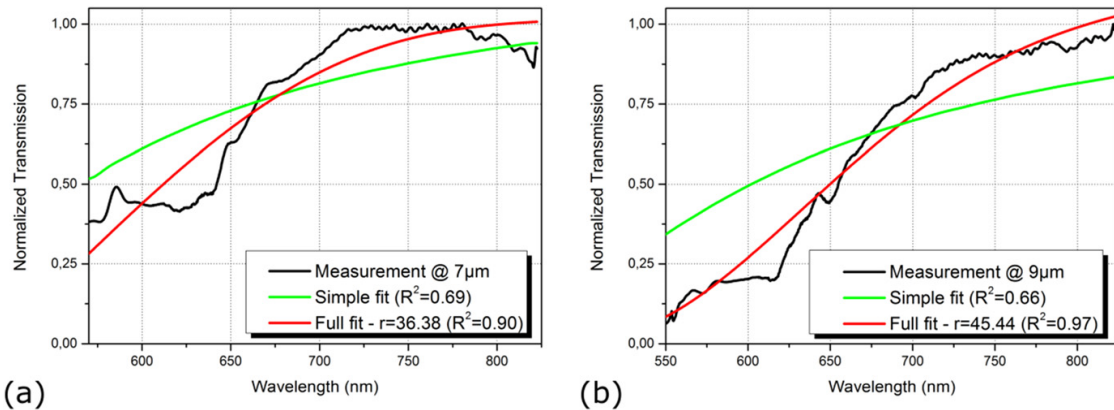


Figure 4. (a) and (b) shows model fits of the normalized source and scatterer spectra ratios obtained for distances between source and scatterer of 7 μm and 9 μm , respectively. The fits with the simple model, as well as the full model containing terms for divergence and coupling of fluorescence to SPP are shown. The fits for the full model are shown in the legends of the graphs with a fit R^2 coefficient.

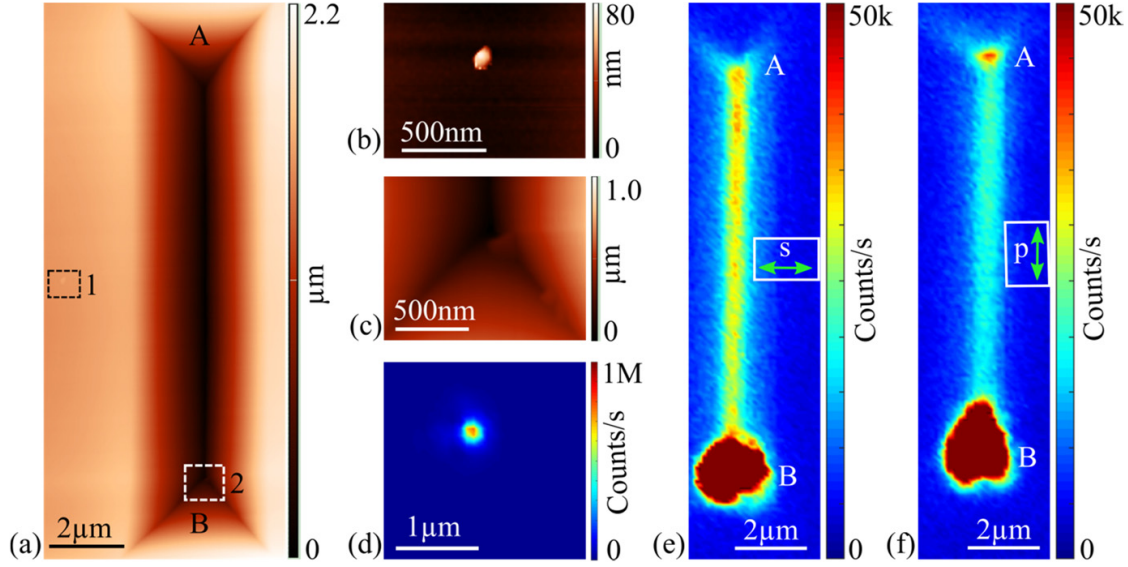


Figure 5. (a) Atomic-force microscope image of a VG structure. The rectangles with dotted lines indicates the areas containing NDs. (b) and (c) zoomed-in images of the areas 1 and 2, respectively, indicated in (a). (d) confocal-microscope fluorescence scan of the area containing the ND presented in (b). (e) and (f) confocal-microscope fluorescence scans of the VG presented in (a) with the excitation polarization indicated in the inset of respective figures. In (a), (e) and (f), A and B indicate the two VG termination mirrors.

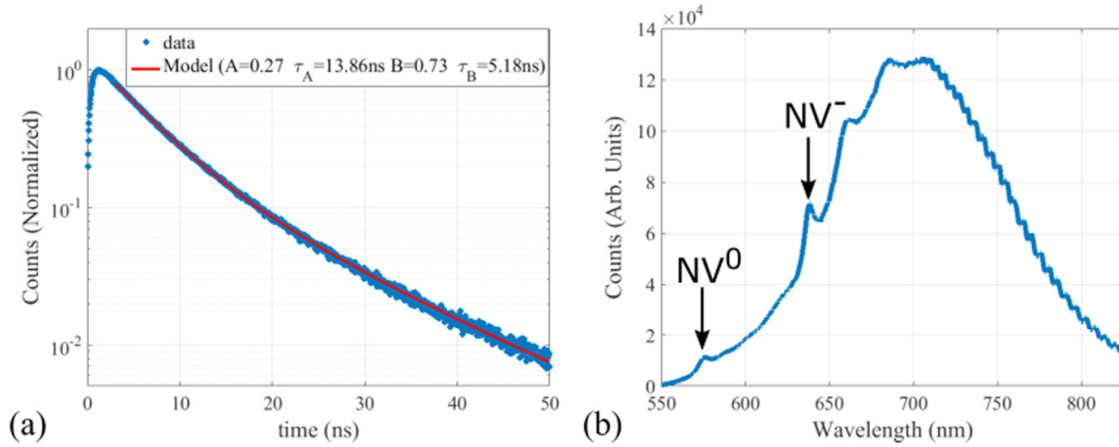


Figure 6. (a) Lifetime measurement data and a two-exponential fit for the fluorescence from the ND presented in figure 5(d). (b) emission spectrum of the ND shown in figure 5(d).

more than it does in figure 5(e), this is due to the structure of the termination mirror which allows the penetration of p-polarized excitation light and the fluorescence is enhanced due to the presence of three corners of the V-groove termination. The termination mirror B of the VG fluoresces more due to the presence of NDs in the region, which can be seen in figure 5(c).

The ND shown in figure 5(b) is further characterized by measuring its lifetime and fluorescence spectrum. The measured lifetime curve as well as a two-exponential fit ($A\exp(-t/\tau_A) + B\exp(-t/\tau_B) + \text{constant}$, where A and B are

amplitudes, t is time, τ_A and τ_B are decay lifetimes) is presented in figure 6(a). We note that NV-centers in NDs are known to have a distribution in decay lifetimes [23]. Our NDs have ~ 400 NV centers and each of the NV centers may have different lifetimes. Here, we have fitted the experimental data with minimum number of exponential decay rates possible. A single decay rate does not fit the data well, and a two exponential decay curve fits the data quite well ($0.9 < R^2 < 1.1$). The first 2 ns of the decay curve are not included in the fit to exclude gold fluorescence [44]. The two lifetimes obtained from the fit are $\tau_A = 13.86$ ns and $\tau_B = 5.18$ ns. These

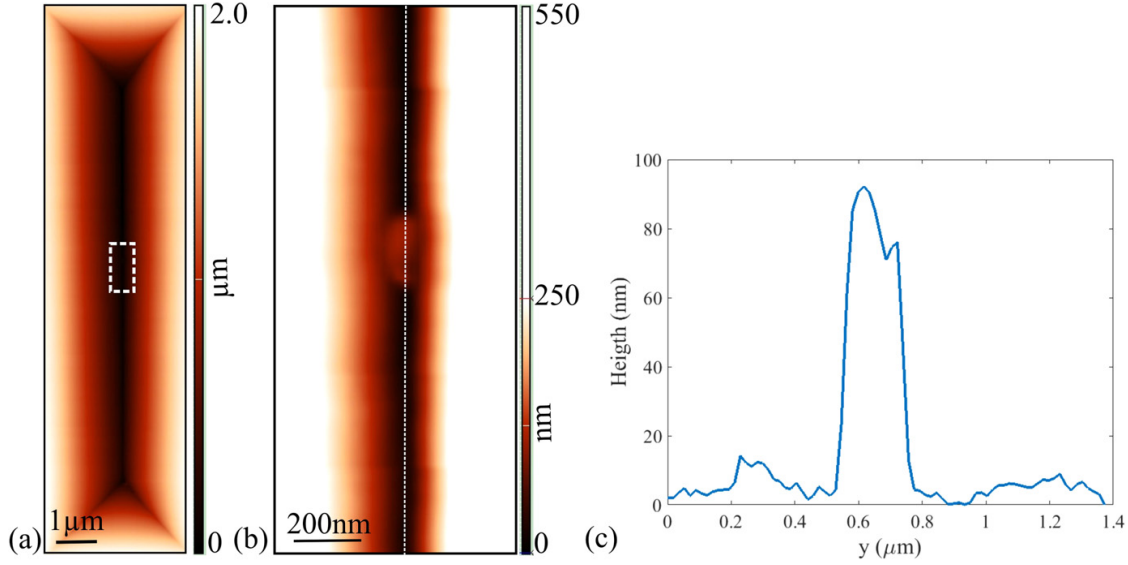


Figure 7. (a) AFM image of the VG after the ND is moved inside. The white rectangle indicates the area containing the ND. (b) zoomed-in image of the ND inside the VG. (c) The cross-section along the dotted white line in figure (b).

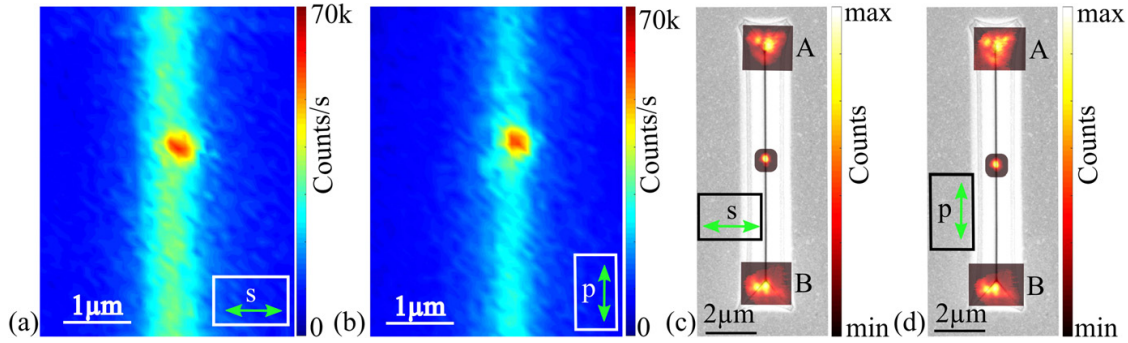


Figure 8. (a), (b) Confocal microscopy scan images of the ND located inside the V-groove with the excitation polarization indicated in the insets. (c) and (d) fluorescence images combined with SEM images indicating the emission from the far ends of the VG. The excitation spot is positioned at the ND and the excitation polarization is indicated in the insets. The three spots in both images were recorded separately. A and B indicate the two VG termination mirrors.

lifetimes are shortened when compared to those obtained when the NDs from the same suspension are spin-coated on a fused silica substrate. In the latter case, we obtained $\tau_A = 34.51$ ns and $\tau_B = 7.77$ ns (averaged over 10 NDs). The difference in lifetimes can be attributed to the excitation of SPPs on the gold–air interface by the NV centers. The fluorescence spectrum of the ND clearly shows (figure 6(b)) the characteristic zero phonon lines of NV^0 (575 nm) as well as NV^- (637 nm) centers.

After characterization of the VG as well as the ND, the ND is moved into the VG using a procedure that has been used previously [22, 24–28]. An AFM image of the VG containing the ND can be seen in figure 7(a). Figure 7(b) shows a zoomed-in image of the ND within the VG, and it can be inferred that the ND is close to the bottom of the VG.

The cross-section along the dotted line in figure 7(b) is presented in figure 7(c). The height of the ND inside the VG is around 90 nm, which is similar to the height observed outside of the VG for the ND.

Figures 8(a) and (b) present the confocal fluorescence image of the area of the VG containing the ND. The excitation laser power is, again, $100 \mu\text{W}$. One can observe a significant decrease in the fluorescence counts obtained from the ND inside the VG when compared to the ND on gold–air interface. This could be due to the reduced intensity of the excitation laser inside the ND. In figures 8(c) and (d), the fluorescence images are overlapped with a SEM image of the VG. The fluorescence images are recorded while focusing the excitation laser on the ND, and the fluorescence images in the middle and those at the VG ends are recorded independently

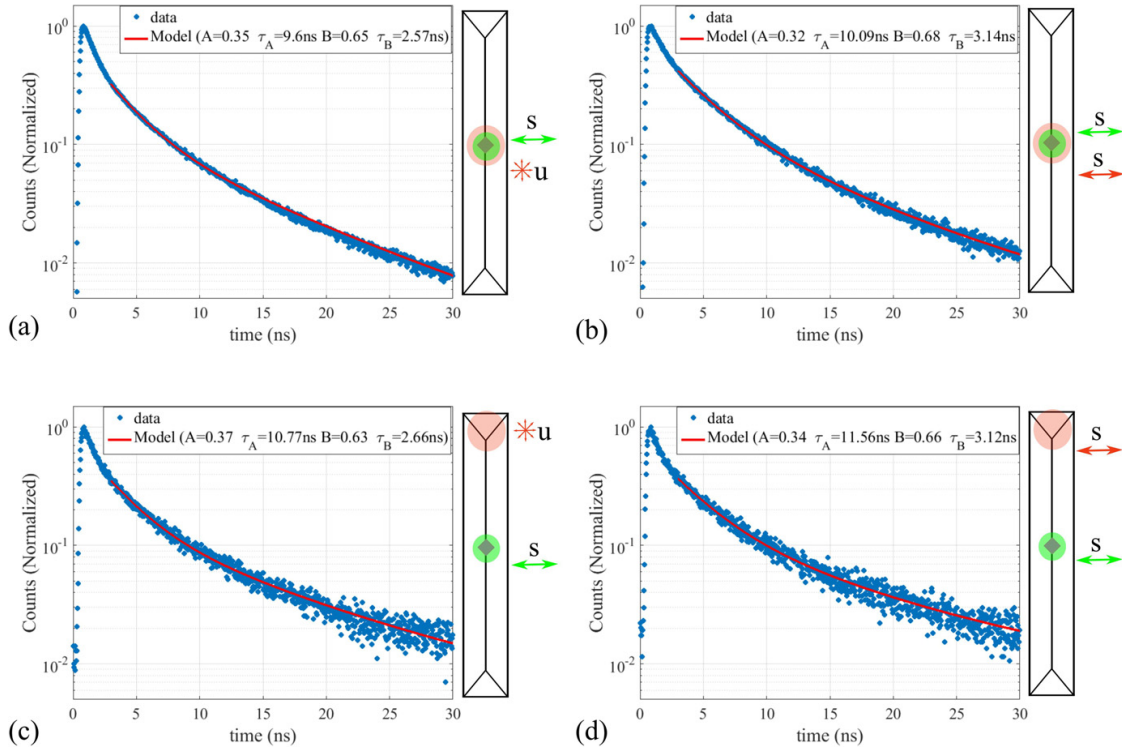


Figure 9. Lifetime measurement data and a two-exponential fit for the fluorescence collected from the ND inside the VG. In sketches next to the graphs, green and red disks represent the excitation and detection spots, respectively, whereas the arrows represent the excitation (green) and analyzed signal polarization (red).

to optimize the signal. The acquisition time for the fluorescence images in the middle is 1 s, whereas for the images at the VG termination mirrors is 60 s. The images suggest that the fluorescence from the ND couples to CPPs supported by the VG, which propagate along the VG and are out-coupled to free space from the termination mirrors of the VG. This sequence is observed for both excitation polarizations, as shown in figures 8(c) and (d). The difference in the far-field images of the two termination mirrors is attributed to the presence of NDs near the VG termination mirror B (figure 5(c)). The emission pattern for both excitation polarizations is the same due to excitation of the CPP modes in both cases.

The ND-VG system is further characterized by measuring the lifetime for different polarizations at the site of the ND, as well as at the VG termination mirrors. Figures 9 and 10 present the lifetimes of the coupled system when the excitation polarization is across the VG (s polarization) and along its axis (p polarization), respectively. In figure 9, it can be observed that the values of lifetimes obtained at the site of the emitter as well as those at VG termination mirror A are very close. This suggests that the NV centers being probed with s polarization are the same, regardless of whether the fluorescent signal is probed at the end of the waveguide or at the site of the ND itself. Under these circumstances, NV

centers with a non-zero projection of dipole moment along the excitation polarization are excited and coupled to the CPP mode of the VG. Previous studies of plasmonic modes in VGs indicate a more uniform distribution of the beta-factor across the profile when compared to cylindrical or wedge waveguides [33], which supports the assumption of a relatively uniform coupling of all the NV centers that are excited with s polarization. Furthermore, the fluorescence lifetime observed for the ND in this case is smaller than the fluorescence lifetime observed for the ND when it lied on the gold surface. The decrease for τ_A is by a factor of 1.32, and τ_B by a factor of 1.81. This is comparable to the lifetime change by a factor of ~ 2.44 observed when a single NV center in an ND lying on a gold surface is moved to inside a VG, in [28]. In figure 10, when the excitation polarization is along the VG axis, one can again observe that the values of lifetimes obtained at the end of the waveguide are very close to those at the site of the ND. However, if we compare the lifetimes obtained for the two orthogonal excitation polarizations, the lifetime in case of p-polarized excitation is longer than for s-polarized excitation. This can be attributed to the NV centers with dipoles across the VG axis, which couple more efficiently to the CPP mode of the VG. If we compare the fluorescence lifetimes of the ND when it is lying on the flat gold surface and when it is lying

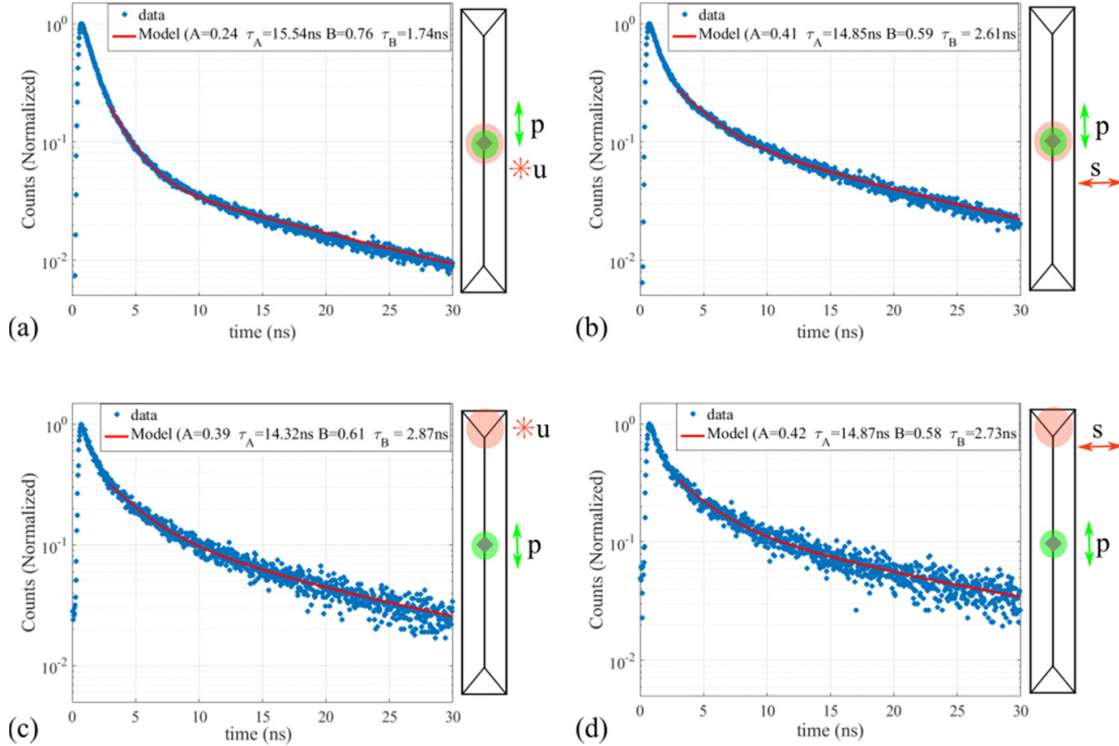


Figure 10. Lifetime measurement data and a two-exponential fit for the fluorescence collected from the ND inside the VG. In sketches next to the graphs, green and red disks represent the excitation and detection spots, respectively, whereas the arrows represent the excitation (green) and analyzed signal polarization (red).

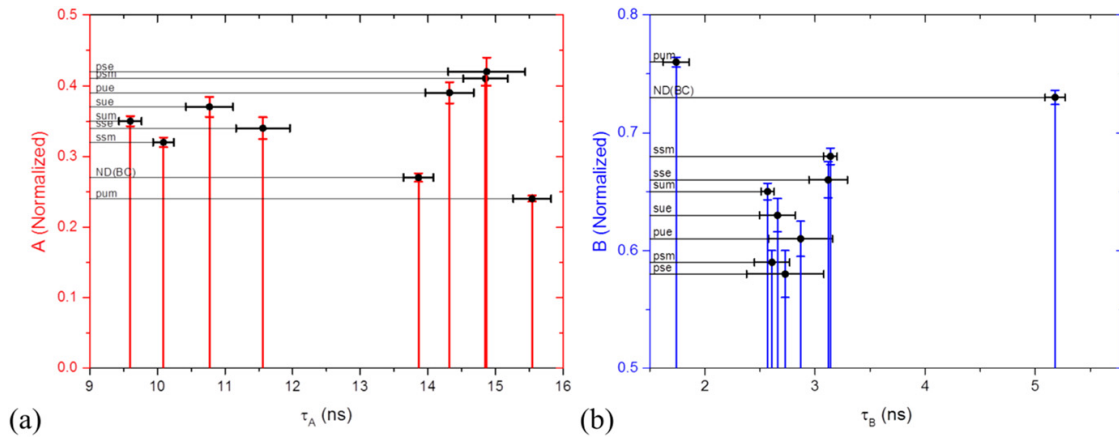


Figure 11. (a) and (b) summarize the lifetimes and amplitudes observed in figures 6(a), 9 and 10. ND(BC) denotes the nanodiamond before coupling to V-groove (figure 6(a)). In all the other symbols, the first letter denotes excitation polarization (s or p), the second letter denotes the analyzed polarization (s, p or u) and the third letter denotes the position of detection (middle (m) or end A (e)).

inside the VG and excited with p-polarized laser, the increase of τ_A is by a factor of 1.07, whereas for τ_B there is a decrease by a factor of 2.08. The slight increase of τ_A can be interpreted as a suppression of emission from dipoles aligned along the VG axis when compared to the ND lying

on a flat gold surface. In figure 11, we summarize all the lifetimes and amplitudes observed for the ND before and after its coupling to the V-groove. The errorbars represents uncertainty in the fitted parameters, that is, the lifetimes and amplitudes.

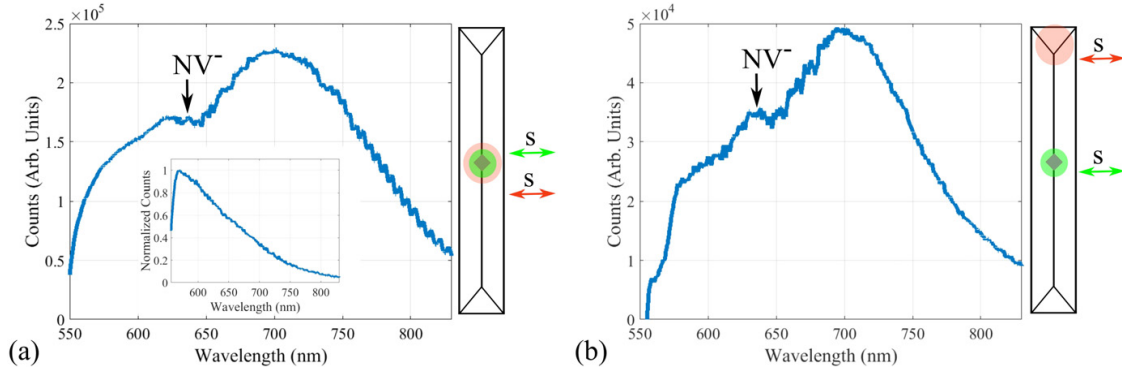


Figure 12. (a) and (b) Spectra taken at the site of the ND and at one of the VG ends, respectively. The excitation and detection polarizations are across the VG (i.e. s-polarized). The inset in (a) shows the fluorescence spectrum measured from a gold film.

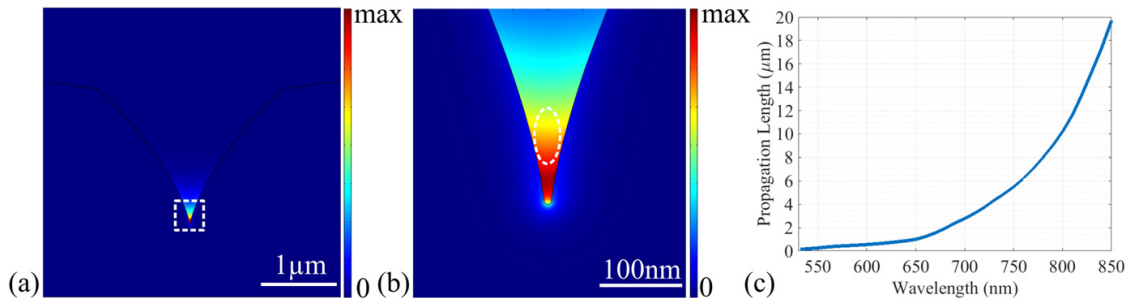


Figure 13. (a) Simulated CPP mode in a V-groove. The dotted rectangle shows the area which is zoomed-in and shown in (b). The oval shape in (b) indicates a possible position for the ND. (c) The CPP propagation distance as a function of wavelength is presented.

In figure 12, we present two fluorescence spectra of the same ND inside the VG, one of which is collected at the site of the ND, whereas the other is out-coupled from the termination mirror A of the VG. In the former case (figure 12(a)), the ND fluorescence spectrum is in superposition with fluorescence from gold, the spectrum of which is presented in the inset. In the latter case (figure 11(b)), the contribution from gold fluorescence is negligible, since it does not couple efficiently to the CPP mode [28]. The zero phonon line of NV^- centers can be observed in the spectrum that is measured at the end of the VG, which supports the argument above. The wavelength-dependent propagation loss of the CPP mode in the VG provides an additional source of modification of the observed spectra.

We simulated the CPP mode that is supported by these VGs using finite-element method (COMSOL Multiphysics). The cross-section is obtained by a numerical process simulation in ATHENA, as has been described in [39]. The dielectric constant of gold is taken from [45]. In figure 13(a), we present the distribution of the electric field of the CPP mode, calculated at a vacuum wavelength of 700 nm. The zoomed-in image in figure 13(b) shows the distribution of electric field along with the possible position for the ND inside the VG. From the dependence of the CPP propagation length on the wavelength (figure 1(c)), the suppression of shorter

wavelength is expected and is in support of the spectrum observed at the VG end.

3. Summary

We have presented the coupling of NDs containing multiple NV centers to SPPs on a silver–dielectric interface and to CPPs supported by a gold VG. The coupling to SPPs is observed by emission from other NDs that are used for scattering the SPPs to the far field. The spectrum of scattered fluorescence is fitted to a model which suggests that the dependence on propagation losses as well as the height of the NDs, both of the source as well as the scatterer must be accounted for. We have also presented the results of coupling of an ND to the CPP mode of a VG. The coupling is demonstrated by the observation of fluorescence from the VG termination mirror while the ND pushed into the VG middle is excited. A lifetime change, when moving the ND from outside to inside the VG, is also observed for the ND fluorescence, which further confirmed the coupling. The change in spectrum with respect to the ND is explained as the change caused by the propagation loss plus the inefficient coupling of gold fluorescence to the CPP mode. The reported experiments demonstrate a way of incorporating NDs containing multiple

NV-centers into plasmonic circuits as well as reveal various factors influencing the formation of fluorescence-excited SPP spectra.

Acknowledgments

The authors gratefully acknowledge the financial support from the European Research Council, Grant No. 341054 (PLAQNAP). CLCS acknowledges financial support from the Danish Council for Independent Research (FTP Grant No. 12-126601).

References

- [1] Ladd T D, Jelezko F, Laflamme R, Nakamura Y, Monroe C and O'Brien J L 2010 Quantum computers *Nature* **464** 45–53
- [2] Doherty M W, Manson N B, Delaney P, Jelezko F, Wrachtrup J and Hollenberg L C L 2013 The nitrogen-vacancy colour centre in diamond *Phys. Rep.* **528** 1–45
- [3] Balasubramanian G *et al* 2009 Ultralong spin coherence time in isotropically engineered diamond *Nat. Mater.* **8** 383
- [4] Jelezko F, Gaebel T, Popa I, Gruber A and Wrachtrup J 2004 Observation of Coherent oscillations in a single electron spin *Phys. Rev. Lett.* **92** 076401
- [5] Gaebel T *et al* 2006 Room-temperature coherent coupling of single spins in diamond *Nat. Phys.* **2** 408
- [6] Hanson R, Mendoza F M, Epstein R J and Awschalom D D 2006 Polarization and readout of coupled single spins in diamond *Phys. Rev. Lett.* **97** 087601
- [7] Kurtseifer C, Mayer S, Zarda P and Weinfurter H 2000 Stable solid-state source of single photons *Phys. Rev. Lett.* **85** 290–3
- [8] Maletinsky P, Hong S, Grinolds M S, Hausmann B, Lukin M D, Walsworth R L, Loncar M and Yacoby A 2012 A robust scanning diamond sensor for nanoscale imaging with single nitrogen-vacancy centres *Nat. Nanotechnol.* **7** 320
- [9] Balasubramanian G *et al* 2008 Nanoscale imaging magnetometry with diamond spins under ambient conditions *Nature* **455** 648–51
- [10] Maze J R *et al* 2008 Nanoscale magnetic sensing with an individual electronic spin in diamond *Nature* **455** 644–7
- [11] Taylor J M, Cappellaro P, Childress L, Jiang L, Budker D, Hemmer P R, Yacoby A, Walsworth R and Lukin M D 2008 High-sensitivity diamond magnetometer with nanoscale resolution *Nat. Phys.* **4** 810–6
- [12] Wolf T, Neumann P, Nakamura K, Sumiya H, Ohshima T, Isoya J and Wrachtrup J A 2015 Subpicotesla diamond magnetometer *Phys. Rev. X* **5** 041001
- [13] Dolde F *et al* 2011 Electric-field sensing using single diamond spins *Nat. Phys.* **7** 459–63
- [14] Kucsko G, Maurer P C, Yao N Y, Kubo M, Noh H J, Lo P K, Park H and Lukin M D 2013 Nanometre-scale thermometry in a living cell *Nature* **500** 54–8
- [15] Mochalin V N, Shenderova O, Ho D and Gogotsi Y 2012 The properties and applications of nanodiamonds *Nat. Nanotechnol.* **7** 11–23
- [16] Babinec T M, Hausmann B J M, Khan M, Zhang Y, Maze J R, Hemmer P R and Loncar M 2010 A diamond nanowire single-photon source *Nat. Nanotechnol.* **5** 195
- [17] Schröder T, Fujiwara M, Noda T, Zhao H-Q, Benson O and Takeuchi S 2012 A nanodiamond-tapered fiber system with high single-mode coupling efficiency *Opt. Express* **20** 10490–7
- [18] Faraon A, Barclay P E, Santori C, Fu K-M C and Beausoleil R G 2011 Resonant enhancement of the zero-phonon emission from a colour centre in a diamond cavity *Nat. Photonics* **5** 301
- [19] Faraon A, Santori C, Huang Z, Acosta V M and Beausoleil R G 2012 Coupling of nitrogen-vacancy centers to photonic crystal cavities in monocrystalline diamond *Phys. Rev. Lett.* **109** 033604
- [20] Wolters J, Schell A W, Kewes G, Nüsse N, Schoengen M, Döscher H, Hannappel T, Öhel B L, Barth M and Benson O 2010 Enhancement of the zero phonon line emission from a single nitrogen vacancy center in a nanodiamond via coupling to a photonic crystal cavity *Appl. Phys. Lett.* **97** 141108
- [21] Choy J, Hausmann B, Babinec T, Bulu I, Khan M, Maletinsky P, Yacoby A and Loncar M 2011 Enhanced single-photon emission from a diamond–silver aperture *Nat. Photonics* **5** 738–43
- [22] Schietinger S, Barth M, Aichele T and Benson O 2009 Plasmon-enhanced single photon emission from a nano-assembled metal-diamond hybrid structure at room-temperature *Nano Lett.* **9** 1694–8
- [23] Kolesov R, Grotz B, Balasubramanian G, Stöhr R J, Nicolet A A L, Hemmer P R, Jelezko F and Wrachtrup J 2009 Wave–particle duality of single surface plasmon polaritons *Nat. Phys.* **5** 470
- [24] Huck A, Kumar S, Shakoor A and Andersen U L 2011 Controlled coupling of a single nitrogen-vacancy center to a silver nanowire *Phys. Rev. Lett.* **106** 096801
- [25] Kumar S, Huck A and Andersen U L 2013 Efficient coupling of a single diamond color center to propagating plasmonic gap modes *Nano Lett.* **13** 221
- [26] Kumar S, Huck A, Chen Y and Andersen U L 2013 Coupling of a single quantum emitter to end-to-end aligned silver nanowires *Appl. Phys. Lett.* **102** 103106
- [27] Kumar S, Huck A, Lu Y-W and Andersen U L 2013 Coupling of single quantum emitters to plasmons propagating on mechanically etched wires *Opt. Lett.* **38** 3838–41
- [28] Bermúdez-Ureña E *et al* 2015 Coupling of individual quantum emitters to channel plasmons *Nat. Commun.* **6** 7883
- [29] Gramotnev D K and Bozhevolnyi S I 2010 Plasmonics beyond the diffraction limit *Nat. Photonics* **4** 83–91
- [30] Chang D E, Sørensen A S, Hemmer P R and Lukin M D 2006 Quantum optics with surface plasmons *Phys. Rev. Lett.* **97** 053002
- [31] Chang D E, Sørensen A S, Hemmer P R and Lukin M D 2007 Strong coupling of single emitters to surface plasmons *Phys. Rev. B* **76** 035420
- [32] Akimov A V, Mukherjee A, Yu C L, Chang D E, Zibrov A S, Hemmer P R, Park H and Lukin M D 2007 Generation of single optical plasmons in metallic nanowires coupled to quantum dots *Nature* **450** 402
- [33] Martín-Cano D, Martín-Moreno L, García-Vidal F J and Moreno E 2010 Resonance energy transfer and superradiance mediated by plasmonic nanowaveguides *Nano Lett.* **10** 3129–34
- [34] Gonzalez-Tudela A, Martín-Cano D, Moreno E, Martín-Moreno L, Tejedor C and Garcia-Vidal F J 2011 Entanglement of two qubits mediated by one-dimensional plasmonic waveguides *Phys. Rev. Lett.* **106** 020501
- [35] Bozhevolnyi S I, Volkov V S, Devaux E, Laluet J-Y and Ebbesen T W 2006 Channel plasmon subwavelength waveguide components including interferometers and ring resonators *Nature* **440** 508–11

- [36] Gramotnev D K and Bozhevolnyi S I 2014 Nanofocusing of electromagnetic radiation *Nat. Photonics* **8** 13–22
- [37] Smith C L C, Stenger N, Kristensen A, Mortensen N A and Bozhevolnyi S I 2015 Gap and channeled plasmons in tapered grooves: a review *Nanoscale* **7** 9355
- [38] Radko I P, Holmgaard T, Han Z, Pedersen K and Bozhevolnyi S I 2011 Efficient channel-plasmon excitation by nano-mirrors *Appl. Phys. Lett.* **99** 213109
- [39] Smith C L C, Thilsted A H, Garcia-Ortiz C E, Radko I P, Marie R, Jeppesen C, Vannahme C, Bozhevolnyi S I and Kristensen A 2014 Efficient excitation of channel plasmons in tailored, UV-Lithography defined V-Grooves *Nano Lett.* **14** 1659–64
- [40] Garcia-Ortiz C E, Kumar S and Bozhevolnyi S I 2015 Local excitation of surface plasmon polaritons using nitrogen-vacancy centers *Opt. Lett.* **40** 16 3830
- [41] Mueller J P B and Capasso F 2013 Asymmetric surface plasmon polariton emission by a dipole emitter near a metal surface *Phys. Rev. B* **88** 121410(R)
- [42] Søndergaard T and Bozhevolnyi S I 2004 Surface plasmon polariton scattering by a small particle placed near a metal surface: an analytical study *Phys. Rev. B* **69** 045422
- [43] Beermann J, Novikov S M, Holmgaard T, Eriksen R L, Albrektsen O, Pedersen K and Bozhevolnyi S I 2012 Polarization-resolved two-photon luminescence microscopy of V-Groove arrays *Opt. Express* **20** 654–62
- [44] Varnavski O P, Mohamed M B, El-Sayed M A and Goodson T III 2003 Relative enhancement of ultrafast emission in gold nanorods *J. Phys. Chem. B* **107** 3101–4
- [45] Palik E D 1985 *Handbook of Optical Constants of Solids* (New York: Academic)

Authorship agreements

Authorship agreement

This authorship agreement concerns the published research work conducted by PhD Student Alexander S. Roberts, Anders Pors, Ole Albrektsen and Sergey I. Bozhevolnyi. The research work includes the following article:

Nano Letters, 14 (2), pp 783-787

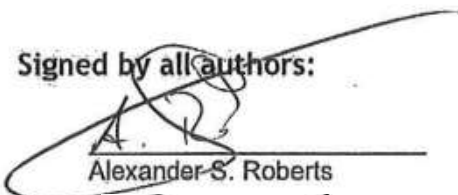
Subwavelength Plasmonic Color Printing Protected for Ambient Use

In accordance with the criteria put forward at the Vancouver Convention for authorship (www.icmje.org), the undersigned Alexander S. Roberts confirms that he as first author is responsible for

- A substantial contribution to the intellectual content
- Main Author (Wrote all drafts and final version of the paper)
- All figures
- Chip- and wafer-scale fabrication of all examined structures
- Scripts for image analysis and exposure of colour prints
- Characterisation of all examined structures
- Treatment of experimental data

Similarly, the undersigned Valentyn Anders Pors, Ole Albrektsen and Sergey I. Bozhevolnyi, confirm that they as co-authors have contributed quantitatively to the conception and design, the critical revision for important intellectual content, the interpretation of experimental evidence, and the final approval of the version to be published. As senior researcher, Sergey I. Bozhevolnyi stands as guarantor and takes public responsibility for the integrity of the research work as a whole, from inception to published articles.

Signed by all authors:



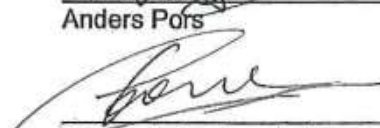
Alexander S. Roberts



Ole Albrektsen



Anders Pors



Sergey I. Bozhevolnyi

Authorship agreement

This authorship agreement concerns the published research work conducted by PhD Student Alexander S. Roberts, Manohar Chirumamilla, Kasper Thilsing-Hansen, Kjeld Pedersen and Sergey I. Bozhevolnyi. The research work includes the following article:

Optics Express 23 (19), A1111-A1119

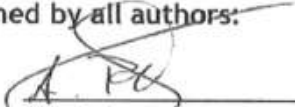
Near-infrared tailored thermal emission from wafer-scale continuous-film resonators

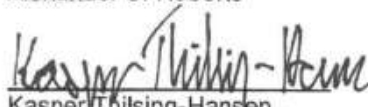
In accordance with the criteria put forward at the Vancouver Convention for authorship (www.icmje.org), the undersigned Alexander S. Roberts confirms that he as first author is responsible for

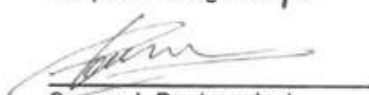
- A substantial contribution to the intellectual content
- Main Author (Wrote all drafts and final version of the paper)
- All figures
- Setup for experimental data acquisition
- Characterisation of all examined structures
- Treatment of experimental data

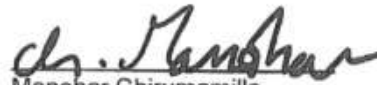
Similarly, the undersigned Anders Pors, Ole Albrektsen and Sergey I. Bozhevolnyi, confirm that they as co-authors have contributed quantitatively to the conception and design, the critical revision for important intellectual content, the interpretation of experimental evidence, and the final approval of the version to be published. As senior researcher, Sergey I. Bozhevolnyi stands as guarantor and takes public responsibility for the integrity of the research work as a whole, from inception to published articles.

Signed by all authors:


Alexander S. Roberts


Kasper Thilsing-Hansen


Sergey I. Bozhevolnyi


Manohar Chirumamilla


Kjeld Pedersen

Authorship agreement

This authorship agreement concerns the published research work conducted by Shailesh Kumar, Jens L. Lausen, Cesar E. Garcia-Ortiz, Sebastian K. H. Andersen, PhD Student Alexander S. Roberts, Ilya P. Radko, Cameron L. C. Smith, Anders Kristensen and Sergey I. Bozhevolnyi. The research work includes the following article:

Journal of Optics, 18 (2), 024002

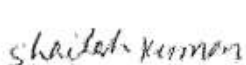
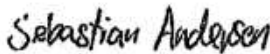
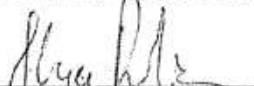
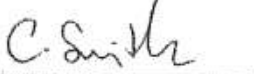
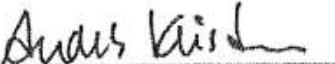
Excitation of surface plasmon polariton modes with multiple nitrogen vacancy centers in single nanodiamonds

In accordance with the criteria put forward at the Vancouver Convention for authorship (www.icmje.org), the undersigned Alexander S. Roberts confirms that he a co-author is responsible for

- A substantial contribution to the intellectual content
- SEM and AFM imaging of nanodiamonds
- Defining PMMA traps for controlled positioning of multiple nanodiamonds
- Constructive and critical feedback on drafts of the paper

Similarly, the undersigned Shailesh Kumar, Jens L. Lausen, Cesar E. Garcia-Ortiz, Sebastian K. H. Andersen, Ilya P. Radko, Cameron L. C. Smith, Anders Kristensen and Sergey I. Bozhevolnyi, confirm that they as co-authors have contributed quantitatively to the conception and design, the critical revision for important intellectual content, the interpretation of experimental evidence, and the final approval of the version to be published. As senior researcher, Sergey I. Bozhevolnyi stands as guarantor and takes public responsibility for the integrity of the research work as a whole, from inception to published articles.

Signatures of all authors:

 Shailesh Kumar	 Jens L. Lausen	 Cesar E. Garcia-Ortiz
 Sebastian K. H. Andersen	 Alexander S. Roberts	 Ilya P. Radko
 Cameron L. C. Smith	 Anders Kristensen	 Sergey I. Bozhevolnyi

Authorship agreement

This authorship agreement concerns the published research work conducted by PhD Student Alexander S. Roberts, Thomas Søndergaard, Manohar Chirumamilla, Anders Pors, Jonas Beermann, Kjeld Pedersen and Sergey I. Bozhevolnyi. The research work includes the following article:

Phys. Rev. B 93, 075413

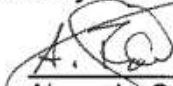
Light extinction and scattering from individual and arrayed high-aspect-ratio trenches in metals

In accordance with the criteria put forward at the Vancouver Convention for authorship (www.icmje.org), the undersigned Alexander S. Roberts confirms that he as first author is responsible for

- A substantial contribution to the intellectual content
- Main Author (Wrote all drafts and final version of the paper, excluding appendices)
- All figures
- Performed all linear spectroscopy measurements and microscopy imaging
- Co-performed TPL measurements
- Performed all finite-element calculations

Similarly, the undersigned Thomas Søndergaard, Manohar Chirumamilla, Anders Pors, Jonas Beermann, Kjeld Pedersen and Sergey I. Bozhevolnyi, confirm that they as co-authors have contributed quantitatively to the conception and design, the critical revision for important intellectual content, the interpretation of experimental evidence, and the final approval of the version to be published. As senior researcher, Sergey I. Bozhevolnyi stands as guarantor and takes public responsibility for the integrity of the research work as a whole, from inception to published articles.

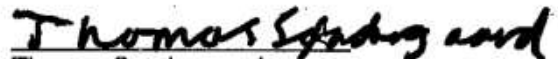
Signed by all authors:


Alexander S. Roberts

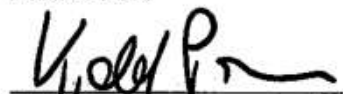

Manohar Chirumamilla


Jonas Beermann


Sergey I. Bozhevolnyi


Thomas Søndergaard


Anders Pors


Kjeld Pedersen

Authorship agreement

This authorship agreement concerns the published research work conducted by Manohar Chirumamilla, Alexander S Roberts, Fei Ding, Deyong Wang, Peter Kjær Kristensen, Sergey I Bozhevolnyi, Kjeld Pedersen. The research work includes the following article:

Optical Materials Express 6 (8), 2704

Multilayer tungsten-alumina-based broadband light absorbers for high-temperature applications

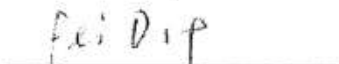
In accordance with the criteria put forward at the Vancouver Convention for authorship (www.icmje.org), the undersigned Alexander S. Roberts confirms that he a co-author is responsible for

- A substantial contribution to the intellectual content
- All transfer-matrix simulations
- Ellipsometric measurements
- Significant input during the drafting phase
- Constructive and critical feedback on drafts of the paper

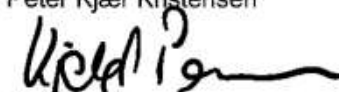
Similarly, the undersigned Manohar Chirumamilla, Fei Ding, Deyong Wang, Peter Kjær Kristensen, Sergey I Bozhevolnyi, Kjeld Pedersen, confirm that they as co-authors have contributed quantitatively to the conception and design, the critical revision for important intellectual content, the interpretation of experimental evidence, and the final approval of the version to be published. As senior researcher, Kjeld Pedersen stands as guarantor and takes public responsibility for the integrity of the research work as a whole, from inception to published articles.

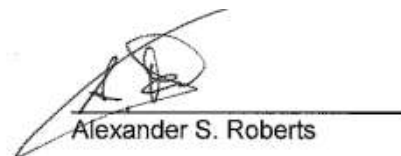
Signatures of all authors:

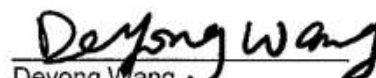

Manohar Chirumamilla

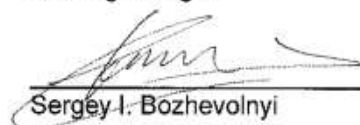

Fei Ding


Peter Kjær Kristensen


Kjeld Pedersen


Alexander S. Roberts


Deyong Wang


Sergey I. Bozhevolnyi

Authorship agreement

This authorship agreement concerns the published research work conducted by Manohar Chirumamilla, Anisha Chirumamilla, Alexander S Roberts, Remo Proietti Zaccaria, Francesco De Angelis, Peter Kjær Kristensen, Roman Krahne, Sergey I Bozhevolnyi, Kjeld Pedersen, Andrea Toma. The research work includes the following article:

Advanced Optical Materials 5 (4), 1600836
Hot-Spot Engineering in 3D Multi-Branched Nanostructures: Ultrasensitive Substrates for Surface-Enhanced Raman Spectroscopy

In accordance with the criteria put forward at the Vancouver Convention for authorship (www.icmje.org), the undersigned Alexander S. Roberts confirms that he a co-author is responsible for

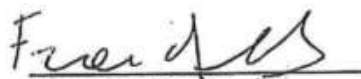
- A substantial contribution to the intellectual content
- All linear optical spectroscopy measurements
- Significant input during the drafting phase
- Constructive and critical feedback on drafts of the paper

Similarly, the undersigned Manohar Chirumamilla, Anisha Chirumamilla, Alexander S Roberts, Remo Proietti Zaccaria, Francesco De Angelis, Peter Kjær Kristensen, Roman Krahne, Sergey I Bozhevolnyi, Kjeld Pedersen, Andrea Toma, confirm that they as co-authors have contributed quantitatively to the conception and design, the critical revision for important intellectual content, the interpretation of experimental evidence, and the final approval of the version to be published. As senior researcher, Kjeld Pedersen stands as guarantor and takes public responsibility for the integrity of the research work as a whole, from inception to published articles.

Signatures of all authors:


Manohar Chirumamilla

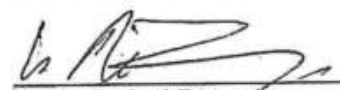

Alexander S. Roberts

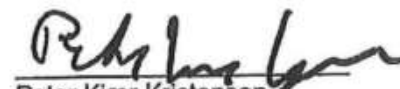

Francesco De Angelis

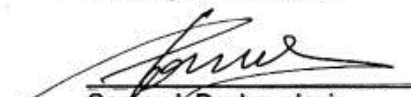

Roman Krahne

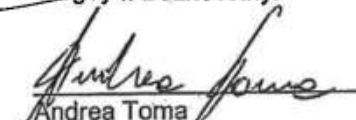

Kjeld Pedersen


Anisha Chirumamilla


Remo Proietti Zaccaria


Peter Kjær Kristensen


Sergey I. Bozhevolnyi


Andrea Toma

References

- [1] I. E. Agency, “Key world energy statistics 2016.” www.iea.org/publications/freepublications/publication/key-world-energy-statistics.html. Accessed 07-April-2017.
- [2] W. Shockley and H. J. Queisser, “Detailed balance limit of efficiency of p-n junction solar cells,” *Journal of applied physics*, vol. 32, no. 3, pp. 510–519, 1961.
- [3] P. Landsberg and P. Baruch, “The thermodynamics of the conversion of radiation energy for photovoltaics,” *Journal of Physics A: Mathematical and General*, vol. 22, no. 11, p. 1911, 1989.
- [4] Y. Xu, T. Gong, and J. N. Munday, “The generalized shockley-queisser limit for nanostructured solar cells,” *Scientific reports*, vol. 5, 2015.
- [5] J. Parrott, “The limiting efficiency of an edge-illuminated multigap solar cell,” *Journal of Physics D: Applied Physics*, vol. 12, no. 3, p. 441, 1979.
- [6] A. Luque and A. Martí, “Increasing the efficiency of ideal solar cells by photon induced transitions at intermediate levels,” *Physical Review Letters*, vol. 78, no. 26, p. 5014, 1997.
- [7] T. Trupke, M. Green, and P. Würfel, “Improving solar cell efficiencies by up-conversion of sub-band-gap light,” *Journal of Applied Physics*, vol. 92, no. 7, pp. 4117–4122, 2002.
- [8] T. Trupke, M. Green, and P. Würfel, “Improving solar cell efficiencies by down-conversion of high-energy photons,” *Journal of Applied Physics*, vol. 92, no. 3, pp. 1668–1674, 2002.
- [9] N.-P. Harder and P. Würfel, “Theoretical limits of thermophotovoltaic solar energy conversion,” *Semiconductor Science and Technology*, vol. 18, no. 5, p. S151, 2003.
- [10] H. Kolm, “Solar-battery power source,” *Quarterly Progress Report*, vol. 13, 1956.
- [11] D. C. White, B. D. Wedlock, and J. Blair, “Recent advances in thermal energy conversion,” in *Proc. of the 15th Annual Power Sources Conference*, pp. 20–22, 1961.
- [12] G. Guazzoni, E. Kittl, and S. Shapiro, “Rare earth radiators for thermophotovoltaic energy conversion,” in *Electron Devices Meeting, 1968 International*, pp. 130–130, IEEE, 1968.
- [13] B. Bitnar, J.-C. Mayor, W. Durisch, A. Meyer, G. Palfinger, F. von Roth, H. Sigg, T. J. Coutts, G. Guazzoni, and J. Luther, “Record electricity-to-gas power efficiency of a silicon solar cell based tpv system,” in *AIP Conference Proceedings*, vol. 653, pp. 18–28, AIP, 2003.

- [14] K. Qiu and A. Hayden, "Thermophotovoltaic power generation systems using natural gas-fired radiant burners," *Solar energy materials and solar cells*, vol. 91, no. 7, pp. 588–596, 2007.
- [15] A. Datas and C. Algora, "Development and experimental evaluation of a complete solar thermophotovoltaic system," *Progress in Photovoltaics: Research and Applications*, vol. 21, no. 5, pp. 1025–1039, 2013.
- [16] A. Lenert, D. M. Bierman, Y. Nam, W. R. Chan, I. Celanović, M. Soljačić, and E. N. Wang, "A nanophotonic solar thermophotovoltaic device," *Nature nanotechnology*, vol. 9, no. 2, pp. 126–130, 2014.
- [17] M. Shimizu, A. Kohiyama, and H. Yugami, "High-efficiency solar-thermophotovoltaic system equipped with a monolithic planar selective absorber/emitter," *Journal of Photonics for Energy*, vol. 5, no. 1, pp. 053099–053099, 2015.
- [18] G. Palfinger, B. Bitnar, W. Durisch, J.-C. Mayor, D. Grützmacher, and J. Gobrecht, "Cost estimate of electricity produced by tpv," *Semiconductor science and technology*, vol. 18, no. 5, p. S254, 2003.
- [19] M. Bianchi, C. Ferrari, F. Melino, and A. Peretto, "Feasibility study of a thermo-photo-voltaic system for chp application in residential buildings," *Applied energy*, vol. 97, pp. 704–713, 2012.
- [20] L. M. Fraas, "Tpv fireplace insert or tpv indoor heating stove," Mar. 14 2000. US Patent 6,037,536.
- [21] L. Fraas, J. Avery, and H. Huang, "Thermophotovoltaic furnace-generator for the home using low bandgap gasb cells," *Semiconductor Science and Technology*, vol. 18, no. 5, p. S247, 2003.
- [22] K. Qiu and A. Hayden, "Implementation of a {TPV} integrated boiler for micro-chp in residential buildings," *Applied Energy*, vol. 134, pp. 143 – 149, 2014.
- [23] K. Qiu and A. Hayden, "Direct thermal to electrical energy conversion using very low bandgap tpv cells in a gas-fired furnace system," *Energy Conversion and Management*, vol. 79, pp. 54–58, 2014.
- [24] N. F. Salstrom, "Recycling heat from industrial processes to generate electricity using a thermophotovoltaic generator," Sept. 16 2003. US Patent 6,620,998.
- [25] A. P. Raman, M. A. Anoma, L. Zhu, E. Rephaeli, and S. Fan, "Passive radiative cooling below ambient air temperature under direct sunlight," *Nature*, vol. 515, no. 7528, pp. 540–544, 2014.
- [26] O. Ilic, P. Bermel, G. Chen, J. D. Joannopoulos, I. Celanovic, and M. Soljačić, "Tailoring high-temperature radiation and the resurrection of the incandescent source," *Nature nanotechnology*, vol. 11, no. 4, pp. 320–324, 2016.
- [27] J. C. Maxwell, "A dynamical theory of the electromagnetic field," *Philosophical Transactions of the Royal Society of London*, pp. 459–512, 1865.

- [28] M. Born and E. Wolf, *Principles of optics: electromagnetic theory of propagation, interference and diffraction of light*. Elsevier, 1980.
- [29] L. Plattner, *A study in biomimetics: nanometer-scale, high-efficiency, dielectric diffractive structures on the wings of butterflies and in the silicon chip factory*. PhD thesis, University of Southampton, 2003.
- [30] J. Chilwell and I. Hodgkinson, "Thin-films field-transfer matrix theory of planar multilayer waveguides and reflection from prism-loaded waveguides," *JOSA A*, vol. 1, no. 7, pp. 742–753, 1984.
- [31] L. A. Pettersson, L. S. Roman, and O. Inganäs, "Modeling photocurrent action spectra of photovoltaic devices based on organic thin films," *Journal of Applied Physics*, vol. 86, no. 1, p. 487, 1999.
- [32] M. C. Tropicovsky, A. S. Sabau, A. R. Lupini, and Z. Zhang, "Transfer-matrix formalism for the calculation of optical response in multilayer systems: from coherent to incoherent interference," *Optics express*, vol. 18, no. 24, pp. 24715–24721, 2010.
- [33] C. C. Katsidis and D. I. Siapkas, "General transfer-matrix method for optical multilayer systems with coherent, partially coherent, and incoherent interference," *Applied optics*, vol. 41, no. 19, pp. 3978–3987, 2002.
- [34] J. Xia, A. K. Jordan, and J. A. Kong, "Inverse-scattering view of modal structures in inhomogeneous optical waveguides," *JOSA A*, vol. 9, no. 5, pp. 740–748, 1992.
- [35] L. Walpita, "Solutions for planar optical waveguide equations by selecting zero elements in a characteristic matrix," *JOSA A*, vol. 2, no. 4, pp. 595–602, 1985.
- [36] H. Raether, *Surface plasmons on smooth surfaces*. Springer, 1988.
- [37] S. I. Bozhevolnyi and J. Jung, "Scaling for gap plasmon based waveguides," *Optics express*, vol. 16, no. 4, pp. 2676–2684, 2008.
- [38] P. B. Johnson and R.-W. Christy, "Optical constants of the noble metals," *Physical review B*, vol. 6, no. 12, p. 4370, 1972.
- [39] F. Mandl, *Statistical Physics*. CIBA Foundation Symposium, Wiley, 1988.
- [40] W. Peter *et al.*, *Physics of solar cells: from principles to new concepts*. John Wiley & Sons, 2008.
- [41] D. R. Williams, "Sun fact sheet." <https://nssdc.gsfc.nasa.gov/planetary/factsheet/sunfact.html>, accessed 15-January-2017.
- [42] D. A. Ostlie and B. W. Carroll, *An introduction to modern astrophysics*. Benjamin Cummings, 2006.

- [43] M. Planck, "Ueber das gesetz der energieverteilung im normalspectrum," *Annalen der physik*, vol. 309, no. 3, pp. 553–563, 1901.
- [44] G. Kirchhoff, "Ueber das verhältniss zwischen dem emissionsvermögen und dem absorptionsvermögen der körper für wärme und licht," *Annalen der Physik*, vol. 185, no. 2, pp. 275–301, 1860.
- [45] J.-J. Greffet and M. Nieto-Vesperinas, "Field theory for generalized bidirectional reflectivity: derivation of helmholtz's reciprocity principle and kirchhoff's law," *JOSA A*, vol. 15, no. 10, pp. 2735–2744, 1998.
- [46] J. H. Kim, S. M. Jung, and M. W. Shin, "High-temperature degradation of one-dimensional metallodielectric (w/sio₂) photonic crystal as selective thermal emitter for thermophotovoltaic system," *Optical Materials*, vol. 72, pp. 45–51, 2017.
- [47] D. Trotter and A. Sievers, "Spectral selectivity of high-temperature solar absorbers," *Applied optics*, vol. 19, no. 5, pp. 711–728, 1980.
- [48] V. Rinnerbauer, A. Lenert, D. M. Bierman, Y. X. Yeng, W. R. Chan, R. D. Geil, J. J. Senkevich, J. D. Joannopoulos, E. N. Wang, M. Soljačić, *et al.*, "Metallic photonic crystal absorber-emitter for efficient spectral control in high-temperature solar thermophotovoltaics," *Advanced Energy Materials*, vol. 4, no. 12, 2014.
- [49] A. S. Roberts, A. Pors, O. Albrektsen, and S. I. Bozhevolnyi, "Subwavelength plasmonic color printing protected for ambient use," *Nano letters*, vol. 14, no. 2, pp. 783–787, 2014.
- [50] A. S. Roberts, T. Søndergaard, M. Chirumamilla, A. L. Pors, J. Beermann, K. Pedersen, and S. I. Bozhevolnyi, "Scattering and extinction from high-aspect-ratio trenches," *Meeting of the Danish Optical Society*, 2015.
- [51] J. Yu, Y. Shen, X. Liu, R. Fu, J. Zi, and Z. Zhu, "Absorption in one-dimensional metallic-dielectric photonic crystals," *Journal of Physics: Condensed Matter*, vol. 16, no. 7, p. L51, 2004.
- [52] N. Ahmad, J. Stokes, N. Fox, M. Teng, and M. Cryan, "Ultra-thin metal films for enhanced solar absorption," *Nano Energy*, vol. 1, no. 6, pp. 777–782, 2012.
- [53] S. Shu, Z. Li, and Y. Y. Li, "Triple-layer fabry-perot absorber with near-perfect absorption in visible and near-infrared regime," *Optics express*, vol. 21, no. 21, pp. 25307–25315, 2013.
- [54] M. Yan, "Metal-insulator-metal light absorber: a continuous structure," *Journal of Optics*, vol. 15, no. 2, p. 025006, 2013.
- [55] M. A. Kats, R. Blanchard, P. Genevet, and F. Capasso, "Nanometre optical coatings based on strong interference effects in highly absorbing media," *Nature materials*, vol. 12, no. 1, pp. 20–24, 2013.

- [56] W. Wang, Y. Cui, Y. He, Y. Hao, Y. Lin, X. Tian, T. Ji, and S. He, "Efficient multiband absorber based on one-dimensional periodic metal–dielectric photonic crystal with a reflective substrate," *Optics letters*, vol. 39, no. 2, pp. 331–334, 2014.
- [57] H. Deng, Z. Li, L. Stan, D. Rosenmann, D. Czaplewski, J. Gao, and X. Yang, "Broadband perfect absorber based on one ultrathin layer of refractory metal," *Optics letters*, vol. 40, no. 11, pp. 2592–2595, 2015.
- [58] J. Nie and H.-Q. Li, "Ultrabroadband perfect terahertz absorber based on a metal-and insulator-stacked structure," *JOSA B*, vol. 33, no. 12, pp. 2602–2608, 2016.
- [59] B. Liu, G. Lu, L. Cui, J. Li, F. Sun, F. Liu, Y. Li, T. Yang, and G. Du, "Experimental investigation of multiple near-perfect absorptions in sandwich structures containing thin metallic films," *Optics Express*, vol. 25, no. 12, pp. 13271–13277, 2017.
- [60] C. Qu, S. Ma, J. Hao, M. Qiu, X. Li, S. Xiao, Z. Miao, N. Dai, Q. He, S. Sun, *et al.*, "Tailor the functionalities of metasurfaces based on a complete phase diagram," *Physical review letters*, vol. 115, no. 23, p. 235503, 2015.
- [61] A. D. Rakić, A. B. Djurišić, J. M. Elazar, and M. L. Majewski, "Optical properties of metallic films for vertical-cavity optoelectronic devices," *Applied optics*, vol. 37, no. 22, pp. 5271–5283, 1998.
- [62] P. Couchman and W. Jesser, "Thermodynamic theory of size dependence of melting temperature in metals," *Nature*, vol. 269, pp. 481–483, 1977.
- [63] M. Zhang, M. Y. Efremov, F. Schiettekatte, E. Olson, A. Kwan, S. Lai, T. Wisleder, J. Greene, and L. Allen, "Size-dependent melting point depression of nanostructures: nanocalorimetric measurements," *Physical Review B*, vol. 62, no. 15, p. 10548, 2000.
- [64] M. Alcoutlabi and G. B. McKenna, "Effects of confinement on material behaviour at the nanometre size scale," *Journal of Physics: Condensed Matter*, vol. 17, no. 15, p. R461, 2005.
- [65] M. Wautelet, "On the shape dependence of the melting temperature of small particles," *Physics Letters A*, vol. 246, no. 3, pp. 341–342, 1998.
- [66] W. Qi, "Size effect on melting temperature of nanosolids," *Physica B: Condensed Matter*, vol. 368, no. 1, pp. 46–50, 2005.
- [67] H.-Y. Chen and F.-H. Lu, "Oxidation behavior of titanium nitride films," *Journal of Vacuum Science & Technology A: Vacuum, Surfaces, and Films*, vol. 23, no. 4, pp. 1006–1009, 2005.
- [68] J. Desmaison, P. Lefort, and M. Billy, "Oxidation mechanism of titanium nitride in oxygen," *Oxidation of Metals*, vol. 13, no. 6, pp. 505–517, 1979.
- [69] M. Mauk and V. Andreev, "Gasb-related materials for tpv cells," *Semiconductor science and technology*, vol. 18, no. 5, p. S191, 2003.

- [70] R. Miles, K. Hynes, and I. Forbes, "Photovoltaic solar cells: An overview of state-of-the-art cell development and environmental issues," *Progress in Crystal Growth and Characterization of Materials*, vol. 51, no. 1, pp. 1–42, 2005.
- [71] C. Liu, Y. Li, Y. Zeng, *et al.*, "Progress in antimonide based iii-v compound semiconductors and devices," *Engineering*, vol. 2, no. 08, p. 617, 2010.
- [72] T. Minami, "Transparent conducting oxide semiconductors for transparent electrodes," *Semiconductor Science and Technology*, vol. 20, no. 4, p. S35, 2005.
- [73] D. S. Hecht, L. Hu, and G. Irvin, "Emerging transparent electrodes based on thin films of carbon nanotubes, graphene, and metallic nanostructures," *Advanced materials*, vol. 23, no. 13, pp. 1482–1513, 2011.
- [74] K. B. Narayana, "View factors for parallel rectangular plates," *Heat transfer engineering*, vol. 19, no. 1, pp. 59–63, 1998.
- [75] A. Cezairliyan, "Measurement of melting-point and electrical resistivity (above 3600 k) of tungsten by a pulse heating method," *High Temperature Science*, vol. 4, pp. 248–252, 1972.
- [76] A. Warren, A. Nylund, and I. Olefjord, "Oxidation of tungsten and tungsten carbide in dry and humid atmospheres," *International Journal of Refractory Metals and Hard Materials*, vol. 14, no. 5-6, pp. 345–353, 1996.
- [77] S. C. Cifuentes, M. Monge, and P. Pérez, "On the oxidation mechanism of pure tungsten in the temperature range 600–800 c," *Corrosion Science*, vol. 57, pp. 114–121, 2012.
- [78] E. Gulbransen and K. Andrew, "Kinetics of the oxidation of pure tungsten from 500 to 1300 c," *Journal of the Electrochemical Society*, vol. 107, no. 7, pp. 619–628, 1960.
- [79] W. W. Webb, J. T. Norton, and C. Wagner, "Oxidation of tungsten," *Journal of The Electrochemical Society*, vol. 103, no. 2, pp. 107–111, 1956.
- [80] J. Perepezko, J. Bero, R. Sakidja, I. Talmy, and J. Zaykoski, "Oxidation resistant coatings for refractory metal cermets," *Surface and Coatings Technology*, vol. 206, no. 19, pp. 3816–3822, 2012.
- [81] O. Lu-Steffes, R. Sakidja, J. Bero, and J. Perepezko, "Multicomponent coating for enhanced oxidation resistance of tungsten," *Surface and Coatings Technology*, vol. 207, pp. 614–619, 2012.
- [82] J. S. Bunch, S. S. Verbridge, J. S. Alden, A. M. Van Der Zande, J. M. Parpia, H. G. Craighead, and P. L. McEuen, "Impermeable atomic membranes from graphene sheets," *Nano letters*, vol. 8, no. 8, pp. 2458–2462, 2008.
- [83] S. Blankenburg, M. Bieri, R. Fasel, K. Müllen, C. A. Pignedoli, and D. Passerone, "Porous graphene as an atmospheric nanofilter," *Small*, vol. 6, no. 20, pp. 2266–2271, 2010.

-
- [84] M. Topsakal, H. Şahin, and S. Ciraci, “Graphene coatings: An efficient protection from oxidation,” *Physical Review B*, vol. 85, no. 15, p. 155445, 2012.
- [85] K. Kim, W. Regan, B. Geng, B. Alemán, B. Kessler, F. Wang, M. Crommie, and A. Zettl, “High-temperature stability of suspended single-layer graphene,” *physica status solidi (RRL)-Rapid Research Letters*, vol. 4, no. 11, pp. 302–304, 2010.
- [86] B.-S. Nguyen, J.-F. Lin, and D.-C. Perng, “1-nm-thick graphene tri-layer as the ultimate copper diffusion barrier,” *Applied Physics Letters*, vol. 104, no. 8, p. 082105, 2014.

List of publications

Articles in peer-reviewed journals

1. A. S. Roberts, A. Pors, O. Albrektsen, and S. I. Bozhevolnyi, "Subwavelength plasmonic color printing protected for ambient use," *Nano letters*, vol. 14, no. 2, pp. 783–787, 2014.
2. A. S. Roberts, M. Chirumamilla, K. Thilsing-Hansen, K. Pedersen, and S. I. Bozhevolnyi, "Near-infrared tailored thermal emission from wafer-scale continuous-film resonators," *Optics express*, vol. 23, no. 19, pp. A1111–A1119, 2015.
3. S. Kumar, J. L. Lausen, C. E. Garcia-Ortiz, S. K. Andersen, A. S. Roberts, I. P. Radko, C. L. Smith, A. Kristensen, and S. I. Bozhevolnyi, "Excitation of surface plasmon polariton modes with multiple nitrogen vacancy centers in single nanodiamonds," *Journal of Optics*, vol. 18, no. 2, p. 024002, 2015.
4. A. S. Roberts, T. Søndergaard, M. Chirumamilla, A. Pors, J. Beermann, K. Pedersen, and S. I. Bozhevolnyi, "Light extinction and scattering from individual and arrayed high-aspect-ratio trenches in metals," *Physical Review B*, vol. 93, no. 7, p. 075413, 2016.
5. A. S. Roberts, F. Ding, D. Wang, P. K. Kristensen, S. I. Bozhevolnyi, and K. Pedersen, "Multi-layer tungsten-alumina-based broadband light absorbers for high-temperature applications," *Optical Materials Express*, vol. 6, no. 8, pp. 2704–2714, 2016.
6. M. Chirumamilla, A. Chirumamilla, A. S. Roberts, R. P. Zaccaria, F. De Angelis, P. Kjær Kristensen, R. Krahne, S. I. Bozhevolnyi, K. Pedersen, and A. Toma, "Hot-spot engineering in 3d multi-branched nanostructures: Ultrasensitive substrates for surface-enhanced raman spectroscopy," *Advanced Optical Materials*, vol. 5, no. 4, 2017.
7. M. Chirumamilla, A. Chirumamilla, Y. Yang, A. S. Roberts, P. K. Kristensen, K. Chaudhuri, A. Boltasseva, D. S. Sutherland, S. I. Bozhevolnyi, and K. Pedersen, "Large-area ultra-broadband absorber for solar thermophotovoltaics based on 3d titanium nitride nanopillars," *submitted*, 2017.
8. A. S. Roberts, M. Chirumamilla, D. Wang, L. An, K. Pedersen and S. I. Bozhevolnyi, "Refractory near-infrared emitter for thermophotovoltaics," *In preparation*, 2017.

9. A. S. Roberts, M. Chirumamilla, S- Xiao, K. Pedersen and S. I. Bozhevolnyi, "Low-temperature thermophotovoltaic device with a bi-layer, unstructured emitter for cogeneration in oxygenous atmosphere," *In preparation*, 2017.

Presentations

1. A. S. Roberts, "Et indblik i nanoverdenen," Invited talk, *IDA, Ingeniørforeningen*, 2014.
2. A. S. Roberts, K. Thilsing-Hansen, R. L. Eriksen, and S. I. Bozhevolnyi, "High temperature plasmonic structures for thermophotovoltaic applications," Poster presentation, *Nanolight*, 2014.
3. A. S. Roberts, T. Søndergaard, M. Chirumamilla, A. L. Pors, J. Beermann, K. Pedersen, and S. I. Bozhevolnyi, "Scattering and extinction from high-aspect-ratio trenches," Poster presentation, *Meeting of the Danish Optical Society*, 2015.
4. A. S. Roberts, M. Chirumilla, K. Thilsing-Hansen, K. Pedersen, and S. I. Bozhevolnyi, "Thermal near-infrared emission by resonant structures," Poster presentation, *NanoMeta*, 2015.
5. A. S. Roberts, M. Chirumilla, F. Ding, D. Wang, K. Pedersen, and S. I. Bozhevolnyi, "Omnidirectional and polarization-insensitive near-infrared emitters and solar absorbers for high-temperature applications," Poster presentation, *NanoMeta*, 2017.